THE UNIVERSITY *of* EDINBURGH

Modelling of wind turbine wakes in complex terrain using Computational Fluid Dynamics

Alexandros Makridis

Thesis submitted in fulfillment of
the requirements for the degree of
Doctor of Philosophy
to the
University of Edinburgh — 2012

Declaration

I declare that this thesis has been composed solely by myself and that it has not been submitted, either in whole or in part, in any previous application for a degree. Except where otherwise acknowledged, the work presented is entirely my own.

Alexandros Makridis

February 2012

Abstract

This thesis focuses on modelling of wind turbine wakes when they are affected by real complex terrain features, such as hills and forests, and also examines the effect of the rotational momentum imparted to the downstream wake from the rotor blades. Modelling work is carried out using the commercial Computational Fluid Dynamics (CFD) solver FLUENT.

Motivation for this project was the fact that there is currently limited knowledge on several issues that affect the operation of a wind farm in a complex terrain environment. Wind developers normally use commercial, easy-to-use software (such as WAsP) to predict the potential wind farm output , which are based on simple linear models to model wakes and wind flow orographic effects and have been calibrated for cases of simple terrain. In cases of complex terrain, they are expected to give errors due to arising non-linearities. After a review of the relevant literature, the chosen CFD procedure is explained. This involves the use of 3-D Reynolds Averaged Navier-Stokes equations using the Reynolds Stress Model for the turbulence closure, in order to account for the anisotropy in atmospheric turbulence. The Virtual Blade Model in FLUENT is demonstrated as a useful tool for modelling the rotor effects without the need of meshing the rotor geometry in detail and avoiding significant computational cost.

The approach is initially validated with the widely documented Nibe measurements, which involved full-scale observations of a single wake over flat terrain. The model is also tested in the case of a wind turbine operating at the summit of

an ideal, Gaussian hill. The wake development is examined in detail and in comparison with another CFD approach. Most notably, a slight divergence is found in the wake path as it evolves downwind. Additionally, the proposed approaches of modelling the neutral atmospheric flow over a real hill and over a forest are validated with full-scale measurements.

Ultimately, the work includes the modelling of real wind farms over complex terrain and validating the results with measurements. A coastal complex terrain wind farm is initially examined and results are validated with SCADA measurements and compared with results using the WAsP wind modelling software. Finally, a wind farm over hilly terrain and near forests is also considered and the effect of the forest in the wake is studied. Results are also validated with full-scale measurements.

Acknowledgements

I am extremely grateful to my supervisor Dr. John Chick, for his helpful guidance and continuing support throughout the research process. His motivating discussions and useful comments in our regular meetings were a key to the final completion of this thesis.

This work would not have been possible without the financial support of the State Scholarships Foundation in Greece (IKY), as it has fully funded my studies in Edinburgh for three and a half years (including one year for the MSc degree). I am also extremely grateful to Prof. Robin Wallace and IES for the generous additional financial support of this work and for providing me with the funding to attend the European Wind Energy Conference 2009.

I am indebted to Peter Stuart and the people in RES Group for providing me with extremely valuable wind farm data, which were used in Chapters 8 and 9 of this thesis. I would also like to thank Peter Stuart for his feedback and fruitful discussions. Deepest gratitude must also go to Nick Forrest for his sincere interest in my work. Without his invaluable help, it would have been impossible to find the necessary data for this work.

I am also grateful to Dr. Rebecca Barthelmie, for giving me useful guidance on the first year of my research, and to Prof. Bill Easson for his help on FLUENT CFD issues and for giving me the opportunity to help in the tutorials of the CFD 5^{th} year course. I would also like to thank Davoud Ahmadyar for the interesting

CFD discussions and I am thankful to the School IT Team for the high quality IT support throughout this thesis.

I would also like to thank Dr. Guillermo Rein for accepting me to the group of demonstrators in the 1st year mechanical engineering Strip and Rebuild labs and to Dr. Guillermo Rein and Dr. John Chick for giving me the chance to help in the 2nd year Mechanical Engineering Design courses and tutorials. Acknowledgements are also due to Dr. Tom Bruce for providing me with the possibility to be a tutor and demonstrator in the 2nd year Fluid Mechanics course and to Dr. Vengatesan Venugopal for giving me the chance to help in the tutorials of the 5th year MSc course, Mechanical Engineering Fundamentals of Renewable Energy. The teaching experience was undoubtedly an enjoyable break from the research work.

Last, but not least, I owe my deepest gratitude to my parents, Eleni Klingou and Dimitris Makridis for their constant support and encouragement, and to Anastasia Karandinou for her invaluable help and motivative discussions. Finally, I would like to thank all of my friends and colleagues in Edinburgh, for making my stay a pleasurable experience.

Contents

List of symbols

Roman Symbols

Δp	pressure drop	[Pa]
ΔS	non-dimensional velocity increase	[−]
$\dot{m}$	air mass per unit length of time	[kg/s]
$\boldsymbol{A}_f$	area of face f	[m^2]
A	cross sectional area	[m^2]
a	axial induction factor	[−]
a'	tangential induction factor	[−]
a_1, b_1, c_1	parameters of Gaussian distribution	[−]
B	empirical constant	[−]
c	chord length	[m]
C_1, C_2	turbulence model constants	[−]
C_D	drag coefficient	[−]
C_d	forest drag coefficient	[−]
C_L	lift coefficient	[−]
C_P	power coefficient	[−]
c_p	specific heat at constant pressure	[J/(kg K)]
C_s	roughness constant	[−]
C_T	thrust coefficient	[−]
C_z	Coefficient used in the canopy model ($= C_d\alpha$)	[−]
$C_{\epsilon 4}$, $C_{\epsilon 5}$	canopy model constants	[−]
C_μ, $C_{\varepsilon 1}$, $C_{\varepsilon 2}$	turbulence model constants	[−]
C_{ij}	Convection tensor in RSM	[−]
E	energy	[J]
E'	empirical wall-function constant	[−]
E_1	estimated fractional error	[−]

F	force	[N]
f	force per unit length	[N/m]
F'	Prandtl's tip loss factor	[−]
F_s	factor of safety	[−]
g	acceleration of gravity	[m/s^2]
h	height	[m]
I	turbulence intensity	[−]
I'	turbulence intensity	[−]
I_u, I_v, I_w	longitudinal, lateral and vertical turbulence intensity	[−]
k	turbulent kinetic energy	[m^2/s^2]
k'	wake decay constant in the WAsP wake model	[−]
K_s	equivalent sand-grain roughness height	[m]
K_s^+	dimensionless equivalent sand-grain roughness height	[−]
L'	half-length of the hill at the upwind mid-height	[m]
l_m	Mixing length	[m]
L_x,L_y,L_z	domain length, width, height	[m]
LAI	leaf area index	[−]
N	number	[−]
P	power	[MW]
p	static pressure	[Pa]
$p_\circ$	total pressure	[Pa]
P_{ij}	Stress Production tensor in RSM	[−]
Q	torque	[N·m]
q	order of convergence	[−]
R	rotor (tip) radius	[m]
r	spanwise coordinate	[m]
r_*	grid refinement ratio	[−]
s	hill slope	[−]
S_ε	source of ε	[kg/(ms^4)]
S_k	source of k	[kg/(ms^3)]
S_u	momentum source	[N/m^3]
sh, sc	parameters of Weibull distribution	[−]
T	temperature	[°C]
t	time	[s]
T'	rotation period	[s]

U	wind velocity	[m/s]
u	wind speed ratio	[−]
u^*, u_τ	wall-function friction velocities	[m/s]
u_*	ABL friction velocity	[m/s]
u_i'	fluctuating velocity component	[m/s]
V	volume	[m^3]
x, y, z	Cartesian coordinates	[m]
y^*	dimensionless wall-adjacent cell distance from the wall	[−]
$z_\circ$	roughness length	[m]
B_i	Boundary zones	[−]

Abbreviations

2-D	two-dimensional
3-D	three-dimensional
a.g.l.	above ground level
a.s.l.	above sea level
ABL	Atmospheric Boundary Layer
BC	Boundary Condition
BEM	Blade Element Momentum
BET	Blade Element Theory
BWEA	British Wind Energy Association
BZ	Bessel Expansion on a Zooming Grid model
CERL	Central Electricity Research Laboratories
CFD	Computational Fluid Dynamics
CLC2000	Corine Land Cover 2000
Corine	COoRdinate INformation on the Environment
CP	Centre Point
CPU	computing
DES	Detached Eddy Simulation
ECN	Energy research Centre of the Netherlands
ESDU	Engineering Sciences Data Unit
GAMBIT	Geometry And Mesh Building Intelligent Toolkit
GCI	Grid Convergence Index
HT	Hilltop
KTH	Royal Institute of Technology
LAD	Leaf Area Density

LES	Large Eddy Simulation
Ma	Mach number
MRF	Multiple Rotating Frame
NPARC	National Program for Applications-oriented Research in CFD
NURBS	Non-Uniform Rational B-Splines
PRESTO	PREssure STaggering Option
RANS	Reynolds Averaged Navier-Stokes
RE	Richardson Extrapolation
Re	Reynolds number
RES	Renewable Energy Systems Ltd.
RH	Richards and Hoxey
Ri	Richardson number
RNG	ReNormalization Group
RS	Reference Site
RSM	Reynolds Stress Model
SCADA	Supervisory Control And Data Acquisition
SIMPLEC	SIMPLE-Consistent
SMM	Sliding Mesh Model
SODAR	SOnic Detection And Ranging
SRF	Single Rotating Frame
SST	shear-stress transport
SWF	Standard Wall Functions
TNO	the Netherlands Organisation for Industrial Research
UDF	User-Defined Function
UDM	User-Defined Memory
VBM	Virtual Blade Model
WAsP	the Wind Atlas Analysis and Application Program
WT	Wind Turbine

Greek Symbols

α	angle of attack	$[^\circ]$
α	forest leaf area density	$[\mathrm{m}^2/\mathrm{m}^3]$
α'	Canopy model dimensionless coefficient ($= 0.05$)	$[-]$
β	pitch angle	$[^\circ]$
β^*	k-ω model constant	$[-]$
β_p, β_d	canopy model constants	$[-]$

β_{du}, β_{dv}, β_{dw}	RSM canopy model constants	[−]
χ	grid spacing	[m]
δ_{ij}	Kronecker delta	[−]
ϵ	relative error	[−]
Γ	adiabatic lapse rate	[°C/(100 m)]
κ	Von Karman constant	[−]
λ	tip speed ratio	[−]
μ	viscosity	[kg/(ms)]
μ_t	turbulent viscosity	[kg/(ms)]
ν	kinematic molecular viscosity	[m^2/s]
Ω	rotational speed	[rad/s]
ω	specific dissipation rate	[s^{-1}]
ϕ	flow variable	[−]
ϕ_{ij}	Pressure Strain tensor in RSM	[−]
ψ	VBM bank angle	[°]
ρ	air density	[kg/m^3]
σ_k, σ_ε	turbulence model constants	[−]
σ_P	standard deviation of power	[MW]
σ_U	standard deviation of velocity	[m/s]
σ_u, σ_v, σ_w	standard deviations of velocity components	[m/s]
τ_w	wall shear stress	[Pa]
τ_{ij}	Reynolds stress tensor	[kg/(ms^2)]
θ	azimuthal angle	[rad]
ε	turbulence dissipation rate	[m^2/s^3]
ε_{ij}	Dissipation tensor in RSM	[−]
φ	angle at which U_{rel} acts to the disc plane	[°]
ξ	vorticity	[1/s]
ζ	normalised turbulent velocity	[−]

Subscripts

$_{tot}$	total
$_\circ$	reference
$_b$	blades
$_D$	drag
$_d$	disc
$_f$	face

$_i$	i direction
$_L$	lift
$_n$	node
$_P$	wall-adjacent cell
$_T$	thrust
$_t$	tangential
$_w$	far wake
$_\infty$	freestream
$_{\text{no WT}}$	no rotor in operation
$_{\text{WT}}$	rotor in operation
$_{abl}$	atmospheric boundary layer
$_{ad}$	adiabatic
$_{cell}$	per cell
$_{def}$	deficit
$_{frac}$	fraction
$_{grid}$	grid cells
$_{ijk}$	indices
$_n$	normal
$_{rel}$	relative
$_{rot}$	rotor cells
$_{xyz}$	Cartesian components

Chapter 1

Introduction

1.1 General context

Wind turbines are frequently clustered in large wind farms. Given the restrictions related to the cost and use of land, the machines tend to be spaced as close as possible to each other. However, such arrangements cause additional problems, as the wakes of wind turbines influence the operation of downwind machines, causing reduced power output and increased loads. For this reason, the optimisation of the machine layout in a wind farm requires successful predictions of wind turbine wakes, in order to avoid their negative effects as much as possible.

This thesis addresses the issue of wind turbine wakes in complex terrain wind farms. Such onshore arrangements are increasingly popular in southern European countries, such as Spain and Greece, but also in Scotland and other parts of continental Europe where complex orographic features or the presence of forests affects the wind flow.

Simple and easy-to-use commercial software and codes used by wind developers are able to predict wake behaviour (especially far wakes) rather successfully for the cases of almost flat or water terrain, but they are expected to fail in complex

terrain conditions, where non-linear effects are expected. CFD modelling can be used in such cases as a more reliable tool for the simulation of the flow.

1.2 Aims and objectives

The main objective of this thesis is to contribute to the understanding of how wind turbine wakes are influenced by certain terrain complexities, such as orographic features or the presence of forest canopies. The main tool for this purpose was the use of the commercial Computational Fluid Dynamics (CFD) software FLUENT.

To achieve the above, a number of separate steps was considered necessary:

- Establish a CFD method of modelling a single wind turbine wake over flat terrain.
- Establish a CFD technique of modelling the wind flow over hilly terrain and over forests.
- Combine the previous two steps and model wind turbine wakes over complex terrain; perform a comparison with flat terrain cases.
- Test the approach in cases of real complex terrain wind farms and validate the results with full-scale measurements.
- Compare the results of the CFD modelling approach with results of using simple models, such as WAsP.

1.3 Thesis outline

The following Chapters of this thesis are organised as follows:

In Chapter 2, a literature review of the most relevant research to date is performed. The analysis includes previous experimental and modelling studies on the field

of wind turbine wakes, wind flow over complex terrain and wakes over complex terrain.

In Chapter 3, the followed CFD methodology is explained in detail. This includes the rotor actuator disc model, the choice of turbulence model, the approach for modelling the neutral Atmospheric Boundary Layer (ABL), the wall functions modifications, the approach concerning the CFD domain and boundary conditions, and the flow solver configurations.

Chapter 4 contains a study of a single wake case of a machine operating in neutral ABL flow. The CFD neutral ABL modelling approach is initially tested in an empty, 2-D domain. The wake modelling technique is then validated against the Nibe, single wake measurements and a grid dependence study is performed.

Chapter 5 involves the investigation of the wind flow and wind turbine wakes over an ideal hill of a Gaussian shape. Different ambient turbulence configurations are used and the results are compared with corresponding wake simulations over flat terrain.

The neutral atmospheric wind flow over real complex terrain was simulated in Chapter 6. The flow over Askervein hill was modelled and validated with full-scale measurements.

In Chapter 7, a model for the simulation of forest canopy flows is described in detail. The approach is tested in the case of a simple forest over flat terrain and results are also validated against full-scale measurements.

A real complex terrain wind farm at a coastal site is modelled in Chapter 8 using the CFD approach developed in the previous chapters, as well as the commercial, wind-developers software, WAsP. The 10-min, SCADA, measurements at the wind turbines are processed and used for the validation of the WAsP and CFD results.

Chapter 9 involves the simulation of another real complex terrain wind farm near forest canopies. The canopy model developed in Chapter 7, was used along with

the techniques of Chapter 8 to investigate the effect of forest canopies in the wakes.

Finally, the main conclusions of the thesis are summarised in Chapter 10.

Appendix A includes some additional information on the airfoils considered: data on the lift and drag coefficients versus the angle of attack which were used in the rotor modelling approach. Appendix B explains in more detail the derivation of some of the forest canopy model constants. Appendix C includes an example of a FLUENT User Defined Function (UDF), used in the CFD simulations.

Chapter 2

Literature review

2.1 Introduction

In this Chapter, the most relevant to this thesis theory and literature-to-date are presented. Initially, some of the main characteristics of the Atmospheric Boundary Layer are discussed. Afterwards, theory and previous work related to wind turbine wakes is presented; published literature on the issue of wind flow over complex terrain is then assessed independently. Finally, the last section presents a review of the body of (experimental and modelling) work involving the combined problem of wakes in complex terrain. In addition to the literature review, the contribution of this thesis to the previous CFD work is added at the end of the following subsections: 2.3.5, 2.4.1, 2.4.2 and 2.5.2.

2.2 The Atmospheric Boundary Layer

The wind turbines are operating in the Atmospheric Boundary Layer (ABL), which is the lowest part of the atmosphere close to the earth's surface, where most of the transport processes (e.g. transport of heat or momentum) take place [1].

The ABL is a layer characterised by wind shear and turbulence. The (vertical) wind shear, also known as vertical wind speed profile, is defined as the variation of wind speed with elevation [2]: wind speed is zero at the ground surface and increases with height. Turbulence is generated by mainly two factors [3]: flow disturbances caused by 'friction' with the earth's surface (ground roughness, topographical features, etc.) and thermal effects causing a vertical movement of air masses when their temperature (and, hence, density) is different from that of their surroundings. The height of the ABL is often defined at the height where turbulence disappears [1].

In the subsections below, two important characteristics of the ABL (turbulence intensity and stability) are explained, as they introduce some fundamental concepts, which are relevant to this thesis.

2.2.1 Turbulence intensity

The turbulence intensity is the most basic measure of turbulence [2]. It is defined as the ratio of the standard deviation of the wind velocity variations to the mean wind velocity, as shown in Eq. (2.1). The length of the time period used in the calculation is usually equal to 10 minutes.

$$I = \frac{\sigma_U}{U} \tag{2.1}$$

where σ_U is the standard deviation of wind velocity variations about the mean wind velocity, U, in the average wind direction.

The turbulence intensity depends on various factors, such as the ground roughness and the height above the ground [3]. It is also affected by certain topographic features, such as hills and mountains, as well as local features, such as trees and buildings, especially when they are located upwind of the location of interest. The

thermal behaviour of the atmosphere is another important factor, because it may generate large-scale turbulence due to buoyancy, as it is explained in Sec. 2.2.2.

Turbulence in the ABL is anisotropic [4], which means that turbulence intensity is not equal in every direction. Therefore, the longitudinal, lateral and vertical components of turbulence intensity (I_u, I_v, I_w) are different. They are calculated as:

$$I_u = \frac{\sigma_u}{U} , \qquad I_v = \frac{\sigma_v}{U} , \qquad I_w = \frac{\sigma_w}{U} \tag{2.2}$$

where σ_u, σ_v and σ_w are the standard deviations of wind velocity variations in the longitudinal, lateral and vertical directions.

2.2.2 Stability

The concept of atmospheric stability is defined as the tendency of the atmosphere 'to resist vertical motion or to suppress existing turbulence' [2]. The vertical distribution of temperature in the atmosphere (temperature gradient) determines the stability type: stable, unstable or neutral. The vertical temperature distribution is affected by the radiative heating or cooling of the ground surface and the resulting convective mixing of the air in close vicinity to the surface [2].

A useful parameter for analysing the atmospheric stability is the adiabatic lapse rate, Γ. Considering that an air element is lifted rapidly enough, so that there is no heat exchange with the surrounding air (adiabatic process), the adiabatic lapse rate is defined as the negative of the change of the element's temperature with height [1, 2]:

$$\Gamma = -\left(\frac{\mathrm{d}T}{\mathrm{d}z}\right)_{ad} = \frac{g}{c_p} \tag{2.3}$$

where T is temperature, z is elevation, g is the gravitational acceleration and c_p is the specific heat at constant pressure.

In dry conditions, Γ is approximately 1 °C/(100 m) and it is also known as the dry adiabatic lapse rate: it expresses the decrease of temperature of the rapidly lifted air element for every 100 m increase of elevation. The comparison of the environmental lapse rate with the adiabatic lapse rate is a measure of the atmospheric stability [2]: Assuming that the air element has the same temperature as the temperature of the surrounding air at the start, and considering that the surrounding air temperature is reduced according to the standard rate of $\frac{\mathrm{d}T}{\mathrm{d}z} = -0.66$ °C/(100 m), the vertically lifted air element will be 0.34 °C cooler than the surrounding air after 100 m of elevation. Consequently, it will be denser and it will fall to a lower level. In such a case, the atmospheric state is called stable.

According to the above, a stable atmosphere occurs when $\frac{\mathrm{d}T}{\mathrm{d}z} > \left(\frac{\mathrm{d}T}{\mathrm{d}z}\right)_{ad}$, which means that the adiabatic cooling of a rising air element is colder than that of the surrounding atmosphere. It is usually observed on cold nights or early mornings, when the lowest surface temperatures are recorded. In this case, turbulence is dominated by surface friction and not by thermal effects. Additionally, a stable atmosphere usually implies weak winds and high wind shear. In the case of inversion ($\frac{\mathrm{d}T}{\mathrm{d}z} > 0$), the atmosphere is considered very stable, although an inversion is not a necessary condition for stability.

Conversely, when $\frac{\mathrm{d}T}{\mathrm{d}z} < \left(\frac{\mathrm{d}T}{\mathrm{d}z}\right)_{ad}$, the atmosphere is unstable. In this case, surface heating causes an air element to rise at a higher level, because it will not be in thermal equilibrium with the surroundings, since the surrounding air cools more rapidly with elevation. As a result, large convection cells and large-scale turbulent eddies are formed in a thick ABL. The unstable state enhances vertical mixing and transfer of momentum, resulting in a more homogeneous vertical wind profile and lower wind shear. Unstable atmosphere is normally observed during daytime.

Finally, the neutral state occurs if the rising air element is in thermal equilibrium with the surrounding air. This implies that $\frac{\mathrm{d}T}{\mathrm{d}z} = \left(\frac{\mathrm{d}T}{\mathrm{d}z}\right)_{ad}$. It is important in wind energy applications, as it occurs at strong winds, when ground roughness causes sufficient turbulence and, consequently, loads on the rotors. Neutral state usually occurs on cloudy nights or days. In this work, only neutral conditions are considered.

A very widely used indicator of stability is the Richardson number, Ri, expressed as [4, 5]:

$$\mathrm{Ri} = \frac{g}{T_\circ} \frac{\left(\frac{\mathrm{d}T}{\mathrm{d}z}\right)}{\left(\frac{\mathrm{d}U}{\mathrm{d}z}\right)^2} \tag{2.4}$$

where $T_\circ$ is a reference temperature.

The Richardson number is a non-dimensional parameter, expressing the relative importance of thermally created turbulence (due to buoyancy) and mechanical turbulence (due to wind shear) [5]. A positive value of Ri indicates a stable atmosphere, whereas a negative Ri means that the atmosphere is unstable. Theoretically, the neutral state is satisfied for ($\mathrm{Ri} = 0$). In practice, however, small values of Ri indicate neutral stratification [4], as the strict condition of ($\mathrm{Ri} = 0$) is rarely satisfied. As an example, Magnusson and Smedman [6] have used the conditions of ($-0.05 < \mathrm{Ri} < 0.05$) for neutral, ($\mathrm{Ri} < -0.05$) for unstable and ($\mathrm{Ri} > 0.05$) for stable atmosphere.

When the Richardson number is above a critical value of 0.25, the atmosphere is not considered turbulent. If ($-0.05 < \mathrm{Ri} < 0.25$), then turbulence is almost entirely mechanical in origin, whereas, for ($\mathrm{Ri} < -0.05$), there is a mixture of both thermally created and mechanical turbulence [5].

2.3 Wind Turbine Wakes

A wind turbine wake is the region of wind flow to the rear of a wind turbine involving a velocity deficit as well as increased turbulence intensity, due to the operation of the machine. The wake has negative effects on the rotors located in a close distance downwind, as the lower velocity causes a significant reduction in their power output, while increased turbulence creates unsteady loads, shortening their lifetime.

As modern wind farm developers tend to build wind turbines in clusters as closely as possible to each other to avoid costs of land and civil works, wake effects are becoming increasingly significant as they are responsible for considerable reductions in the efficiency of wind farm power production, as well as premature failures of machines densely spaced [7]. It is estimated, that total energy losses due to wakes of a typical wind farm will range from 5% to over 15% depending on the layout [8]. However, for full wake conditions, the power losses can be significantly higher, $30 - 40\%$ [9]. According to the above, it can be concluded that the understanding of the wake mechanisms is important for the assessment of the performance of a wind farm and increase the accuracy of wind power prediction.

The following assessment of the theory and previous work on wind turbine wakes was based on a number of comprehensive reviews: the studies of Snel [10, 11], Crespo et al. [12], Vermeer et al. [13], Sanderse [9], Sumner et al. [14] and Sanderse et al. [15].

2.3.1 Wake aerodynamics

A brief overview of the fundamental theory behind wake behaviour is presented in this subsection, based on wind energy textbooks [2, 3, 16] and the reviews of Crespo et al. [12], Sanderse [9] and Vermeer et al. [13]. The actuator disc principle

is initially explained, as a simple approach to describe the energy-extracting operation of a wind turbine using linear momentum theory. The approach is then extended to include wake rotational effects and, subsequently, the Blade Element Momentum (BEM) theory is explained. Finally, the 'real' flow field in the wake of a wind turbine is described using a distinction between near and far wake.

The actuator disc principle

The actuator disc model is based on a linear momentum theory applied on an ideal turbine rotor [2], as the real rotor is replaced by a permeable actuator disc of equivalent diameter. The basic assumptions of such an analysis are [2]: 'homogeneous, incompressible, steady-state flow; no frictional drag; infinite number of rotor blades; uniform thrust over the disc; a non-rotating wake; the static pressure far upstream and downstream of the rotor is equal to the undisturbed ambient static pressure'.

As the rotor extracts kinetic energy from the wind, it creates a sudden drop of static pressure and it gradually reduces the wind speed of the mass of air passing through the disc. Downstream of the rotor, the static pressure recovers to ambient levels, while velocity is further reduced, due to the rise of pressure.

The variations of pressure and velocity upstream and downstream the actuator disc are shown in Fig. 2.1. Considering only the flow of the affected mass of air, a stream-tube is formed, where ∞ denotes the upstream conditions, d refers to the conditions at the disc and w refers to the wake conditions. The ambient incoming velocity U_∞ gradually reduces to U_w in the rotor wake. The ambient static pressure of the incoming flow, p_∞, increases to a value of p_d^+ in front of the rotor disc and drops suddenly to a value of p_d^- immediately behind the disc, as a result of the axial force applied by the actuator disc. Further in the rotor wake, static pressure gradually recovers to the ambient value of p_∞, while velocity

reduces further as a result of the rise of pressure. Velocity reaches the lowest value of U_w, at the point where the wake pressure is fully recovered to the ambient value of p_∞.

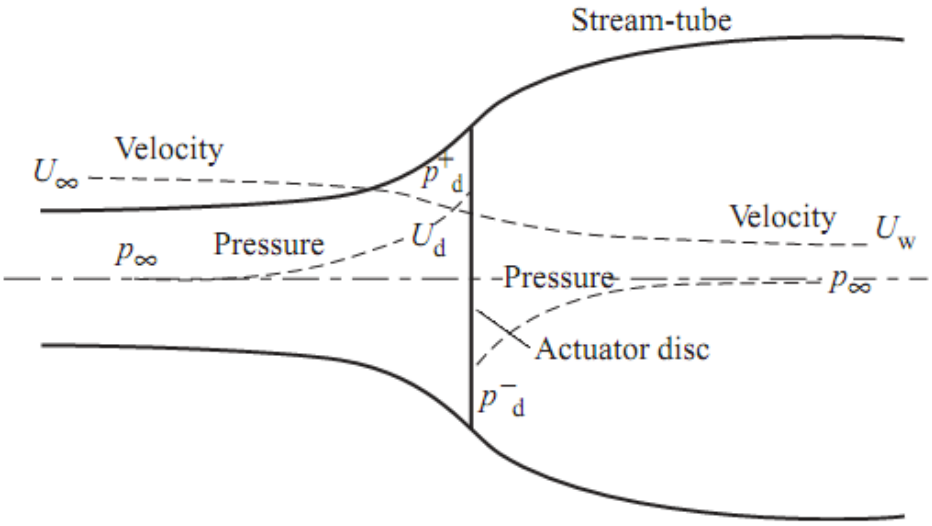

Figure 2.1. Flow field through an actuator disc. Source: Burton et al. [3].

As there is no wind flow across the boundaries but only across the ends of the stream-tube, the conservation of mass flow rate (continuity) needs to apply:

$$\dot{m} = \rho\, A_\infty\, U_\infty = \rho\, A_d\, U_d = \rho\, A_w\, U_w \tag{2.5}$$

where $\dot{m}$ is the air mass per unit length of time and ρ is the air density, considered as constant.

From Eq. (2.5), and since axial velocity on the rotor (U_d) is reduced due to the energy extraction, the cross-sectional area of the stream-tube at the disc (A_d) needs to be increased to maintain a constant mass flow rate. The streamwise reduction of the axial upstream velocity on the disc is expressed by means of an axial induction factor a and, thus, the axial velocity at the disc is calculated as

in Eq. (2.6).

$$U_d = (1 - a)\, U_\infty \tag{2.6}$$

Applying the conservation of linear momentum across the stream-tube, the rate of change of momentum is equal and opposite to the thrust force, F_T, which is the wind force exerted on the rotor:

$$F_T = \dot{m}\,(U_\infty - U_w) \tag{2.7}$$

The thrust force can also be expressed by means of the pressure drop across the actuator disc:

$$F_T = A_d\left(p_d^+ - p_d^-\right) \tag{2.8}$$

The energy extracted by the rotor, E, is equal to the reduction of the kinetic energy:

$$E = \frac{1}{2}\, m\left(U_\infty^2 - U_w^2\right) \tag{2.9}$$

The power extracted by the rotor, P, can be expressed as the extracted energy per unit time:

$$P = \frac{1}{2}\, \dot{m}\left(U_\infty^2 - U_w^2\right) \tag{2.10}$$

The extracted power can also be expressed as the rate of work done by the force, F_T, acting on the rotor disc:

$$P = F_T\, U_d = \dot{m}\,(U_\infty - U_w)\; U_d \tag{2.11}$$

Using Eqs. (2.10) and (2.11):

$$U_d = \frac{1}{2}\left(U_\infty + U_w\right) \tag{2.12}$$

Using Eqs. (2.6) and (2.12):

$$U_w = \left(1 - 2a\right) U_\infty \tag{2.13}$$

The power coefficient, C_P, is defined as the fraction of the available wind power which is extracted by the rotor:

$$C_P = \frac{P}{\frac{1}{2}\rho U_\infty^3 A_d} \tag{2.14}$$

Using Eqs. (2.11), (2.5), (2.6) and (2.13) in Eq. (2.14):

$$C_P = 4a\left(1 - a\right)^2 \tag{2.15}$$

The maximum value of C_P is determined by taking the derivative of C_P with respect to a and setting it equal to zero, resulting in $a = 1/3$. Thus:

$$C_{P,max} = \frac{16}{27} = 0.593 \tag{2.16}$$

This maximum theoretical value of the power coefficient is known as the Betz limit. In reality, the maximum achievable power coefficient is further reduced, due to three additional effects [2]: wake rotation; finite blade number and tip losses; non-zero aerodynamic drag.

Similarly to Eq. (2.14), the thrust coefficient, C_T, is defined as the non-dimensionalised thrust force:

$$C_T = \frac{F_T}{\frac{1}{2}\rho U_\infty^2 A_d} \tag{2.17}$$

Using Eqs. (2.7), (2.5), (2.6) and (2.13) in Eq. (2.17):

$$C_T = 4a\,(1-a) \tag{2.18}$$

From Eqs. (2.17) and (2.7) it can be shown that the thrust coefficient is proportional to the velocity drop in the wake, $(U_\infty - U_w)$, which is also the reason of the wake expansion, $A_\infty < A_w$, according to the conservation of mass in Eq. (2.5). An increase of C_T results in a larger wake expansion.

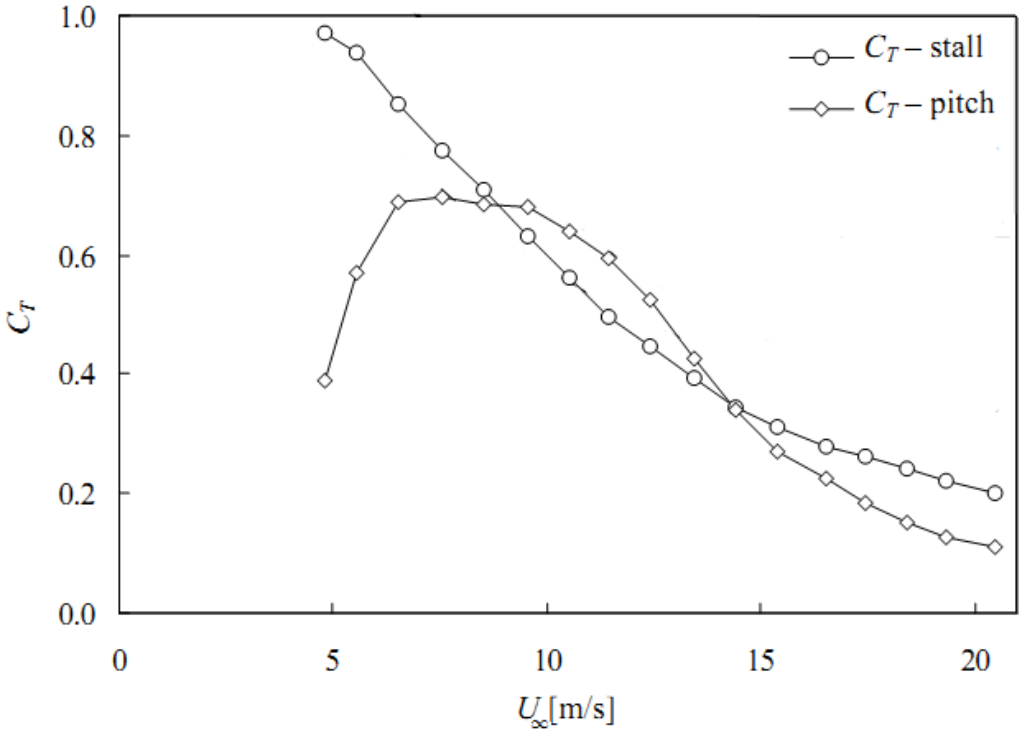

Figure 2.2. Measured C_T as a function of wind speed for stall and pitch controlled machines. Source: Frandsen [17].

In reality, the thrust coefficient is wind turbine specific and it is determined by the blade geometry, the rotor rotational speed and the control strategy [17]: there are significant differences in the thrust coefficient of stall and pitch controlled machines. Fig. 2.2 shows an example of the measured thrust coefficient as a function of wind speed for stall and pitch controlled machines (Source: Frandsen [17]).

C_T is lower at increasing wind speeds in both cases, although at pitch-regulated machines, C_T is also reduced at very low wind speeds, near the cut-in value.

Ideal rotor with wake rotation

In the simple actuator disc approach no rotor rotation is taken into account. However, this analysis can be used combined with other theories such that it may also account for rotating wake flow. In such a case, the ideal rotor is considered to have a number of blades rotating at an angular velocity, Ω, about an axis parallel to the wind direction and normal to the rotor plane.

The blade rotation generates angular momentum in the flow, which is related to the rotor torque [2]. The air passing through the rotor exerts a torque on the disc in the direction of rotation. In order to maintain the rotational speed constant, an equal and opposite torque on the air is required [3], which is responsible for the rotation of the wake in a direction opposite to the rotor rotational direction, as shown in Fig. 2.3.

The consideration of the rotor rotation adds a tangential velocity component in the wake. This results in an higher wake kinetic energy as compared to the wake kinetic energy of a simple actuator disc without rotation. This increase of the wake velocity is counterbalanced with an additional fall of static pressure [3].

This analysis is based on an annular stream-tube of radius, r, and thickness, δr, as shown in Fig. 2.3. The cross-sectional area of the stream-tube at the rotor disc is $\delta A_d = 2\pi r \delta r$, representing the area of an annular ring of δr thickness and r radius. The annular ring is considered as acting independently from the other parts of the disc, affecting the momentum of the air flowing in the stream-tube. The flow upstream of the rotor disc is non-rotating, while the flow rotation downstream is taken as constant throughout the wake. The rotation is transferred to the flow across the disc thickness [3].

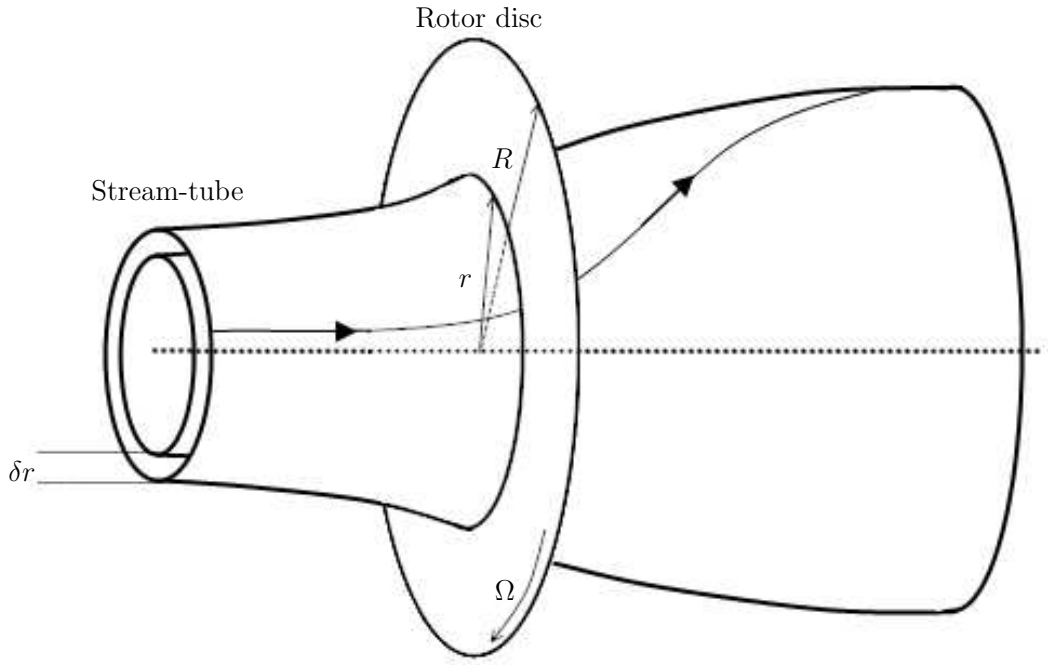

Figure 2.3. Stream-tube and trajectory of a particle in the case of an ideal rotor rotation. Source: [16].

The change of tangential velocity in the flow is expressed by means of the tangential induction factor, a' [3]. Upstream of the rotor disc, the tangential velocity is zero. Immediately downstream, the tangential velocity is considered as equal to $2\Omega r a'$ and it is opposite to the rotational direction of the rotor. At the middle of the disc thickness the tangential velocity reaches the value of $\Omega r a'$.

The thrust force on the rotor ring is equal to the rate of change of axial momentum, $\delta F_{T,1}$, plus the additional axial force corresponding to the static pressure drop due to rotation, $\delta F_{T,2}$.

The first term, related to the change of axial momentum, can be calculated as:

$$\delta F_{T,1} = \delta \dot{m} \left(U_\infty - U_w \right) \tag{2.19}$$

and using Eqs. (2.13) and (2.5) in Eq. (2.19):

$$\delta F_{T,1} = 4a(1-a)\rho U_\infty^2 \pi r \delta r \tag{2.20}$$

The second term, related to the additional pressure drop due to rotation, can be calculated using the increase of dynamic pressure due to rotation, Δp_{rot}:

$$\Delta p_{rot} = \frac{1}{2}\rho \left(2\Omega r a'\right)^2 \tag{2.21}$$

Thus, $\delta F_{T,2}$ is calculated as:

$$\delta F_{T,2} = \delta A_d \, \Delta p_{rot} = 4\rho \left(a'\Omega r\right)^2 \pi r \delta r \tag{2.22}$$

Consequently, the total thrust force, on the rotor ring, δF_T, is:

$$\delta F_T = \delta F_{T,1} + \delta F_{T,2} = 4\rho \left[U_\infty^2 a(1-a) + \left(a'\Omega r\right)^2\right] \pi r \delta r \tag{2.23}$$

According to the conservation of angular momentum, the torque exerted on the rotor ring, δQ, is equal to the rate of change of angular momentum of the air flowing in the stream-tube and through the ring. This is expressed as:

$$\begin{aligned} \delta Q &= \delta \dot{m} \left(2\Omega r a'\right) r = \left[\rho \delta A_d U_\infty (1-a)\right] \left(2\Omega r a'\right) r \\ &= 4\rho U_\infty a'(1-a)\Omega \pi r^3 \delta r \end{aligned} \tag{2.24}$$

The above expressions of thrust and torque in Eqs. (2.23) and (2.24), are also used in the Blade Element Momentum theory, which is described in the next paragraphs.

The Blade Element Momentum theory

The Blade Element Momentum (BEM) theory is essentially the combination of the momentum theory and the Blade Element Theory (BET) [2]. The momentum theory refers to the previous analysis, which calculates the blade forces according to the conservation of angular and linear momentum. The BET refers to the analysis of aerodynamic forces at a blade section using information on the blade geometry. Consequently, BEM theory can link the rotor blade characteristics with the energy extraction process.

According to the Blade Element Momentum approach, the rotor blade is divided into a number of spanwise sections (or elements), as shown in Fig. 2.4. As the blade rotates, each blade element sweeps out an annular ring. The basic assumption in the BEM theory is that the change of momentum of air passing through the annular ring is solely caused by the aerodynamic force on the blade element [3]. This hypothesis implies that there is no radial flow interaction between the spanwise elements, which is strictly true if there is no radial variation of the axial flow induction factor [3]. Even though a is not always uniform in practice, experimental observations of flow through propeller discs have shown that the assumption of no radial flow interaction is acceptable [3].

The analysis considers the rotation of a blade element of δr spanwise length and r radius with Ω rotational speed, as shown in Fig. 2.4. As no aerodynamic interaction between the blade elements is assumed, velocity in the spanwise direction is ignored. Assuming that the flow upwind of the rotor has no rotation, the wind velocity around the rotating blade element becomes rotational, with the addition of a tangential component as shown in Fig. 2.5. At the middle of the chord thickness, which corresponds to the d region of the actuator disc in Fig. 2.1, the induced tangential component of velocity is expressed as $\Omega r a'$, where a' is the tangential induction factor. As explained in previous paragraphs, the tangential

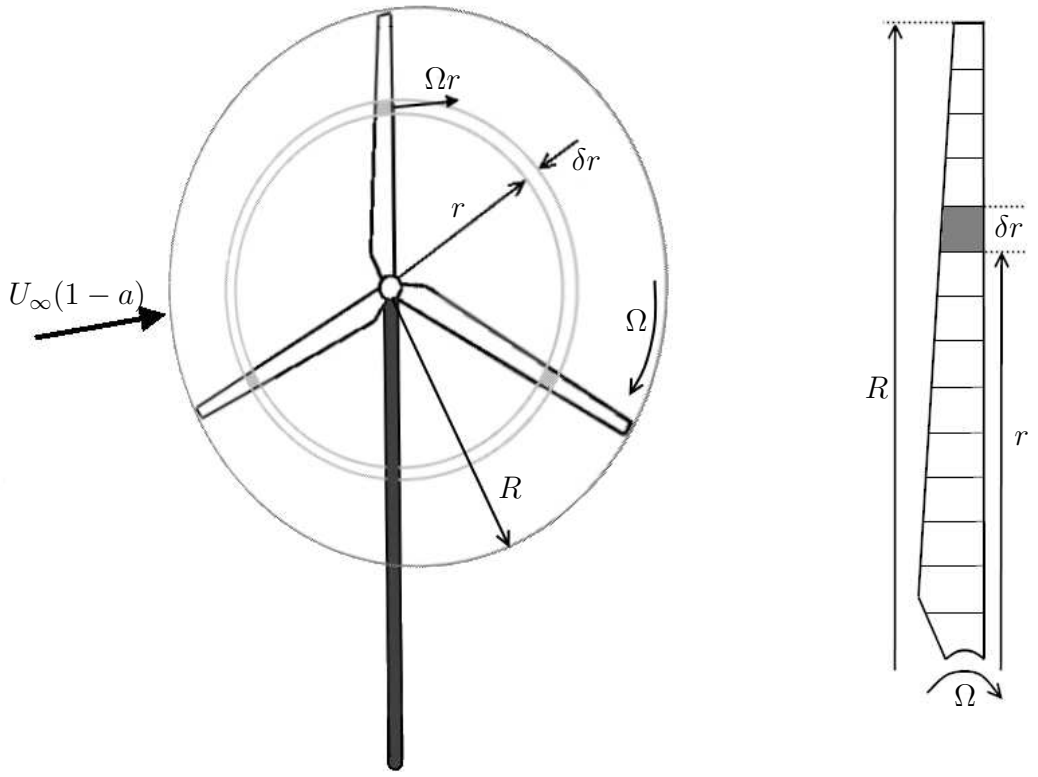

Figure 2.4. A rotor blade element rotating in an energy extracting rotor, where δr is the blade element spanwise length; r, radius; R, rotor (tip) radius; and Ω is the rotor rotational speed.

velocity direction is opposing the blade motion, since it is generated as a reaction to the blade rotation.

After transforming the velocity vectors in Fig. 2.5 to a coordinate reference system rotating together with the blade element, the resulting tangential velocity, U_t, can be calculated as:

$$U_t = \Omega r a' + \Omega r = \Omega r \left(a' + 1\right) \tag{2.25}$$

Fig. 2.6a shows the velocity vectors relative to the blade element cross-section using a coordinate reference system attached to the blade, where β is the pitch angle, namely the angle between the airfoil zero lift line and the disc plane [2],

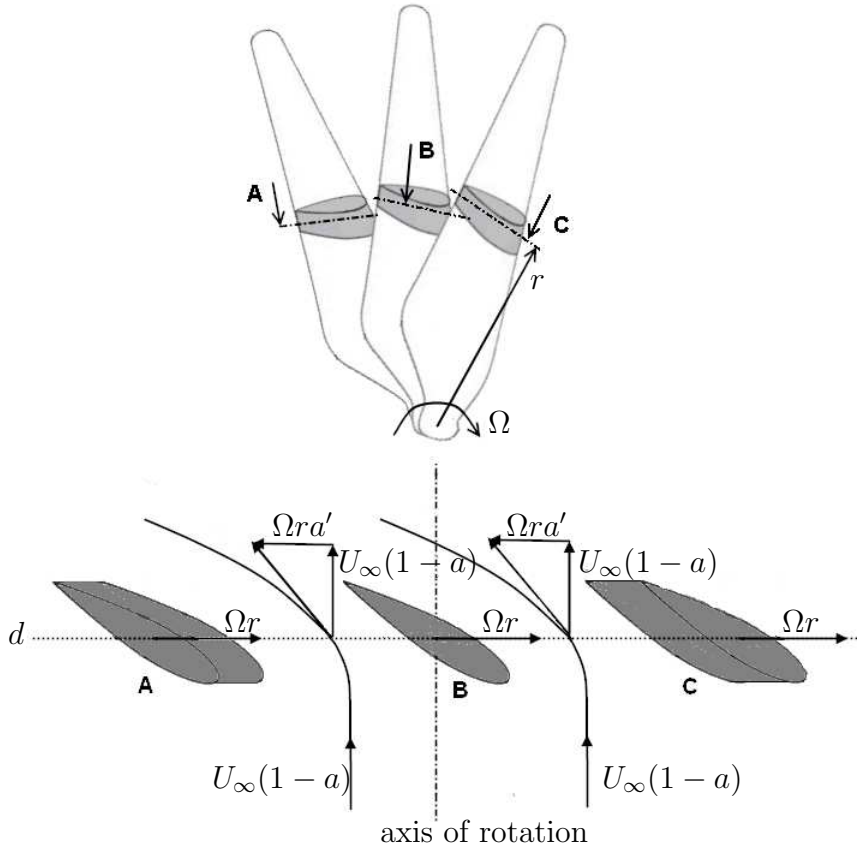

Figure 2.5. Velocity around a rotating blade element

and α is the angle of attack, namely the angle between the resulting relative wind velocity U_{rel} and the airfoil zero lift line.

Taking into account the axial wind velocity in Eq. (2.6) and the tangential velocity in Eq. (2.25), the resulting relative wind velocity, U_{rel}, is calculated as:

$$U_{rel} = \sqrt{U_\infty^2(1-a)^2 + (\Omega r)^2\,(1+a')^2} \tag{2.26}$$

and the angle at which U_{rel} acts to the disc plane, φ, is calculated as:

$$\sin\varphi = \frac{U_\infty(1-a)}{U_{rel}} \quad \text{and} \quad \cos\varphi = \frac{\Omega r(1+a')}{U_{rel}} \tag{2.27}$$

The angle of attack, α, is then calculated as:

$$\alpha = \varphi - \beta \tag{2.28}$$

According to the BET, the forces on the blade elements are attributed to the lift and drag characteristics of their airfoil shape. Considering the blade element in Fig. 2.5, the direction of U_{rel} is calculated from the angle φ in Fig. 2.6a. The directions of lift (δF_L) and drag (δF_D) in Fig. 2.6b are also linked to φ, as they are perpendicular and parallel to U_{rel} direction respectively.

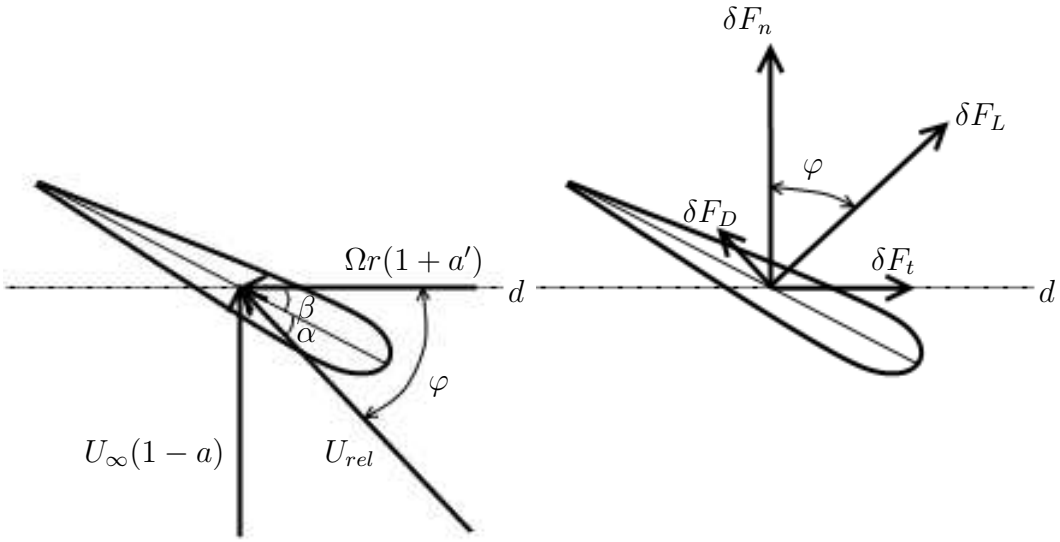

(a) Velocities (b) Forces

Figure 2.6. Velocities and forces using the blade coordinate system.

The resulting lift and drag forces on the element can be calculated using the two-dimensional (2-D) airfoil lift and drag coefficients, as:

$$\delta F_L = C_L \, \frac{1}{2} \rho U_{rel}^2 \, c \, \delta r \tag{2.29}$$

$$\delta F_D = C_D \, \frac{1}{2} \rho U_{rel}^2 \, c \, \delta r \tag{2.30}$$

where C_L and C_D are the 2-D airfoil lift and drag coefficients and c is the airfoil chord length.

According to Fig. 2.6b, the axial and the tangential forces on the blade element (δF_n and δF_t respectively) can be determined as:

$$\delta F_n = \delta F_L \cos\varphi + \delta F_D \sin\varphi \tag{2.31}$$

$$\delta F_t = \delta F_L \sin\varphi - \delta F_D \cos\varphi \tag{2.32}$$

Considering that the rotor has N_b blades and using Eqs. (2.29)–(2.30), the total axial and tangential forces on the annular ring of thickness δr and radius r, are calculated as:

$$\delta F_n = N_b \, \frac{1}{2} \rho U_{rel}^2 \, c \, \delta r \;\; (C_L \cos\varphi + C_D \sin\varphi) \tag{2.33}$$

$$\delta F_t = N_b \, \frac{1}{2} \rho U_{rel}^2 \, c \, \delta r \;\; (C_L \sin\varphi - C_D \cos\varphi) \tag{2.34}$$

It is convenient to define C_n and C_t as:

$$C_n = C_L \cos\varphi + C_D \sin\varphi \tag{2.35}$$

$$C_t = C_L \sin\varphi - C_D \cos\varphi \tag{2.36}$$

The total thrust force (F_T) on the rotor disc can be found by integrating Eq. (2.33), as:

$$F_T = \int_0^R N_b \, \frac{1}{2} \rho U_{rel}^2 \, C_n(r) \, c(r) \, \mathrm{d}r \tag{2.37}$$

which can be transformed using Eq. (2.26) and the non-dimensionalised radius,

$r' = r/R$, and chord length, $c' = c/R$, as:

$$F_T = N_b \, \frac{1}{2}\rho \, R^2 \int_0^1 \left[U_\infty^2 (1-a)^2 + (\Omega R r')^2 \, (1+a')^2\right] \, C_n(r') \, c'(r') \, \mathrm{d}r' \quad (2.38)$$

Another useful non-dimensional variable is the tip speed ratio, λ, defined as the ratio of the blade tip speed to the free stream wind speed:

$$\lambda = \frac{\Omega R}{U_\infty} \quad (2.39)$$

The rotor thrust coefficient can be calculated from Eq. (2.17) using Eqs. (2.38), (2.39) and $A_d = \pi R^2$:

$$C_T = \frac{N_b}{\pi} \int_0^1 \left[(1-a)^2 + (\lambda r')^2 \, (1+a')^2\right] \, C_n(r') \, c'(r') \, \mathrm{d}r' \quad (2.40)$$

Eq. (2.40) links the thrust coefficient to the 2-D drag and lift coefficients of each blade section.

The power generated at each annular ring, δP, is linked to the torque, δQ, which is related to the tangential force, δF_t according to:

$$\delta P = \Omega \, \delta Q = \Omega \, \delta F_t \, r \quad (2.41)$$

The total power generated at the rotor disc, can be found by integrating Eq. (2.41), and using Eqs. (2.34) and (2.36):

$$P = \int_0^R \Omega \, N_b \, \frac{1}{2}\rho U_{rel}^2 \, C_t(r) \, c(r) \, r \, \mathrm{d}r \quad (2.42)$$

Using Eq. (2.26) and non-dimensional values:

$$P = \Omega\ N_b\ \frac{1}{2}\rho\ R^3 \int_0^1 \left[U_\infty^2(1-a)^2 + (\Omega R r')^2\ (1+a')^2\right]\ C_t(r')\ c'(r')\ r'\ \mathrm{d}r' \quad (2.43)$$

The rotor power coefficient is defined in Eq. (2.14). Using Eqs. (2.43), (2.39) and $A_d = \pi R^2$ in Eq. (2.14), the following expression for C_P can be derived:

$$C_P = \frac{N_b\ \lambda}{\pi} \int_0^1 \left[(1-a)^2 + (\lambda r')^2\ (1+a')^2\right]\ C_t(r')\ c'(r')\ r'\ \mathrm{d}r' \quad (2.44)$$

In Eq. (2.44), the power coefficient is linked to the blade element characteristics and the 2-D airfoil lift and drag coefficients.

Tip losses

The BEM analysis assumes that the force by the blade elements on the flow at each annular ring is constant. This assumption is valid for an infinite number of rotor blades, but in reality, the rotor has a finite and small number of blades; e.g., a 3-bladed rotor is one of the most common rotor forms. As a consequence of the small number of blades, some of the fluid particles passing through the rotor disc will interact with the blades, while most of the particles will pass between them [3]. This effect is significantly more pronounced near the edge of the rotor disc and it is associated with the tip losses.

The tip losses occur in close proximity to the rotor disc edge, because of an increasingly strong secondary flow around the blade tip [18]. As pressure on the upwind side of the blade (lower surface) is higher than on the downwind side (upper surface), the air flows around the tip from the lower to the upper surface, reducing the lift force [2]. On the lower surface, the secondary flow moves towards the blade tips, while on the upper surface, the flow moves towards the blade root. As lift is reduced, torque is also reduced near the tip resulting in power losses.

In order to account for tip losses, a correction factor, F', can be introduced in the equations of forces derived from the momentum theory. F' is known as Prandtl's tip loss factor and expresses the reduction of the blade forces at a radius r along the blade. It is a function of the number of blades, N_b, the angle of relative wind, φ, and the spanwise position on the blade, $r' = r/R$.

Based on this method [2]:

$$F'(r') = \frac{2}{\pi} \cos^{-1} \left\{ \mathrm{e}^{-\left[\frac{(N_b/2)(1-r')}{r' \sin\varphi} \right]} \right\} \tag{2.45}$$

where the angle resulting from the inverse cosine function is given in radians. F' is always between 0 and 1.

Description of real wake behaviour

Most of the wake studies distinguish between two main regions of the wake field: the near and the far wake region [13]. The former, is considered the region just behind the rotor, where the rotor properties (e.g. blade geometry) play a dominant role, applying an axial pressure gradient which develops the wake deficit. The near wake is usually considered to extend up to approximately one diameter (D) downstream [13], while according to others [7, 19, 20] it may reach up to 4 D downstream. The far wake spreads beyond the near wake, where effects are viewed in a wind farm perspective and the rotor geometry becomes less important. The latter region is where wake modelling, wake interaction, turbulence modelling and topographical effects become significant. The near wake research is focused on the individual rotor power extraction process, while the far wake is related to the assessment of the wind farm efficiency. For this reason, the far wake research will be given the most consideration, since the focus is on wake effects in wind farms.

Near wake As mentioned in Sec. 2.3.1, immediately behind the rotor, there is a reduction of wind speed and a sudden drop of pressure, as kinetic energy is extracted at the machine. Downwind of the rotor plane, pressure increases and velocity is further reduced, until ambient pressure is restored [12]. This defines the wake expansion region, which is estimated to be at 1 D downstream [12], while Schepers [21] considered it to be 2.25 D, based on experiments. According to Ainslie [19], maximum velocity deficit is reached after approximately 1–2 D. The velocity deficit in the wake is directly related to the thrust coefficient of the machine, since the axial thrust determines the change of momentum in the flow.

The wind speed gradient between the low-speed wind inside the wake and the higher speed wind outside, forms a shear layer containing mainly large-scale, shear-generated, turbulent eddies. As a result, the turbulence profile in the near wake has two peaks, but it is also vertically non-uniform, due to the atmospheric wind shear: shear-generated turbulence intensity in the upper part is higher than in the lower part, nearer to the ground, where the wind speed gradient is lower. A higher thrust coefficient, which results in a lower wake velocity, U_w, induces larger shear and, thus, shear-generated turbulence.

This shear layer turbulence assists in the mixing of the ambient wind speed with the lower wind speed inside the wake. In this way, momentum is transferred from the free flow into the wake, gradually reducing the velocity deficit. The mixing region expands both inwards and outwards due to turbulent diffusion: the outward expansion increases the wake width, while the inward thickening finally reaches the wake axis at around 2–5 D downstream, marking the end of the near wake region [12]. Fig. 2.7 illustrates the turbulent shear layer expansion when the rotor is operating in atmospheric wind shear.

Apart from the wind shear, there are also some other sources of turbulence in the near wake: turbulence related to the wind turbine itself (blades, nacelle and tower), also known as ‘mechanical” turbulence, and the ambient turbulence, also

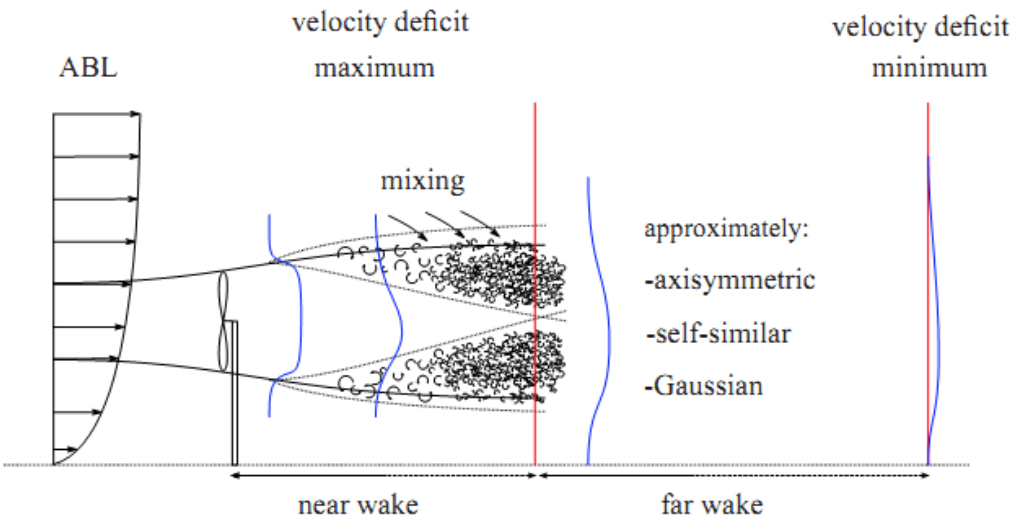

Figure 2.7. Wake velocity profile. Source: Sanderse [9].

present in the far wake. Each rotor blade generates a vortex sheet, shed from the blade trailing edge. Additionally, strong vortices are generated at the blade tips and, following helical trajectories downstream [12], they merge into a 'cylindrical sheet of rotating turbulence' [2]. The tip vortices are responsible for the tip losses [2]. Turbulence is also generated by the flow disturbance of the nacelle and the tower. The 'mechanical' turbulence is of high frequency and decays quickly. According to Ainslie [19], the tip vortices decay within 2–3 D, due to the action of ambient turbulence.

Far wake In the far wake region, the velocity deficit is gradually reduced and axial pressure gradients become less important. The wake becomes wider, but shallower downstream, until the flow is fully-recovered [3]. The rate of decay of the velocity deficit is strongly dependent on the ambient turbulence levels as well as the wake turbulence. Higher ambient turbulence results in faster wake recoveries, due to increased turbulence mixing.

An illustration of the velocity deficit profile in the far wake is presented in Fig. 2.7. Assuming the absence of ambient wind shear, the velocity deficit and turbulence intensity profiles may be approximated to have an axisymmetric, self-similar

(Gaussian) profile in the wake cross-sections [12]. The self-similarity assumption is used in a number of wake models, also known as kinematic models, which are described in Sec. 2.3.4. However, this assumption is not completely valid if the ground effect and the ambient wind shear are taken into account. According to observations, the maximum velocity deficit is usually below the turbine axis, while the maximum turbulence intensity above it (due to the higher shear), as shown in Fig. 2.8. This behaviour of the velocity deficit has been attributed to the shear of the incoming flow and the presence of the ground [22].

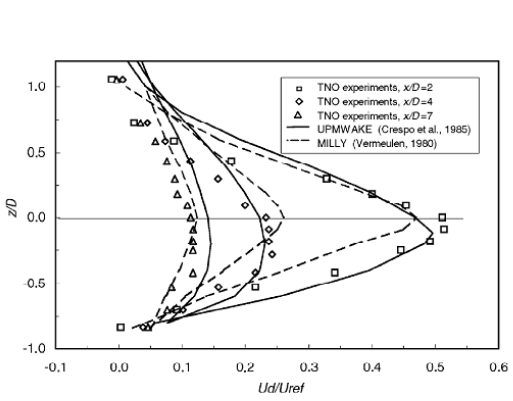

(a) Velocity deficit. Source: [13]

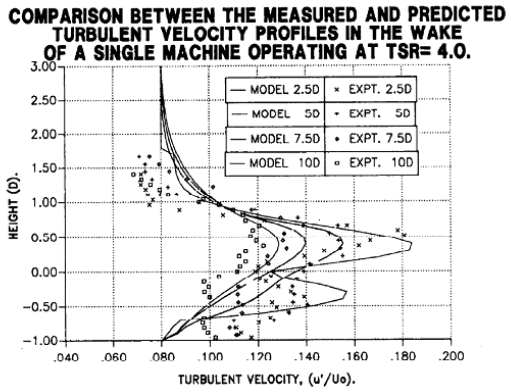

(b) Turbulent velocity. Source: [23]

Figure 2.8. Comparison of velocity deficit and turbulent velocity profiles at various distances downstream.

In addition to the aforementioned ground effects, which are related to the wind shear of the incoming flow, Troldborg [24] observed some additional effects related to the presence of the ground: the wake expands more upwards, than downwards, while the ambient flow accelerates below the rotor and the wake.

Turbulence in the wake is anisotropic, but not as much as in the free ambient flow [25]. There is also a tendency for wake turbulence to be isotropic towards the wake centre [26], while peaks of turbulence intensity are observed in the wake shear layer [9], as shown in Fig. 2.8b. Turbulence effects have been found to be more persistent and the decay of wake velocity deficit is faster than the decay of wake turbulence [13].

2.3.2 Wind farm aerodynamics

As mentioned above, wakes reduce the power output of the wind turbines and contribute to an increase in their loading. A wind farm consists of a number of wind turbines and their wakes can interact affecting several machines in a wide range of wind directions.

Optimal selection of array layout

Lissaman et al. [27] used three key input parameters for the optimal selection of the array layout: characteristics of the wind resource, site and wind turbine.

The main wind characteristics were the annual distribution of wind speed and direction (wind rose), the turbulence level and the distribution of wind speed on the site. At sites with a particular prevailing wind direction, it is possible to decrease the crosswind spacing of some rotors, reducing the required land area without compromising the wind farm performance. If ambient turbulence is high, turbulence mixing in the wake is enhanced, leading to a faster wake recovery. In low turbulence levels, as is the case offshore, wakes tend to recover more slowly. Apart from the ambient turbulence, the turbulence generated by the machines is also important; the wake of a downstream machine will recover faster than the one of the upstream machine, as a result of the acceleration in the turbulent mixing process. Finally, the distribution of wind speed on the site is particularly important for cases of complex terrain, where local wind speed may vary $5-50\%$.

According to Lissaman et al. [27], the array layout can be generally defined in terms of the crosswind and downwind spacing with reference to the prevailing wind direction. On a site with a strong prevailing wind direction, a crosswind spacing of 3–5 D may lead to a small energy loss. In the case of downwind machines, it was found that a spacing of less than 10 D may have a significant effect in the array efficiency (defined as the energy output of the array divided by the energy

output of the same machines as if they operated without interference). A 12 D spacing is needed for a typical site with 10% turbulence in order to maintain 90% array efficiency, while a spacing of 5 D and 5% turbulence results in 50% efficiency [27].

Wind turbines in-line

When there are many machines positioned in-line, it has been observed [12, 28] that there is a significant decrease of power in the second turbine, but much smaller losses in the machines further downwind. Regarding the turbulence development, there is evidence in the wind-tunnel study of Builjes and Vermeulen [29], that turbulence intensity reaches an equilibrium value after three to four rows of turbines, while the maximum value was observed in the second row.

Wake meandering

Wake meandering is described as the large scale movement of the entire wake observed in field experiments [9, 12]. This phenomenon has been attributed to eddies which are large in comparison with the wake size. As a result of wake meandering, the downstream turbines may be significantly misaligned as the wake is swept in and out of the downstream rotor planes. This may lead to an increase of loading, but also a reduction of the mean wake deficit and, thus, power losses.

The effect of wake meandering is usually excluded in most of the wake models, as well as in wind-tunnel tests. This may be a significant reason for discrepancies between the prediction of such wake models and full-scale, field experiments: the measured maximum velocity deficit in the field experiments will be lower than the predicted and measured velocity fluctuations due to the meandering may be interpreted as additional turbulent kinetic energy [12].

2.3.3 Experimental work on wakes

The experimental studies on wind turbine wakes can be categorized into wind-tunnel tests and field (open air) experiments. Vermeer et al. [13] have performed an elaborate overview of the experimental work, focused either in the near or the far wake. A review of some of the most important of the studies in the far wake is performed in this Section, focusing on the full-scale experiments.

Wind-tunnel experiments

Some early (1979) wind-tunnel tests of wind turbine clusters were performed by Milborrow [30] in the CERL (Central Electricity Research Laboratories) wind-tunnel in England. The aim was to investigate the relationship between the total power output and the spacing and number of the machines. Most of the tests were carried out using ABL simulation techniques, whereas two tests were performed using a clear tunnel.

Also in 1979, Alfredsson and Dahlberg [31] contacted experiments on a small, 2-blade wind turbine model investigating the wake in various ambient flow conditions. The purpose was to provide data for comparison with theoretical models, especially the one developed by Lissaman [32]. The wind-tunnel K1 at the Royal Institute of Technology (KTH) in Stockholm was used, which was a return type tunnel with an octagonal test section. To establish turbulent flow with a constant mean velocity, two different grids were used: a fine grid, placed inside the contraction of the wind tunnel and a coarser grid, positioned at the beginning of the test section [31]. The ABL was simulated using a technique developed by Counihan [33].

In 1980, Alfredsson et al. [34] compared the results of the aforementioned Alfredsson and Dahlberg tests [31] with theoretical predictions of a modified version of the Lissaman [32] model (see Sec. 2.3.4). Agreement of the centreline

velocity deficit profiles was reasonably good when ambient turbulence was present, but less satisfactory in the case without ambient turbulence.

In 1981, Alfredsson and Dahlberg [35] also studied the interaction of two rotors in various configurations at four different ambient flow conditions using the same wind-tunnel and rotor models as in [31]. At high turbulence levels, they observed faster wake recoveries, but not significant changes in the wake width. In the case of the two rotors aligned to the flow direction, the presence of the downstream rotor was found to affect the upstream wake by 'pushing it aside'. In the case of two upstream rotors placed 2 D apart, facing the wind direction, it was found that the combined wake decayed slower than a single wake, indicating that applying a linear superposition of wakes is an oversimplification when the machines are placed close together.

Builtjes and Milborrow [36] used two different sets of wind-tunnel test results. The simulations were performed at the Netherlands Organisation for Industrial Research (TNO) and at the CERL; the neutral ABL was simulated in both cases. The aim of the study was to investigate the performance of wind turbine clusters and results highlighted the importance of the cluster size and the spacing of the individual machines in affecting the wind farm efficiency. Builtjes and Vermeulen [29] further investigated the turbulence within wind turbine clusters in the TNO wind-tunnel, where the ABL above rural terrain was simulated. They found that turbulence reaches an equilibrium value within the cluster, as mentioned in Sec. 2.3.2.

In the early 90's, Smith [37] and Smith and Taylor [23] investigated the interaction of two turbine models positioned in-line along and across the wind direction. A Counihan type [33] ABL simulation was applied in the Marchwood Engineering Laboratory atmospheric wind-tunnel. They found the wake of the downstream machine to recover more rapidly than that of the upstream machine, which is explained by the momentum diffusion caused by the high turbulence levels in the

wake. Smith and Taylor [23] observed the turbulence intensity maximum of the far wake to be above the turbine axis, which is probably attributed to the way wake turbulence is developed in the near wake [13].

In 2004, Maeda et al. [38] studied a single wake as well as a wake interaction between neighbouring wind turbine models. They used a large wind-tunnel of circular type and they simulated two types of wind conditions: thick boundary layer flow with large ambient turbulence and boundary layer flow over smooth surface with small ambient turbulence. The wind turbine models were positioned at an open section of the wind-tunnel. They found that increased wind shear and turbulence enhanced the single wake recovery. A lateral wake 'drift' was also visible in the high wind shear and turbulence case, after 6 D downstream. Additionally, they examined the arrangements of two rows of machines at a distance of 3–4 D suggesting optimal spacings.

Medici et al. [39–42] performed a large number of wake experiments in the MTL (Minimum Turbulence Level) wind-tunnel at KTH Mechanics. The wind-tunnel was a closed-loop circuit facility [41] simulating stable conditions, as ambient temperature was controlled by means of a heat exchanger. Some of the tests were run with the addition of a grid to generate ambient turbulence. Medici [40] and Medici and Alfredsson [41] tested model wind turbines with one, two [41] and three blades, measuring all three velocity components in the wake. Experiments were run both for the case where the rotor was positioned normal to the incoming flow and also under various yaw conditions [40] (the rotor inclined to the incoming flow direction in an angle of 0–30°). At 1 D downstream, the wake rotated in the opposite direction to the rotor and the flow field had a fairly axisymmetric shape. Investigating the effects of ambient turbulence, they found them to be negligible in the near wake, whereas after 3 D downstream the wake started a faster recovery under higher ambient turbulence levels [41]. Under yawed conditions, the turbine was found to deflect the wake to the side. Consequently, yawing the machine could potentially enable an active control of the wake flow.

Additionally, evidence of wake meandering was found both with and without ambient turbulence including the cases of yawed rotors and it was attributed to the instabilities due to vortex shedding. After further investigation by Medici and Alfredsson [42], the parameters of the blade number, pitch angle and tip speed ratio were found to influence the meandering.

In 2007, España et al. [43], used a rotor model in a simulated rough ABL to study the far wake. The measurements were performed in the Malavard wind-tunnel, a close-circuit type facility at the University of Orleans, France. Two different rotor models were considered in two different ambient turbulence configurations. Turbulence intensity results were in good agreement with the Smith and Taylor [23] observations that maximum turbulence is located above the rotor axis. The downshift of the maximum velocity deficit below the rotor axis, observed by Crespo et al. [22], was found only after 6 D downstream and it was suggested that it might be related to the different types of ABL considered.

In 2009 and 2010, Chamorro and Porté-Agel [44, 45] used hot-wire anemometry to measure the wake of a model wind turbine in a boundary-layer wind-tunnel at the University of Minnesota; the tunnel was operated as a closed return loop and air was pumped by a large axial fan. Detailed data of velocity and turbulence intensity at various distances downstream were collected. The machine was placed over both rough and smooth surfaces under neutral [44] as well as stable [45] conditions. It was found that the increased wind shear and ambient turbulence due to higher roughness enhances the development of higher turbulence in the upper part of the wake. The velocity deficit was found to be nearly axisymmetric, except near the surface downwind of the location where the wake touches the surface. This distance was found to decrease with increased roughness. The effects of velocity deficit and turbulence intensity in the wake remained non-negligible, even at a distance of 15 D downstream. Later experiments in the same wind-tunnel [46, 47], indicated that there is additionally a clear lateral (y)

asymmetry in the wake of the model rotor, as shown at a lateral cross-section 5 D downstream.

Field experiments

Full scale wake measurements of a 2 MW turbine were performed by Högström et al. [48] at Näsudden, Sweden. The machine had a rotor diameter of 75 m and a hub height of 77 m and was located at flat terrain. Several measurement techniques were employed: a high resolution SODAR (SOnic Detection And Ranging) measured mean velocity and turbulence intensity at 2–3.6 D downstream; turbulence instruments located on a 145 m tower, 3 D downstream, provided data of velocity and turbulence at three levels and Tala kites measured the velocity deficit and longitudinal turbulence at the centre line, up to 10.5 D.

A well-documented measurement campaign was the Nibe project [49]. Two machines of 40m diameter were positioned 200m apart and four measurement towers were positioned on the intermachine axis to provide data of wind speed and turbulence characteristics. One tower employed five anemometers and the others seven anemometers at different levels. Further information on the Nibe project is provided in Chapter 4, where the data is used for the validation of the CFD simulations.

Magnusson et al. [50] and Magnusson and Smedman [6] performed measurements at the Alsvik wind farm (Sweden). Two meteorological masts of 54 m high were employed, one to measure the undisturbed wind wind profile and the other to measure the wakes of three 180 kW wind turbines in a downstream distance of 4.2 D, 6.2 D and 9.6 D respectively. The masts were equipped with wind sensors at eight levels. The machines had a rotor diameter of 23 m and a hub height of 35 m. They found the lateral and vertical distribution of the velocity deficit to have an approximate Gaussian shape [6].

Results from a 2-year measurement campaign at the Wind Turbine Test Station

Wieringermeer (EWTW) of the Energy research Centre of the Netherlands (ECN) [51] have also been recently presented [52] for the validation of wake models. The test site consists of five 2.5 MW machines positioned in a row and a 108 m high meteorological mast. The wind turbines hub height and rotor diameter was 80 m. The data comprised of turbine SCADA (Supervisory Control And Data Acquisition) data and wind speed and turbulence intensity at 2.5 D and 3.5 D distance for various ambient wind speed and turbulence intensity.

Some other, well-documented field tests of wind farms are the Sexbierum [13], Middelgrunden [53], Horns Rev [54, 55], Nysted [56] and Vindeby [57]. Apart from the Sexbierum experiment, all other cases are offshore and not all data is publicly available.

2.3.4 Wake models

A detailed review of the several wake models has been performed by Crespo et al. [12], Vermeer et al. [13], Sanderse [9] and Sanderse et al. [15]. An overview of the most important models is given in the following paragraphs, focusing on the kinematic and the parabolic models.

Kinematic models

As mentioned previously, the kinematic models are based on self-similar velocity deficit profiles in the far wake. Wake growth is considered to be controlled by the sum of ambient, shear generated and turbine generated turbulence. The initial velocity deficit is usually found using the rotor thrust coefficient, while the maximum velocity deficit at each position downwind is calculated assuming a global momentum conservation. Despite their disadvantages due to some simplified assumptions, the kinematic models may provide reasonable predictions in simple cases provided that the appropriate parameters are chosen [12].

Lissaman [32] and Voutsinas et al. [58] used theoretical descriptions of the decay of jets to derive the wake velocity profiles, while Vermeulen [59] used a similar profile of Gaussian type. Crespo et al. [60] based their simple model on the approaches of Lissaman [32] and Vermeulen [59] introducing an antisymmetric wake to account for zero velocity perturbation at the ground. Nevertheless, the consideration of the ground effect remains a fundamental weakness of the kinematic models.

Katic [61] further developed a wake decay model by Jensen [62] providing a simplified wake velocity profile, by assuming the velocity constant inside the wake (also known as 'top hat' profile). The wake was considered to have an initial diameter equal to the rotor diameter and to spread linearly with downwind distance, according to a predefined decay coefficient. The model is the basis of the WAsP wake model and further details can be found in Sec. 8.4.1.

More recently, Larsen et al.[63] developed a kinematic model based on the classical wake theory of turbulent boundary layer flows [64]. The model considers the wake flow to be axisymmetric and incorporates empirical relations for the calculation of wake turbulence intensity and length scale. It also assumes that the velocity deficit decays with downstream distance x according to $x^{-2/3}$, the turbulence intensity decays as $x^{-1/3}$, while the wake width increases by $x^{1/3}$.

Parabolic wake models

The parabolic models, also known as boundary-layer wake models, solve a simplified form of the Reynolds Averaged Navier-Stokes (RANS) equations. Based on the assumption that the flow is steady-state, in one predominant direction and cross-flow is negligible [65], the diffusion and pressure gradients in the streamwise direction are neglected [15]. This leads to a faster simulation, space-marching downstream, but the wake expansion cannot be predicted successfully [15].

Ainslie [19, 66] developed a parabolic eddy viscosity model (EVMOD) assuming axisymmetric wake flow and ignoring ground effects and flow variations with

height. The approach provided reasonable results when compared to wind tunnel experiments. This model was the basis for improvements incorporated in later models [67, 68]. However, due to the assumption of axisymmetric flow, the maximum velocity deficit and turbulence intensity are wrongly predicted to be on the turbine axis.

Crespo et al. [60] developed the UPMWAKE model taking into account the ground roughness and atmospheric stability. The code uses the k-ε model for turbulence closure and does not assume axial symmetry. The UPMWAKE predictions were validated using the commercial CFD PHOENICS code, as well as wind-tunnel and full-scale experiments providing acceptable agreement, with the exception of the near wake region, where the predicted velocity deficit was smaller than the measured [69].

The UPMWAKE code was the basis for the development of the WAKEFARM model [21] by ECN. The model was further improved to take into account wake expansion [70]. The UPM-ANIWAKE model [25] was also developed as an extension of the UPMWAKE code to consider anisotropic turbulence in the atmosphere as well as in the wake. The anisotropy of turbulence in wind turbine wakes was further studied using an algebraic stress model by Gómez-Elvira et al. [26].

2.3.5 CFD wake modelling

A fundamental distinction of the several approaches of modelling the rotor is between the full-rotor computations (direct modelling) and the actuator models. In the former category, the detailed geometry of the blades is considered (e.g. Sørensen and Johansen [71], Zahle and Sørensen [72]). Despite the higher detail, they are computationally expensive, especially if multiple rotors need to be considered. In the second category, the approaches are based on the actuator disc principle, explained in Sec. 2.3.1. Instead of considering the actual geometry,

they apply equivalent forces to model the rotor, which are added as momentum sinks to the flow equations. In this way, they avoid the need for resolving the airfoil viscous boundary layer, saving significant computational cost. Since an actuator disc approach is used in this thesis, an outline of other actuator disc models is given in the following paragraphs, based on the reviews of Trolborg [24], Réthoré [73] and Sanderse et al. [15]. Sanderse et al. [15] also included a detailed overview of the direct modelling approaches.

Ammara et al. [74] and Masson et al. [75] modelled the rotor as an actuator disc by applying surface forces which are linked to the drag and lift coefficients (see Sec.3.1.2). A Control-Volume Finite Element Method was employed for solving the steady-state [74] or unsteady [75] Navier-Stokes equations. A finer grid on the actuator disc surface was created in order to increase the accuracy of the surface force integral. A similar approach of modelling the actuator disc by means of surface forces was also applied by Alinot and Masson [76, 77] using the commercial code FLUENT with the k-ε turbulence model. The technique was developed for the simulation of rotors operating in the ABL under various stratifications. In a more recent study, El Kasmi and Masson [78] used FLUENT with an extended k-ε model. They modelled the rotor using the 'fan' model, which introduces a pressure jump at the rotor. The results were validated with various full-scale tests and compared with the performance of the Crespo et al. [60] model, showing better results.

Unsteady computations were performed by Sørensen and Kock [79] and Sørensen et al. [80] using cylindrical coordinates at the actuator disc. Sørensen and Kock [79] calculated the rotor forces, based on tabulated airfoil data [79], while Sørensen et al. [80] assumed a constant loading, with a Gaussian regularization function to smoothly distribute the loading to the mesh, avoiding numerical difficulties.

Cabézon et al. [81] used the simple approach of calculating the actuator force from

the thrust coefficient C_T, assuming a uniform loading. They compared several CFD modelling approaches and validated the results with a full-scale experiment. They found the Reynolds Stress Model (RSM) to provide the best predictions of velocity deficit and turbulence intensity in the far wake, compared to the standard, modified [78] and realizable k-ε models. Prospathopoulos et al. [82, 83] used the same approach of modelling the rotor along with the k-ω turbulence model; they proposed an iterative procedure of calculating C_T from the axial induction factor (defined in Sec.2.3.1). Jimenez et al. [84–86] also used a constant loaded rotor along with Large Eddy Simulation (LES).

Sørensen and Shen [87] developed the actuator-line technique, where the forces act on rotating lines representing the blades. This approach was also studied by Mikkelsen [88] and was implemented in EllipSys3D, which is the Risø-DTU in-house CFD code using a finite-volume RANS solver. The EllipSys3D solver and the actuator-line technique were further used along with LES by Ivanel [89], Ivanel et al. [90, 91], Mikkelsen et al. [92], Troldborg [24] and Troldborg et al. [93–95] to model either single wakes or wake interactions.

Shen et al. [96] extended the actuator line model to the actuator surface approach. Instead of using a line to simulate the blade, the approach introduces the use of a planar surface. In a comparison with the actuator-line approach, some improvements were found in the representation of the tip vortices and the flow near the airfoil [96]. Dobrev et al. [97] presented an actuator surface hybrid model, representing the blades with their mean surfaces and applying a pressure jump along them. It was implemented in FLUENT 6.2 commercial CFD code modelling the blades as 'fan' boundary conditions.

Réthoré [73] and Réthoré et al. [98] developed the actuator shape approach. The method essentially distributes forces from a shape grid in the computational domain, allowing for the shape to be determined independently. The forces are proportionally redistributed to the domain grid based on the intersecting

polygons. Even though the mean velocity results of the model are satisfactory, the model fails to account for the added small scale turbulence, generated by the blades, which needs to be added independently.

Porté-Agel et al. [46] and Wu and Porté-Agel [47] used the actuator disc concept with Large Eddy Simulation (LES). They included rotational effects and a distributed, non-uniform force loading on the disc and they validated the results with wind-tunnel measurements. They showed that the inclusion of rotation and distributed loading leads to a significant improvement of the mean velocity and turbulence predictions in comparison with the approach without rotation and with uniform loading. The latter approach was overestimating the velocity deficit and turbulence intensity up to approximately 5 D downstream.

In this thesis, the Virtual Blade Model (VBM), an actuator disc model, based on the BET, was used to model wind turbine wakes. The approach was implemented using the commercial solver FLUENT 12.0, while turbulence closure was achieved using the Reynolds Stress Model (RSM). In Chapter 4, results of the model were validated with the full-scale Nibe measurements [49] of a single wake. The wake deficit predictions were in general good agreement with the measured values, although there was an overestimation of the lateral deficit profile above the turbine axis and an underestimation near the ground. Additionally, the model consistently overpredicted turbulence intensity.

2.4 Wind flow over complex terrain and near forest canopies

The previous work on wind flow over complex terrain and near forest canopies is reviewed separately in this Section. This literature is relevant to the Chapters 6 and 7, involving the CFD modelling of flow over a real hill and over a forest respectively, without the presence of wind turbines.

2.4.1 Wind flow over complex terrain

The various studies of wind flow over complex terrain are reviewed in three separate categories: the most basic simple models, a number of the most important experimental studies and CFD modelling approaches, which are validated with some of the full-scale experiments.

Simple models

Many efforts in modelling the ABL flow over complex terrain can be found in the literature since the mid-seventies [99]. In one of the most influential studies, Jackson and Hunt [100] performed a linear analysis of turbulent flow over two-dimensional, low hills. Provided that the slope of the hill was small, the analysis was able to perform predictions of the increase in mean wind speed near the hill surface. One of the main outcomes was that the flow can be broadly divided into an inner layer close to the surface, where turbulence is important and an outer layer, where the flow can be considered as inviscid. Mason and Sykes [101] extended the Jackson and Hunt analysis to three dimensions and Mason and King made further improvements developing the Mason-King model D [102]. Walmsley et al. [103] used the Mason-Sykes 3-D extension of Jackson and Hunt theory in combination with their own developed model (MS3DJH) of flow over hills [104] and created MS3DJH/3R, a model of neutrally stratified flow over complex terrain taking into account surface roughness variations.

In another study, Zeman and Jensen [105] developed a simple model for the investigation of turbulence in neutral flows over two dimensional isolated hills. The equations were solved in a streamline coordinate system and their results highlighted the importance of streamline curvature in determining turbulence structure. Troen [106] presented another linearised model, BZ (Bessel Expansion on a Zooming Grid) model [106], also based on Jackson - Hunt theory and similar to the MS3DJH model. The BZ model was integrated into WAsP (the Wind

Atlas Analysis and Application Model) and it has been used extensively for the calculation of the mean flow perturbations in complex terrain.

The models of WAsP [106] and MS-micro (the microcomputer equivalent of MS3DJH/3R [107]) have been historically the most common approaches used by wind developers for modelling the flow over complex terrain [3, 14]. They assume neutral atmospheric flow conditions and they have performed well in cases of gently sloping terrain and low hills. However, in a more complex terrain where non-linear effects such as flow separation and recirculation occur, the simple models fail to provide valid predictions. The calculations of Ayotte [108] suggest that for a hill slope greater than 0.2, the linear model errors become significant.

Experimental studies

Several full-scale experiments provided relevant data for the validation of the several modelling approaches detailed above. Mason and Sykes [101] performed an early experimental study of flow over Brent Knoll, a moderately sloped, isolated hill. Other significant measurement campaigns were performed over Black Mountain [109], Blashaval Hill [102], Nyland Hill [110], Kettles Hill [111]. Some of the models in Sec. 2.4.1 (Mason-King Model D, MS-micro, BZ-WAsP) were compared with observations of mean wind flow and turbulence statistics made at Blashaval Hill [102] and the results showed good agreement [107].

An extensive and important study was made over Askervein [112–115]. The Askervein Hill project provided an extensive dataset for studies of wind flow and turbulence over low hills in near-neutral stratification using numerical and wind-tunnel models [116]. Measurements at Askervein showed satisfactory agreement with the Zeman and Jensen model predictions [105]. Linear models based on Jackson-Hunt theory performed excellently in terms of the mean flow predictions on the upwind slopes and at the crest of the hill, but less well on the lee slopes [116]. Several wind-tunnel studies of flow over Askervein also produced

good agreement with the full-scale observations [116]. Finardi et al. [117] used wind tunnel data from RUSHIL experiment in order to compare MS3DJH, another linearised (FLOWSTAR) and two mass consistent models (MATHEW and MINERVE) over the modelling of the wind flow over two-dimensional hills of analytical shape and varying slope.

Measurements of the horizontal turbulence intensity in complex terrain were also performed by Skupniewicz et al. [118] and a model of surface-layer turbulence intensity was developed based on the theory by Panofsky [119]. Founda et al. [120] presented turbulence measurements at the summit of a highly complex terrain hill in Andros island (Greece). A recent study was performed by Vosper et al. [121] examining the momentum budget close to the surface of Tighvein Hill, a moderately sloped hill. Most recently, a new extensive measurement campaign over the small isolated island of Bolund was performed by Risø DTU with the aim of providing a new dataset for the validation of various flow models in real complex terrain [122, 123].

CFD modelling

CFD has been used for modelling the wind flow over real complex terrain mostly at a research level, whereas the linear models were preferred by wind farm developers, mainly due to their simplicity and resulting lower computational requirements and fast implementation. However, CFD is expected to significantly improve the accuracy of the wind flow and turbulence predictions in highly complex terrain compared to the linear models, especially in cases of flow separation or when thermal effects become important [124]. Palma et al. [125] have demonstrated the use of CFD in combination with conventional techniques, such as linear models and wind measurements, for wind resource assessment and micro-siting. In an analysis of a coastal site in Madeira Island, they showed that CFD can be used to obtain a global view of the wind flow over the site as well as identify regions of

flow separation, unsuitable for the installation of wind turbines. Sumner et al. [14] provided an up-to-date review of the CFD research of wind flow over complex terrain.

Kim and Patel [126] published results using various two-equation turbulence models for flow over Sirhowy Valley (Wales), an embankment on the Rhine (Germany) and Askervein Hill (Scotland). Among the tested models, the RNG k-ε model gave the best mean velocity and turbulence predictions, as well as the size of the separated flow region. Kim et al. [127] presented further results using the RNG k-ε model for flows over Cooper's Ridge, Kettles Hill, Askervein Hill and Sirhowy Valley. The approach provided good results of velocity increase, especially upstream of the hill crest (in Cooper's Ridge, Kettles and Askervein hills) and it performed well in predicting separation and reattachment points at Cooper's Ridge. However on the Askervein case, it slightly underestimated the velocity increase at the hilltop, but most importantly, it underestimated the turbulent kinetic energy at the lee side of the hill. Similar results were recorded by Undheim [128] also using the same model on the Askervein case. The RNG k-ε model was also used by El Kasmi and Masson [129] for the flow simulation over Blashaval Hill and it provided poor predictions in the recirculation zones.

Cabezón et al. [130] tested the performance of some of the most common two-equation turbulence models, such as the k-ε model with several approaches of modified constants to account for ABL flow, the RNG k-ε and the realizable k-ε models. Comparison was made with full-scale measurements from the Alaiz site in Spain, which were previously used to compare linear and non-linear models [131, 132].

The Askervein Hill project provided a significant benchmark for the validation of a large number of CFD ABL modelling approaches, such as [1, 126–128, 133–147]. Notably, Castro et al. [139] used a wide range of computational grids and flow conditions applying the standard k-ε model along with unsteady RANS

calculations and demonstrating the importance of the vertical discretisation. Comparisons in terms of velocity increase were good, however they over-predicted turbulent kinetic energy upstream of the hilltop, which was attributed to the limitations of the k-ε in cases of streamline curvature. Eidsvik [142] used a k-ε closure together with an algebraic stress model [148] to account for anisotropic turbulence. Velocity results are satisfactory, turbulence however is under-predicted at the lee side of the hill. Bergeles et al. [135] and more recently, Prospathopoulos and Voutsinas [143] provided guidelines for the implementation of RANS solvers in complex terrain cases validating their results with the Askervein velocity measurements. The effect of the boundary conditions in the quality of the predictions was underlined in both cases. Prospathopoulos and Voutsinas [143] in particular, applied a k-ε model with modified constants and highlighted the importance of the wall function approach in the prediction of the flow deceleration at the lee side of the hill.

A recent development was the blind comparison [149] of several approaches of wind flow simulation over the Bolund hill and the validation with measurements [123]. The different approaches included wind-tunnel experiments, the use of linear models, RANS simulations and LES. The 10 top performing simulations were all RANS based, using 7 different solvers with an error of $13 - 17\%$ for principal wind directions. The wind-tunnel experiments gave good predictions of velocity increase but poor results on turbulence, whereas LES was found difficult to implement. The comparison results prompted the use of RANS-based models as a state-of-the-art approach in the simulation of flows over complex terrain [149].

In this thesis (Chapter 6), the flow over Askervein hill was modelled using the commercial software FLUENT 12.0. The approach was RANS-based and turbulence closure was achieved with the RSM in order to account for the anisotropy of atmospheric turbulence. The streamwise variations of velocity increase and turbulence were found to be in good agreement with their measured values. However, some discrepancies the model underpredicted the velocity

increase at the hilltop, as well as the increase of turbulence at the lee side of the hill.

2.4.2 Wind flow near forest canopies

Complex terrain sites often include the presence of forested regions. For this reason, the understanding of the influence of forests to the wind flow over an area can be crucial for the successful assessment of a potential wind farm site.

The flow over forest canopies features a number of complex characteristics, which differentiate it from any ordinary ABL flow. Momentum is absorbed from the wind, not only due to the presence of the ground, but also through the whole canopy depth as aerodynamic drag on the foliage [5].

Moreover, two additional processes related to turbulence production and dissipation occur. The work of the wind flow against the aforementioned aerodynamic drag, transforms some of the mean kinetic energy into turbulent kinetic energy in the wake of the canopy elements [150] with a length scale equal to their size [151]. The second process is known as the spectral short-circuiting of the energy cascade and it is related to an additional loss of turbulence energy within the canopy due to the aerodynamic drag, as large shear-generated eddies are transformed into smaller scales in the foliage wake [151]. As a consequence, the normal energy cascade process (transfer of turbulence energy from large scale to smaller [152]) is short-circuited and the dissipation rate is increased.

Experimental studies

A limited number of full-scale studies of wind flow near a forest edge has been published in the literature (see Lee [153] for a comprehensive review). Raynor [154] measured wind velocity near the edge of a pine forest and Gash [155] performed a study of wind velocity and turbulence downwind of a forestmoorland

transition. Gardiner [156] performed observations above and within a dense spruce forest, while Irvine et al. [157] performed a measurement study of wind velocity and turbulence at a moorland to forest transition. The examined forest consisted of 7.5 m high Sitka spruce trees and the experimental results provided a reference for the validation of several numerical models, while a comparison was also performed with relative wind-tunnel studies [158]. More recently, Dupont et al. [159] presented the results of a measurement campaign performed over a period of two years at a maritime pine forest with a mean tree height of approximately 22 m. The data were also used for the validation of a LES numerical approach [160].

CFD modelling

Several approaches have been developed for modelling canopy flows; Raupach and Thom [151] and Finnigan [150] published two extensive review papers, 20 years apart, describing the research-to-date. Apart from the RANS based approaches, Finnigan [150] also examined some LES modelling attempts.

A fair number of the recently proposed RANS-based CFD methods to model the effect of forest canopies on the wind flow, involved various modifications to two-equation turbulence models and mainly the k-ε model [161–170] (see Katul et al.[165] for a review of the main approaches). Svensson and Häggkvist [161] developed a simple canopy model based on k-ε closure applying momentum sinks and k and ε sources in the equations. Their approach was also applied by Lopes da Costa et al. [168] in a study of the wind flow over two potential wind farm sites of moderately complex terrain near forests. The simulations highlighted the importance of the complex interactions between wind direction, terrain shape and the distribution of the wake generating forest canopies over the region of interest. The presence of a forest was found to increase turbulence levels up to two orders of magnitude.

Sanz [164] also used the k-ε model and further developed previous approaches [162, 163]. Following the work of Green [162], Sanz used a source term for k to account for the wake turbulence production and a sink term to account for the short-circuiting of the turbulence cascade. Source and sink terms were also added in the ε equation according to a model proposed by Liu et al. [163] as an improvement of the simpler approach of only adding a source term which was not in agreement with wind-tunnel data [163].

Lopes da Costa [171] tested four canopy models used along with the k-ε model, Svensson and Häggkvist [161], Green [162], Liu et al. [163] and Sanz [164] models, and found that the Sanz [164] model performed better than the other three. He also extended the Sanz procedure [164] to the k-ε-$\overline{u^2}$-f turbulence model and derived new values for the β_p and β_d constants.

More recently, Dalpé and Masson [170] used FLUENT 6.2 with the k-ε modifications of Sanz [164] and Katul et al [165] to model the forest canopy as a porous medium. A new formulation of the wall function inside the forest was applied, assuming a negligible shear stress at the ground far from the edges of the forest [165]. Results were validated with the Irvine et al. [157], Raynor [154] and Gash [155] full-scale experiments and wind velocity predictions were good, however the turbulence intensity increase inside the forest was not predicted accurately.

Out of the available turbulence models, RSM is expected to more accurately predict the complex turbulent flow in and around the canopy [165]. Most of the use of the commercial codes was focused on the two-equation models, mainly due to their low computational cost, but also because they often provide good predictions of fundamental wind properties, such as wind speed and turbulent kinetic energy [172]. However, such first-order models cannot provide information of each of the Reynolds Stresses, which is important in most cases [165]. The

applicability of second or higher order closure models for modelling canopy flow has been investigated in the past [173–180].

Notably, Ayotte et al. [179] following the work of Wilson [174] used wake production and dissipation terms in the normal Reynolds Stress equations. The production terms were assumed to be allocated isotropically among the normal Reynolds Stresses and they express the conversion of the mean kinetic energy of the flow into turbulence in the wake of the trees. Ayotte et al. [179] also parametrized turbulence dissipation into the isotropic conventional term, solved in the ε equation, and an anisotropic part as the canopy drag extracts energy from the turbulent eddies and converts it into small-scale turbulence of canopy element size [174]. The second part is anisotropic, as it diminishes the normal Reynolds Stress parallel to the flow more than on the other two directions in order to isotropise turbulence inside the canopy.

In Chapter 7 of this thesis, a 3-D canopy model was developed, using FLUENT 12.0, following the work of Sanz [164] and Lopes da Costa [171]. Using the RSM, source terms were applied in the equations of the normal Reynolds Stresses. A similar approach to the approach of Ayotte et al. [179] was followed and the wake turbulence production term was isotropically partitioned, whereas the dissipation term was anisotropically partitioned. The model was verified using the Irvine et al. [157] experiments and results were satisfactory.

2.5 Wind turbine wakes in complex terrain

As this thesis addresses the issue of wind turbine wakes in complex terrain, the relevant literature (experimental and CFD modelling studies) is examined in this section separately.

2.5.1 Experimental work

The effect of complex terrain on wake behaviour was studied in a wind-tunnel by Taylor and Smith [181] and Smith [182]. They examined the wake of a simulator positioned at five different streamwise locations on an idealised hill applying an approximately logarithmic incoming flow profile and showed that complex terrain can have an important effect on the wake characteristics. When the turbine was located on the upstream side of the hill, there was a more pronounced downward displacement of the maximum velocity deficit point and a faster wake recovery in comparison to a flat terrain case; in particular, when the rotor was placed at the middle of the up-slope, the wake was almost fully recovered at 10 D downstream. They also observed that the wake delayed the flow separation on the lee side of the hill. However, when the turbine model was placed on the hilltop, considerable increase of the velocity deficit and turbulence intensity was found and the effect was still evident even at 17 D downwind the simulator. In this case, the wake did not appear to delay the flow separation.

An early full-scale measurement campaign was performed by Baker and Walker [183]. The site was located at Goodnoe Hills, Washington with an elevation of approximately 790 m. Three two-bladed wind turbines of 2.5 MW rated power, 91 m diameter and hub height of 61 m were positioned in a triangular pattern and measurements were performed at several locations downwind of two rotors using kite anemometers. The double wake deficit under stable atmospheric conditions were found 15–18% at 9 D and 30–40% at 3–5 D, whereas under more turbulent conditions the wake dissipated faster and the deficits were 15–20% at 7 D and negligible at 9 D.

Elliot and Barnard [184] employed nine meteorological towers at the same site (Goodnoe Hills) and studied several wake characteristics, such as velocity deficit, turbulence intensity, wake width and trajectory at various distances 2–10 D downwind. The effect of ambient wind speed and turbulence intensity on the

velocity deficit was also examined. In some directions examined, the presence of trees (mostly pine and juniper trees) was less than 500 m away and affected the results. Velocity deficit was found higher for low ambient wind speed and low turbulence intensity, while it was lower for high wind speed (low thrust coefficient) and high turbulence intensity (higher dissipation). Turbulence effects on the velocity deficit were significantly higher at low, rather than at high, ambient wind speed; the effect of the ambient wind speed on the velocity deficit was higher at lower, than at high, turbulence intensity.

Another early experimental wake study in complex terrain was performed by Scott [185] at a site of two medium-sized wind turbines on Burgar Hill, Orkney. Despite the fact that the slopes of the hill were not sufficiently complex for flow separation, the hill was considered to be located in complex terrain. The one machine was two-bladed, of 250 kW rated power, 20 m rotor diameter and 16.3 m hub height and the other was three-bladed, of 300 kW rated power, 22 m rotor diameter and 22 m hub height. They were spaced approximately 6 D apart and three, 30 m-high met masts were employed on the inter-turbine axis, each equipped with six anemometers. The full wake deficits were found to be 4–10% of the upwind power.

Wake measurements in complex terrain were also presented by Helmis et al. [186] and Papadopoulos et al. [187]. They examined the near wake structure of a three-bladed 100 kW wind turbine located in complex terrain site on Samos Island, Greece.

Stefanatos et al. [188] presented full-scale wake measurements from the Kalivari wind farm, located on the mountainous island of Andros, Greece. The wind farm consisted of seven 225 kW upwind machines of 27 m rotor diameter and 31.5 m hub height. Data were collected using two meteorological masts, each equipped with a cup anemometer and a wind vane at three height levels. Two single wake and two multiple wake cases were presented. The single wake velocity deficit was

found to be considerably less than the deficit measured at Alsvik wind farm [50], which is located on coastal, flat terrain site, where wind was blowing from the sea at low turbulence levels. This is in agreement with other studies indicating that a higher turbulence level accelerates the wake recovery. The double wake turbulence intensity and velocity deficit measured were comparable to the values measured from a single wake indicating that a linear superposition of the wakes is not correct.

2.5.2 Modelling

Most of the wake models were applied and validated for flat terrain cases [13]. There are several models that take into account the effect of terrain and topography on wakes, such as those proposed by Voutsinas et al. [189], Hemon et al. [190] and Migoya et al. [191]. Commercial CFD programs have also been used together with numerical calculations to study wake and terrain interaction for simple cases [192].

Crespo et al. [193] applied the UPMWAKE model in a moderately irregular terrain wind farm by superposing wake and terrain effects. The study showed that if the velocity irregularities of the terrain and the wake velocity deficit are of similar order of magnitude, the linear superposition approach seems to provide acceptable results, although this assumption is generally not valid for wake interaction.

Chaviaropoulos and Douvikas [194] developed an in-house Navier-Stokes solver for wind prediction over complex terrain taking into account distributed arrays of wind turbines acting as momentum absorbers. The k-ω model was used for turbulence closure and the method was used to investigate single wake and wake interaction on flat terrain.

Migoya et al. [191] presented a hybrid method of calculating wakes in complex terrain wind farms and validated the results with measurements at the Sotavento

wind farm in Galicia, Spain. They considered different approaches for the estimation of the topographic and the wake effects. For cases of simple orography, the topographic effects were studied using UPMORO and WAsP, where UPMORO is a linear model for estimating topographic effects, developed by the Polytechnic University of Madrid [191]. For more complex terrain cases, the CFD code FLUENT was employed using a k-ε turbulence closure, with some modifications of the constants. The wake effects were considered using the UPMPARK code, which is the extension of the UPMWAKE model (see Sec. 2.3.4) to include multiple rotors.

Lee et al. [195] modelled the wind farm site located on the eastern mountainous area of Korea, using the commercial code STAR-CD v4.08. The total number of 49 rotors were modelled according to the frozen rotor method, by setting multiple reference frames to consider the rotational effects. They solved the steady, incompressible, 3-D Navier Stokes equations along with the standard k-ε model. The terrain effects were considered using a 10 m resolution digitized map, covering a 10 km $\times$ 12 km area. They demonstrated that the method can represent the detailed flow around the rotor but the computational cost was very high, as the grid contained a total number of approximately 22,000,000 cells. Using a 20-CPU (2.5 GHz, 64-bit processor) cluster, it required 2 days for the solution to converge, after 1,000 iterations.

In later developments, Montavon et al. [196] used the ANSYS CFX commercial CFD software to model the Vindeby offshore wind farm [197] and the Black Law onshore wind farm in Scotland, UK. Despite the small height variations (approximately 170 m), the latter case can be considered a complex terrain case, since it is nearly surrounded by forest canopies. They demonstrated a novel meshing approach, splitting the domain in blocks and allowing for the easy consideration of various inlet wind directions. The k-ω Shear Stress Transport (SST) model [198] was used for turbulence closure. The forest canopies were modelled according to the Svensson and Häggkvist canopy model [161] and the wakes were simulated assuming a constant loaded actuator disc, calculating the

forces based on the rotor thrust coefficient. They modelled all 54 Siemens 2.3 MW machines of the Black Law wind farm and validated the results with measured wind speed on the turbine nacelles. It was shown that the presence of the forest canopies can affect the wake shape downstream, significantly increasing the velocity deficit and turbulence intensity. Agreement with the measurements was fair, although there was an indication that a more accurate representation of the forest was needed.

Prospathopoulos et al. [199, 200] used a Navier Stokes solver along with k-ω closure to investigate a single wake of a 5 MW wind turbine located on top of two different Gaussian hill cases considering varying wind directions and ambient turbulence intensities. The wind turbine was modelled as a uniformly loaded actuator disc, and the force acting as momentum sink was calculated from C_T. In the results, the velocity deficit remained significant at 20 D, even at 40 D for low ambient turbulence, while in a flat terrain case using the same rotor, the wake recovered almost fully at 20 D. An increase of ambient turbulence resulted in faster wake recoveries, as expected. However, the wake did not dissipate monotonically, as in the flat terrain case, especially at high ambient turbulence levels. They also found that the downwards shift of the maximum velocity deficit to be more pronounced in the hill case, as compared to a flat terrain case. The work was part of the project UpWind [200], investigating wakes of large wind farms in complex terrain and offshore. Results of the project were presented by Barthelmie et al. [201–203].

More recently, Prospathopoulos et al. [204] used the same approach [199, 200] on two wind farms: one in flat (the ECN test farm) and one in complex terrain (in Spain). The second wind farm consisted of 43 machines organized in 5 rows; the final grid consisted of 7,000,000 cells, which resulted in a high computational cost. The results were validated in terms of normalised power across four downstream rows of machines. The results of the first row compared well, but further downstream the predictions underestimated the wake effects.

Cabézon et al. [205] simulated the aforementioned wind farm of 43 machines using the wake model CFDWake 1.0, a combination of the actuator disc approach with the CFDWind 1.0 wind model, both developed by CENER and using FLUENT 6.3. They investigated two different approaches of calculating the wakes: initially they calculated the wake and terrain effects separately and applied a superposition, while the second approach was using one single calculation including both wake and terrain effects. They showed that the latter approach provided better results, implying that the superposition of wake and terrain effects is not accurate in complex terrain, due to non-linearities.

Following the UpWind project case studies [200], the single wake of a 5 MW wind turbine positioned on top of a 'quasi 3-D' Gaussian hill was investigated in this thesis (Chapter 5) using the FLUENT 12.0 commercial solver. The RANS equations were solved along with the RSM for turbulence closure. The VBM (based on the actuator disc approach and the BET) was used to model the rotor. A neutral ABL flow was assumed and different ambient turbulence conditions were considered implicitly, by changing the ground surface roughness length. In the results, a comparison was made with the wake of the same rotor over flat terrain case at similar ambient conditions. Some of the UpWind observations [200] were confirmed: faster wake recovery at higher ambient turbulence intensity and a non-monotonic wake dissipation at high ambient turbulence in the hill case, instead of a monotonic wake dissipation in the flat case. A lateral wake 'drift' from the expected streamwise path was also observed in the hill case and at high ambient turbulence levels. This effect was linked to the combination of the wake rotation and the flow disturbance due to the terrain shape. The simulations were extended to the case of two rotors positioned next to each other with a crosswind spacing of 2 D and it was found that the double wake dissipation was slower as compared to the single wake dissipation.

Finally, the aforementioned CFD approach was also applied in two real complex terrain wind farm case studies: one located at a coastal site (Chapter 8)

and one situated on a hilly terrain with forest canopies in close proximity (Chapter 9). The results were validated with SCADA, 10 min. measured averages of power output. The coastal wind farm case involved simulations of single wake and wake interaction of rotors approximately aligned to the flow direction. Predictions using the commercial software WAsP were also used for validation with the measurements. The CFD results were satisfactory and more accurate in comparison with the WAsP predictions, especially when a single wake was modelled. In the second case study, the aim was to investigate the effect of forest canopies to the wake deficit, wind shear and turbulence intensity. The forest canopy model developed in Chapter 7 was applied. In the cases when the forest canopy was located downwind of the rotor, wake deficit and turbulence intensity were found to increase considerably, especially near the ground; wind shear and wake width were also increased. The maximum wake velocity deficit moved upwards, above the turbine axis, and the maximum wake turbulence intensity moved downwards, below the turbine axis. In the case when the forest was located upwind of the first rotor over an ascending slope, the canopy was discovered to have a minimal effect on the wake.

Chapter 3

Methodology

In this chapter, the general approach for modelling wind turbine wakes in the neutral atmospheric flow over flat or complex terrain is presented. All the models and modifications discussed were available or additionally applied using the commercial Computational Fluid Dynamics (CFD) solver FLUENT 12.0.

3.1 Rotor modelling

The Virtual Blade Model (VBM) of FLUENT is used to model the wind turbine rotors in this thesis. It is a method developed by Ruith [18] for analysing the aerodynamic performance of rotors based on previous approaches by Zori [206] and Yang [207]. The theoretical basis for the development of the VBM is linked to the actuator disc approach and the Blade Element Theory (BET), which are presented in Sec. 2.3.1 of this thesis.

The VBM has been designed to be implemented in FLUENT for cases of rotating flow where there is a need for modelling the time-averaged cumulating effects of the rotor blades [18]. The rotor is modelled in an implicit manner, by means of source terms in the momentum equations: based on the BET, momentum sinks are used on an actuator disc allowing for varying chord, twist and airfoil types

without the need for detailed meshing of the rotor blades. The model was initially applied on helicopter rotors [18, 208–212], but its use on wind turbines has also been demonstrated [210].

3.1.1 VBM compared to other FLUENT approaches

Apart from the VBM, the FLUENT solver provides several other tools for modelling the effects of rotating blades, such as the FAN model, the Single/Multiple Rotating reference Frame models (SRF/MRF) and the Sliding Mesh Model (SMM) [213].

The FAN model is the simplest option; it applies a time-averaged pressure jump across the rotor (fan) defined as a function of the local fluid velocity normal to the fan with an option of specifying the radial and tangential components of the swirl velocity. Although the model is quick and easy to implement as well as fast to run, there is no account for the local flow variations due to the blade geometry (ex. airfoil profile, blade twist and pitch) and thus important details of the flow are missed.

The SRF/MRF and SMM models are mainly recommended for blade design purposes [209, 211]. Blades are individually meshed and no advanced knowledge of the blade aerodynamics is required. SRF/MRF models apply source terms to model the rotational effects whereas in SMM, blade meshes are rotated in real time providing a time-accurate (rather than time-averaged) solution. In both approaches, the solution accuracy is increased at the cost of large cell sizes and high computational resources, Fig. 3.1.

The VBM was introduced in an attempt to combine increased accuracy at the minimum possible computational cost. It provides better flow physics and accuracy compared to the much simpler FAN model [209], since it takes into account information related to the blades, such as pitch angle and sectional

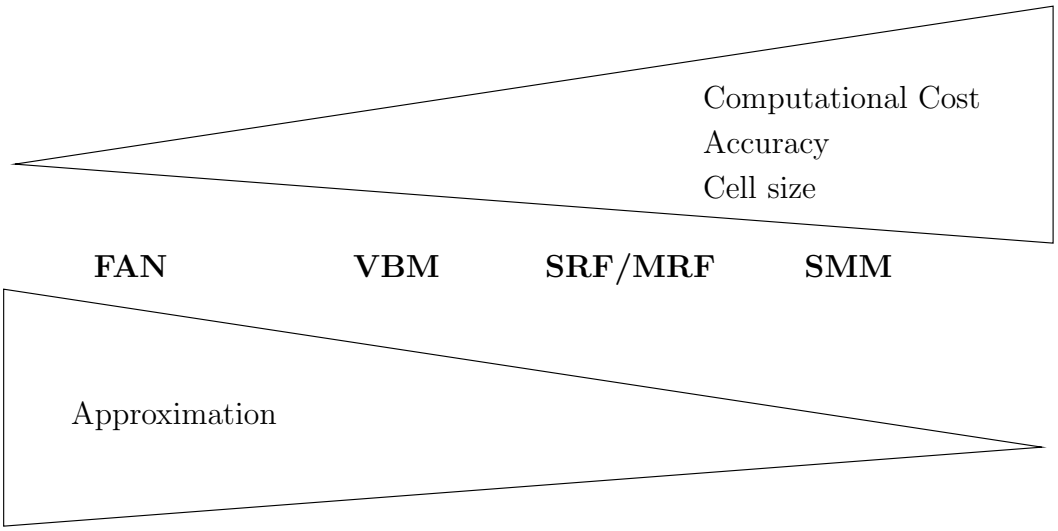

Figure 3.1. The VBM compared to other models in FLUENT. Taken from [211].

(spanwise) variation of twist angle, airfoil section and chord length. Unlike SRF/MRF and SMM models, the VBM eliminates the need for explicitly meshing the blades, significantly reducing the mesh cell count and providing lower computational cost (in terms of mesh generation and simulation time). The accuracy, however, is comparable to the accuracy of the MRF model [209].

For all the aforementioned reasons, the VBM appears one of the best available options for the need of modelling wake effects of wind turbines in wind farms over flat or complex terrain. In such cases the rotating blades are only a small part of the overall domain and so the increased resolution, which SRF/MRF and SMM models provide at high computational cost, is not necessary. The VBM is able to match the average cumulative effects of the blade rotation with the time-averaged Navier Stokes equations allowing for an unstructured mesh which is usually necessary in complex geometries.

3.1.2 The VBM approach

Following the actuator disc approach (Sec. 2.3.1), the rotor is replaced by a rotor disc fluid zone located at the annular area swept by the rotor, without meshing

the individual blades. In a similar approach to Zori [206], the rotor effects are represented by time-averaged source terms added in the momentum equations solved by FLUENT at the grid cells of the rotor disc fluid zone. The source terms are unknown at the start and they later evolve as part of the solution, until convergence is achieved.

Similarly to BET (Sec. 2.3.1), the VBM allows the discretisation of the rotor into a finite number of (up to 20) spanwise sections. Blade properties, such as chord length, airfoil type, and blade twist angle, are allowed to vary and are assumed constant on each spanwise section. To calculate the source terms, the initially computed velocity field is used to obtain the local angle of attack, α, at each blade element, after transforming the velocity components from the reference frame used by FLUENT to solve the flowfield, into a reference frame relative to the rotating blade (Fig. 2.6a). Using Eq. (2.28), φ is calculated from the flowfield solution and β is taken from the pitch and twist angles, which are inputs in the model:

$$\alpha = \varphi - \beta \tag{2.28}$$

The aerodynamic forces are then calculated similarly to Eqs. (2.30) and (2.29). Using a look-up table with the 2-D lift and drag coefficients (C_L and C_D) vs. angle of attack (α) for different Mach (Ma) and Reynolds (Re) numbers, Eq. (3.1) calculates the (instantaneous) aerodynamic forces per unit length, f, on each of the rotor sections:

$$f_{L,D} = C_{L,D}(\alpha, \mathrm{Ma}, \mathrm{Re}) \cdot c(r/R) \cdot \frac{\rho\, U_{rel}^2}{2} \tag{3.1}$$

where U_{rel} is the relative velocity 'seen' by the airfoil section calculated during the flowfield solution and has been explained in Sec 2.3.1.

Since the solution is time-averaged, only a fraction of the forces on Eq. (3.1) need

to be used in the computational cells. Assuming constant rotational speed, Ω, the time needed for the centre of each blade element to rotate one revolution is:

$$T' = \frac{2\pi}{\Omega}$$

where T' is the period of rotation.

The time that the same element spends in a given control volume of width $\delta\theta$ radians is:

$$\delta t = \frac{\delta\theta}{\Omega}$$

Therefore, the fraction of time spent in a cell is:

$$t_{frac} = \frac{\delta\theta}{2\pi}$$

For a rotor of N_b blades, the (time-averaged) lift/drag forces per each cell are calculated in Eq. (3.2).

$$F_{L,D_{cell}} = N_b \cdot \frac{\delta r \cdot \delta\theta}{2\pi} \cdot f_{L,D} \tag{3.2}$$

where N_b is the number of blades, r, θ are the spanwise and azimuthal coordinates respectively.

This approach allows the use of either structured or unstructured mesh consisting of both hexahedral and/or prismatic grid elements. The force vector calculated in Eq. (3.2) is then transformed from the rotor reference frame back into the reference frame of the general flowfield and afterwards, the time-averaged source term is calculated:

$$S_{u,cell} = -\frac{F_{cell}}{V_{cell}} \tag{3.3}$$

The source terms are then added to the momentum equations, Eq. (3.5b).

As mentioned previously, the VBM uses the assumption of 2-D flow, when calculating the local aerodynamic (lift and drag) forces at each spanwise location of the blade. However, this assumption is violated near the blade tip, where the increased secondary flow around the tip results in a reduced lift. This effect is related to the tip losses, as described in Sec. 2.3.1. The VBM takes into account the tip loss effect in a simple approach [18]: a % value of normalised span is selected, to define the blade spanwise location separating the near tip region, where lift forces are not accounted for and only drag forces are still computed in the equations (using the 2-D assumption). A selected value of e.g. 96%, means that the last 4% of the blade near the tip produces no lift, but it still produces drag, which is calculated in a similar way as at the rest of the blade. The default value of 96% was kept in all of the VBM calculations.

3.2 Turbulence Modelling

3.2.1 Reynolds-Averaged Navier Stokes equations

It is common in CFD practice to model the turbulent wind flow using the well known and documented equations of fluid dynamics, the Reynolds Averaged Navier-Stokes (RANS) equations. The equations are based on the decomposition of the flow variables into a mean and fluctuating part, Eq. (3.4), first presented by Reynolds in 1895 [214].

$$u_i(t) = U_i + u_i' \tag{3.4}$$

where U_i is the mean and u_i' the fluctuating part of the instantaneous velocity $u_i(t)$ in the i direction.

The RANS equations express the conservation of mass and momentum of a

Newtonian fluid and, assuming incompressible, steady-state, turbulent flow with constant viscosity (μ), they can be expressed as [215]:

$$\frac{\partial U_i}{\partial x_i} = 0 \tag{3.5a}$$

$$\rho U_j \frac{\partial U_i}{\partial x_j} = -\frac{\partial p}{\partial x_i} + \mu \frac{\partial}{\partial x_j}\left(\frac{\partial U_i}{\partial x_j} + \frac{\partial U_j}{\partial x_i}\right) + \frac{\partial}{\partial x_j}(-\rho\overline{u_i' u_j'}) + S_{u,i} \tag{3.5b}$$

where p is the mean pressure, μ the viscosity, $S_{u,i}$ the momentum source (or sink) in the i direction and $-\rho\overline{u_i' u_j'}$ is known as the Reynolds stress tensor τ_{ij} [216].

The turbulent kinetic energy (k) is related to the sum of the normal Reynolds stresses ($-\rho\overline{u_i' u_i'}$) divided by the density, as shown on Eq. (3.6).

$$k = \frac{1}{2}\overline{u_i' u_i'} \tag{3.6}$$

The problem of turbulence closure results from the need for modelling the time-averaged fluctuating velocity components, i.e. the Reynolds stresses $-\rho\overline{u_i' u_j'}$, in the momentum equation (3.5b). The various turbulence models apply some extra transport equations to account for turbulence using empirical constants and information about the mean flow.

3.2.2 The Boussinesq approximation

The simplest approach for solving the turbulent stresses $-\rho\overline{u_i' u_j'}$ in Eq. (3.5b) is the Boussinesq hypothesis which assumes that the turbulent shear stress ($-\rho\overline{u_i' u_j'}$ for $i \neq j$) is related linearly to mean strain rate (velocity gradients) by means of the turbulent (or eddy) viscosity μ_t in the same way as in laminar flow the (laminar) viscosity, μ, is used [65]. Eq. (3.7) satisfies the Boussinesq hypothesis for Reynolds-averaged incompressible flow. It is important to note that this approach assumes that μ_t is an isotropic scalar, whereas in many cases, such as the case of

neutral atmospheric flow, turbulence is anisotropic.

$$-\rho\overline{u_i' u_j'} = \mu_t \left(\frac{\partial U_i}{\partial x_j} + \frac{\partial U_j}{\partial x_i} \right) - \frac{2}{3}\rho k \delta_{ij} \tag{3.7}$$

where μ_t is the turbulent viscosity and δ_{ij} is the Kronecker delta:

$$\delta_{ij} = \begin{cases} 0 & \text{if } i \neq j \\ 1 & \text{if } i = j \end{cases} \tag{3.8}$$

Some relatively simple turbulence modelling approaches are based on the Boussinesq approximation and involve the use of one or two extra transport equations (corresponding to one-equation and two-equation models) to be added to the RANS equations.

3.2.3 Selection of turbulence model

The FLUENT solver (version 6.3.26 and above) provides a wide range of options for turbulence modelling [213]. The choice of the option suitable for each examined case depends on various factors such as the flow physics, well-established practices related to the specific problem, the required accuracy level and the available computational time and resources [213]. A summary of the turbulence modelling options available in FLUENT and an estimated comparison of their computational cost is shown in Fig. 3.2. There is a basic distinction between the models based on the RANS equations and the Large Eddy Simulation (LES).

Eddy viscosity models

The eddy viscosity models are a subcategory of the RANS based models and they use the Boussinesq approximation (Sec. 3.2.2) to model the turbulent stresses. Depending on the extra transport equations they may include, they are classified

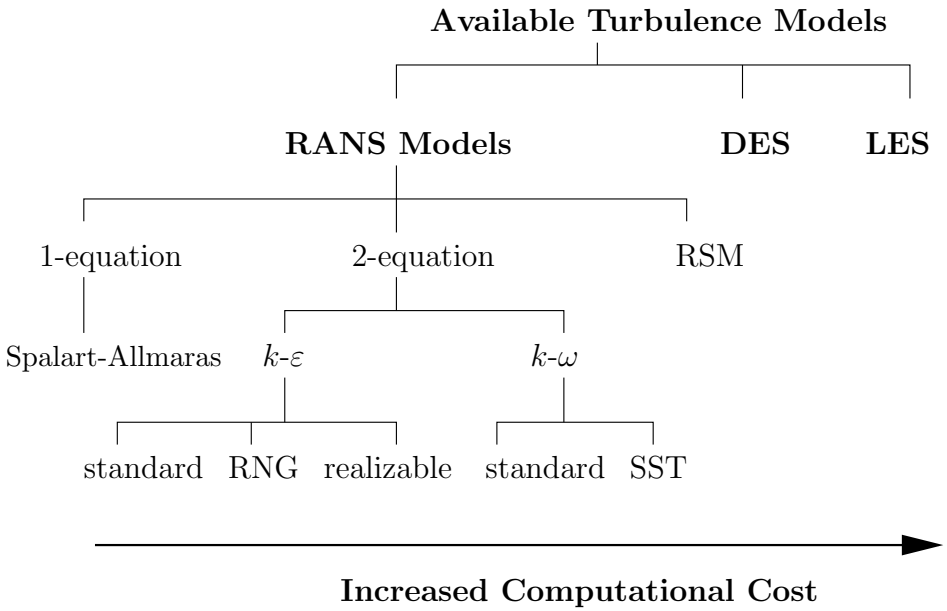

Figure 3.2. Turbulence models available in FLUENT [217].

into one- and two-equation models. The Spalart-Allmaras model from the one-equation models and several variations of the k-ε and k-ω models are available in FLUENT 12.0, Fig. 3.2.

Spalart-Allmaras model The Spalart-Allmaras is a one-equation model and one of the relatively simplest options available in FLUENT. It includes one transport equation for a kinematic eddy (turbulent) viscosity parameter. The model was initially designed for aerospace applications related to wall-bounded flows and it has been found to perform well in boundary layer flows with adverse pressure gradients [213] and turbomachinery. Advantages of the model are low computational cost and fast solution convergence.

***k*-*ε* models** The k-ε model options include the standard k-ε, RNG k-ε and realizable k-ε approaches.

The standard k-ε [218] is the simplest, most popular and widely validated two-equation model. Turbulence closure is achieved with the use of two transport

equations, one for the turbulent kinetic energy k and one for the turbulent kinetic energy dissipation rate ε. The model is robust, computationally economical and performs particularly well in cases of confined flows [216] but it also carries well-documented limitations for cases of complex flows, such as some unconfined flows, cases with large extra strains (ex. curved boundary layers, swirling flows), adverse pressure gradients (ex. separated flows) rotating flows and cases of anisotropic turbulence [216].

The RNG k-ε model is another version of the k-ε model using a mathematical technique called 'renormalization group' (RNG) method. The model is similar to the standard k-ε model with some modifications, such as an additional term in the ε equation to improve analysis of rapidly strained flows and an account for the effect of swirl [213]. The model provides improved predictions for a number of cases including high streamline curvature, high strain rate, separating or swirling flows [219].

The realizable k-ε model differs from the standard version as it uses an alternative formulation for the turbulence viscosity μ_t and a new transport equation for the dissipation rate ε (the k equation is the same). The 'realizability' concerns the application of certain mathematical constraints related to the turbulence physics on the Reynolds stresses. The realizable k-ε model is found to perform better in cases of planar and round jets, boundary layers with strong adverse pressure gradients, flows of separation, recirculation, rotation and streamline curvature.

***k*-ω models** FLUENT provides two variations, the standard [220] and the shear-stress transport (SST) [221] k-ω models.

The standard k-ω model proposed by Wilcox [220] uses two transport equations, one for the turbulent kinetic energy k and one for the specific dissipation rate ω, defined as $\omega = \varepsilon/(\beta^* k)$, where β^* is a model constant. The model was proven

to be more accurate than the k-ε model in certain cases, such as boundary layer, free shear or separated flows [215].

The SST k-ω model, developed by Menter [221] is a hybrid model combining the use of the standard k-ω model in the near-wall region with the standard k-ε model in the fully-turbulent region away from the wall. It also uses a modified turbulent viscosity formulation compared to the standard k-ω model. The model performs particularly better than the rest of the two-equation models in cases of flow separation under adverse pressure gradients and it is recommended for high accuracy boundary layer simulations [222].

Reynolds Stress Model

The Reynolds Stress Model (RSM) is the most sophisticated turbulence model in FLUENT [213]. Turbulence closure is achieved by applying one transport equation for each of the Reynolds stresses and one additional equation for the dissipation rate ε corresponding to $6 + 1 = 7$ additional equations in 3-D applications, avoiding the Boussinesq hypothesis of isotropic turbulence (Sec. 3.2.2).

Compared to the other RANS models, RSM is potentially the most general and physically the most complete, since it calculates each of the Reynolds stresses separately. It is expected to provide better results for a number of complex cases, such as streamline curvature, swirl, rotation and high strain rate. Additionally, it has the potential of accurately predicting anisotropic turbulent flows, which is an important advantage compared to the eddy viscosity models limited by the Boussinesq approximation. Since the number of transport equations is increased, RSM requires significantly more computational time and CPU memory compared to the simpler two- or one-equation models. According to the FLUENT manual [213] RSM requires on average $50 - 60\%$ more time per iteration and $15 - 20\%$ more memory compared to the k- ϵ and k- ω models.

The use of the RSM was chosen for the number of the aforementioned benefits, but most importantly for the fact that the neutral atmospheric turbulence is anisotropic and eddy viscosity models would not have been able to provide detailed predictions for each of the Reynolds stresses.

Large Eddy Simulation

LES takes into account the division of turbulent flow into large and small eddies. The large eddies are considered mainly responsible for the transfer of mass, momentum, energy and other scalars. They are anisotropic and strongly dependent on the flow properties and the problem geometry and boundary conditions. The small eddies are more isotropic, less dependent on the flow configuration and they are expected to be easier to model using a turbulence model. Consequently, LES explicitly (numerically) resolves large eddies using the time-dependent Navier-Stokes equations and only models small eddies (Subgrid-Scale Modelling), which are detected by means of mathematical 'filtering'.

Such an analysis requires a significantly finer mesh and higher computational cost (time and resources) compared to the RANS based options and the use of parallel computing is necessary. Given the limited computational resources and amount of licenses to be used in parallel, this option was not followed in the current study. Furthermore, another important reason for excluding this option was the fact that the VBM was created to be matched with the RANS equations and the use in LES would most probably require changes in the VBM source code.

Detached Eddy Simulation

The Detached Eddy Simulation (DES) is often referred to as a hybrid RANS/LES approach [213, 223] and it was originally proposed by Spalart [224]. It combines an unsteady version of a RANS model in the near-wall region with LES in the free-shear layers away from the wall. FLUENT provides three options for the

choice of the turbulence model: the Spalart-Allmaras, the realizable k- ϵ, and the SST k- ω models.

DES offers the advantages of LES in the free-shear layers in a reduced computational cost and lower grid resolution demands but it is nevertheless a computer intensive method compared to any of the RANS models. Since DES is not incorporating the RANS equations, the VBM would have been incompatible with this option in the same way as with LES, therefore it was dismissed as an option for modelling wind turbine wakes in the current study.

3.2.4 The k-ε model

The simplest and most popular two-equation model is the standard k-ε model, which involves the use of two extra transport equations, one for the turbulent kinetic energy k and one for the kinetic energy dissipation rate ε, which is defined in Eq. (3.9).

$$\varepsilon = \nu \overline{\frac{\partial u_i'}{\partial x_k} \frac{\partial u_i'}{\partial x_k}} \tag{3.9}$$

where $\nu = \mu/\rho$ is the kinematic molecular viscosity.

The two extra transport equations for the k, Eq. (3.10), and ε, Eq. (3.11), are taken from Wilcox [215].

$$\rho U_j \frac{\partial k}{\partial x_j} = -\rho \overline{u_i' u_j'} \frac{\partial U_i}{\partial x_j} + \frac{\partial}{\partial x_j} \left[\left(\mu + \frac{\mu_t}{\sigma_k} \right) \frac{\partial k}{\partial x_j} \right] - \rho\varepsilon + S_k \tag{3.10}$$

$$\rho U_j \frac{\partial \varepsilon}{\partial x_j} = C_{\varepsilon 1} \frac{\varepsilon}{k} (-\rho \overline{u_i' u_j'}) \frac{\partial U_i}{\partial x_j} - C_{\varepsilon 2} \rho \frac{\varepsilon^2}{k} + \frac{\partial}{\partial x_j} \left[\left(\mu + \frac{\mu_t}{\sigma_\varepsilon} \right) \frac{\partial \varepsilon}{\partial x_j} \right] + S_\varepsilon \tag{3.11}$$

where σ_k, σ_ε, $C_{\varepsilon 1}$, $C_{\varepsilon 2}$ are model constants and S_k, S_ε are turbulence source/sink terms which can be used additionally.

The Reynolds stresses $-\rho \overline{u_i' u_j'}$ are calculated from the Boussinesq approximation,

Eq. (3.7), and turbulent viscosity, μ_t, is calculated from Eq. (3.12).

$$\mu_t = \rho C_\mu \frac{k^2}{\varepsilon} \tag{3.12}$$

where C_μ is a model constant.

3.2.5 The Reynolds Stress Model

In the current work, the k-ε model is only employed for the initial iterations and the linear-pressure strain RSM is used to provide results. The RSM includes a set of Reynolds stress equations for the turbulence closure, shown in Eq. (3.13).

$$\underbrace{\rho U_k \frac{\partial \overline{u_i' u_j'}}{\partial x_k}}_{\text{Convection}} = \underbrace{\frac{\partial}{\partial x_k}\left[\left(\frac{\mu_t}{\sigma_k} + \mu\right)\frac{\partial \overline{u_i' u_j'}}{\partial x_k}\right]}_{\text{Diffusion}} + P_{ij} + \phi_{ij} - \varepsilon_{ij} + S_{\overline{u_i' u_j'}} \tag{3.13}$$

where the turbulent viscosity μ_t is calculated in a similar way as in the k-ε model, using Eq. (3.12) and σ_k is a model constant which differs from the one used in the k-ε model. In RSM, $\sigma_k = 0.82$ according to Lien and Leschziner [225].

Eq. (3.13) is solved for each of the different Reynolds stresses. Using 3-D rectangular Cartesian coordinates, the corresponding Reynolds stresses can be written as $-\rho\overline{u'u'}$, $-\rho\overline{v'v'}$, $-\rho\overline{w'w'}$, $-\rho\overline{u'v'}$, $-\rho\overline{u'w'}$, $-\rho\overline{v'w'}$ totalling six extra transport equations.

Eq. (3.13) contains a number of terms, some of which need to be modelled. P_{ij} is the Stress Production term calculated from Eq. (3.14):

$$P_{ij} = -\ \rho\left(\overline{u_i' u_k'}\,\frac{\partial U_j}{\partial x_k} + \overline{u_j' u_k'}\,\frac{\partial U_i}{\partial x_k}\right) \tag{3.14}$$

ϕ_{ij} is the Pressure Strain term, modelled according to Eq. (3.15) according to the

Linear Pressure Strain Model.

$$\phi_{ij} = -C_1\rho\,\frac{\varepsilon}{k}\left(\overline{u_i'u_j'} - \frac{2}{3}\delta_{ij}k\right) - C_2\left(P_{ij} - C_{ij} + \frac{1}{3}\delta_{ij}C_{kk}\right) \tag{3.15}$$

where C_1, C_2 are model constants and C_{ij} is the Convection term in the first part of Eq. (3.13), calculated in Eq. (3.16):

$$C_{ij} = \rho U_k \frac{\partial \overline{u_i'u_j'}}{\partial x_k} \tag{3.16}$$

ε_{ij} is the Dissipation term, modelled as:

$$\varepsilon_{ij} = \frac{2}{3}\delta_{ij}\rho\varepsilon \tag{3.17}$$

The final term, $S_{\overline{u_i'u_j'}}$, is the source of the ij Reynolds stress which can be added as extra by the user.

Similar to the k-ε model, equations for the k, Eq. (3.18), and ε, Eq. (3.19), are also solved. However, only the values of ε calculated from Eq. (3.19) are used globally, whereas the values of k obtained from Eq. (3.18) are used only for the boundary conditions, even though the equation is also solved globally [213].

$$\rho U_i \frac{\partial k}{\partial x_i} = \frac{\partial}{\partial x_j}\left[\left(\mu + \frac{\mu_t}{\sigma_k}\right)\frac{\partial k}{\partial x_j}\right] + \frac{1}{2}P_{ii} - \rho\varepsilon + S_k \tag{3.18}$$

$$\rho U_i \frac{\partial \varepsilon}{\partial x_i} = \frac{\partial}{\partial x_j}\left[\left(\mu + \frac{\mu_t}{\sigma_\varepsilon}\right)\frac{\partial \varepsilon}{\partial x_j}\right] + C_{\varepsilon 1}\frac{1}{2}P_{ii}\frac{\varepsilon}{k} - C_{\varepsilon 2}\rho\frac{\varepsilon^2}{k} + S_\varepsilon \tag{3.19}$$

where σ_ε, σ_k, $C_{\varepsilon 1}$, $C_{\varepsilon 2}$ are model constants.

According to Eq. (3.6), the turbulent kinetic energy k is linked to the normal Reynolds stresses $\overline{u_i'u_i'}$. Using rectangular Cartesian coordinates, Eq. (3.6) can be rewritten as:

$$k = \frac{1}{2}\left(\overline{u'u'} + \overline{v'v'} + \overline{w'w'}\right) \tag{3.20}$$

where $\overline{u'u'}$, $\overline{v'v'}$, $\overline{w'w'}$ are the mean velocity fluctuations on the x, y and z direction respectively.

Since solution convergence is not as easy as in the other eddy viscosity models, the FLUENT user manual [213] suggests using the k-ε model for the initial iterations providing an initial guess and switching later to the RSM. The values for each of the Reynolds Stresses when switching to RSM are initialised according to Eqs. (3.21) and (3.22).

$$\overline{u'u'} = \overline{v'v'} = \overline{w'w'} = \frac{2}{3}k \tag{3.21}$$

$$\overline{u'v'} = \overline{v'w'} = \overline{u'w'} = 0 \tag{3.22}$$

However, such an approach was not considered and RSM was used from the start of the iterations.

3.3 Modelling the neutral Atmospheric Boundary Layer

3.3.1 Velocity and turbulence profiles

In order to model the fully developed wind flow in the neutral Atmospheric Boundary Layer (ABL), appropriate profiles for velocity and turbulence needed to be applied at the boundaries. The profiles were implemented by means of FLUENT User-Defined Functions (UDFs) [213] — see Appendix C for an example.

The well-established [226, 227], logarithmic velocity profile was applied:

$$U_x = \frac{u_*}{\kappa} \ln\left(\frac{z + z_\circ}{z_\circ}\right) \tag{3.23}$$

where u_* is the friction velocity, calculated using Eq. (3.24); κ is the von Karman constant, taken as equal to 0.4187, according to the FLUENT manual [213]; and $z_\circ$ is the roughness length.

$$u_* = \frac{\kappa \, U_{h_{abl}}}{\ln\left(\frac{h_{abl}+z_\circ}{z_\circ}\right)} \tag{3.24}$$

where h_{abl} is the height of the ABL.

The normal Reynolds stresses were taken from Panofsky and Dutton [4]:

$$\overline{u'u'} = (2.4 \; u_*)^2 \qquad \overline{v'v'} = (1.9 \; u_*)^2 \qquad \overline{w'w'} = (1.25 \; u_*)^2 \tag{3.25}$$

while the rest of the Reynolds stresses were approximated as:

$$\overline{u'w'} = -u_*^2 \; (1 - z/h_{abl})^2 \qquad \overline{u'v'} = \overline{v'w'} = 0 \tag{3.26}$$

with the shear stress $\overline{u'w'}$ profile taken from ESDU 85020 [228].

The equation for the turbulent kinetic energy k was derived using Eq. (3.20) along with the values of Eqs. (3.25):

$$k = 5.48 \; u_*^2 \tag{3.27}$$

Finally, the ε profile was taken to vary with height according to Eq. (3.28), which is a well-established expression in the literature [226, 227].

$$\varepsilon = \frac{u_*^3}{\kappa \, (z + z_\circ)} \tag{3.28}$$

All the profiles explained in the current section were applied at the domain inlet and the top boundary cells, taking into account a reasonable height for the ABL h_{abl}; above that height, turbulence was not taken into account.

3.3.2 Modifications of turbulence model constants

Several modifications to the original k-ε model constants have been proposed to account for neutral atmospheric flow. According to a review by Cabezón [130], the best performing modifications were found to come from a procedure using the constants proposed by Panofsky and Dutton [4]. The same procedure was also followed in the literature by Alinot and Masson [76, 77, 229].

This approach was also followed in the current study using the RSM, since turbulence viscosity, μ_t, is calculated according to the same expression, as in Eq. (3.12).

According to Panofsky and Dutton [4] and assuming neutral atmospheric conditions, turbulence viscosity can be expressed as:

$$\mu_t = \rho \, \kappa \, u_* \, (z + z_\circ) \tag{3.29}$$

Using Eqs. (3.29), (3.27) and (3.28) in Eq. (3.30), the C_μ constant is calculated as:

$$C_\mu = \frac{1}{5.48^2} = 0.033 \tag{3.30}$$

A summary of the standard and modified RSM constants are shown in Table 3.1:

Table 3.1. Modified constants of the RSM

	C_μ	$C_{\varepsilon 1}$	$C_{\varepsilon 2}$	C_1	C_2	σ_k	σ_ε
standard	0.090	1.44	1.92	1.8	0.6	0.82	1.00
modified	0.033	1.44	1.92	1.8	0.6	0.82	1.00

Richards and Hoxey (RH) [226] proposed some further modifications for the k-ε

model constants, according to Eq. (3.31), to account for a neutral atmosphere.

$$\sigma_\varepsilon = \frac{\kappa^2}{\sqrt{C_\mu}\,(C_{\varepsilon 2} - C_{\varepsilon 1})} \tag{3.31}$$

However, the modifications are linked to the k and ε equations which are different than the Reynolds stress equations. Therefore, this approach was not followed in the RSM and the other constants of the turbulence model were kept as default.

3.4 Wall functions

An important parameter for successfully modelling the ABL flow over any — and especially complex — terrain with CFD is the accurate consideration of the ground surface effect on the flow. The ground is modelled as a 'wall' boundary and an equivalent grain roughness K_s (roughness height) is used to express the effect of ground roughness on the flow by means of wall functions which are applied in order to calculate the scalars of the wall-adjacent cells.

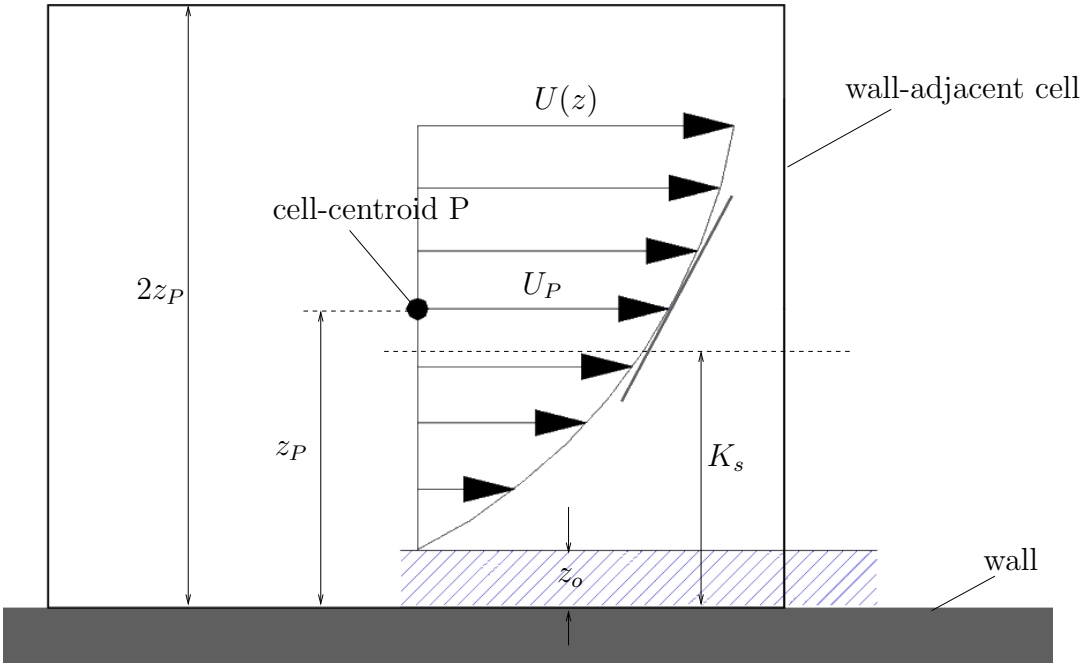

Figure 3.3. Wall-adjacent cell requirements

Some basic requirements for this procedure are summarized by Blocken [227], based on CFD literature and software manuals [213, 226, 230] and some updated recommendations can also be found in [231]. The first requirement is for reasonably high mesh resolution close to the wall boundary representing the ground (e.g. the height of first cell $z_P < 1$ m). Secondly, the use of the appropriate wall roughness corresponding to the fully-developed ABL flow properties in order to avoid any horizontal streamwise gradients. Furthermore, there is a need for an established relationship between the roughness height K_s and the corresponding aerodynamic roughness length $z_\circ$. The roughness length is defined as the height at which the velocity in Eq. (3.23) is zero [5], whereas the roughness height — also mentioned as 'equivalent sand-grain roughness' — is a 'geometric' parameter related to the roughness element height [215]. From the definition of the roughness height, and from FLUENT recommendations [213], the height z_P of the wall-adjacent cell centroid needs to be larger than the roughness height K_s (Fig. 3.3), otherwise it is not physically meaningful to have grid points within the roughness element height [227].

In order to relate K_s with $z_\circ$ and define the scalars at the wall-adjacent cells, the use of a wall function is necessary. FLUENT wall functions are related to the roughness height K_s, instead of the roughness length $z_\circ$, which is usually estimated for a case of atmospheric flow. The formula used to link K_s with $z_\circ$ is shown in Eq. (3.32), taken from Blocken [227, 232].

$$K_s = \frac{E'\, z_\circ}{C_s} \tag{3.32}$$

where C_s is a roughness constant with a default value of 0.5 and $E' = 9.793$ is an empirical constant.

Using Eq. (3.32) and making sure that the height of the wall-adjacent cell centroid z_P is greater than K_s, the value of K_s is calculated. As mentioned previously, the $z_P > K_s$ condition needs to be always satisfied (Fig. 3.3), because alternatively,

if $z_P < K_s$, FLUENT code modifies K_s, setting it equal to z_P without further warning [233].

3.4.1 Standard wall functions

The standard wall function in FLUENT is given in Eq. (3.33) following the logarithmic law of the wall:

$$\frac{U_P u^*}{u_\tau^2} = \frac{1}{\kappa}\ \ln\left[\frac{E' u^* z_P}{\nu\,(1 + C_s K_s^+)}\right] \tag{3.33}$$

where u^* and u_τ are two different wall-function friction velocities calculated in Eqs.(3.34) and K_s^+ is the dimensionless sand-grain roughness height or 'dimensionless physical roughness height' shown in Eq. (3.35).

$$u^* = C_\mu^{1/4} k_P^{1/2} \qquad\qquad u_\tau = (\tau_w/\rho)^{1/2} \tag{3.34}$$

where k_P is the turbulent kinetic energy calculated at the wall-adjacent cell-centroid P (Fig.3.3) and τ_w is the shear stress at the wall.

$$K_s^+ = \frac{u^* K_s}{\nu} \tag{3.35}$$

The factor $(1 + C_s K_s^+)$ in Eq. (3.33) is the roughness modification in the wall function which is controlled by the user by modifying the values of K_s and C_s.

Considering an equilibrium boundary layer, $u^* = u_\tau$ and in a fully-rough regime (which is the case of ABL flow over terrain): $1 + C_s K_s^+ \approx C_s K_s^+$, because $C_s K_s^+ \gg 1$. A simplified form of Eq. (3.33) is given in Eq. (3.36):

$$\frac{U_P}{u^*} = \frac{1}{\kappa}\ \ln\left(\frac{E' u^* z_P}{\nu\ C_s K_s^+}\right) \tag{3.36}$$

The turbulent kinetic energy at the wall k_P is calculated from the k-equation

according to Eq. (3.37) applying a production of k term [213] shown in Eq. (3.38).

$$\frac{\partial k}{\partial n} = 0 \tag{3.37}$$

where n is the local coordinate normal to the wall.

$$G_k \approx \tau_w \frac{\partial U}{\partial z} = \frac{\tau_w^2}{\kappa \rho C_\mu^{1/4} k_P^{1/2} z_P} \tag{3.38}$$

The turbulent dissipation rate ε at the wall is calculated from Eq. (3.39).

$$\varepsilon = \frac{u^{*3}}{\kappa z_P} \tag{3.39}$$

In FLUENT, the logarithmic law is employed when $y^* > 11.225$ [213], with y^* being a non-dimensional distance between the wall-adjacent cell centroid and the wall:

$$y^* = \frac{u^* z_P}{\nu} \tag{3.40}$$

where u^* is a wall-function friction velocity defined in Eq. (3.34).

If $y^* < 11.225$, then instead of the logarithmic law, FLUENT employs a linear law to model the 'viscous sublayer' [213]:

$$\frac{U_P}{u^*} = \frac{u^* z_P}{\nu} \tag{3.41}$$

3.4.2 Modifications

The default use of standard wall functions is not sufficient for the successful modelling of the ABL flow [227]. One important reason is the fact that for such cases, K_s calculated from Eq. (3.32) becomes very large for rough terrain and the wall-adjacent cells will need to become even larger in size in order to prevent

$z_P < K_s$ (see Fig. 3.3). As an example, using a typical roughness length of a grass-covered terrain, $z_\circ = 0.03$ m, $K_s \approx 0.6$ m from Eq. (3.32), which would mean that the height of the first cell ($2z_P$) will need to be more than 1.2 m. Such a choice conflicts with the need for a relatively high mesh resolution near the ground, at least in simulations related to the pedestrian level [227, 230] or simulations including forest modelling, but it may be sufficient for simple wind energy applications, where the wind turbines are placed relatively high above the ground. Another important reason for the need of modifications is the fact that when meshing a domain with very complex ground topography, it is practically difficult to maintain a fixed height for the wall adjacent cells; inevitably some cells may become small in size violating the requirement of $z_P > K_s$ and in that case the FLUENT code sets $K_s = z_P$ without further warning [233].

For all the aforementioned reasons one of the alternative options mentioned in the literature [227] is the use of $z_\circ$-type wall functions instead of K_s-type, avoiding the requirement of $z_P > K_s$. An appropriate set of such wall-functions for modelling ABL flow has been provided by Richards and Hoxey [226] and they are similar to the profiles shown in Eqs. (3.23), (3.27) and (3.28). The RH approach for modelling the ABL with CFD [226] has been proven the most successful among others [234]. In a blind-test using different CFD software in modelling the ABL, the RH approach was the only one able to maintain the k profile at the outlet and provided the closest match with the full-scale results [235].

Using Eq. (3.35), the wall-function of Eq. (3.36) can be rewritten as:

$$\frac{U_P}{u^*} = \frac{1}{\kappa} \ln\left(\frac{E' z_P}{C_s K_s}\right) \tag{3.42}$$

According to a procedure explained by Blocken et al. [233] and since only the value of the product $C_s K_s$ is used in the calculations for fully-rough walls in Eq. (3.42), C_s is modified from its default value (0.5) to allow for K_s to take lower values. Similar to Blocken et al. [233], K_s was chosen equal to z_P and C_s

was then calculated from (3.32) for each cell using the ground roughness length $z_\circ$:

$$C_s = \frac{E'\ z_\circ}{K_s} \tag{3.43}$$

The modifications were made for each cell with the application of User-Defined Functions (UDFs), otherwise the FLUENT code does not allow C_s to be modified beyond the $[0; 1]$ limits. An example of such a UDF is shown in Appendix C.

Using Eq. (3.43) in Eq. (3.42), the wall-function can be rewritten in a $z_\circ$ form:

$$\frac{U_P}{u^*} = \frac{1}{\kappa}\ \ln\left(\frac{z_P}{z_\circ}\right) \tag{3.44}$$

Eq. (3.44) is similar to Eq. (3.23), which is the RH approach [226]. Eq. (3.39) of the standard wall-functions is also similar to Eq. (3.28). Nevertheless, it should be noted, that since an 'equilibrium' wall-function is applied, some errors related to turbulent kinetic energy production in Eq. (3.38) should be expected. Such errors are analysed by Hargreaves [234] and a comparison between the standard wall functions of the k-ε model and the RH wall functions is performed. However, the linear-pressure strain RSM includes an extra wall-reflection term to ensure a redistribution of the normal Reynolds stresses next to the wall [213, 236]. It tends to suppress the normal stress perpendicular to the wall, while enhancing the stresses parallel to the wall. Consequently, the exact discrepancies between the linear-pressure strain RSM and the RH wall-function turbulence may provide a useful topic for future research.

3.5 Domains and Boundary Conditions

The computational domain and mesh of all the case studies in this thesis were generated in GAMBIT version 2.3.16 [237]. GAMBIT (Geometry And

Mesh Building Intelligent Toolkit) is the preprocessor package of FLUENT. The rectangular Cartesian coordinate system was used in the computational domain. Simple layouts of the approach followed and the direction of the coordinate system is shown on Fig 3.4 for the case of flat (Fig. 3.4a) or complex terrain (Fig. 3.4b).

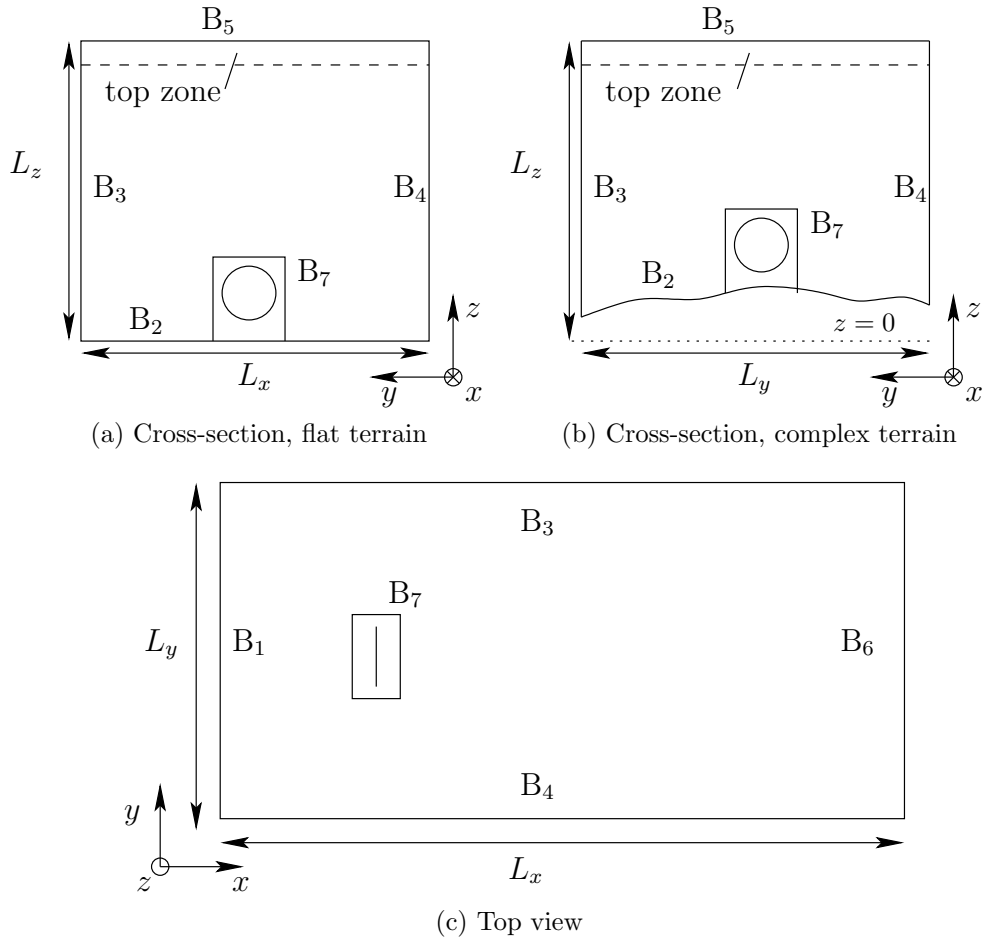

(a) Cross-section, flat terrain

(b) Cross-section, complex terrain

(c) Top view

Figure 3.4. Computational domains

The grid dimensions are $L_x \times L_y \times L_z$, where L_x is the domain length (the direction of the flow is the x direction), L_y the width and L_z the height of the domain.

The boundary conditions applied at the boundaries shown on Fig. 3.4 are summarised in Table 3.2.

The equations described on Sec. 3.3 were used at the 'Velocity Inlet' boundary. The faces at B_7 were created as 'Interface', allowing for the mesh to have an

Table 3.2. Summary of the Boundary Conditions applied on the domain

Boundaries on Fig. 3.4	Boundary Conditions in FLUENT
B_1	Velocity Inlet
B_2	Wall
B_3, B_4, B_5	Symmetry
B_6	Pressure Outlet
B_7	Interface
top cell zone	Fixed Velocity and turbulence

unstructured form at the 'box' in the rotor proximity and a structured form at the rest of the domain. The faces on the left, right and the top of the domain were selected as 'Symmetry' boundary, implying that the velocity vector is parallel to the surface, while the outlet face was created as a 'Pressure Outlet' boundary. The ground was applied as a 'Wall' boundary, using the approach described on Sec. 3.4.

According to Richards and Hoxey [226], particular consideration is needed for the boundary condition (BC) at the top of the domain. Following the approach of Blocken et al. [227], the (turbulence and velocity) values from the inlet profiles were fixed in the top layer of cells in the domain. This particular type of top BC was applied, as other types, such as symmetry or slip wall, could have caused undesirable streamwise gradients [227].

3.6 Flow solver configuration

The 3-D, double-precision, version of ANSYS FLUENT 12.0 was used in the simulations. A double-precision version was chosen, since the geometry involved very disparate length scales: a need for a dense mesh around the rotor and near the ground and coarser mesh near the top of the domain.

The governing flow equations, such as the RANS and the Reynolds stress equations of Sec. 3.2, are in differential form and need to be transformed into

algebraic expressions in order to be solved at each of the discrete locations defined by the domain mesh. There are three main approaches of numerical solution: the finite-difference, the finite-element and the finite-volume methods.

The finite-difference method is the simplest; it provides numerical solutions of the flow variables at each discrete node point of a structured grid. The partial derivatives of the flow equations are replaced with algebraic difference quotients, based on Taylor series expansions, yielding algebraic equations at each grid point. More details of the method can be found in Anderson [238].

The finite-element method was originally developed for structural analysis. It requires the subdivision of the domain into an unstructured grid of triangular (in 2-D) or tetrahedral (in 3-D) elements and the specification of a certain number of points at the boundaries and/or inside the elements. Simple functions are then defined to represent the variation of the solution inside the element. A substitution of the simple approximating functions into the governing equations generates a residual to measure the errors. The residuals are then reduced with the use of weighting formulas and integrating [239]. More details of the technique can be found in Zienkiewicz et al. [240].

The finite-volume method is followed by most of the commercial and well-established CFD codes such as CFX/ANSYS, PHOENICS, STAR-CD as well as FLUENT, and it is used in this thesis. A good description of the method can be found in Versteeg and Malalasekera [216]. The domain is divided into a number of smaller, non-overlapping sub-regions, creating a grid (or mesh) of cells (also known as control volumes). The governing equations are integrated over all the control volumes, constructing discretised algebraic equations for the flow variables (e.g. velocities, pressure, turbulence k and ε). In FLUENT, the discretised equations are then linearised and solved to produce updated values of the flow variables [213].

3.6.1 Choice of solver

Two solver technologies were available in FLUENT: the pressure-based and the density-based solvers. The density-based approach is recommended for high-speed compressible flows, whereas the pressure-based solver has been traditionally used for incompressible flows [213] and was therefore selected.

In the pressure-based solver, the velocity field is obtained from the momentum equations, while the pressure field is found from a pressure (or pressure correction) equation. The latter equation is derived from the combination of the continuity (conservation of mass) and momentum equations in a way that the resulting velocity field satisfies the continuity. This procedure requires iterative steps until the solution is converged [213].

The pressure-based solver utilizes two different types of algorithms: segregated or coupled. In the segregated algorithm, each of the governing equations are solved successively and 'decoupled' from the others. Such a procedure is memory-efficient, since it requires only one discretised equation to be stored in memory each time; a disadvantage is the slow solution convergence. Detailed information on the algorithm steps can be found in the FLUENT manual [213]. The coupled algorithm solves simultaneously a system of momentum and pressure-based continuity equations, while the remaining equations are solved in a decoupled way, as in the segregated algorithm. The result is faster solution convergence, but a 1.5–2 times increase of the CPU memory requirements. The (default) segregated algorithm was selected.

As mentioned above, the pressure-velocity coupling is achieved with a combination of the continuity and momentum equations. Using a 'guessed' value of pressure in the combined equation, the resulting velocity field needs to satisfy the continuity equation. When the latter condition is not satisfied, the pressure-based solver applies a pressure-correction equation, modifying the pressure as well as the velocity field until convergence is achieved. Among the options available in

FLUENT pressure-based solver, the SIMPLEC (SIMPLE-Consistent) algorithm was used as a variation of the standard SIMPLE algorithm with a potential to improve convergence; both SIMPLE and SIMPLEC approaches are outlined in FLUENT User's Guide [213].

3.6.2 Discretisation

Spatial discretisation schemes

The solver stores the discrete values of the flow variables, ϕ, at the centre of each cell. However, face values at the borders of the cells, ϕ_f, are also needed in the calculations and need to be interpolated from the neighbouring cell centres. Out of the options available in FLUENT for that purpose, the second-order Upwind scheme was applied for the interpolation of velocities, k, ε and Reynolds Stresses, while the PRESTO! scheme was used for the calculations of the face pressure. An overview of the aforementioned techniques is given below.

According to the Upwind scheme, the face values are derived from the upstream (or 'upwind') cell, relative to the normal velocity [213]. More information on the scheme can be found in Versteeg and Malalasekera [216].

In the first-order Upwind scheme, the cell-centre value is considered as a cell-average value, valid throughout the cell. Thus, the face value is set equal to the value of the upstream shell. According to Versteeg and Malalasekera [216], this scheme provides limited accuracy in the flow computations.

The second-order Upwind scheme uses a more complex approach in calculating the face values and it is recommended for higher accuracy of cell faces computations. It applies a Taylor series expansion of the cell-centred solution and calculates the face value by taking into account the gradient of the upstream cell value as well

as the value itself [213], according to Eq. (3.45).

$$\phi_f = \phi + \nabla\phi \cdot \boldsymbol{r} \tag{3.45}$$

where ϕ is the upstream cell-centred value and $\boldsymbol{r}$ is the displacement vector from the upstream cell centroid to the face centroid.

The PRESTO! (PREssure STaggering Option) scheme incorporates an approach similar to the 'staggered' grid schemes applied in structured meshes [241], and can be applied for all meshes. The discretised continuity equation is used on a 'staggered' (displaced) grid, about the faces of the control volumes. The PRESTO! scheme is recommended for flows with high swirl, cases involving porous media or flows in strongly curved domains [213], and it was the option selected in this thesis.

Calculation of gradients

The aforementioned gradients of the flow variables on each cell, $\nabla\phi$, are also needed in the discretisation of the convection and diffusion terms in the flow conservation equations, e.g. Eq. (3.13). The Green-Gauss Node-Based approach was used for the computations of $\nabla\phi$, as it is known to provide better accuracy in unstructured meshes than the default cell-based scheme.

According to the semi desecrate version of the Green-Gauss theorem, the gradients of the flow variables at the cell centre $c0$ can be written as:

$$(\nabla\phi)_{c0} = \frac{1}{V}\sum_f \overline{\phi}_f \, \boldsymbol{A_f} \tag{3.46}$$

where V is the cell volume and $\boldsymbol{A_f}$, the area of face f. The summation includes all the faces enclosing the cell.

The node-based approach calculates the face value, $\overline{\phi}_f$, as the arithmetic average

of the nodal values on the face, according to Eq. (3.47). The node values, $\overline{\phi}_n$, are computed as the weighted average of the values of the surrounding cells [213], maintaining a second-order spatial accuracy.

$$\overline{\phi}_f = \frac{1}{N_f} \sum_{n}^{N_f} \overline{\phi}_n \tag{3.47}$$

where N_f is the number of nodes on the face.

Chapter 4

Single wake modelling

In this section, the CFD modelling approach explained in Chapter 3 is initially tested in an empty domain in order to examine if the neutral ABL profiles are maintained along the domain length. The wind turbine modelling approach using the VBM is later used for the prediction of a single wind turbine wake on flat 3-D terrain and it is validated with full-scale measurements.

4.1 Neutral Atmospheric Boundary Layer flow simulation

4.1.1 2-D test case

The neutral ABL modelling of Sec. 3.3 was applied in an empty 2-D domain, with no wind turbine present. The domain, mesh and initial conditions were chosen to match the test performed by Blocken et al. [227]. The domain dimensions were $L_x \times L_z = 10,000$ m $\times$ 500 m and the mesh was structured, consisting of $46,000$ cells with an equal spacing of $\Delta x = 10$ m in the horizontal direction. The nearest

cell to the wall had a wall-distance of $z_p = 0.25$ m. According to the test case, $z_\circ = 0.1$ m and $u_* = 0.912$ m/s.

The inlet profiles at the 'Velocity Inlet' boundary condition (BC) were chosen according to the specifications described in Sec. 3.3. The top boundary was chosen as a 'Symmetry' BC and the (velocity and turbulence) scalars were fixed at the top layer of cells according to the equations in Sec. 3.3, following the approach in Sec. 3.5. The outlet BC was chosen as 'Pressure Outlet' and the ground wall modifications in Sec. 3.4.2 were applied. The RSM was chosen for turbulence closure, according to the modifications described in Sec. 3.3.2. The SIMPLEC algorithm was used for the pressure-velocity coupling. Spatial discretisation was PRESTO! for Pressure and second-order Upwind for Momentum, Turbulent Kinetic Energy, Turbulent Dissipation Rate and Reynolds Stresses, as explained in Sec. 3.6.

4.1.2 Results

The results are shown in Fig. 4.1. The left figures show velocity U and turbulence profiles from the ground to the top of the domain (500 m), while the right figures only show up to 50 m height. The turbulence intensity, I', was calculated from the turbulent kinetic energy k, according to Blocken et al. [227]:

$$I' = \frac{\sqrt{2k/3}}{U} \tag{4.1}$$

Four different horizontal distances downstream of the inlet were selected in the results, to check whether the inlet profiles of the main scalars are maintained along the x-direction and, thus, represent the fully developed neutral ABL flow. The chosen x-coordinates were $x = 100$ m, $x = 500$ m $x = 1000$ m and $x = 10000$ m, which corresponds to the outlet boundary. The same x-coordinates were also chosen by Blocken et al. [227] for the presentation of their results.

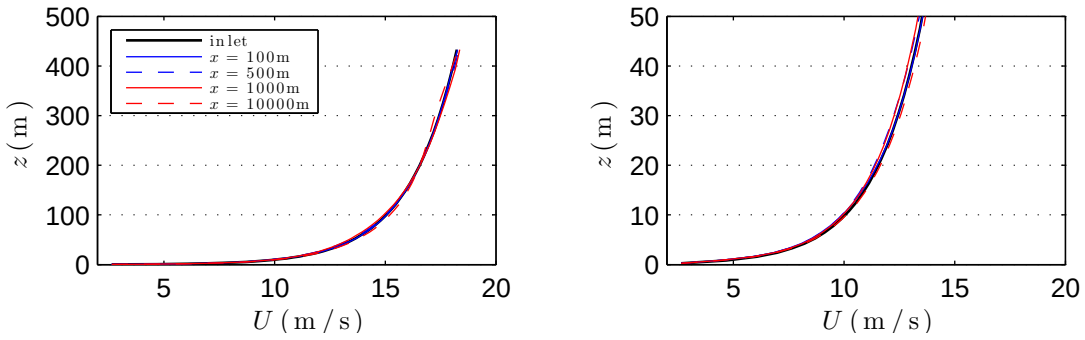

(a) Velocity

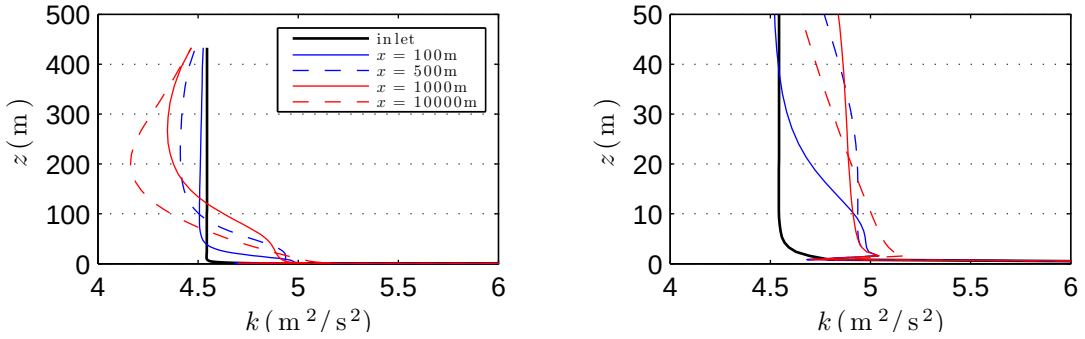

(b) Turbulent kinetic energy

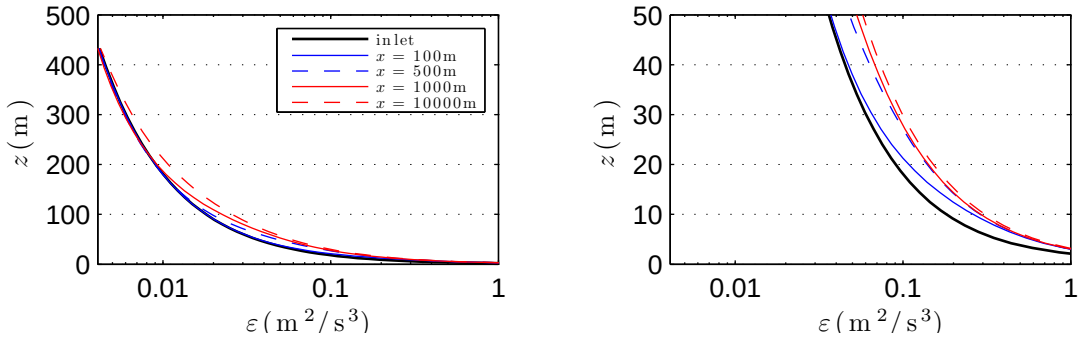

(c) Turbulent dissipation rate

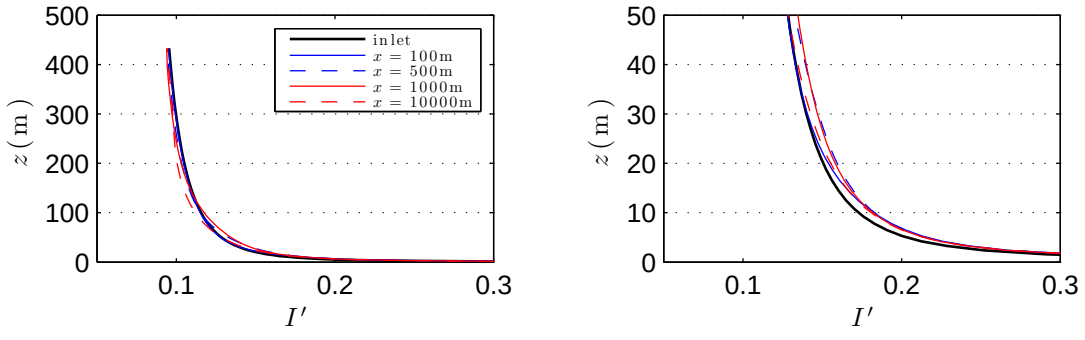

(d) Turbulence intensity

Figure 4.1. CFD simulation results: Blocken [227] and current modifications

The velocity results in Fig. 4.1a show a very good match between the velocity profiles, especially close to the ground, indicating that the modified wall function provides acceptable velocity values at the near-wall cells. The turbulent kinetic energy k profile is relatively well-maintained along the x-axis, until $x = 100$ m; for $x > 100$ m, k is increased near the ground and reduced above 100 m height. Thus, the k profile is not maintained as constant and the maximum deviations are found near the wall and at $z \approx 200$ m. The ε profile at $x = 100$ m seems to slightly differ from the inlet profile for $z < 30$ m, but it stabilises after $x = 1000$ m. Fig. 4.1d shows that the turbulence intensity profile is relatively well maintained.

Fig. 4.2 shows the error relative to the inlet profiles for two variables, U and I', as a function of the x-coordinate at two different heights above ground level (a.g.l.), $z = 2$ and 20 m. The error was calculated as:

$$\text{error}(\%) = 100 \left| \frac{\phi_{(x)} - \phi_{(x=0)}}{\phi_{(x=0)}} \right| \tag{4.2}$$

where ϕ is one of the flow variables.

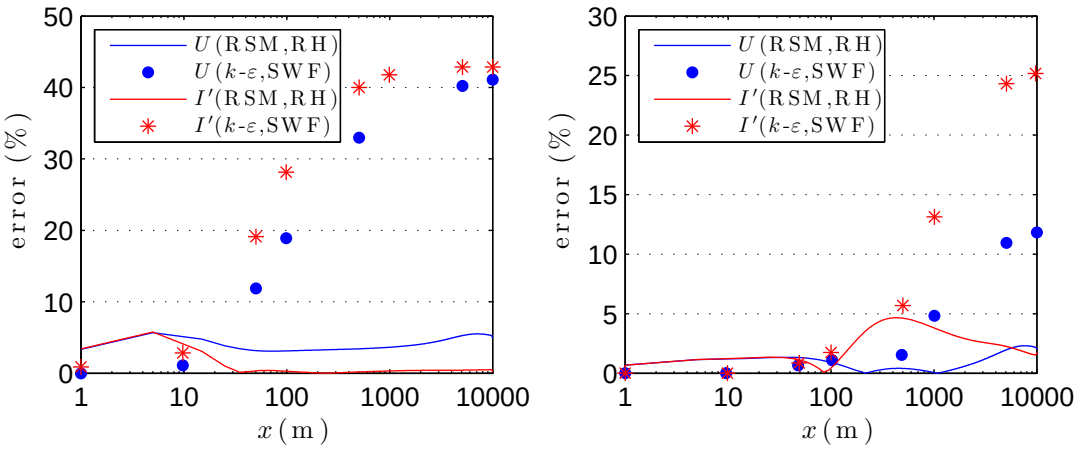

(a) $z = 2$ m (b) $z = 20$ m

Figure 4.2. relative error compared to inlet profiles

A comparison between the errors of the current approach of using RSM and Richards and Hoxey wall functions (RSM,RH) and the Blocken et al. [227]

approach of using a modified k-ε model with standard wall functions (k-ε,SWF) is also shown in Fig. 4.2. The error in the approach of this thesis (RSM,RH) is maintained in relatively low levels in comparison to the (k-ε,SWF) approach. At $z = 2$ m above the ground (Fig. 4.2a), the turbulence intensity error is approximately zero for $x > 50$ m, while the velocity error is kept below 8%. At $z = 20$ m above the ground (Fig. 4.2b), the velocity error remains very low for $x < 1000$ m and then it increases up to approximately 2.5% at the outlet; the turbulence intensity error is slightly higher, with a peak of approximately 5% at $x \approx 700$ m, whereas for $x > 700$ m it decreases monotonically.

4.2 The Nibe site and wind turbines

The full-scale measurements used for the validation of the CFD approach on wake modelling were taken from the Nibe site, Denmark [49]. The Nibe wind turbine site is coastal, located near Aalborg, northern Jutland. Two 630 kW wind turbines were constructed at the site, as part of a wind energy R&D programme initiated in Denmark [242]. Near the wind turbines lies an area of at least 6 km of open, shallow water to the West, as shown in Fig. 4.3.

Details of the site were presented by Taylor [49] along with the full-scale measurement results. The ground is flat and open, consisting of rough grassland with no significant obstacles over a distance of 1–2 km. The predominant wind direction was found to be approximately West-East, whereas the wind flow was considered uniform, without any interference due to topography or other obstacles. However, directional changes were found to affect wake behaviour due to differences in turbulence intensity between westerly winds over the sea and the rest of the directions corresponding to wind over grassland.

The two Nibe wind turbines shared mainly common features: they were both upwind, 3-bladed machines of 630 kW installed power, a rotor diameter of

Figure 4.3. Nibe-B and Nibe-A seen from the SouthEast (1979). Source: Hau [243]

D = 40 m and a hub-height of 45 m above the ground. Their main difference was that rotor-A was stall regulated, with limited pitch control over the outer 2/3 of the blades, whereas rotor-B was operated with pitch control. Table 4.1 summarises the principal characteristics of the Nibe wind turbines. Further technical specifications of the machines can be found in the work of Pedersen and Nielsen [244] and Nielsen [242].

The two machines were positioned 200 m (5 D) apart and 150 m away from the coast, along an approximately North-South axis parallel to the coastline (Fig. 4.3). Four masts were erected at the inter-machine axis in order to obtain wake measurements: Mast-1 was located at the centre of the inter-machine axis (2.5 D from each rotor), Mast-2 and Mast-3 were placed 1 D South and North of Nibe-A respectively and Mast-4 was located 2.5 D North of Nibe-A. A layout of the masts and wind turbines is shown in Fig. 4.4.

Table 4.1. Nibe turbine characteristics

rated power	630 kW
rotor orientation, configuration	upwind, 3 blades
rotor diameter	40 m
hub height	45 m
cut-in, rated, cut-out wind speed	6 m/s , 13 m/s , 25 m/s
rotor speed	34 rpm
blade tip speed	70 m/s
blade construction	steel/fibre glass spar fibre glass shell
blade airfoil	NACA 4412 – 4434 standard roughness
blade twist	11°
cone, tilt angle	6° , 6°
yawing	active

4.3 Previous work

The Nibe full-scale measurements have been used extensively in the literature for the validation of various wake models. Hassan et al. [245] used a simple mathematical expression to describe the mean wake velocity deficit and calibrated the parameters to fit with the measurements using empirical relationships from wind tunnel experiments. According to this expression, the wake is represented as a 2-D Gaussian deficit superimposed on the logarithmic mean wind speed profile. Crespo and Hernández [246] used the measurements to test the near-wake turbulence prediction of their numerical model (UPMWAKE) [22]. The numerical results successfully predicted higher turbulence in the upper part of the shear layer at 1 D downstream. Wessel and Lange [247] validated a simple semi-empirical method to estimate the wake turbulence intensity with the data and the development of the lateral variation of turbulence intensity was well described.

Voutsinas et al. [58] used the Nibe measurements to validate a kinematic model regarding velocity deficit predictions. The model was based on Abramovich's

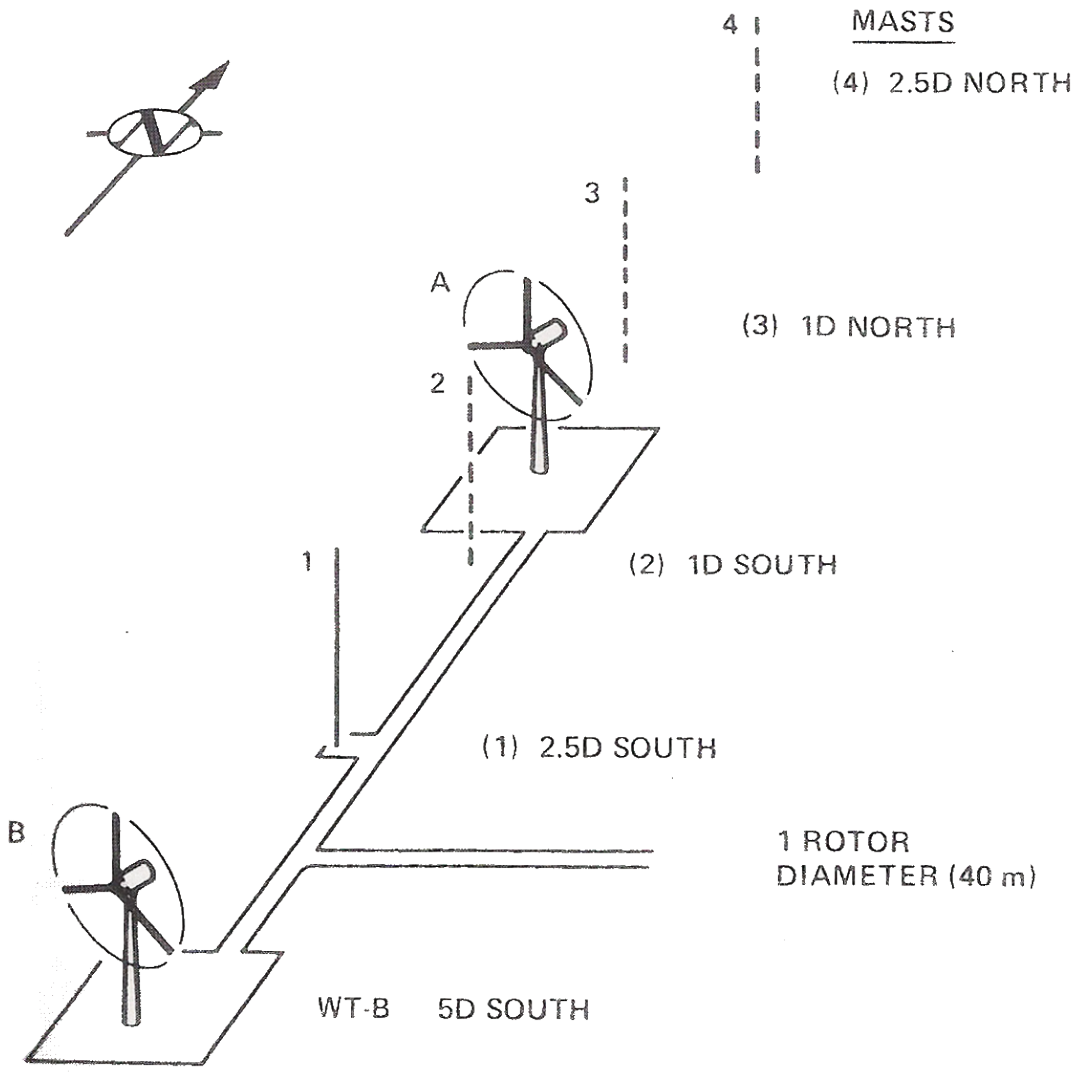

Figure 4.4. Nibe site layout. Source: Hassan et al. [245]

theory of turbulent jets [248], assuming symmetric wake without swirl and the ground effects were taken into account with the use of boundary layer velocity profiles. In a later study, Voutsinas et al. [249, 250] used the Nibe data for validating another approach involving the combination of a vortex method, a viscous (k-ε) model and a similarity model without taking into account ground effects. The wake was considered as a steady and axisymmetric flow divided into the near-wake and the far-wake region, where similarity was assumed. The far-wake predictions were closer to the measured data, whereas the near-wake results

were not as a good match. Consequently, one important conclusion was that simple methods were not able to provide an accurate treatment of the near-wake region.

In a more recent work, El Kasmi and Masson [78] developed a model based on the actuator disc and the BET to model wakes. The model involved an extended version of the k-ε model adding an extra term in the ε equation and using FLUENT to solve the equations in the 2-D mode without swirl. Validation was made using the Nibe data including a comparison with the standard k-ε model and the model constants proposed by Crespo et al. [60], showing a better match with the measurements.

Prospathopoulos et al. [82] summarized the performance of three different modelling approaches in predicting the velocity deficit and added turbulence intensity in the Nibe Turbine-B wake. The first approach was similar to El Kasmi and Masson [78], the second involved a correction in the turbulent decay ratio and the third a correction in turbulent time scale. The rotor was modelled through momentum sinks linked to the thrust coefficient and a version of the k-ω turbulence model was chosen for the turbulence equations. After validation with the Nibe measurements, all the CFD approaches showed an underestimation of the near wake deficit (2.5 D). The approaches decreased the turbulent production in the near wake and adjusted the wind speed deficit, but the need for further improvement was noted.

Réthoré et al. [73, 251–253] also used the Nibe measurements for validating a modified k-ε model adding momentum sinks and turbulence sources on the actuator disc taken from canopy models developed for forest areas. The model seemed to provide satisfactory results in the near-wake, but underestimated the wake deficit in the far-wake.

4.4 Nibe single wake case

The examined single wake case, involves only the measurements when Nibe-B was operating alone (southerly winds), which is the case with the most data records [49]. The four masts (Fig. 4.4) provided wake measurements at various distances downwind of Nibe-B (Table 4.2).

Table 4.2. Masts and normalized distance from Nibe-B

	Nibe-B	Mast-1	Mast-2	Nibe-A	Mast-3	Mast-4
downwind distance	0 D	2.5 D	4 D	5 D	6 D	7.5 D

The parameters used to describe the wake in the full-scale measurements [49] were also used for the CFD validation. The wind speed was normalised using the wind speed of the undisturbed flow at 45 m height:

$$u(z,y) = \frac{U(z,y)}{U_\circ(z = 45 \text{ m})} \tag{4.3}$$

where U is the calculated wind speed and $U_\circ(z = 45$ m) is the free-stream wind speed at $z = 45$ m.

Turbulence was considered in two different ways: turbulence intensity, I_u, and normalised turbulent velocity, ζ. Turbulence intensity was calculated according to Eq. (4.4), where the velocity U is varying with height. The normalised turbulent velocity was computed according to Eq. (4.5), where only a constant freestream velocity, $U_\circ(z = 45$ m), is considered.

$$I_u(z,y) = \frac{\sigma_u(z,y)}{U(z,y)} \tag{4.4}$$

$$\zeta(z,y) = \frac{\sigma_u(z,y)}{U_\circ(z = 45 \text{ m})} \tag{4.5}$$

where $\sigma_u(z, y)$ is the standard deviation of the wind speed component at the x-coordinate.

The operational case DSB-1 of the full-scale results [49] was chosen in this study. The data records were binned against the wind direction measured at 45 m on Mast-2, using an interval of 2.5°. They were also averaged using an averaging period of 1 min.

The dataset DSB-1 corresponded to an incident wind speed range of $8.0 - 9.1$ m/s at hub height and turbulence intensity of $10 - 15\%$. The Nibe-B thrust coefficient was estimated as $C_T \approx 0.82$ and the pitch angle was in the range of $0 - 1°$. As no mast was located upwind of the Nibe-B rotor to measure the ambient conditions in southerly winds, the incident wind speed was estimated from the electrical power output using the measured power curve of the Nibe-B machine [49]. The ambient turbulence intensity was measured at 3 m a.g.l. on Mast-1, assuming that it was not affected by the rotor wake [49].

4.5 Setup of the Nibe case in CFD

The CFD approach explained in Sec. 3 of this thesis was applied for the simulation of the Nibe single wake case DSB-1: southerly winds and the single wake of Nibe-B measured at four masts (Table 4.2). The RSM was used to model turbulence and the VBM was applied to model rotor effects using FLUENT. It is important to note, that this modelling approach does not take into account the effect of the nacelle and the tower. The interference of Nibe-A was also not considered, although the rotor was present in the wake centreline (Fig. 4.4), but not in operation (parked rotor). The Nibe-A nacelle and tower affected the measurements at the masts in close proximity, as it is shown in the results.

The CFD simulation parameters were chosen to match the full-scale case scenario: velocity was taken as 8.5 m/s at hub-height ($z = 45$ m) and a uniform roughness

length of $z_\circ = 0.01$ m was chosen, as recommended in the literature [3] for flow simulations over flat grassy plains. Given the aforementioned conditions, the resulting turbulence intensity I_u was approximately 11.9% at hub-height and 17.6% at 3 m a.g.l., slightly higher than the range of $10 - 15\%$ in the full-scale measurements [49]. A turbulence intensity value of $I_u(\mathrm{z} = 3) = 15\%$ in the equations corresponds to a roughness length value of $z_\circ = 0.0037$ m, which was considered very low for an onshore case. It was suggested that the low ambient turbulence of the incoming flow in the measurements was a result of the effect of the flow over the sea, whereas in the CFD case, the ambient turbulence over a uniform terrain was considered.

An actuator disc was created with a diameter of 40 m, 6° tilt and 1 m width, located at $z = 45$ m hub-height. Some of the wind turbine characteristics presented in Table 4.1 were used as inputs to the VBM: the cone angle (6°), the number of blades (3) and the rotational speed (34 rpm). Additionally, a constant value of 0.5° was assumed for the pitch angle, taken as the average in the $0 - 1°$ range given in the DSB-1 dataset [49].

Lift and drag coefficient tables were created using digitized data published by NACA [254]. The data were chosen for a Reynolds (Re) number of 6×10^6 and standard roughness. They were further processed in order to provide the desirable form: a table of C_L and C_D vs. angle of attack (α) at a range of $-180°$ to 180°. The process was made using AirfoilPrep, an Excel workbook for generating airfoil tables [255]. The workbook was used in order to extrapolate the NACA data to a $-180°$ to 180° range of α and then interpolate them into a common list of α.

A flat 3-D domain was created in GAMBIT with dimensions of $(L_x, L_y, L_z) =$ (105 D, 50 D, 26.25 D), according to the specifications of Sec. 3.5. The rotor was positioned at $x = 20$ D from the inlet boundary, thus a downwind distance of 85 D was used for the wake to develop without a disturbance from the outlet boundary (Fig. 4.5). A larger vertical domain dimension (L_z) was also tested, in

order to confirm that the vertical distance of 22.25 D does not affect the results (see Sec. 4.7).

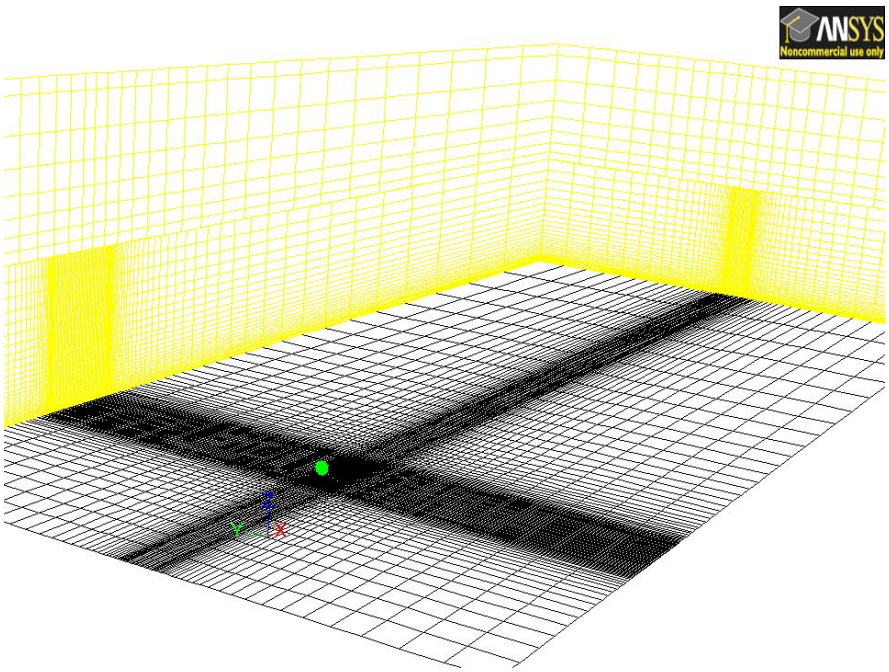

Figure 4.5. Nibe-B wind turbine and domain size in CFD simulation

The final mesh consisted of 262,397 mixed elements and it was denser at areas of high pressure and velocity gradients: mainly in close proximity to the rotor and the ground surface. The grid cells were gradually increasing in size from the ground to the top and from the rotor towards the inlet, outlet, as well as right and left 'Symmetry' planes.

A 'brick' was created around the rotor, in order to separate the dense mesh around the actuator disc from the mesh in the rest of the domain, as shown in Fig. 4.6. Inside the 'brick', unstructured tetrahedral elements were created, whereas the rest of the grid elements outside were structured hexahedrals. The two different grid structures were possible to implement using the 'interface' BCs in FLUENT [213].

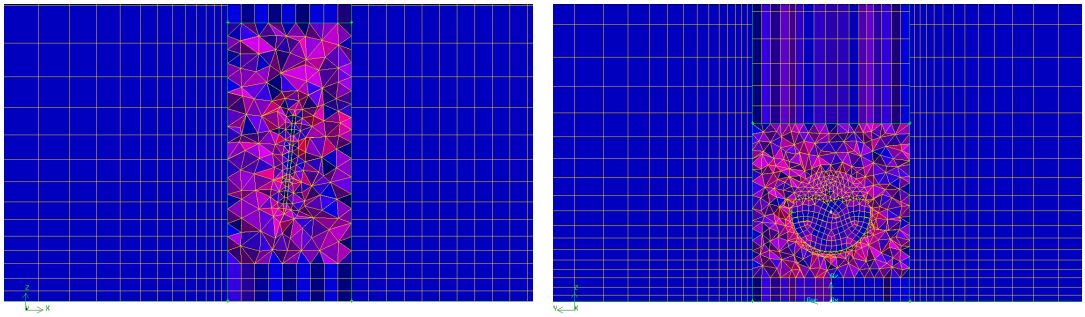

(a) plane $y \approx y_{hub}$ (b) plane $x \approx x_{hub}$

Figure 4.6. Mesh around the rotor

4.6 Results and comparison

The VBM is able to capture the vorticity induced by the rotor rotation; pathlines showing the rotational effect of the rotor in the flow are shown in Fig. 4.7 in the form of ribbons twisted according to vorticity magnitude. The directional change of the particles, as well as the added vorticity due to the rotation is clearly shown.

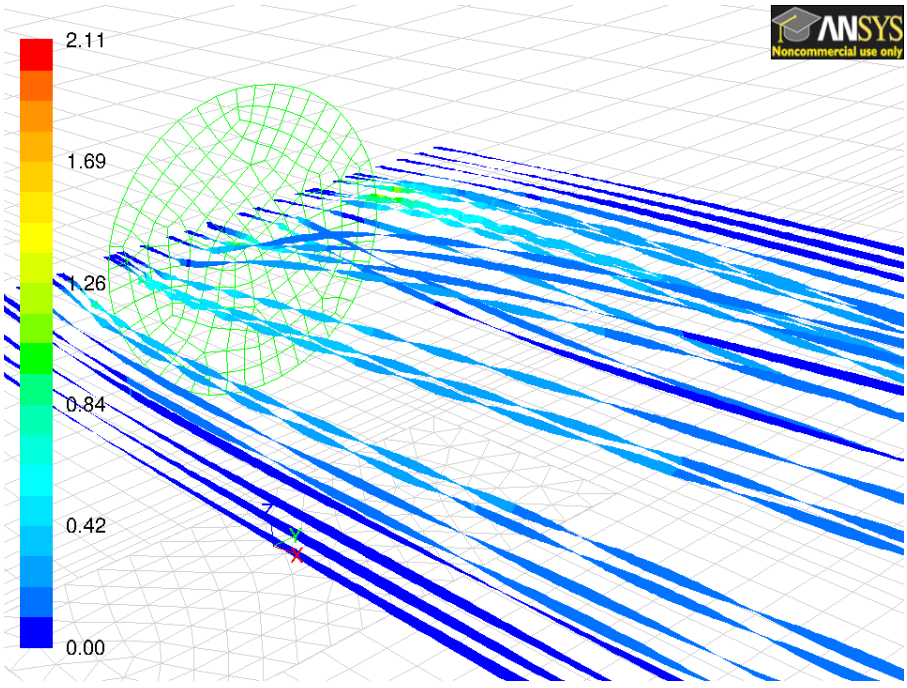

Figure 4.7. Pathlines (ribbons) in the wake of Nibe-B coloured by vorticity magnitude (s^{-1})

4.6.1 Velocity

Fig. 4.8 shows a comparison between the measurements and the CFD results in the lateral direction. The full-scale results were expressed at 'binned' incident wind directions and they were further processed and transferred into the normalised y/D coordinate.

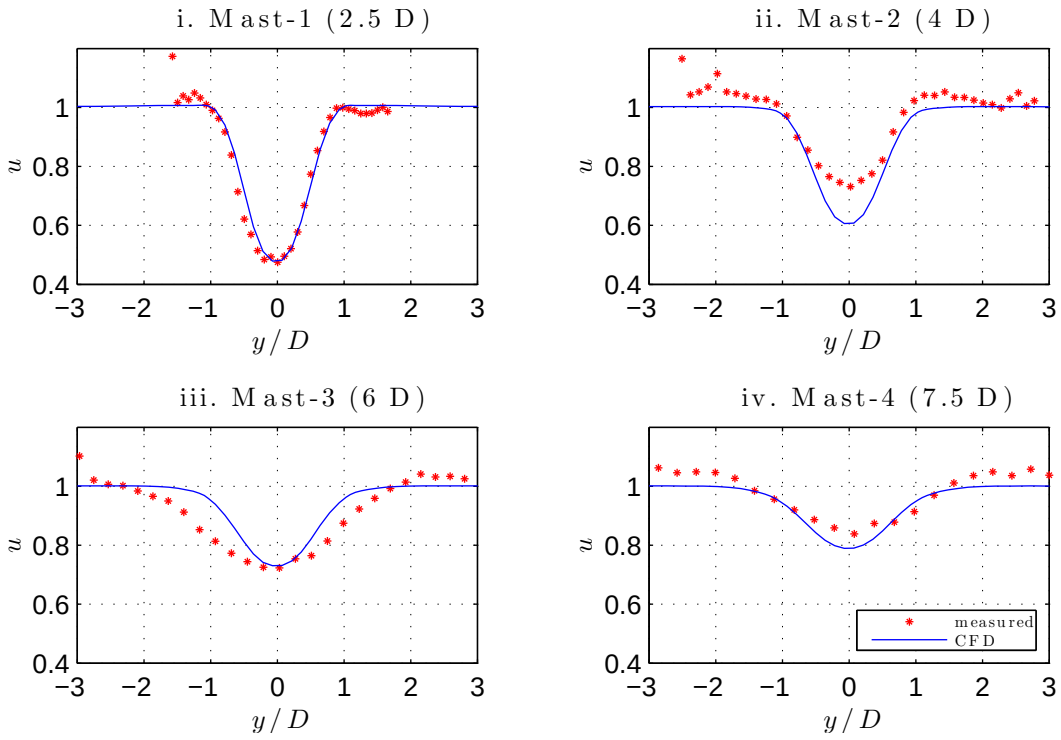

Figure 4.8. Lateral distribution of u: measured [49] and CFD results

The CFD results match very well with the measurements at Mast-1, implying that the near wake was successfully predicted. The wake width at Mast-2 was also well predicted, although the maximum wake deficit was overestimated. At Mast-3, the predicted wake was narrower than the measured, whereas the maximum deficit was very close to the measured values. The results at Mast-4 showed a satisfactory match, although the measured wake shape was clearly not symmetrical in contrast to the symmetrical wake shape of the CFD results.

The small increase of the wind speed ratio above 1.0 at masts 2–4, in lateral

directions away from the wake centre, can be attributed to errors related to the estimation of the free-stream wind speed which was used in the normalisation [49]. If the free-stream wind speed at the hub height at each mast was used, then the values of the wake normalised velocities would have been lower.

Additionally, the full-scale results were non-symmetric with respect to the turbine axis. This was observed, because the easterly winds ($y/D < 0$), blowing from land, were more turbulent than the westerly winds ($y/D > 0$), blowing from the sea, and a higher ambient turbulence results in faster wake recoveries (Sec. 2.3.1). In the CFD simulation a constant value of ambient turbulence and ground roughness length was assumed and as a result, the wake was more symmetrical in the lateral direction.

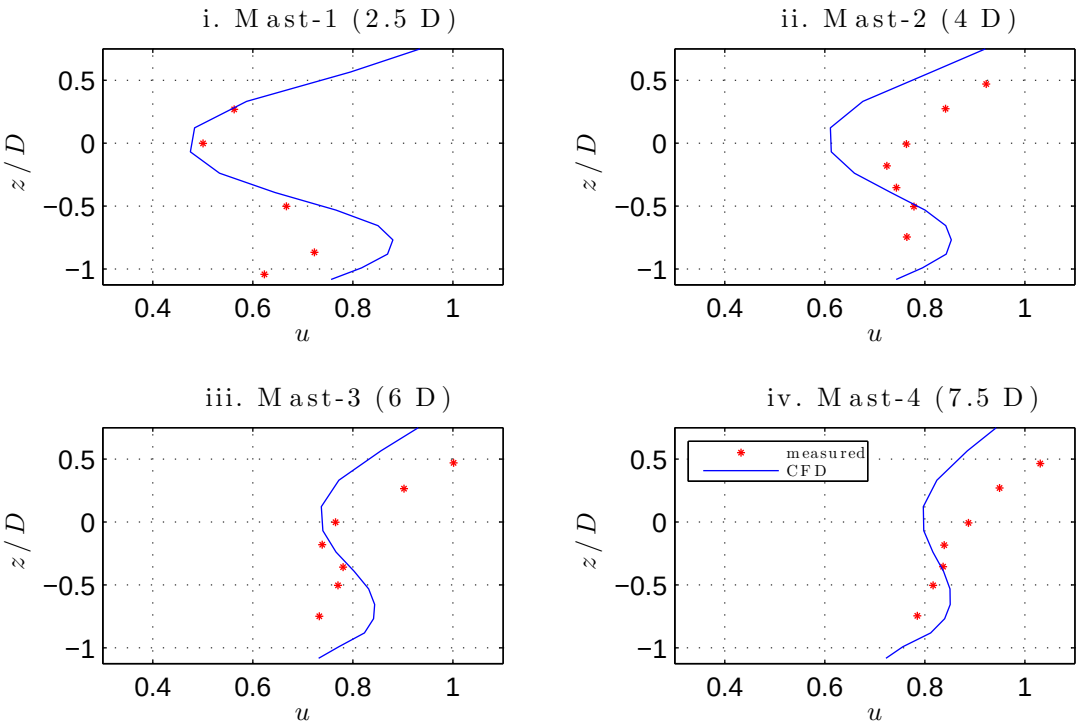

Figure 4.9. Vertical distribution of u: measured [49] and CFD results

Moreover, the measured data at masts 3 and 4 were affected by the nacelle and tower of turbine A (Fig. 4.4), even though this rotor was parked during the measurements [49]. This may explain the almost identical maximum velocity

deficit observed between Mast-2 and Mast-3. Such perturbations were expected to be limited near the wake centreline [49]. The CFD simulation did not take into account the effect of rotor A.

Fig. 4.9 shows the comparison of vertical wake velocity profiles. Results at Mast-1 compared relatively well, especially near the hub height. At masts 2–4, the CFD simulation consistently underestimated the wake deficit near the ground, and overestimated it away from the ground. It did not predict the slight downshift of the maximum wake deficit below the turbine axis, which was observed in the measurements. The wake deficit profiles measured at masts 2 and 3 were very similar below hub height, but not above it. Such an observation suggests that the interference of the turbine A nacelle and tower delayed the wake recovery at Mast-3 [49]. At Mast-4, the measured wake deficit was more 'flattened' than the wake deficit of the CFD model.

4.6.2 Turbulence

The comparison of turbulence results in the lateral direction is presented in Fig. 4.10, where Figs. 4.10a and 4.10b show the comparison of turbulent velocity and turbulence intensity profiles respectively.

The CFD model successfully predicted the double peak of turbulent velocity in the near wake shear layer (Fig. 4.10a, Mast-1). The peaks in the CFD results were maintained up to Mast-4, where turbulence spread more in the lateral direction. The full-scale results at Mast-1 and Mast-2 were asymmetric near the rotor, which can be attributed to the higher wind shear and ambient turbulence for easterly winds ($y/D < 0$), where roughness was higher. Turbulent velocity CFD predictions were relatively accurate near the rotor at masts 1 and 2, where the double peak was more pronounced. At masts 3 and 4 wake turbulence was consistently overpredicted, but the lateral shape was similar, as wake turbulence decayed and became more uniform.

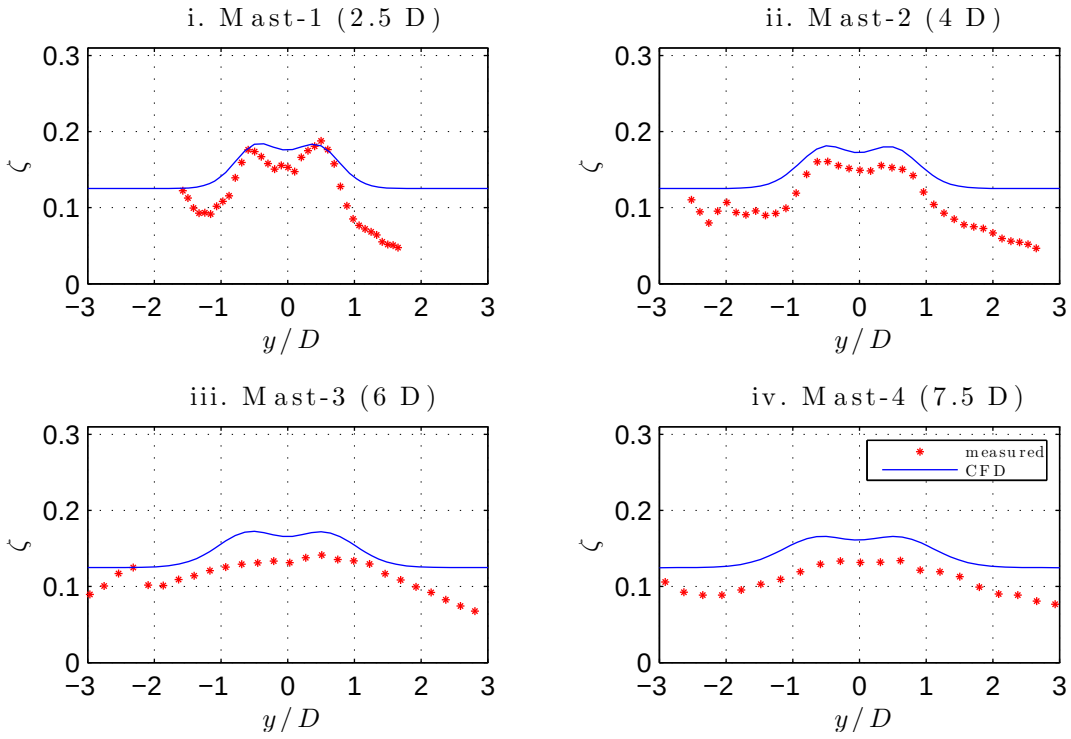

(a) turbulent velocity

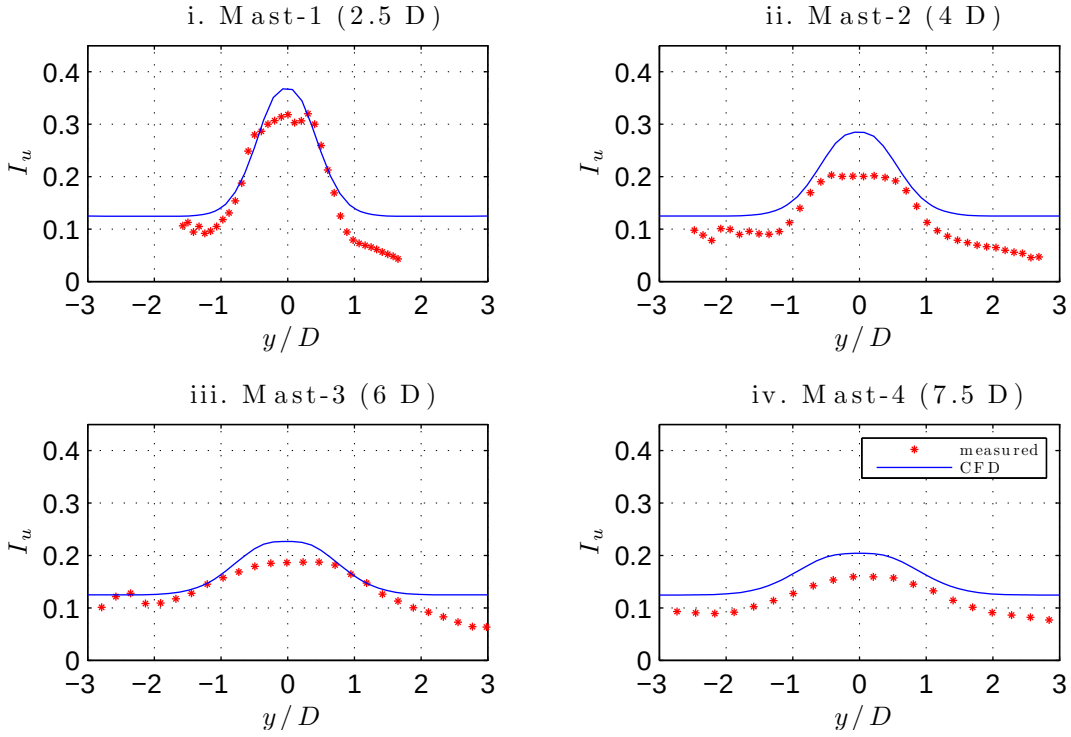

(b) turbulence intensity

Figure 4.10. Lateral distribution of turbulent velocity (4.10a) and turbulence intensity (4.10b): measured [49] and CFD results

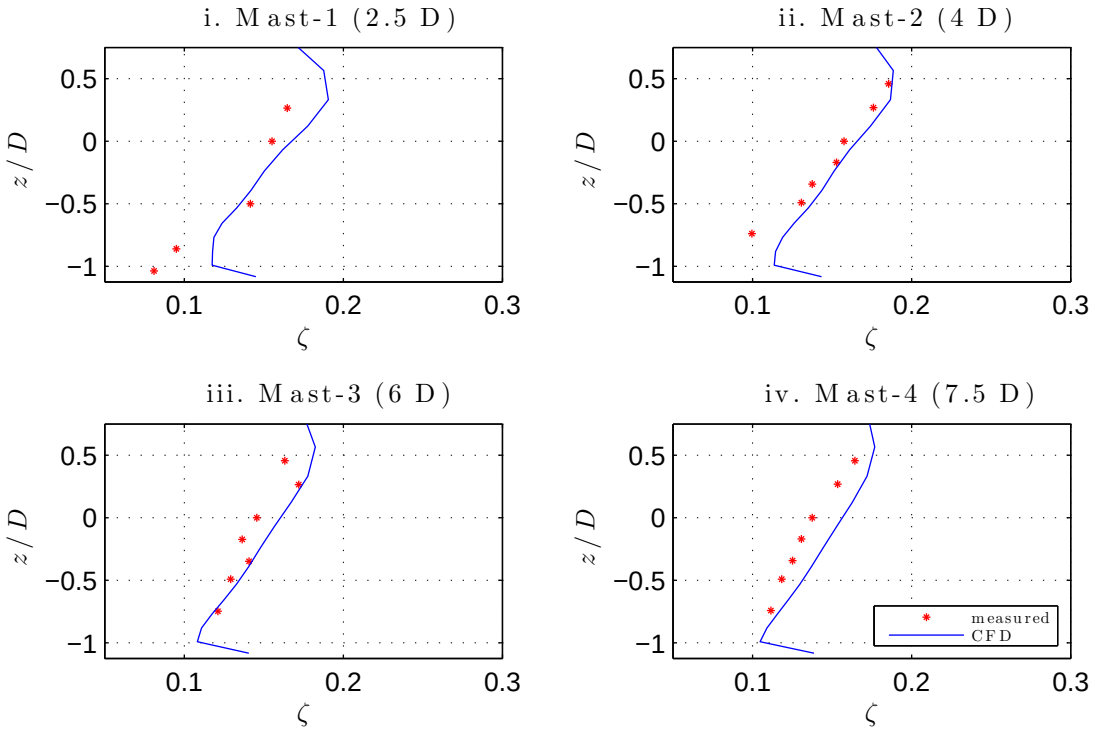

(a) turbulent velocity

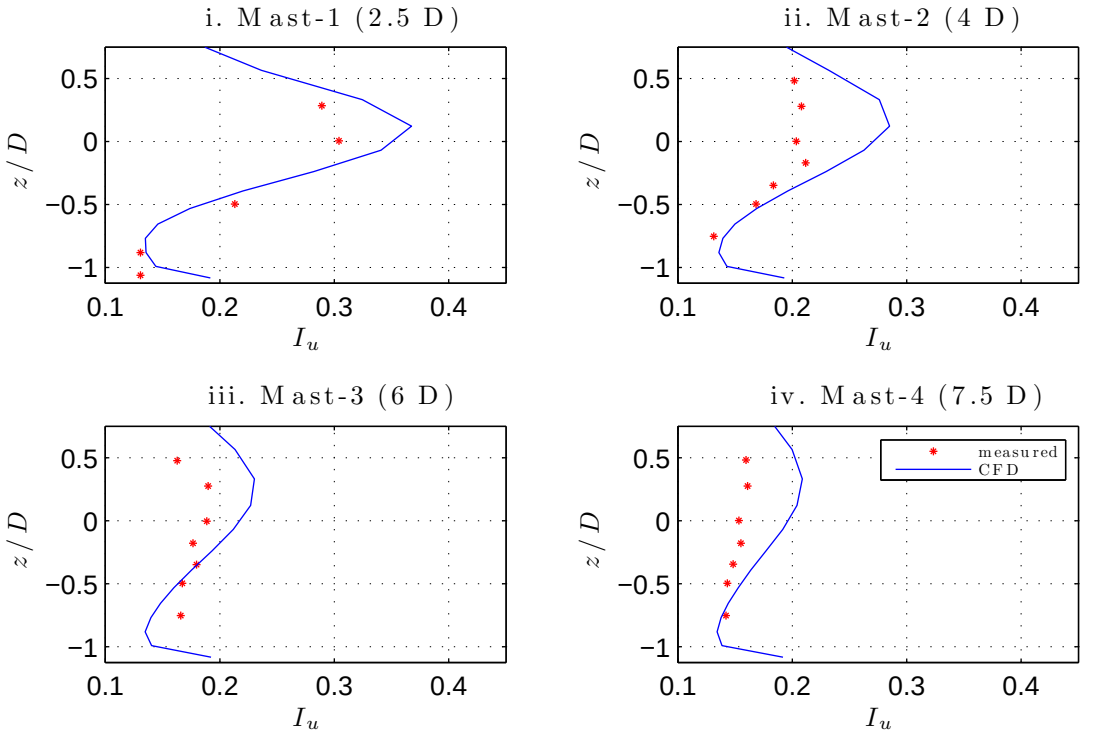

(b) turbulence intensity

Figure 4.11. Vertical distribution of turbulent velocity (4.11a) and turbulence intensity (4.11b): measured [49] and CFD results

The local turbulence intensity results in Fig. 4.10b showed a generally good comparison. However, the CFD simulation consistently overpredicted the peak of turbulence intensity near the wake centreline, especially at Mast-2. The flat shape of the measured turbulence intensity near the wake centreline suggests an interference of the rotor A mast and nacelle, located only 1 D downwind of Mast-2. At Mast-3, the predictions were in good agreement with the measurements away from the wake centreline, while at Mast-4 the CFD simulation overestimated turbulence intensity by approximately 4% almost uniformly.

Fig. 4.11 shows the comparison in the vertical direction, where Figs. 4.11a and 4.11b show the turbulent velocity and turbulence intensity profiles respectively.

The CFD predictions of turbulent velocity in Fig. 4.11a are in very good agreement with the measurements. Maximum turbulent velocity found at the shear layer above the turbine axis, where the velocity gradients are higher (Sec. 2.3.1).

The turbulence intensity simulation results in Fig. 4.11b show a good match with the measurements at Mast-1. At Mast-2 there is a clear divergence of the results near the hub-height, where turbulence intensity was overpredicted by approximately 8%. This can be attributed to the divergence of the vertical velocity profiles (Fig. 4.9, Mast-2). At masts 3 and 4 the discrepancies are smaller. The peak of turbulence intensity was suggesfully predicted above the turbine axis, where the velocity gradients were higher (Sec. 2.3.1).

4.7 Top boundary distance sensitivity

The choice of the vertical dimension (L_z = 26.25 D) needed to be tested in order to verify that it did not affect the wake results. For this purpose, a larger domain similar to the initial domain, but with the vertical dimension extended to

$L_z = 50$ D, was additionally simulated. The new mesh consisted of 266, 807 grid elements.

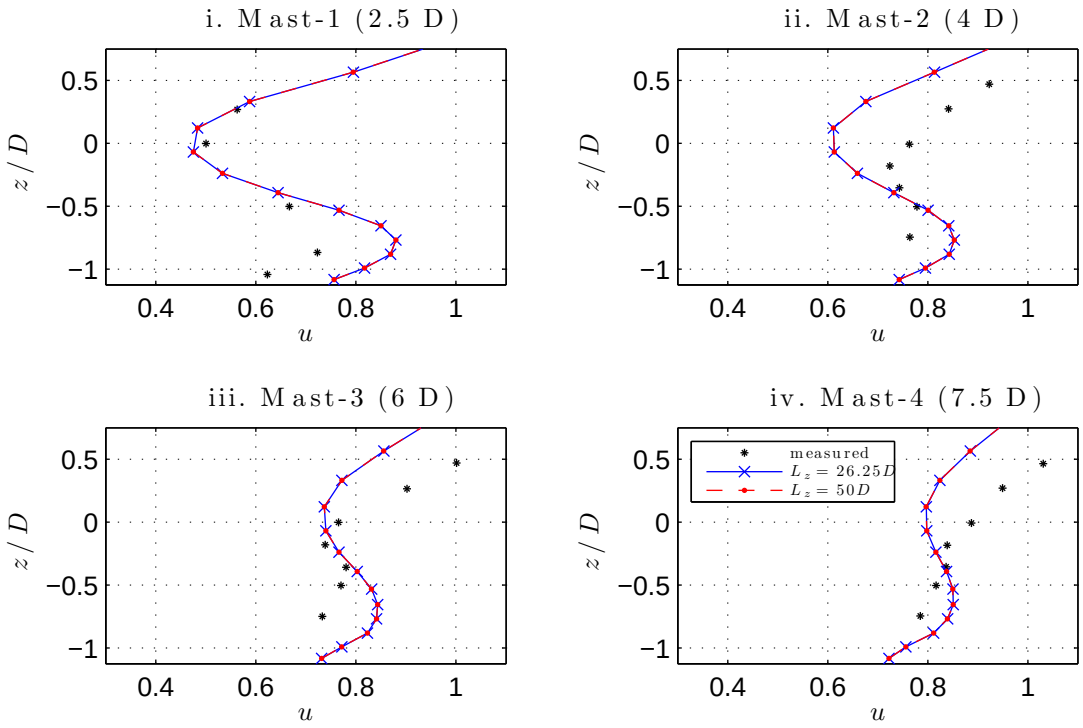

Figure 4.12. Vertical distribution of u

The results of velocity and turbulence vertical profiles using the two different grids were compared in Figs. 4.12 (velocity) and 4.13 (turbulence). According to both figures, the vertical profiles of velocity and turbulence using a higher value of L_z were not affected. Therefore the initial vertical dimension value of $L_z = 26.25$ D is considered a valid choice.

4.8 Grid independence study

A grid independence study was performed using a method given by NPARC [256] to determine the spatial discretisation error in the CFD simulation (NPARC is the National Program for Applications-oriented Research in CFD, a partnership between NASA and the US Air Force). The discretisation error is the error

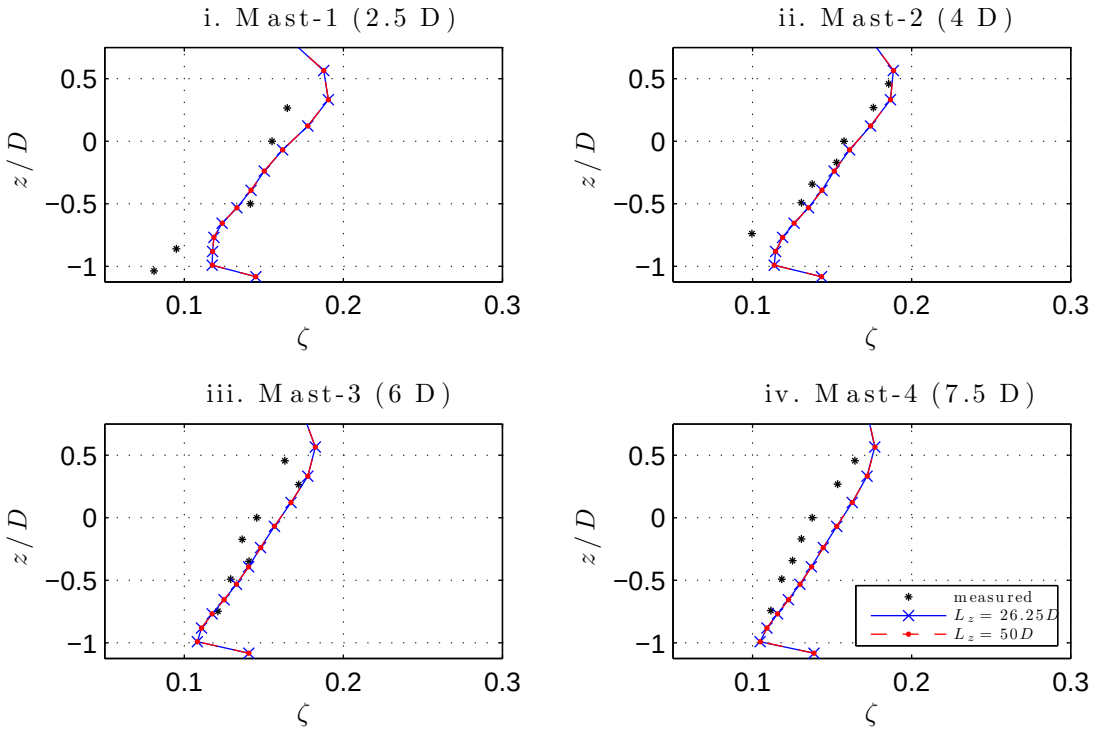

(a) turbulent velocity

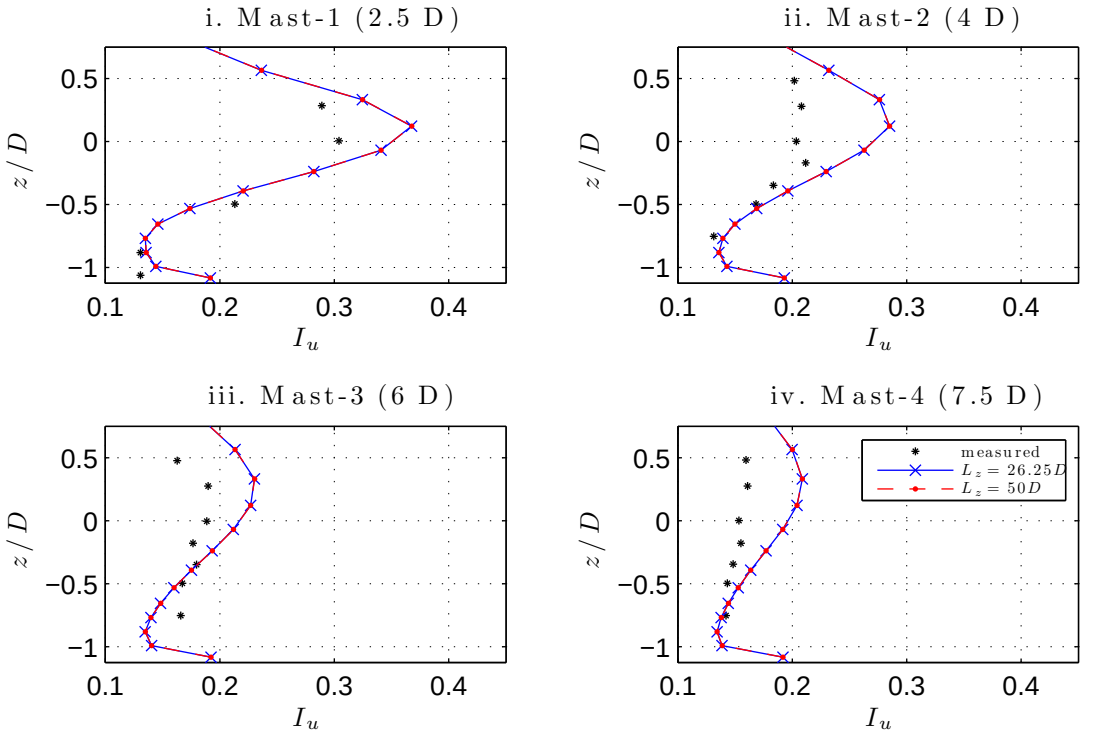

(b) turbulence intensity

Figure 4.13. Vertical distribution of turbulent velocity (4.13a) and turbulence intensity (4.13b)

introduced by the use of discretised algebraic equations in the control volumes, instead of solving the governing flow equations (Sec. 3.6). The NPARC method involves the use of a number of different grid resolutions in the simulations in order to estimate the solution of a grid with zero spacing by means of Richardson extrapolation.

4.8.1 Richardson extrapolation

The Richardson extrapolation (RE) is a method for estimating a continuum value at zero grid spacing (higher-order estimate) using a series of low-order discrete values. The discrete solution of a variable ϕ can be expressed in a form of series expansion, as:

$$\phi = \phi_{\chi=0} + g_1\chi + g_2\chi^2 + g_3\chi^3 + ... \tag{4.6}$$

where χ is the grid spacing, g_1, g_2, etc. are functions independent of the grid spacing and $\phi_{\chi=0}$ is the value at zero grid spacing.

In a second order solution, $g_1 = 0$. Assuming that there are two discrete solutions, ϕ_1 and ϕ_2 corresponding to two different grids of spacing χ_1 (fine grid) and χ_2 (coarse grid), then two equations can be derived from Eq. (4.6). Neglecting third and higher order terms, solving the one equation for g_2 and substituting into the second equation, the following expression for $\phi_{\chi=0}$ can be derived:

$$\phi_{\chi=0} \cong \phi_1 + \frac{\phi_1 - \phi_2}{r_*^2 - 1} \tag{4.7}$$

where $r_* = \chi_2/\chi_1$ is the grid refinement ratio.

The RE can be generalised to q^{th} order methods, as:

$$\phi_{\chi=0} \cong \phi_1 + \frac{\phi_1 - \phi_2}{r_*^q - 1} \tag{4.8}$$

Using the solutions from three different grids and a constant grid refinement ratio $r_* = \chi_2/\chi_1 = \chi_3/\chi_2$, the order of convergence, q, can be calculated as:

$$q = \ln\left(\frac{\phi_3 - \phi_2}{\phi_2 - \phi_1}\right) / \ln\left(r_*\right) \tag{4.9}$$

Eq. (4.9) can be derived from Eq. (4.6), in a similar procedure as the method for obtaining the second order solution. Three equations can be derived from Eq. (4.6), assuming three discrete solutions ϕ_1, ϕ_2 and ϕ_3 corresponding to three different grids of spacing χ_1, χ_2 and χ_3. Considering only the q^{th} order term, g_q and $\phi_{\chi=0}$ can be eliminated by substitution between the three equations, leading to Eq. (4.9).

In Eq. (4.8), the difference of the fine grid solution, ϕ_1, and $\phi_{\chi=0}$ can be an estimator of the error in the fine grid solution. This is expressed as the estimated fractional error E_1 for the fine grid solution:

$$E_1 = \frac{\epsilon}{r_*^q - 1} \tag{4.10}$$

where ϵ is the relative error, defined as:

$$\epsilon = \frac{\phi_2 - \phi_1}{\phi_1} \tag{4.11}$$

The estimated fractional error, E_1, is an ordered error estimator, i.e. it tends to zero, as the discretisation improves [257]. It is a more informative error estimator than the relative error ϵ, which does not take into account r_* or q; for example, ϵ may become artificially small by using r_* close to 1. E_1 is a good approximation to the discretisation error of the fine grid solution if the accuracy of ϕ_1 and ϕ_2 is reasonable ($E_1 \ll 1$). From Eqs. (4.10) and (4.11), if ϕ_1 is zero or very small in comparison to $\phi_2 - \phi_1$, then E_1 becomes meaningless.

4.8.2 Grid Convergence Index

Although the estimated fractional error, E_1, is based on a sound theory, it does not provide a bound on the error. According to Roache [258], what is needed in the reporting of the CFD calculations is not a true 'error bound', but an 'error band', which is a tolerance on the accuracy of the solution; this tolerance may be exceeded, but it provides 'some practical level of confidence'. The error estimator E_1 does not provide a good confidence interval; according to Roache [258], 'it is equally probable that E_1 be optimistic as conservative', i.e. it is just as likely that the actual error is greater than E_1 as less than E_1 (50% error band).

However, it is generally accepted [258] that a marginal confidence level is achieved, if ϵ of Eq. (4.11) is used along with a grid doubling ($r_* = 2$) and a second order method ($q = 2$). In this case, ϵ is considered to provide a reasonable error band. Note, that for $r_* = 2$ and $q = 2$, E_1 is only 1/3 of ϵ in Eq. (4.10).

The Grid Convergence Index (GCI) was proposed by Roache [258] and relates the ϵ of Eq. (4.11), obtained with any r_* and q, to the ϵ that would be expected in the same problem, with the same fine grid, but with $r_* = 2$ (grid doubling) and $q = 2$ (second order method). The GCI was defined as the absolute value of an equivalent ϵ, that would produce the same E_1 with $r_* = 2$ and $q = 2$, as the E_1 calculated from the actual ϵ, r_* and q. It is expressed as:

$$\mathrm{GCI}_{fine} = F_s \frac{|\epsilon|}{r_*^q - 1} \tag{4.12}$$

where $F_s > 1$ is a factor of safety, with a conservative value of $F_s = 3$ recommended by Roache [258]. Using the values of $F_s = 3$, $r_* = 2$ and $q = 2$ in Eq. (4.12), then $\mathrm{GCI}_{fine} = |\epsilon|$, as intended. If $F_s = 1$, then $\mathrm{GCI}_{fine} = |E_1|$ for any r_* or q corresponding to a 50% error band. The recommended [256] values for the factor of safety are $F_s = 3$, when comparing two grids, and $F_s = 1.25$, when comparing over three or more grids.

When the analysis involves a large number of CFD simulations, then the GCI may be expressed as the correction to the coarse grid solution ϕ_2 [257], as:

$$\mathrm{GCI}_{coarse} = r_*^q \, \mathrm{GCI}_{fine} \tag{4.13}$$

This equation can be used in a three grid convergence study to calculate the GCI of the medium and coarse grid solutions. Alternatively, the medium grid GCI may also be calculated using Eq. (4.12), with ϕ_1 and ϕ_2 representing the medium and coarse grid solutions. In this case, Eq. (4.13) can be used to check if the computed solutions are in the asymptotic range of convergence.

4.8.3 Results and error estimation

In this study, four different grid densities were used: fine (1), medium (2), coarse (3) and extra-coarse (4). A grid refinement ratio of $r_* = \sqrt{2}$ was chosen in each direction of the uniform mesh, while the height of the wall-adjacent cells was kept constant. Since the rotor disc thickness was one cell (corresponding to a 2-D problem), the rotor grid points were multiplied/divided by a factor of 2.

Table 4.3 and Fig. 4.14 show a comparison of results of each grid in the near wake ($x/D = 2.5$, hub-height) and in the far wake ($x/D = 7.5$, hub-height) with respect to normalised velocity (u) and turbulent velocity (ζ). The number of grid cells (N_{grid}) and rotor cells (N_{rot}) of each grid are also shown in Table 4.3.

Table 4.3. Results and error estimation using four different grids

			$x/D = 2.5$				$x/D = 7.5$			
Grid	N_{grid}	N_{rot}	u	ϵ_{RE} %	ζ	ϵ_{RE} %	u	ϵ_{RE} %	ζ	ϵ_{RE} %
extra-coarse (4)	31,684	50	0.644	45.02	0.150	−18.83	0.832	4.66	0.143	−16.51
coarse (3)	132,473	89	0.607	36.76	0.154	−16.54	0.820	3.12	0.147	−13.91
medium (2)	262,397	186	0.488	9.88	0.170	−7.99	0.798	0.33	0.158	−7.74
fine (1)	745,122	275	0.456	2.65	0.178	−3.86	0.795	0.03	0.164	−4.31
RE(2-1)			0.444	–	0.185	–	0.795	–	0.171	–

Richardson extrapolation was performed using Eq. (4.8) and taking into account the results from the fine and the medium grids (1 and 2). The RE value, ϕ_{RE}, was considered as the best estimate of the continuum value. In Table 4.3, the percentage errors relative to the RE value, ϵ_{RE}, were calculated as:

$$\epsilon_{RE}\ (\%) = 100\ \frac{\phi_i - \phi_{RE}}{\phi_{RE}} \tag{4.14}$$

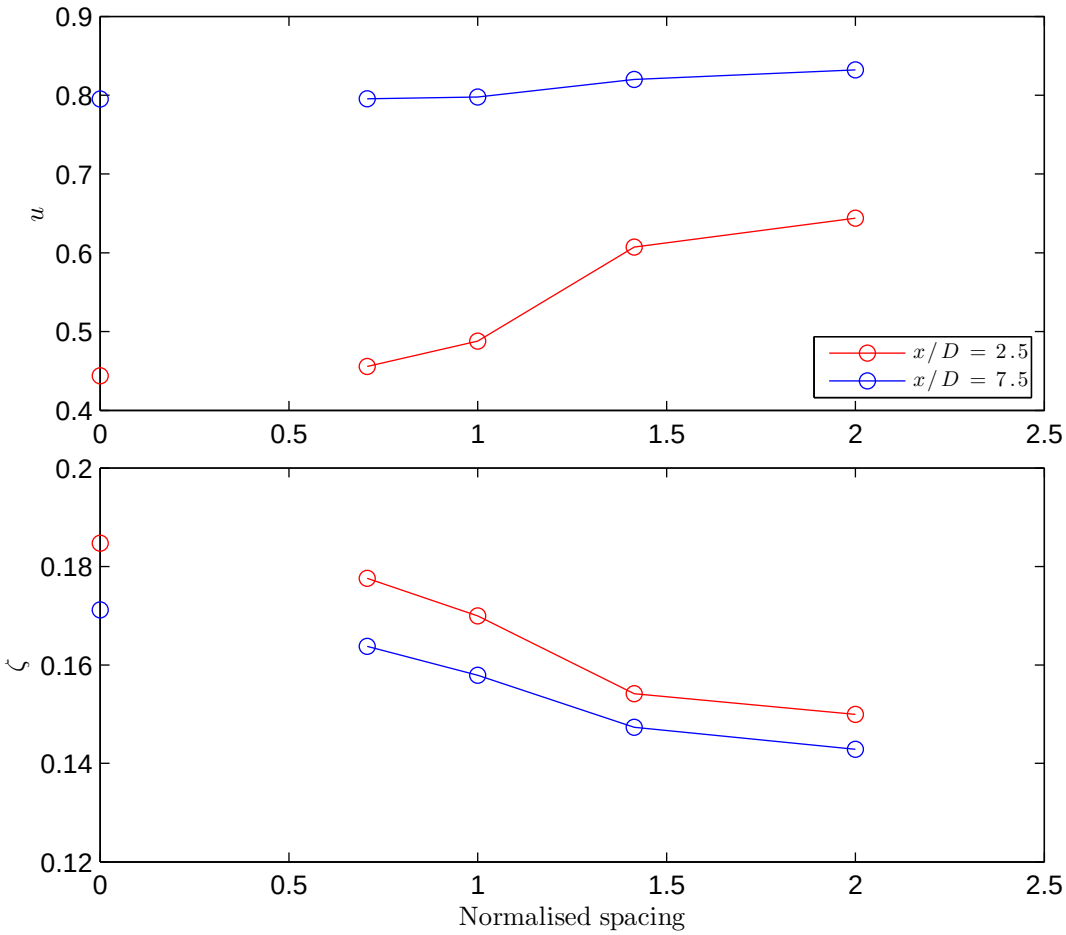

Figure 4.14. Convergence of normalised velocity and turbulent velocity vs. normalised grid spacing.

The results in Fig. 4.14 and Table 4.3 show that the solution was converging as the grid became finer. According to Table 4.3, the errors relative to the RE value were

generally higher in the near wake region as compared to the errors in the far wake. The normalised velocity errors were higher in the near wake as compared to the turbulent velocity errors, with the exemption of the fine grid solution, where the near wake turbulent velocity errors were higher. In the far wake, velocity errors reduced considerably, whereas turbulent velocity errors remained significant, or even increased in comparison to the errors in the near wake (fine grid solution).

Table 4.4 shows the Grid Convergence Indices derived from the fine (1), medium (2) and coarse (3) grids. The ratio of $\mathrm{GCI}_{23}/\left(r_*^q \mathrm{GCI}_{12}\right)$ is also shown in the table; a close to 1 value indicates that the solutions are in the asymptotic range of convergence. A comparison of the GCIs (GCI_{12} and GCI_{23}) with the percentage errors relative to the RE value ($\epsilon_{RE,1}$ and $\epsilon_{RE,2}$ in Table 4.3 respectively) shows that the GCIs provided a more conservative estimate of the error, as expected.

Table 4.4. Grid Convergence Indices

	$x/D = 2.5$		$x/D = 7.5$	
	u	ζ	u	ζ
q_{123}	3.79	2.10	6.48	1.69
GCI_{12} (%)	3.23	5.03	0.04	5.63
GCI_{23} (%)	11.24	10.86	0.41	10.49
$\mathrm{GCI}_{23}/\left(r_*^q \mathrm{GCI}_{12}\right)$	0.934	1.045	0.997	1.037

The results presented in Figs. 4.8–4.11 correspond to the medium grid (2) in Table 4.3. According to Tables 4.3 and 4.4, the errors relative to the RE were less than 10% in the near wake velocity and less than 8% in the near and far wake turbulent velocity. The far wake velocity errors were very small (less than 0.5%). Taking into account that the velocity predictions in the far wake were of primary concern (as they are related to a wind farm power production), the medium grid solution errors were considered within acceptable levels. Consequently, similar grid densities were pursued throughout the use of VBM in this thesis.

Chapter 5

Wind flow and wakes over a Gaussian hill

5.1 Introduction

A 'Gaussian' hill was selected as a simple case of an ideal complex terrain in order to compare the wind turbine wake behaviour with that over flat terrain of the same roughness applying similar inlet velocity and turbulence boundary conditions.

5.2 Description of Test Case

5.2.1 The Gaussian hill

In order to have a basis for comparison, the properties of the Gaussian hill were chosen to match the 'quasi 3-D' test case of the UpWind project, Deliverable 8.3 [200]. The 'quasi 3-D' hill was preferred to the axisymmetric 3-D counterpart in the report, since the hill effects were found to be more pronounced

in the first case [200]. The Gaussian hill shape corresponds to the formula in Eq. (5.1).

$$z = h\, \mathrm{e}^{\left[-0.5\left(\frac{x}{\sigma}\right)^2\right]}, \text{ with } \sigma = L'/1.774 \tag{5.1}$$

where h is the hill height and $L' = x(z = h/2)$ is the half-length of the hill at the upwind mid-height [259]. The hill slope, s, is defined as the average slope of the hill top-half, upstream of the crest [259], according to Eq. (5.2).

$$s = \frac{h}{2L'} \tag{5.2}$$

The used values of $h = 700$ m and $L' = 1750$ m correspond to a mean slope value of $s = 0.2$ and the resulting hill shape is shown in Fig. 5.1.

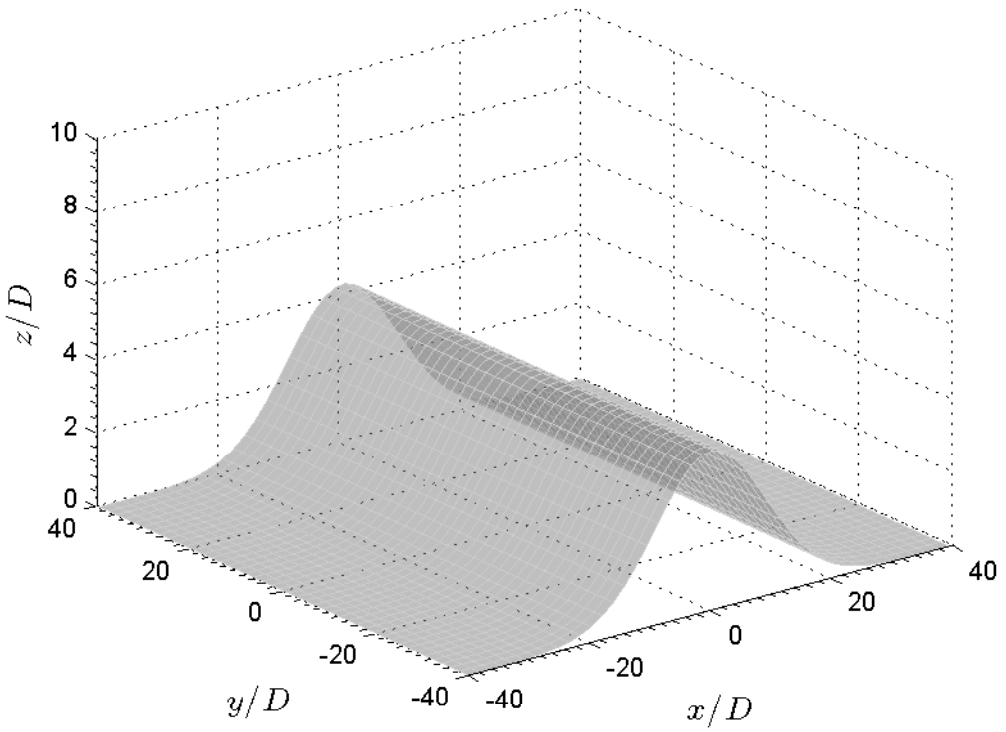

Figure 5.1. The 'quasi 3-D' Gaussian hill.

The inflow wind speed profile is taken as logarithmic with $U = 10$ m/s at hub height ($z = 90$ m) and an Atmospheric Boundary Layer height (h_{ABL}) of 500 m. Three different considerations of inlet turbulence intensity ($I_{in} =$ 5%, 13% and 20%), corresponding to three different values of roughness length ($z_\circ = 2.29 \cdot 10^{-7}$ m, 0.0445 m and 0.639 m respectively [200]) were considered, in order to examine the effect of roughness and compare the results with the UpWind project [200].

The aforementioned considerations were applied for cases of complex terrain (Gaussian hill) with no wind turbines and with one machine at the hilltop. Additionally, the case of two machines operating at the hilltop was examined only for inlet turbulence intensity of $I_{in} = 13\%$. Similar simulations for flat terrain were also necessary for the comparison between wakes over flat and hilly terrain.

The approach described in Sec. 3.5 was followed in the construction of the computational domains and the choice of Boundary Conditions. The domain dimensions are shown in Table 5.1. Four grid meshes were finally constructed for each of the examined cases: one and two wind turbines over flat and complex terrain. In each case, 885 cells were used for meshing the rotor disc, while the total cell count was approximately 6×10^5 and 7×10^5 for the flat and hill case with one machine and 1.4×10^6 and 1.5×10^6 for the corresponding cases with two machines.

Table 5.1. Domain dimensions.

Test case	L_x	L_y	L_z
Flat terrain	60 D	20 D	8 D
Gaussian hill	190 D	150 D	80 D

The simulations without wind turbines were performed using the grid with the rotor meshes, but deactivating the VBM, thus no momentum sources applied at the rotor cells. Velocity results from the simulations without wind turbines

were also stored in the memory (UDM) using a 'Define on Demand' User-Defined Function (UDF) in FLUENT, before activating the VBM in order to calculate the turbulence intensity and velocity deficit, for which the results of the simulation without the machine was necessary. An example of such an approach is shown in Appendix C.

5.2.2 The 5 MW wind turbine

Similarly to the UpWind project [200], a 5 MW wind turbine with a diameter (D) of 126 m and a hub-height of 90 m was used for modelling wakes. The NREL 5 MW wind turbine [260, 261] was found to have similar main characteristics and was used as a reference for selecting the necessary information for the VBM. A summary of the main characteristics of the NREL 5 MW machine is shown in Table 5.2.

Table 5.2. 5 MW turbine characteristics

rated power	5 MW
rotor orientation, configuration	upwind, 3 blades
rotor diameter	126 m
hub height	90 m
cut-in, rated, cut-out wind speed	3 m/s , 11.4 m/s , 25 m/s
cut-in, rated rotor speed	6.9 rpm , 12.1 rpm
rated tip speed	80 m/s
control	variable speed, collective pitch

According to the methodology described in Chapter 3, the use of the VBM requires additional blade information; such information was found in a NREL report by Jonkman [260], investigating a NREL 5 MW baseline wind turbine. The blade was separated into 19 sections with different twist angle, chord length and aerodynamic profile (Table 5.3). The aerodynamic data of each airfoil were also taken from the Jonkman report [260] and they are presented in Appendix A.

The simulated rotor was a variable-pitch-to-feather wind turbine [260, 261]. In

Table 5.3. Distributed NREL 5 MW blade aerodynamic properties

Node [−]	Radial location [m]	Twist angle [°]	Chord length [m]	Airfoil type [−]
1	0.00	13.31	3.00	Cylinder 1
2	2.87	13.31	3.54	Cylinder 1
3	5.60	13.31	3.85	Cylinder 1
4	8.33	13.31	4.17	Cylinder 2
5	11.75	13.31	4.56	DU 40
6	15.85	11.48	4.65	DU 35
7	19.95	10.16	4.46	DU 35
8	24.05	9.01	4.25	DU 30
9	28.15	7.80	4.01	DU 25
10	32.25	6.54	3.75	DU 25
11	36.35	5.36	3.50	DU 21
12	40.45	4.19	3.26	DU 21
13	44.55	3.13	3.01	NACA 64618
14	48.65	2.32	2.76	NACA 64618
15	52.75	1.53	2.52	NACA 64618
16	56.17	0.86	2.31	NACA 64618
17	58.90	0.37	2.09	NACA 64618
18	61.63	0.11	1.42	NACA 64618
19	63.00	0.11	1.42	NACA 64618

this technology, the power output is controlled above the rated wind speed by increasing the blade pitch angle. As the pitch angle is increased, the angle of attack is decreased, and, thus, the lift force and the torque are reduced [3]. Jonkman [260] and Jonkman et al. [261] modelled a baseline full-span, rotor-collective, blade-pitch controller of such a technology. The results of the rotor speed and blade pitch as a function of wind speed are presented in Table 5.4. A linear interpolation of the data in Table 5.4 was used for the calculation of the rotor speed and collective blade pitch in the VBM, based on the calculated wind speed at the hub.

5.2.3 Current approach vs. UpWind project

Although the test cases of the single wake were chosen to be similar to the UpWind project, Deliverable 8.3 [200], the CFD methodology was different. An outline of the main differences is shown in Table 5.5.

Table 5.4. NREL 5 MW rotor speed and blade pitch vs wind speed [260, 261]

wind speed [m/s]	rotor speed [rpm]	pitch angle [°]
3 (cut-in)	6.9	0.00
11.4 (rated)	12.1	0.00
12	12.1	3.83
13	12.1	6.60
14	12.1	8.70
15	12.1	10.45
16	12.1	12.06
17	12.1	13.54
18	12.1	14.92
19	12.1	16.23
20	12.1	17.47
21	12.1	18.70
22	12.1	19.94
23	12.1	21.18
24	12.1	22.35
25	12.1	23.47

Table 5.5. Outline of main differences with the UpWind approach [200].

	Current thesis	UpWind Project [200]
CFD solver	FLUENT	CRES-flowNS
Turbulence Model	RSM modified (Sec. 3.2.5)	k-ω model modified
Wall function	modified (Sec. 3.4.2)	not mentioned
Rotor modeling	VBM	momentum sink, C_T based

Apart from the different characteristics of the flow solvers themselves, an important dissimilarity was the choice of the turbulence model, which is expected to be responsible among other factors for the discrepancies in the results. The choice of the RSM provided the advantage of taking into account the anisotropy of atmospheric turbulence. Differences in the wall function approach may also have been responsible for discrepancies, but it was difficult to evaluate the effect, since there was little information on the wall function used in the UpWind report.

One of the main differences was the rotor modelling approach. In UpWind, the momentum sink was calculated based on the pre-calculated thrust coefficient and

it was uniform along the disc, without taking into account any rotational effects. In the current thesis, the VBM source terms were not known and they evolved as part of the solution (see Sec. 3.1.2). This was a more detailed approach, taking into account specific characteristics of the wind turbine allowing the momentum sinks across the disc to vary with radius. Additionally, the rotational effects were also taken into account.

The comparison of the results using the two CFD approaches was aimed at identifying the differences between them; since there were no experimental observations available, this Chapter does not include the validation of the results. For this purpose, Chapter 4 contains the validation of the CFD approach of modelling a single wake and Chapter 6 includes the validation of the CFD modelling of the neutral atmospheric wind flow over a hill (Askervein hill). According to Zeman and Jensen [105], the Askervein hill shape along the principal direction can be approximated with a Gaussian curve.

5.3 Hill flow without wind turbines

All simulations were initially run without the effect of the rotor, in order to establish a reference for the later estimation of the wakes. The results were studied with reference to wind velocity and turbulence intensity. The horizontal wind velocity was normalised with the velocity at the top boundary (equalling the velocity at h_{ABL}), as shown in Eq. (5.3), whereas the turbulence intensity was calculated according to Eq. (5.4). All the Cartesian coordinate variables (x, y and z) have been normalised with the rotor diameter, D.

$$u_x = \frac{U_x}{U_{top}} \tag{5.3}$$

$$I_u = \frac{\sigma_u}{U_x} \tag{5.4}$$

As previously stated (Sec. 5.2.1), each case of inlet turbulence intensity corresponds to different values of roughness length. Consequently, calculated values of top velocity U_{top} from Eq. (3.23) using $z = h_{abl}$ are different. Table 5.6 shows a summary of the calculated values of $z_\circ$ and U_{top} for different values of inlet turbulence intensity I_{in}.

Table 5.6. Calculated U_{top} and $z_\circ$ for different I_{in}.

I_{in}	$z_\circ$ (m)	U_{top} (m/s)
5%	$2.29 \cdot 10^{-7}$	10.87
13%	0.0445	12.25
20%	0.639	13.45

The simulation results are presented in terms of streamwise and vertical variations of normalised velocity and turbulence intensity in Secs. 5.3.1 and 5.3.2.

5.3.1 Streamwise variations

The streamwise variations of normalised horizontal wind speed and turbulence intensity at hub height are shown in Figs. 5.2a and 5.2b respectively. The origin of the x-axis was selected to coincide with the hilltop, which is also where the rotor was placed in the single wake case. Therefore, a positive x/D corresponds to the downstream, lee side of the hill and a negative x/D refers to locations upstream the hilltop.

The wind flow exhibits some common characteristics in all three cases: an initial flow deceleration (due to a rise of pressure) at the windward side of the hill; a flow acceleration and a decrease of turbulence near the hilltop; and a significant flow deceleration and a rise of turbulence intensity at the lee side of the hill. For low roughness values ($I_{in} = 5\%$), wind velocity and turbulence variations seem nearly symmetrical at each side, along the hilltop (the variation of turbulence intensity is

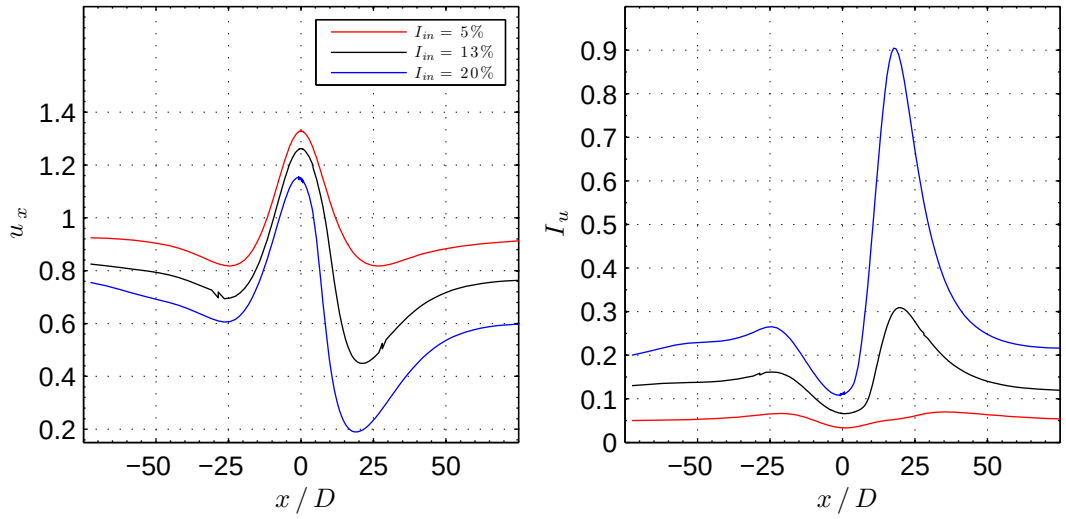

(a) Normalised velocity (b) Turbulence Intensity

Figure 5.2. Variation of streamwise u_x and I_u at z_{hub} for various I_{in} (no rotors).

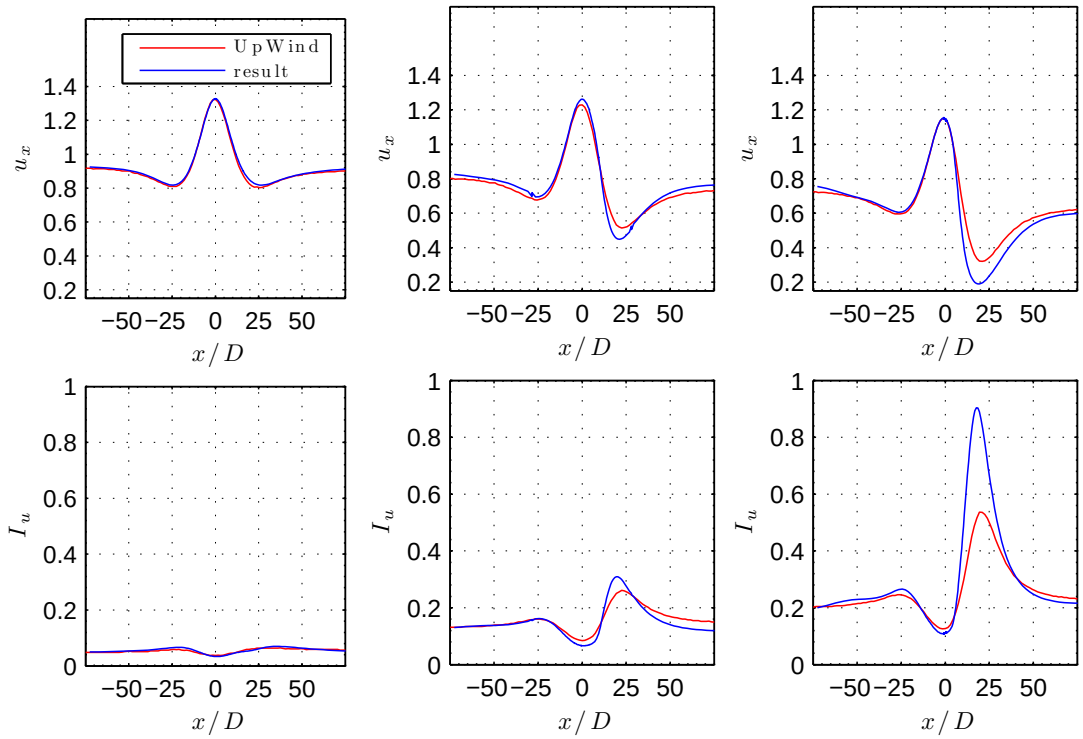

(a) $I_{in} = 5\%$ (b) $I_{in} = 13\%$ (c) $I_{in} = 20\%$

Figure 5.3. Comparison of u_x and I_u with UpWind for various I_{in} (no rotors).

minimum). An increase of roughness causes the variations (velocity deceleration and rise of turbulence) at the lee side of the hill to be more pronounced.

The same effects, but less pronounced, were observed in the UpWind project [200]. Fig. 5.3 presents the comparison with the UpWind results. The results seem almost identical in the low-roughness case ($I_{in} = 5\%$) and the only discrepancies are found at the lee side of the hill of the rough cases ($I_{in} = 13\%$ and 20%), where the current approach calculated increased flow deceleration and turbulence intensity. The divergence of the results is especially noticable in the case with the highest roughness ($I_{in} = 20\%$), at which the peak of turbulence intensity at the lee side is more than 4 times the inlet turbulence intensity I_{in}, whereas the UpWind predicted it to be 3 times I_{in}. Nevertheless, the maximum flow deceleration as well as turbulence intensity is found to occur at a similar location of $x \approx 20$ D downwind of the hilltop.

5.3.2 Vertical Profiles

The vertical profiles of normalised streamwise velocity, u_x, and turbulence intensity, I_u, at the lee side of the hill without the rotor in operation, are shown in Figs. 5.4a and 5.4b respectively. The positions were selected to cover different locations downwind of the hilltop. The origin of the z-axis was selected to be at the rotor hub height ($z = 90$ m).

The results confirm some of the conclusions made in Sec. 5.3.1: near the hilltop, the flow is accelerated and there is low level turbulence, while further downstream there is a significant flow deceleration and a rise of turbulence intensity, especially at high ambient turbulence levels, 20 D downwind of the hilltop. Additionally, the near-hilltop wind velocity profile is very flat at low ambient turbulence, whereas wind shear is considerable at high ambient turbulence. Turbulence intensity is also significant near the ground in the latter case. Further downstream and as the flow gradually decelerates, there is an increase of wind shear and near-ground

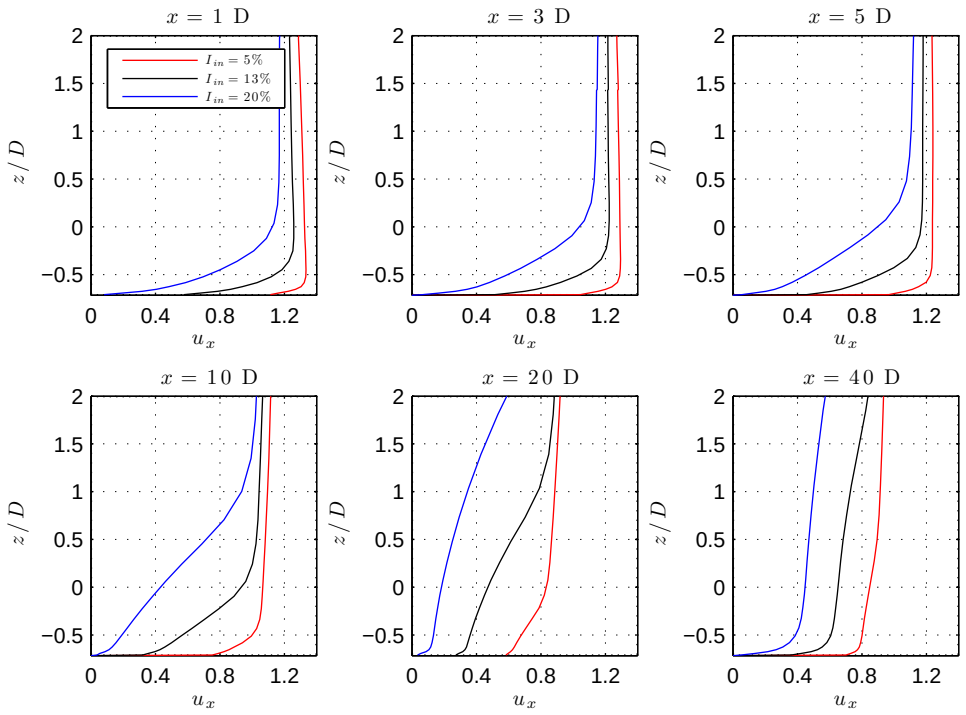

(a) Normalised velocity

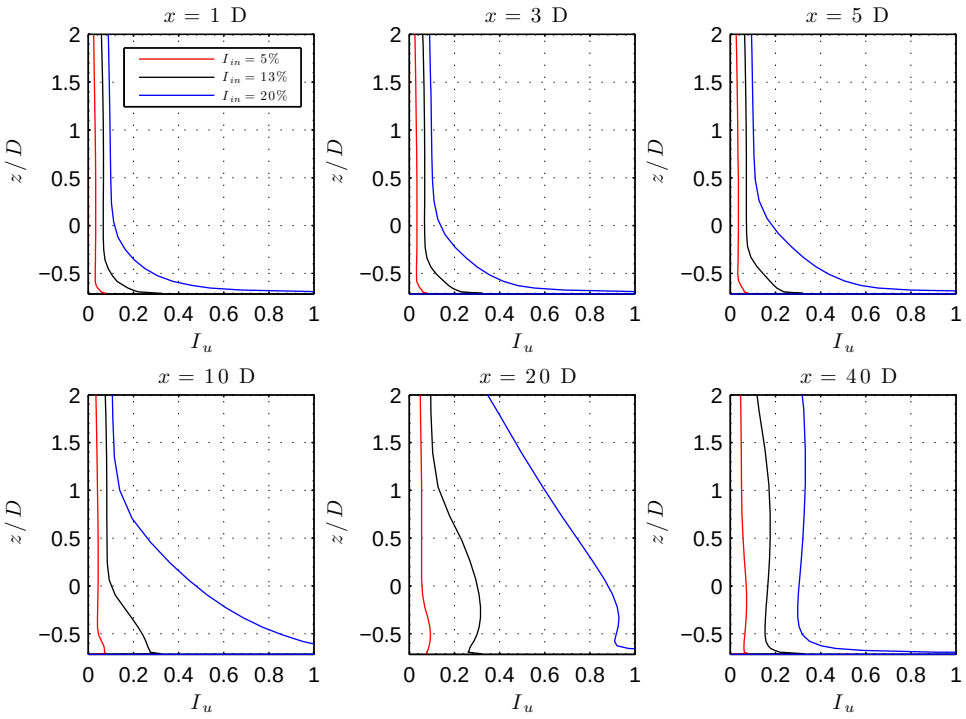

(b) Turbulence Intensity

Figure 5.4. Vertical profiles of u_x and I_u downwind of the hilltop for various I_{in} (no rotors).

turbulence intensity. The effects stretch vertically and they are most pronounced at $x = 20$ D downwind of the hilltop, at high ambient turbulence intensity. At $x = 40$ D downwind of the hilltop, where elevation is very low (Fig. 5.1), the flow seems to recover a semi-logarithmic vertical shape. However, in the case of high ambient turbulence ($I_{in} = 20\%$), a significant level of turbulence remains.

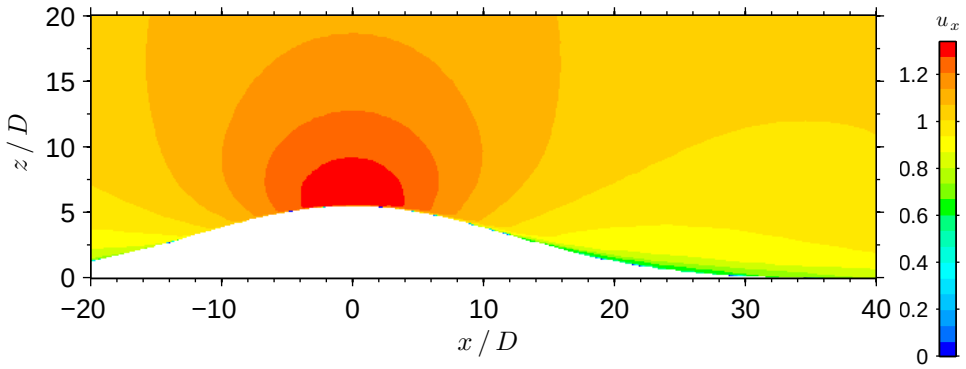

(a) $I_{in} = 5\%$

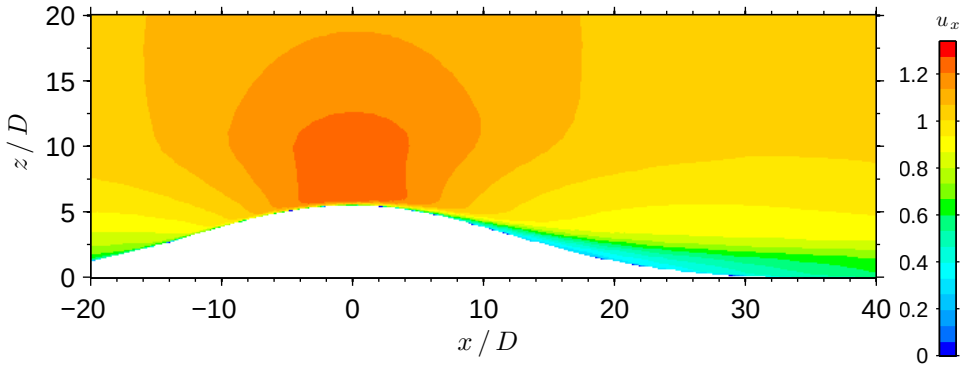

(b) $I_{in} = 13\%$

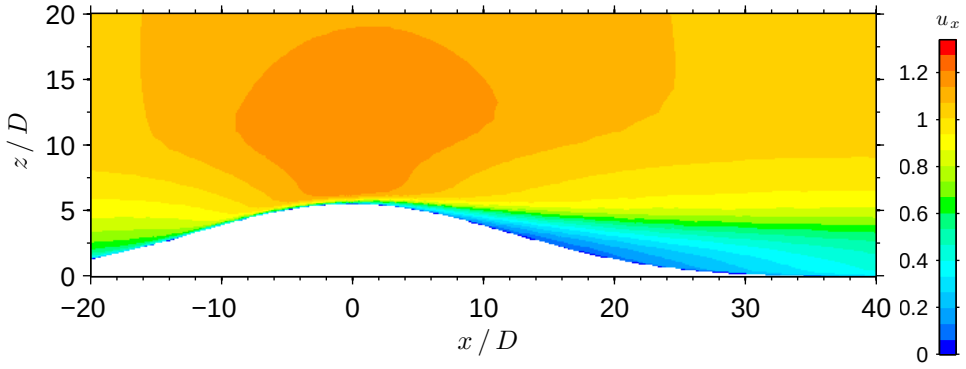

(c) $I_{in} = 20\%$

Figure 5.5. Contours of normalised horizontal velocity at the $y = 0$ plane.

Fig. 5.5 shows the contours of the normalised horizontal velocity u_x at the $y = 0$ plane, in all three different ambient turbulence configurations. The origin of the x-axis was selected at the location of the hilltop. The results confirm that there was no flow separation (at the lee side of the hill and near the ground), even at high ambient turbulence levels (high roughness).

5.4 Single wake over the hill

In order to examine the wake flow over the hill, the case of a machine positioned at the hilltop, at a hub-height of 90 m, was investigated. The rotor was considered facing the wind, with zero yaw misalignment and zero tilt angle. The wind speed measured at the hub location (Table 5.7) was used as reference for the estimation of the turbine rotational speed. In all cases, the rotor was found to be operating above rated speed, thus the rated rotational speed (12.1 rpm) was used as input in the VBM.

In the results, the normalised horizontal velocity was calculated according to Eq. (5.3) and the turbulence intensity was found from Eq. (5.4), using the results of U_x without the effect of the rotor, as shown in Eq. (5.5).

$$I_u = \frac{\sigma_u}{U_{x(\text{no WT})}} \tag{5.5}$$

The values of $U_{x(\text{no WT})}$ had been previously saved from the simulation without the VBM by means of the User-Defined Memory (UDM) option in FLUENT UDFs [213].

For a better evaluation of the wake results, the wake velocity deficit profiles were additionally examined. The velocity deficit was calculated based on the saved values of the same simulation without the effect of the rotor, using Eq. (5.6). This expression of velocity deficit including the thrust coefficient was selected for

a comparison with the UpWind results [200].

$$U'_{def} = \frac{U_{x(\text{no WT})} - U_x}{C_T \cdot U_{x(\text{no WT})}} \tag{5.6}$$

where C_T is the rotor thrust coefficient.

As shown in Chapter 2, the thrust coefficient is related to the thrust force F_T of the rotor, according to Eq. (2.17):

$$C_T = \frac{F_T}{\frac{1}{2}\rho U_\infty^2 A_d} \tag{2.17}$$

The thrust can also be expressed by means of the pressure drop $\Delta p = \left(p_d^+ - p_d^-\right)$ through the actuator disc [2], as previously shown in Eq. (2.8):

$$F_T = A_d \left(p_d^+ - p_d^-\right) \tag{2.8}$$

Combining Eqs. (2.17) and (2.8), the thrust coefficient can be calculated from the solution as:

$$C_T = \frac{\Delta p}{\frac{1}{2}\rho U_{\infty,hub}^2} \tag{5.7}$$

where $U_{\infty,hub}$ refers to the wind speed calculated at the rotor hub height, but without the effect of the rotor. It denotes the 'local' ambient wind speed measured at the rotor hub taking into account the effect of the terrain (hill) in the ambient flow.

The same calculated wind speed ($U_{\infty,hub}$) was also used for the estimation of the rotor rotational speed Ω and the blade collective pitch, based on the data of Table 5.4 and linear interpolation. The calculated velocities and thrust coefficients as well as the interpolated rotational speed for each case are presented in Table 5.7.

Table 5.7 also includes a comparison with flat terrain simulations using the same Boundary Conditions. It is shown that the calculated thrust coefficient values in

the flat terrain case are almost double compared to the corresponding values of the hilly terrain, which was expected, since the flow is accelerated at the hilltop.

Table 5.7. Reference velocities and C_T for different I_{in}.

Boundary Conditions		Gaussian hill			Flat terrain		
I_{in}	U_{top} (m/s)	$U_{\infty,hub}/U_{top}$	C_T	Ω (rpm)	$U_{\infty,hub}/U_{top}$	C_T	Ω (rpm)
5%	10.87	1.33	0.303	12.1	0.92	0.608	11.4
13%	12.25	1.24	0.291	12.1	0.81	0.603	11.4
20%	13.45	1.15	0.276	12.1	0.72	0.596	11.4

For a comprehensive study of the wake behaviour, results of wake deficit (U'_{def}) and turbulence intensity (I_u) were examined in all three directions: the hub-height streamwise (x) and lateral (y), as well as the vertical (z) direction. Comparisons were also performed with the UpWind CFD results [200] and with a similar rotor case operating over flat terrain.

5.4.1 Streamwise variations

Results of streamwise variation of velocity and turbulence in the single wake over the hill are shown in Figs. 5.6a and 5.6b respectively. The dashed lines in the figures show the simulation results without the wind turbines (also presented in Fig. 5.2).

Fig. 5.6a shows a rapid velocity drop at the hilltop, caused by the operation of the wind turbine. This velocity reduction seems to also have a contribution to the flow deceleration at the lee side of the hill, although this effect is significantly more pronounced in the case of low ambient turbulence intensity ($I_{in} = 5\%$). The wake recovery in the latter case, is significantly slower, as expected. In the other two cases, wind speed is recovered after 10 D for $I_{in} = 13\%$ and 5 D for $I_{in} = 20\%$. According to Fig. 5.6b, there is an increase of turbulence intensity near the hilltop, due to the wake. In comparison to the undisturbed flow, this increase is quickly diminished at the lee side of the hill of all cases, apart from the case with low

ambient turbulence, where turbulence intensity continues to increase in the far wake. The wake effects in the low turbulence case are apparent, even at distances greater than 50 D downwind of the rotor.

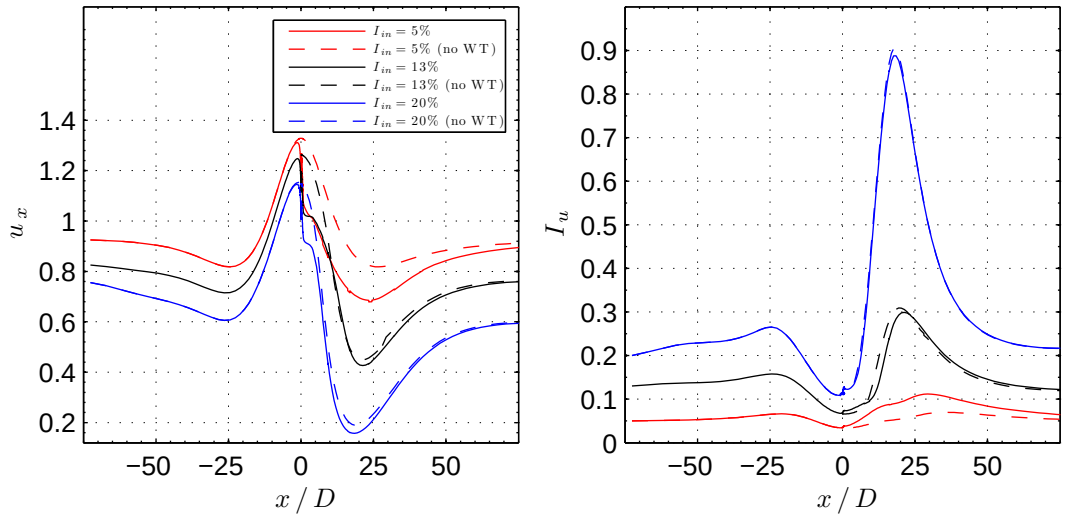

(a) Normalised velocity (b) Turbulence Intensity

Figure 5.6. Variation of streamwise u_x and I_u at z_{hub} for various I_{in} (1 rotor).

Fig. 5.7 shows a comparison with the UpWind CFD wake simulations. The results have a better match for the case of low ambient turbulence ($I_{in} = 5\%$), where the wake effects are more pronounced. In all cases, the predicted wake deficit is higher compared to the UpWind prediction. Similarly to the simulations without rotors (Sec. 5.3.1), the current approach predicts a higher maximum flow deceleration and a faster recovery of wind velocity at the lee side of the hill ($x > 20$ D). Wake turbulence predictions near the turbine were slightly lower compared to UpWind, but similarly to Fig. 5.3, the predicted rise of turbulence due to the hill geometry further downstream, is higher. All the aforementioned discrepancies are more pronounced for the case of high ambient turbulence ($I_{in} = 20\%$).

A flat terrain case with the same inlet boundary conditions and rotor type was also considered, in order to examine the differences in the wake behaviour. Table 5.7 shows the comparison of the streamwise variations of velocity deficit between the

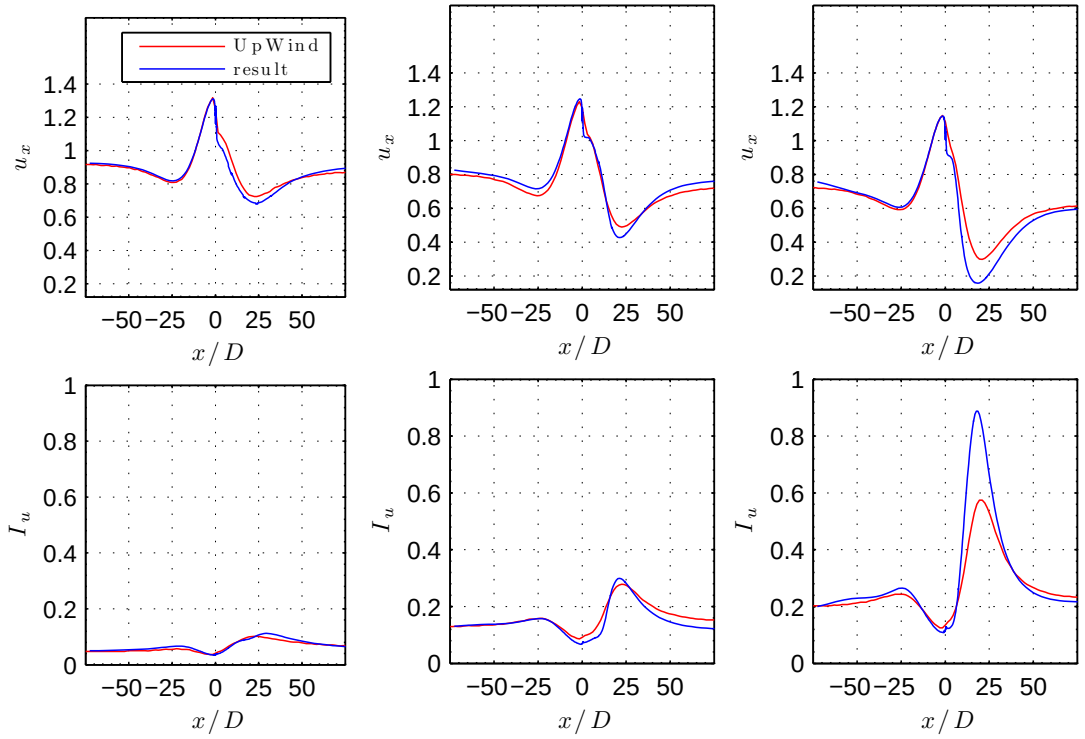

(a) $I_{in} = 5\%$ (b) $I_{in} = 13\%$ (c) $I_{in} = 20\%$

Figure 5.7. Comparison of u_x and I_u with UpWind for various I_{in} (1 rotor).

flat and the hilly case. The streamwise variations of wake deficit and turbulence intensity for different ambient turbulence conditions, are shown in Fig. 5.8.

On flat terrain (Fig. 5.8b), the maximum deficit is higher and always located in the near wake, while further downwind, the wake is monotonically dissipating. An increase in ambient turbulence results in lower wake deficit with a maximum closer to the rotor and a faster flow recovery.

Over complex terrain, there are significant differences in the trend of the wake deficit, depending on the ambient turbulence. Contrary to the flat terrain case, the maximum deficit is found in the high-ambient turbulence case, further downstream of the near wake. In low ambient turbulence ($I_{in} = 5\%$), the wake deficit is maximised between 5 D and 10 D downstream and then monotonically dissipates, but the flow recovery is not as fast as that over flat terrain. In the other

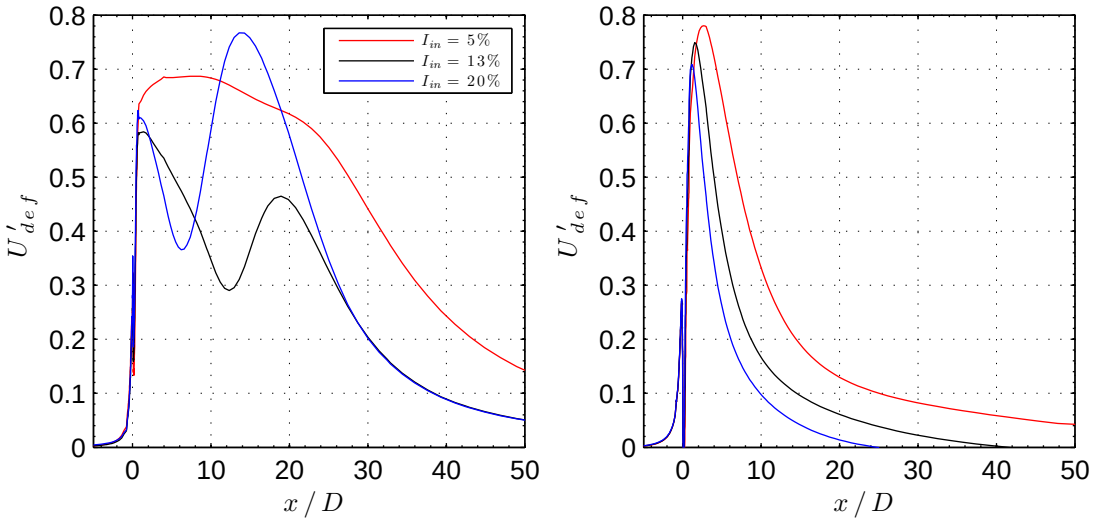

(a) Gaussian hill (b) Flat terrain

Figure 5.8. Comparison of streamwise U'_{def} of 1 rotor at hilltop with flat terrain for various I_{in}.

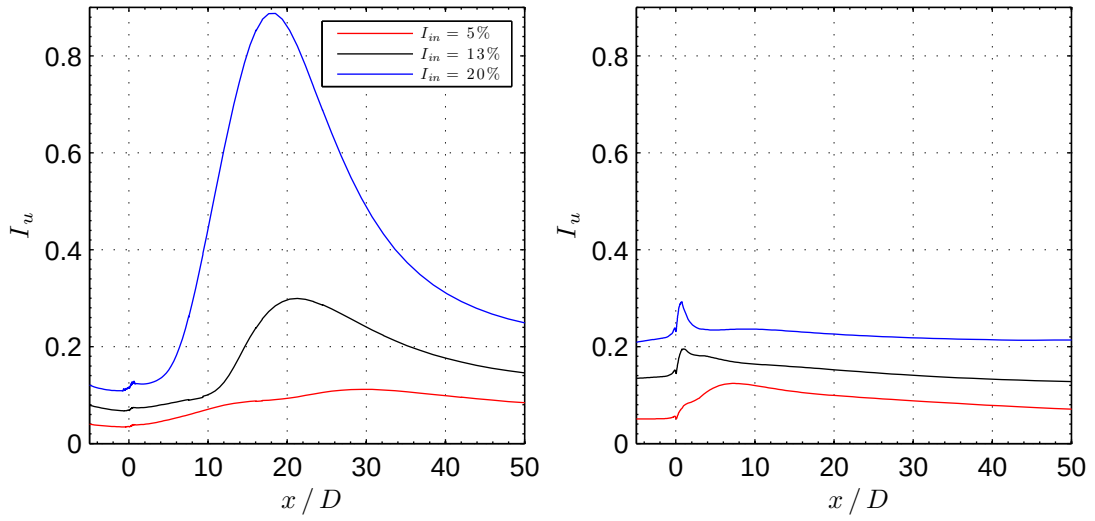

(a) Gaussian hill (b) Flat terrain

Figure 5.9. Comparison of streamwise I_u of 1 rotor at hilltop with flat terrain for various I_{in}.

two cases of increased ambient turbulence, the wake deficit appears to exhibit a peak in the near wake and a second peak in the far wake, at $x \approx 19$ D and $x \approx 14$ D for $I_{in} = 13\%$ and 20% respectively. This behaviour is more pronounced in the high ambient turbulence case ($I_{in} = 20\%$), where the second peak is also the

maximum wake deficit. This can be attributed to the fact that the wind speed is decelerating significantly in that region. For $x > 28$ D the wake deficit has almost exactly the same streamwise variation for the high-turbulence cases ($I_{in} = 13\%$ and 20%), as it gradually dissipates.

Results of turbulence intensity are compared in Fig. 5.9. It is clear that the flat terrain case has significantly faster wake turbulence dissipation. Increased ambient turbulence levels result in a faster dissipation, while the maximum turbulence is located closer to the rotor in the near wake. In the hill case, it is clear that the dominant role in the turbulence production is played by the hill geometry, leading to significantly higher turbulence levels at the lee side of the hill. Near the rotor however, wake turbulence is lower, as the turbulence at the hilltop is decreased.

5.4.2 Lateral variations

Fig. 5.10 presents a comparison of the lateral (y-axis) profile of wake velocity deficit between the hill case and flat terrain. The origin of the y-axis was selected to coincide with the rotor hub location. Therefore, a positive or negative lateral distance y/D corresponds to the left or right with respect to the streamwise, x-direction. At $x = 1$ D the wake over the hill has a similar inverse shape and width for all cases of ambient turbulence. However, in the flat terrain case, the wake deficit is higher and wider, while the shape is an inverse W and it is slightly asymmetrical (Fig. 5.10b), especially for low ambient turbulence. At $x = 10$ D and 20 D the wake in the hill case widens significantly with increased ambient turbulence. Although the maximum wake deficit near the centreline is at low ambient turbulence ($I_{in} = 5\%$), further away from the centreline, at $y < -0.5$ D and $y > 0.5$ D, the maximum deficit is located at the case of the highest roughness ($I_{in} = 20\%$), due to the higher lateral expansion.

A noticeable effect in the hill case (Fig. 5.10a), is a slight asymmetry, a ‘wake

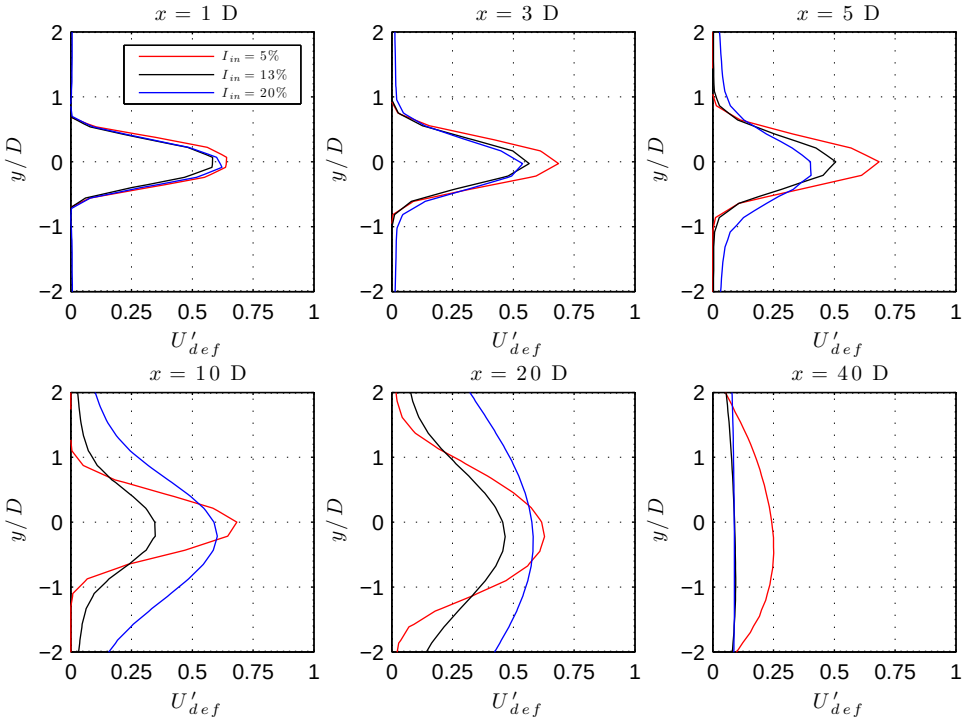

(a) Gaussian hill

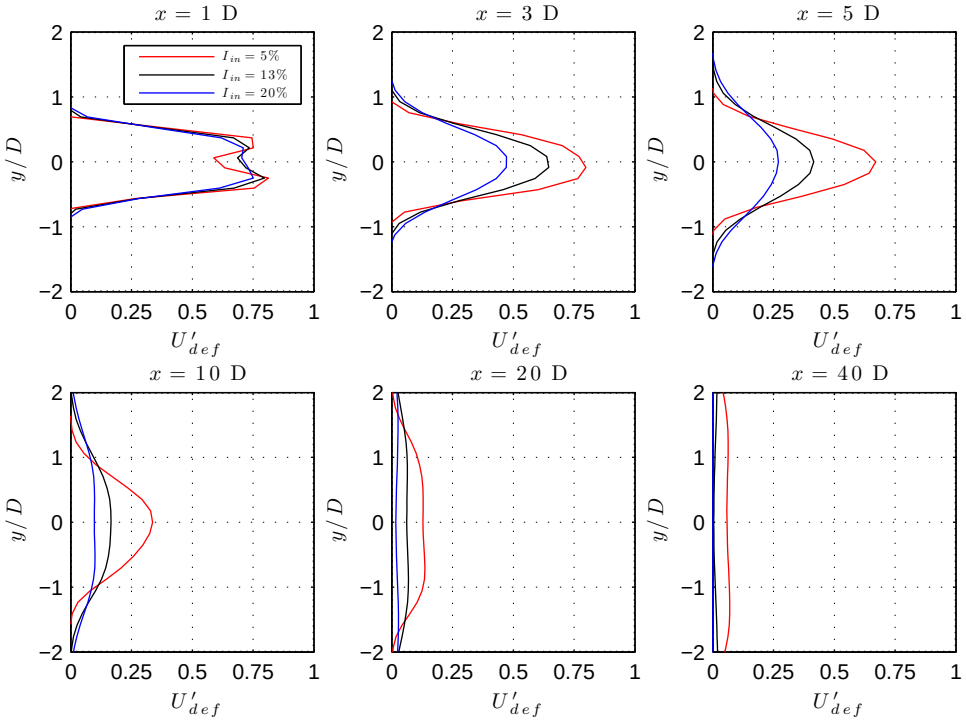

(b) Flat terrain

Figure 5.10. Comparison of lateral U'_{def} of 1 rotor between hilly and flat terrain for various I_{in}.

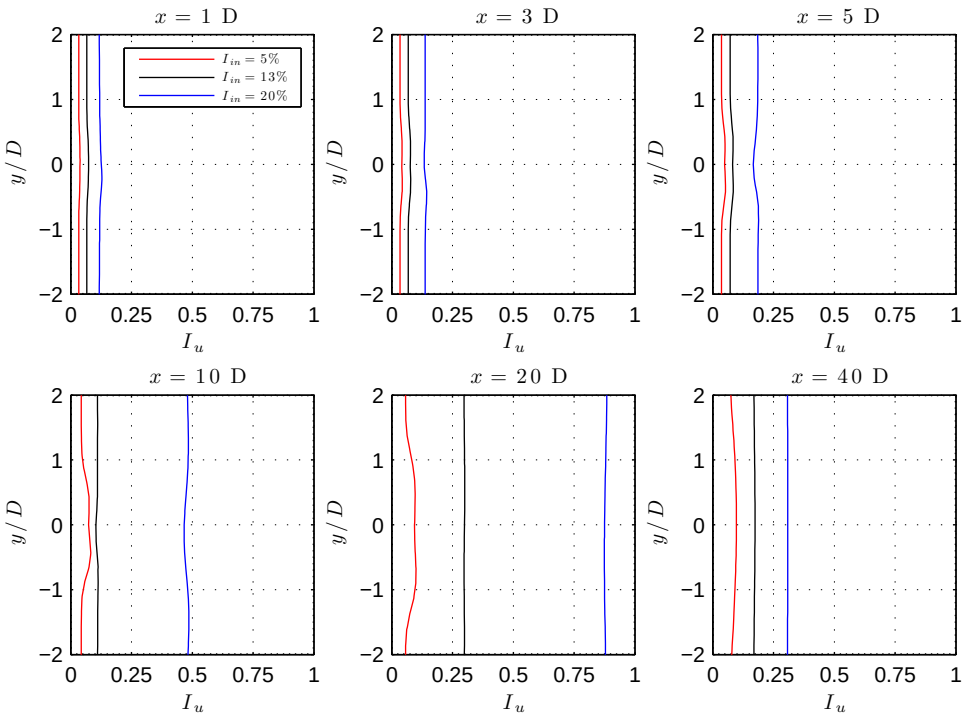

(a) Gaussian hill

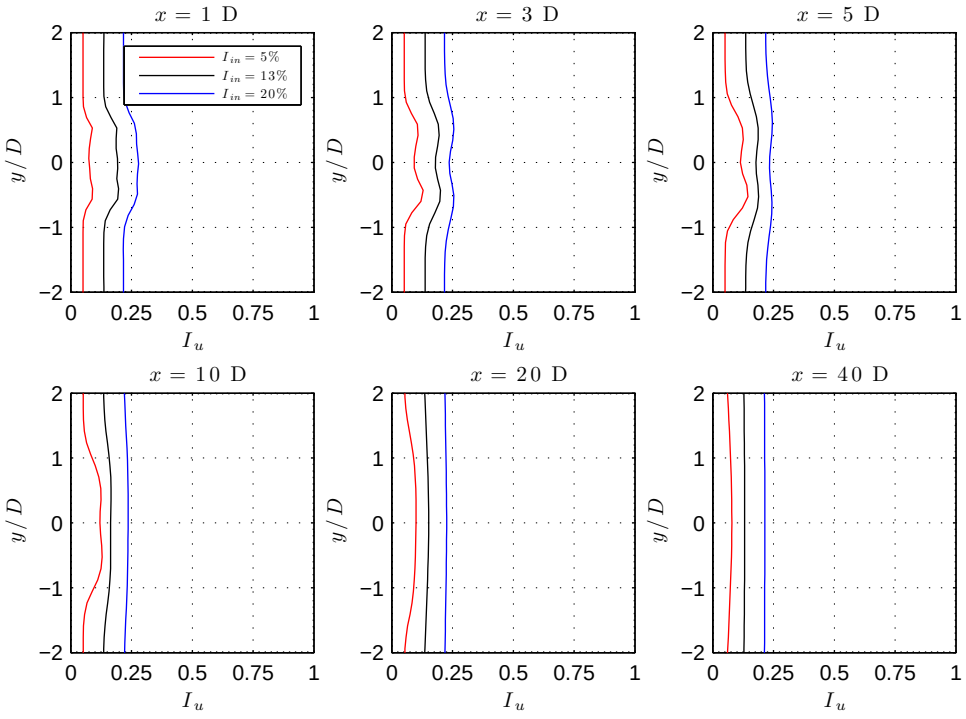

(b) Flat terrain

Figure 5.11. Comparison of lateral I_u of 1 rotor between hilly and flat terrain for various I_{in}.

drift' from the centreline $y = 0$ towards the negative y-direction, found to be more pronounced in the case of high ambient turbulence ($I_{in} = 20\%$) at 3 D$< x <$ 10 D. At x = 10 D and 20 D downwind of the hilltop, the wake is found to 'drift' approximately 0.3 D at high ambient turbulence. In flat terrain, this behaviour is almost negligible. The wake drift was not observed in the UpWind project CFD simulation results [200], where the rotor rotation was not taken into account. A change of the direction of the blade rotation, resulted in a change of the direction of the wake 'drift'. The two latter facts indicated that this behaviour is related to the rotor rotation. A more detailed examination of the wake 'drift' is presented in Sec. 5.4.5.

A similar case of asymmetry was also discussed by Troldborg [24]. It has been suggested that the combination of high wind shear and the rotor rotational effects cause low velocity wind from the bottom to move upwards, towards one side while high velocity wind from the upper part of the wake to move downwards, towards the other side. This suggestion is further supported by the fact that the wake 'drift' is found at a lee side location, where the flow is rapidly decelerated.

The effect is more pronounced in the case of high turbulence intensity ($I_{in} = 20\%$), where the wind shear is also higher (Fig. 5.2a) and it is almost negligible for low turbulence, where the wind profile is almost flat (Fig. 5.2a). The fact that the asymmetry was not reproduced in several simulations without the account of rotor rotation [58, 85] further supports the link between the asymmetric wake and the rotational effects of the rotor.

The lateral variations of turbulence intensity are shown in Fig. 5.11. It is clear that the contribution of the wake in the turbulence intensity of the hill case is very small, with only the variations at 10 D and 20 D downstream at low ambient turbulence to show some significance. However, in the flat terrain case, the effects are more significant until 10 D downstream of the rotor. The two peaks of wake turbulence intensity due to the wind shear layer in the wake are also visible, as

they gradually move towards the wake centre due to the expansion of the shear layer. The effects are more pronounced at low ambient turbulence levels.

5.4.3 Vertical Profiles

Fig. 5.12 shows a comparison of the velocity deficit vertical profiles between the flat (Fig. 5.12b) and the complex terrain case (Fig. 5.12a).

The origin of the z-axis was selected to be at the hub-height, 90 m a.g.l.. At $x = 1$ D on hilly terrain, the deficit develops an inverse V-shape with the peak close to the hub-height; at the same location on flat terrain, the deficit is higher and more vertically spread, while it is formed into an inverse W shape. The latter shape is not completely symmetrical with the highest asymmetries found for low roughness ($I_{in} = 5\%$), where the maximum peak is found close to the ground. For downwind distances of $x = 3$ D and 5 D, the wake behaviour exhibits similar behaviour over both flat and hilly terrain: the wake centre moves upwards, above the turbine axis, at increased ambient turbulence levels and downwards, below the turbine axis, at low ambient turbulence. However, the wake over flat terrain is wider.

At the hill case, after 10 D downwind, the U-shape is maintained at $x = 10$ D for $I_{in} = 5\%$ and 13%, but in the high-turbulence case ($I_{in} = 20\%$), the deficit develops into an approximately exponential decay shape, as it is highly increased near the ground and then decreases with height. Further downwind, at $x = 20$ D, a similar development of the wake shape occurs also for $I_{in} = 13\%$. As a consequence, the maximum wake deficit below the hub-height at $x = 10$ D and 20 D occurs at the high-turbulence case ($I_{in} = 20\%$) near the ground. Only the low roughness case ($I_{in} = 5\%$) maintains the U-shape until $x = 40$ D. While the far wake deficit spreads vertically with increased roughness in the hill case, the flat terrain wake deficit gradually diminishes after $x = 10$ D. At $x = 40$ D, U'_{def} remains moderately significant only in the hill case, especially in

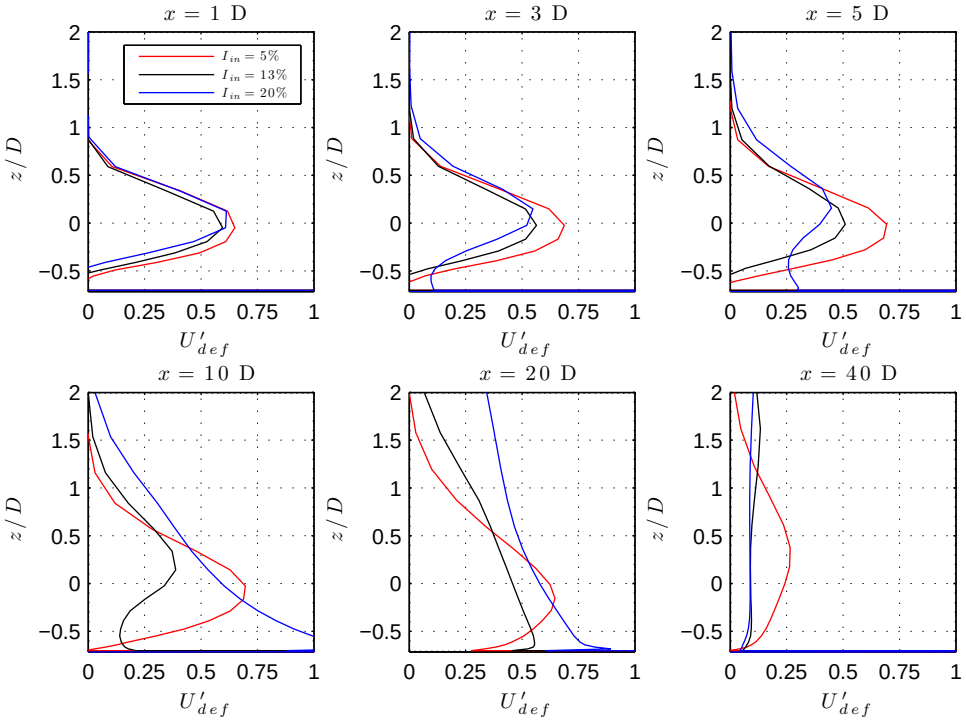

(a) Gaussian hill

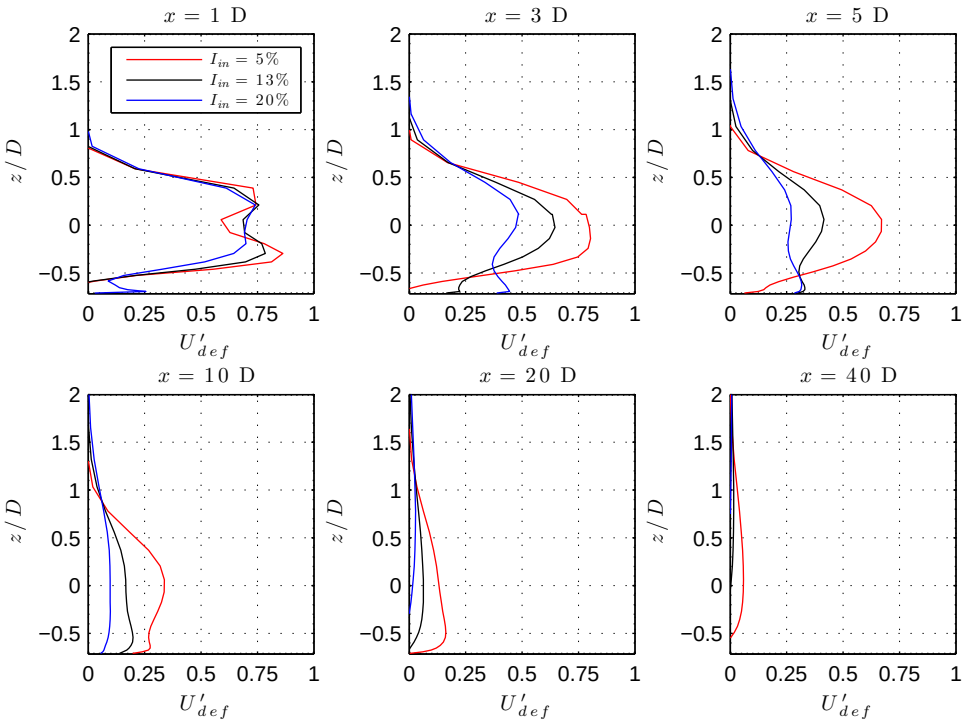

(b) Flat terrain

Figure 5.12. Comparison of U'_{def} vertical profiles of 1 rotor at hilltop with flat terrain for various I_{in}.

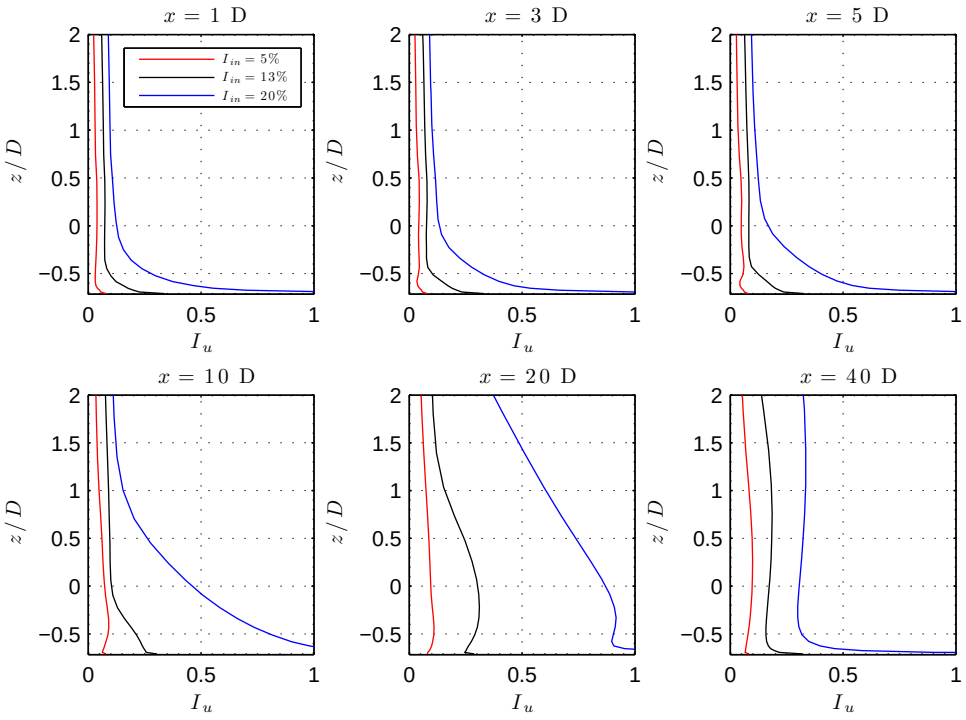

(a) Gaussian hill

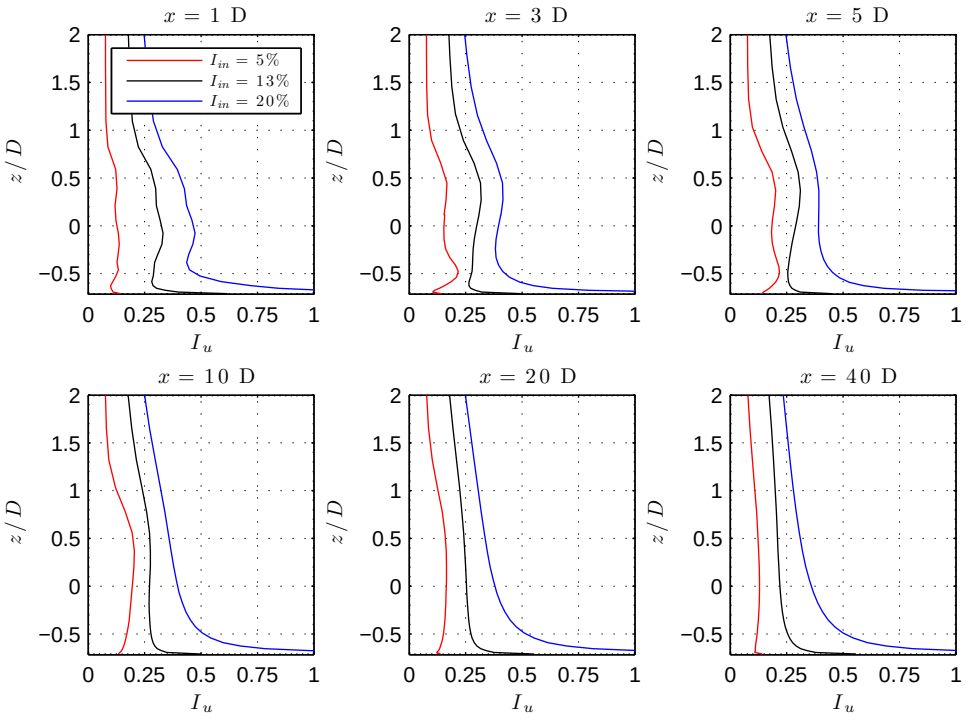

(b) Flat terrain

Figure 5.13. Comparison of I_u vertical profiles of 1 rotor at hilltop with flat terrain for various I_{in}.

the low turbulence scenario (I_{in} = 5%) at z = 1 D, while spreading vertically wider at higher ambient turbulence. The effects of the downwards and upwards displacement of the maximum deficit seem to be more pronounced in the hill case, especially in the far wake.

The vertical distribution of turbulence intensity in the hill and the flat terrain cases are shown in Fig. 5.13. The turbulence in the near wake of the hill case seems to be little affected by the wind turbine. However, in the flat terrain case, the disturbance is visible. There are two peaks of turbulence in the near wake (x = 1 D), corresponding to the shear layer. Further downstream, wake turbulence is dissipated faster in the high ambient turbulence case.

5.4.4 Velocity contours

Fig. 5.14 shows the contours of u_x for each ambient turbulence case at the hub-height (left) and at the $y = 0$ plane (right). The origins of the x and y axis were again chosen to coincide with the rotor centre at the hilltop, while the origin of the z axis was chosen as $z(x = 20$ D).

According to the velocity contours at hub-height (left), the wind is accelerated at the hilltop (x = 0), and the effect of the rotor operation enforces the flow deceleration at the lee side of the hill. The centreline of $y = 0$ is also plotted at hub-height in order to illustrate the wake 'drift' from the straight path, which is clearer in the higher ambient turbulence cases (I_{in} = 13% and 20%). The $y = 0$ plane contours (right) show that the U-shape wake is maintained mainly in the low-turbulence case (I_{in} = 5%), whereas in the higher turbulence cases there is high interaction with the flow deceleration due to the hill, which is especially noticeable near the ground. The lateral wake spread of the higher turbulence cases is also visible.

Fig. 5.15 depicts the velocity deficit contours at hub-height (left) and $y = 0$ plane

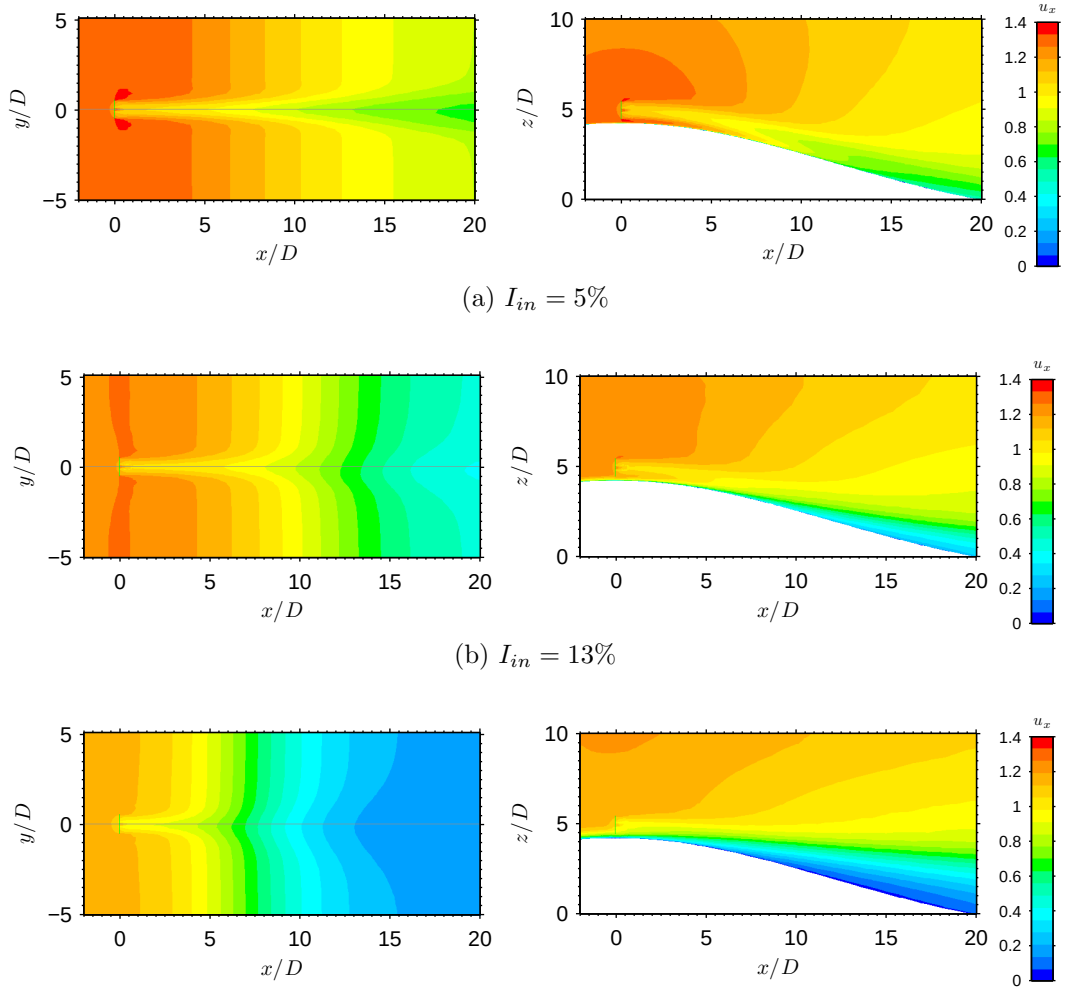

(a) $I_{in} = 5\%$

(b) $I_{in} = 13\%$

(c) $I_{in} = 20\%$

Figure 5.14. Contours of normalised velocity

(right). At low ambient turbulence (Fig. 5.15a), the wake seems to be confined and not spread significantly, either laterally or vertically. In fact, at the $y = 0$ plane (Fig. 5.15a, right), the wake seems to almost follow the shape of the hill, with the maximum deficit maintained at the centre of the wake. This behaviour is different in the other two cases (Figs. 5.15b and 5.15c), where the wake is spread more at higher turbulence, both vertically and laterally.

An important observation is the creation of two high-deficit regions: one in the near wake, as expected, and another in the far wake, as found in Sec. 5.4.1. In the high inlet turbulence case (Fig. 5.15c, left), the second region of high deficit

is wider and closer to the rotor (starting at $x \approx 12$ D); it is also the region with the highest deficit (instead of the near wake region). As it shown in Figs. 5.15b and 5.15c (right), this region is attached to the ground. Figs. 5.15b and 5.15c (left) also confirm the appearance of the wake 'drift' responsible for the lateral shift of the second maximum deficit region towards the negative y-direction.

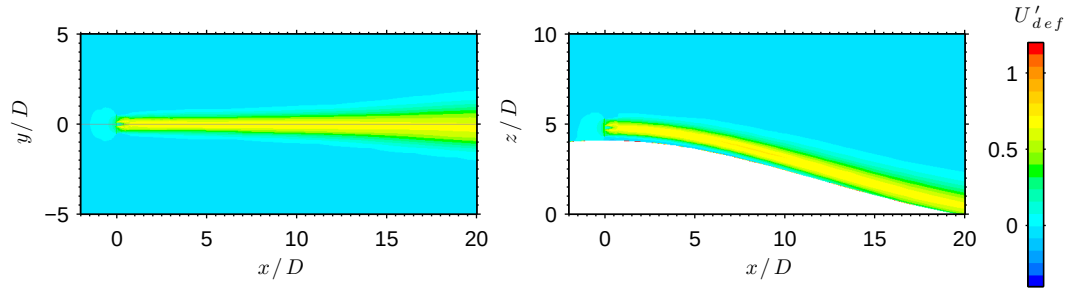

(a) $I_{in} = 5\%$

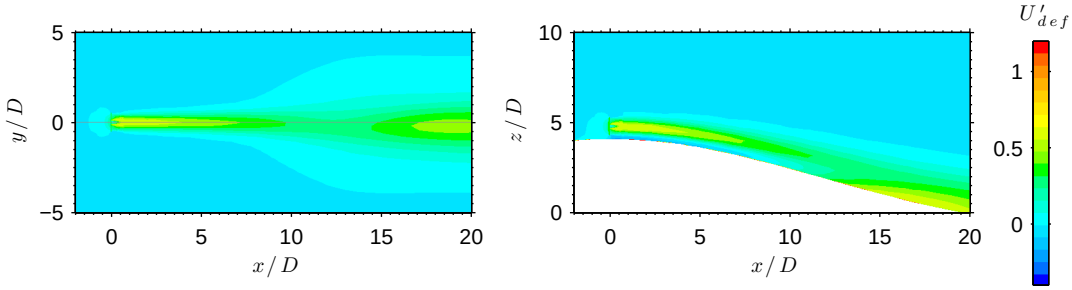

(b) $I_{in} = 13\%$

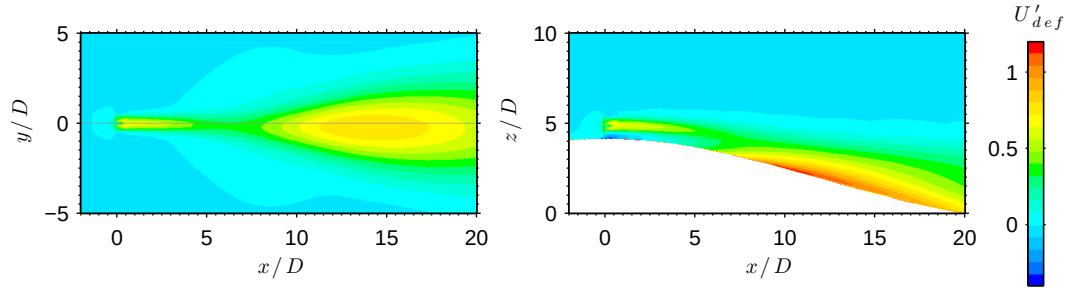

(c) $I_{in} = 20\%$

Figure 5.15. Contours of velocity deficit

5.4.5 Wake drift

The high-turbulence case ($I_{in} = 20\%$) was selected to further examine the development of the wake drift, as it was more pronounced in that case. Fig. 5.16 shows the contours of normalised velocity (horizontal u_x and vertical u_z). In a similar approach to Eq. (5.3), the vertical velocity U_z was normalised using the velocity at the top:

$$u_z = \frac{U_z}{U_{top}} \tag{5.8}$$

According to Fig. 5.16b (right), the hill slope causes the wind to flow downwards, especially between 5 and 10 D downstream of the hilltop. Fig. 5.16b (left) shows that the wake rotation causes the wake vertical velocity to be higher (more negative) for $y > 0$; this results in a vertical flow acceleration on this side. However, for $y < 0$ the vertical flow is decelerated, as the upwards movement caused by the rotor rotation is opposed to the downwards movement of the flow at the lee side of the hill. This may be contributing to the wake 'drift', as the vertical velocity becomes a streamwise component of the velocity at the lee side of the hill.

Fig. 5.17 shows the contours of pressure (static and total). The total pressure ($p_\circ$) was calculated as:

$$p_\circ = p + \frac{1}{2}\rho U^2 \tag{5.9}$$

where p is the static pressure.

Static pressure is low at the hilltop (where there is a speed-up) but the presence of the wind turbine creates an additional pressure drop (Fig. 5.17a). At the lee side of the hill, static pressure is increasing as velocity is reduced. However, a wake region of lower static pressure is maintained, even at 20 D downwind of the

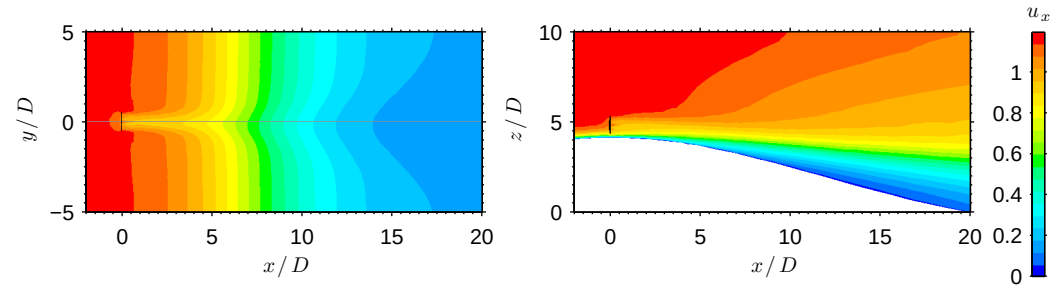

(a) Normalised horizontal velocity

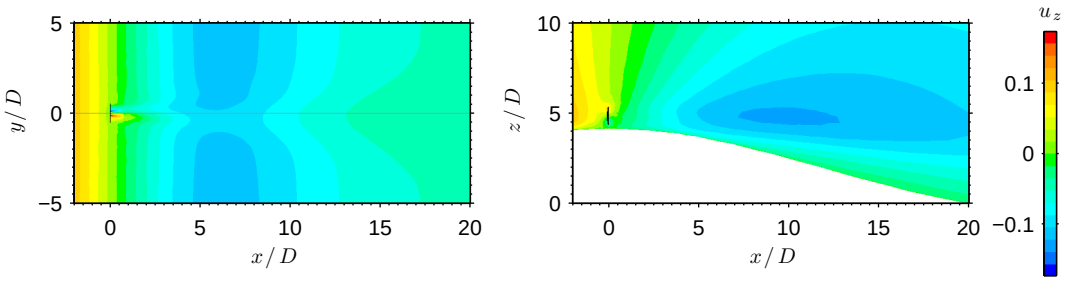

(b) Normalised vertical velocity

Figure 5.16. Contours of normalised velocity for $I_{in} = 20\%$.

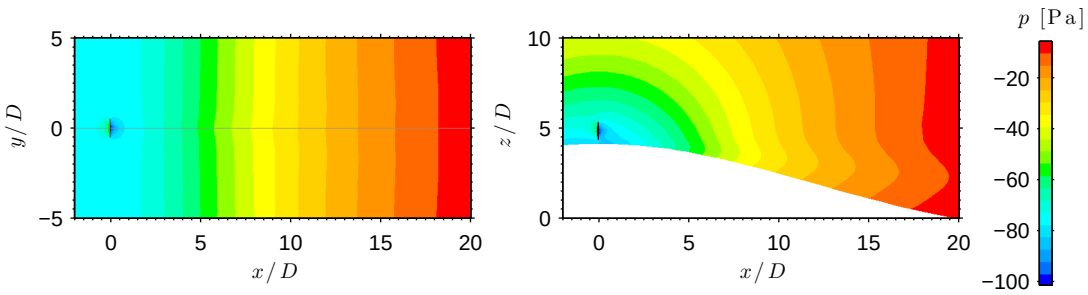

(a) Static pressure

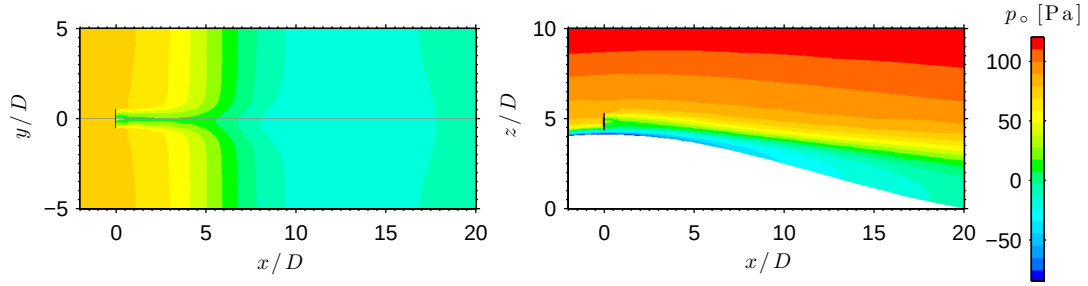

(b) Total pressure

Figure 5.17. Contours of pressure for $I_{in} = 20\%$.

hilltop. The drop of total pressure in the wake (Fig. 5.17b) is mainly due to the drop of velocity at the lee side of the hill.

The contours of x-vorticity (ξ_x) and y-vorticity (ξ_y) are shown in Fig. 5.18. The x-vorticity is related to the rotation of the wind turbine and it is present up to 5 D downwind of the rotor (Fig. 5.18a). The y-vorticity is caused by the hill slope and it is maximised between 6–9 D at hub height (Fig. 5.18b). It is shown that the operation of the rotor reduces the y-vorticity downwind (Fig. 5.18b, left).

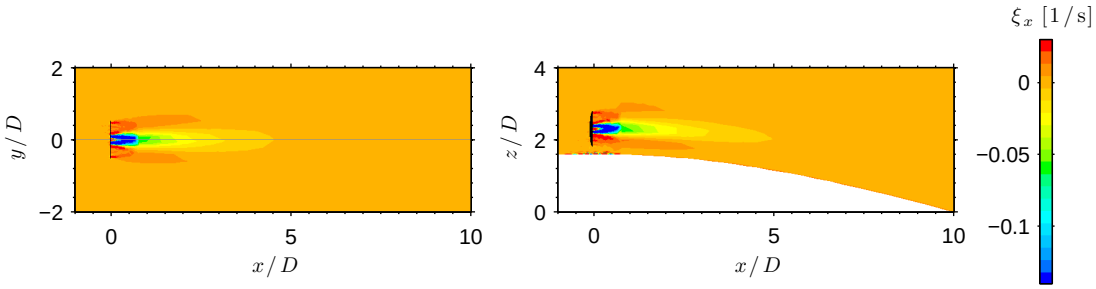

(a) x-vorticity

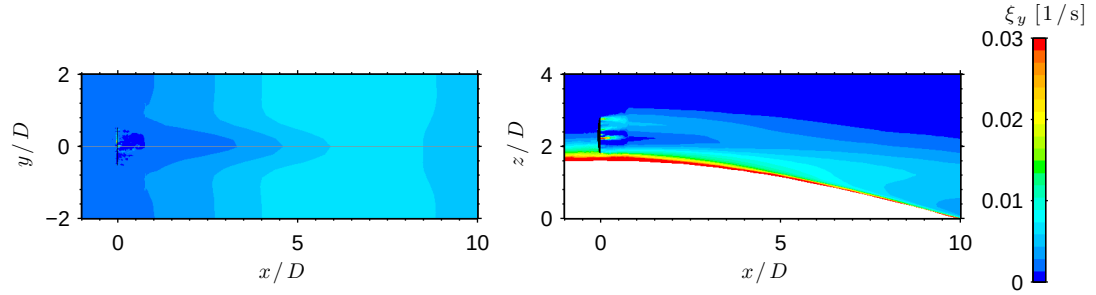

(b) y-vorticity

Figure 5.18. Contours of vorticity for $I_{in} = 20\%$.

Fig. 5.19 shows the results of the normalised horizontal velocity (u_x) in the yz plane at 6 different positions (x/D = 0, 0.5, 1, 3, 5, 8) facing towards the flow direction (positive x). The vectors in the figure represent the in-plane velocity. The flow becomes highly rotational in the near wake ($x = 0 - 1$ D), as the air rotates in the opposite direction from the rotor rotational direction, due to the reaction torque imposed by the rotor (Sec. 2.3.1). After $x/D = 3$, there is a downwards movement of the air, due to the hill slope, while wind shear is

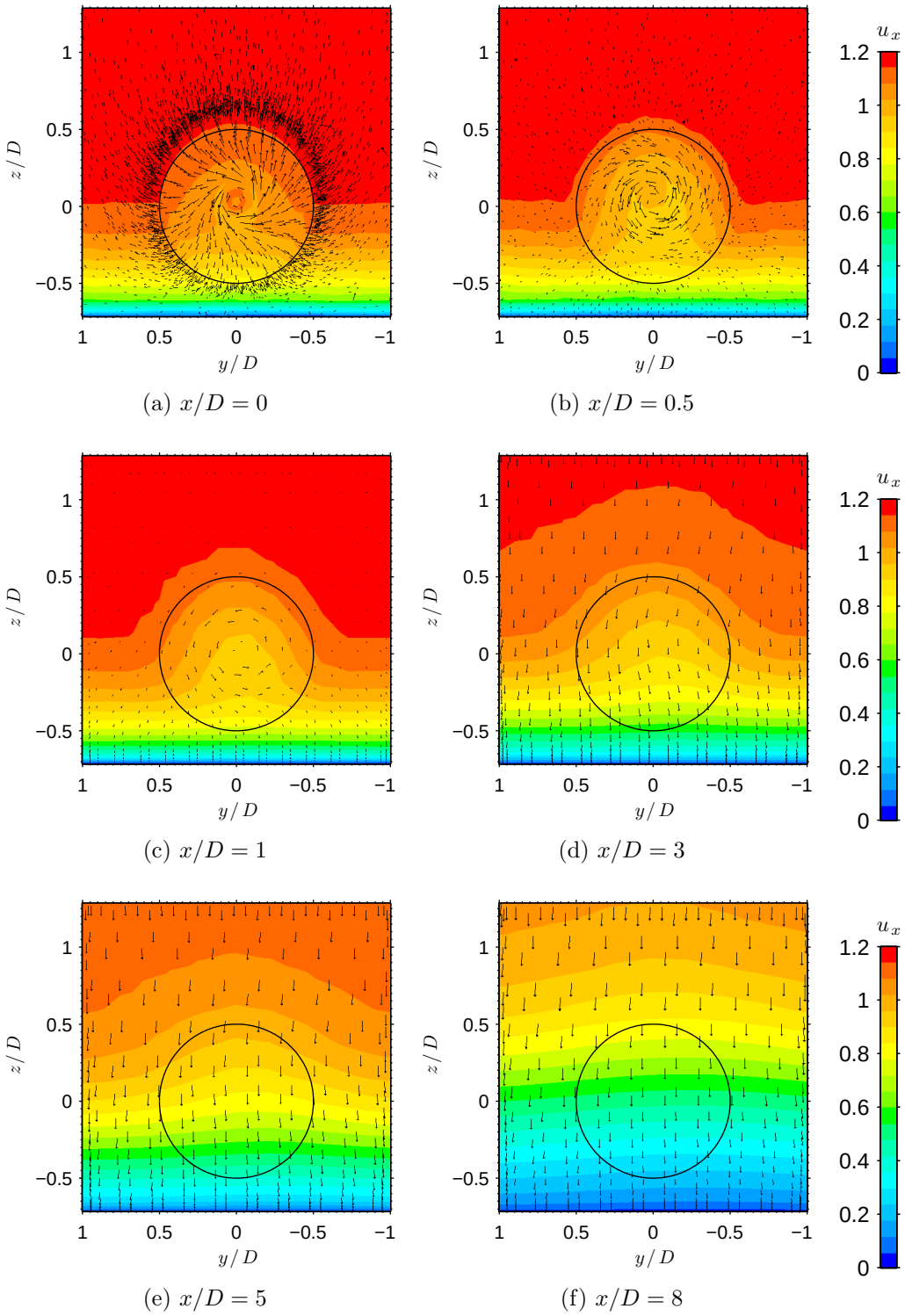

(a) $x/D = 0$ (b) $x/D = 0.5$

(c) $x/D = 1$ (d) $x/D = 3$

(e) $x/D = 5$ (f) $x/D = 8$

Figure 5.19. Contours at yz plane of u_x for $I_{in} = 20\%$

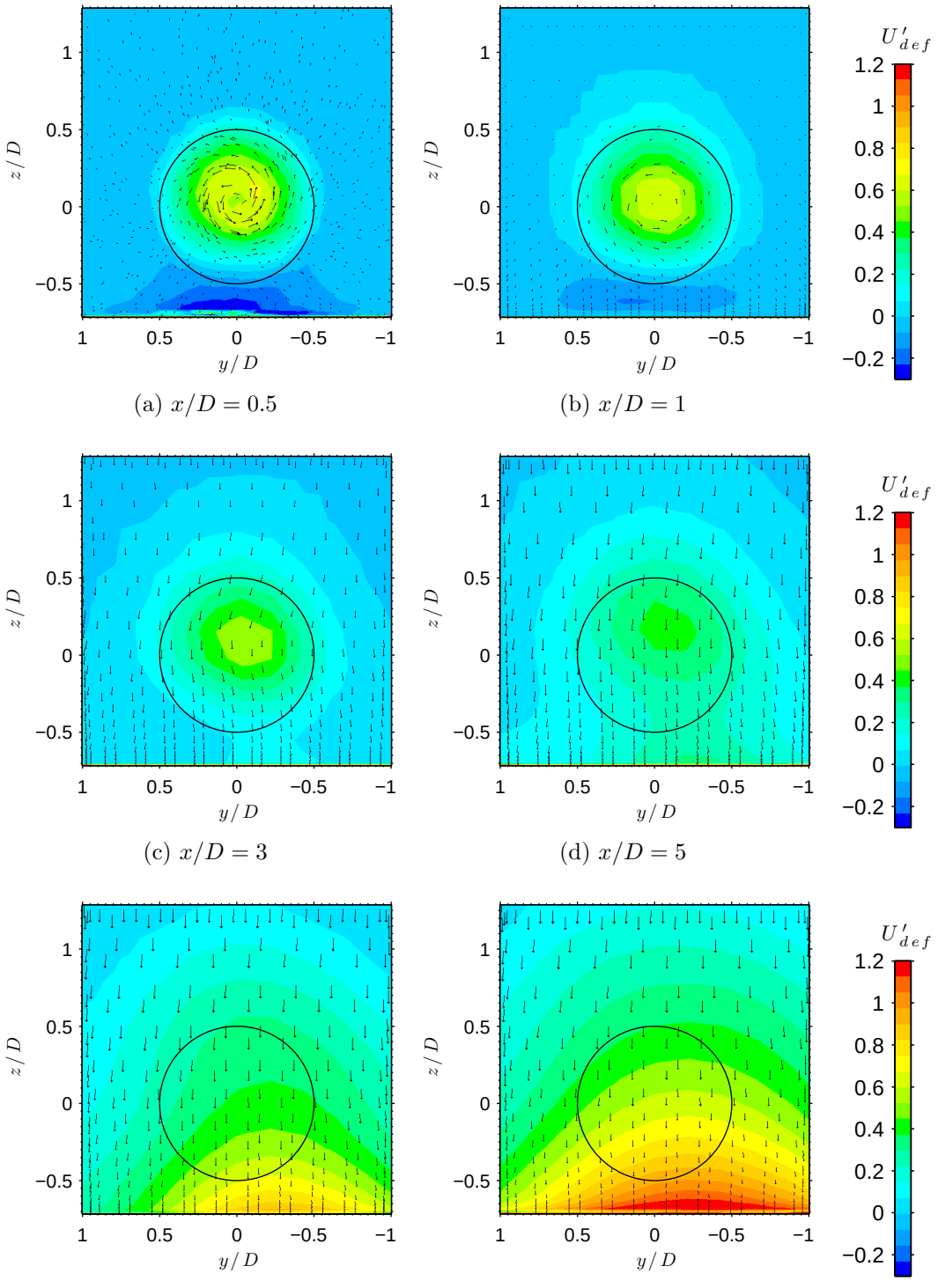

(a) $x/D = 0.5$ (b) $x/D = 1$

(c) $x/D = 3$ (d) $x/D = 5$

(e) $x/D = 8$ (f) $x/D = 10$

Figure 5.20. Contours at yz plane of U'_{def} for $I_{in} = 20\%$

increased, as there is an increasing region of low velocity near the ground. As a result of the combination of rotational flow and high wind shear, low velocity wind below hub-height moves downwards and towards $y < 0$, whereas higher velocity wind above hub-height moves downwards, but towards $y > 0$.

The wake 'drift' is clearer in Fig. 5.20, where the velocity deficit, U'_{def}, is examined in the yz plane and at 6 downstream positions ($x/D = 0.5$, 1, 3, 5, 8 and 10). At $x = 0.5-1$ D, the deficit is nearly symmetrical. However, for $x = 3-5$ D, the wake deficit diverges above the turbine axis and towards $y < 0$. At $x = 8 - 10$ D, the flow is highly decelerated near the ground which is also where the maximum deficit is located. At $x = 8$ and 10 D, the wake centreline was moved at approximately $y = -0.25$ D.

5.5 Double wake over the hill

Finally, the wake interaction of two rotors identical to the machine used at the single wake study was considered. The machines were placed at the hilltop ($x = 0$) at a spacing of 2 D ($y_{\mathrm{WT1}} = 1$ D and $y_{\mathrm{WT2}} = -1$ D) using the same boundary conditions as in the single wake case and $I_{in} = 13\%$. The corresponding flat terrain case with the same spacing was also considered for comparison in the same way as in the single wake case. The velocity deficit was calculated according to Eq. (5.6) with C_T found from Eq. (5.7), and the results for each case are shown in Table 5.8.

Table 5.8. Reference velocities and C_T for the case of two rotors.

Boundary Conditions		Gaussian hill (2 rotors)			Flat terrain (2 rotors)		
I_{in}	U_{top} (m/s)	$U_{\infty,hub}/U_{top}$	C_T	Ω (rpm)	$U_{\infty,hub}/U_{top}$	C_T	Ω (rpm)
13%	12.25	1.24	0.288	12.1	0.81	0.590	11.4

Fig. 5.21 shows the comparison of the lateral wake deficit between the hill and

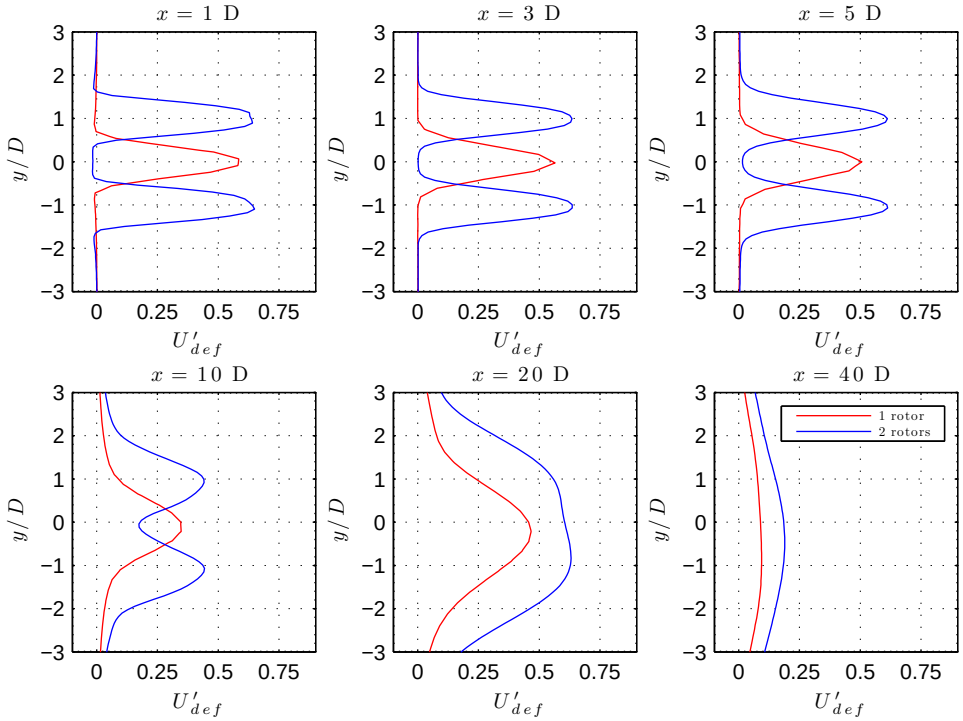

(a) Gaussian hill

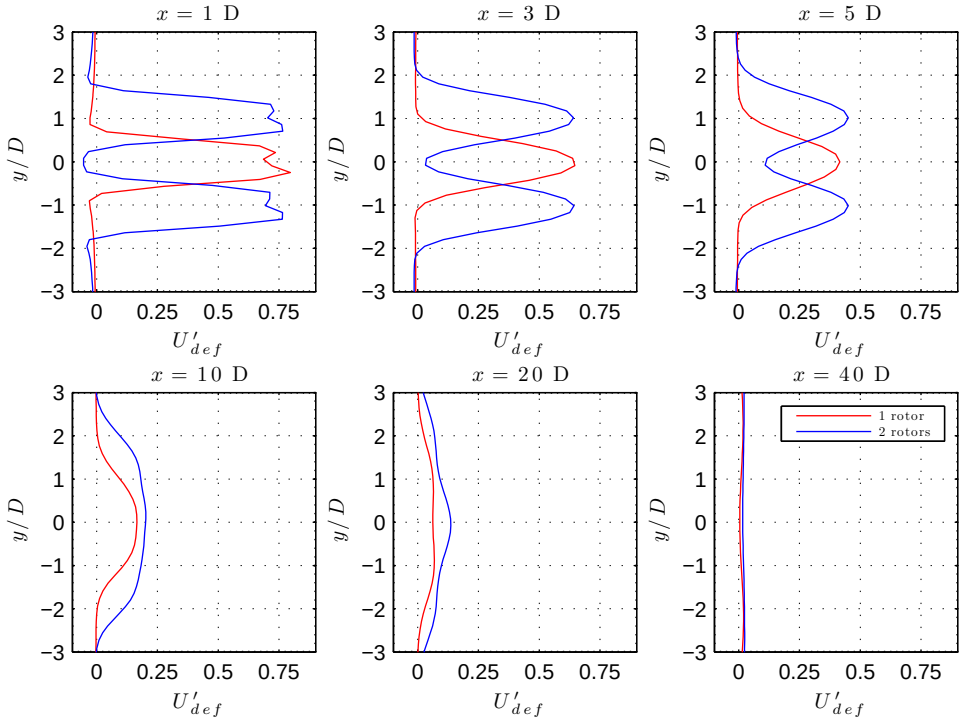

(b) Flat terrain

Figure 5.21. Comparison of lateral U'_{def} of 2 rotors between hilly and flat terrain for $I_{in} = 13\%$.

the flat terrain case, with the rotors being placed at $y = 1$ D and $y = -1$ D. The one-rotor simulations are also shown for comparison.

At $x = 1$ D the double and single wakes are almost identical in both cases (flat terrain and Gaussian hill). However, further downwind, it is clear that the combined wake decays slower than the single wake; this effect is more pronounced in the hill case. In the two-rotor simulation, the wakes seem to merge earlier in the flat terrain case at $x = 10$ D, as opposed to $x = 20$ D in the hill case. At $x = 20$ D of the hill case, the wake 'drift' is also visible as the two wakes are merged.

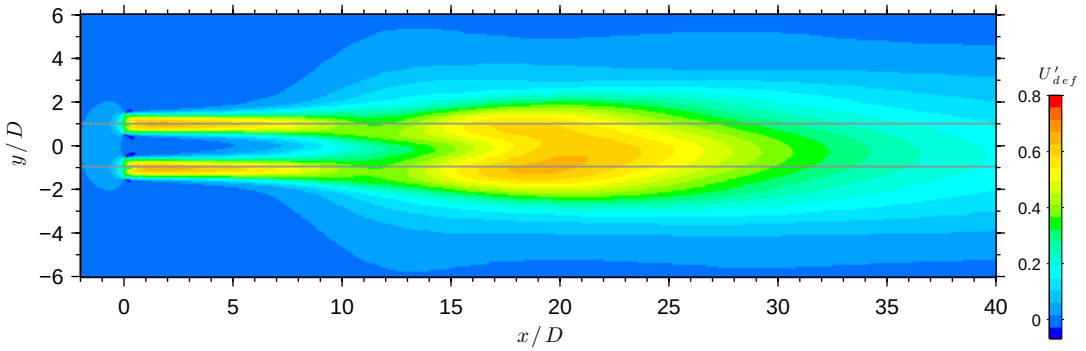

(a) Gaussian hill

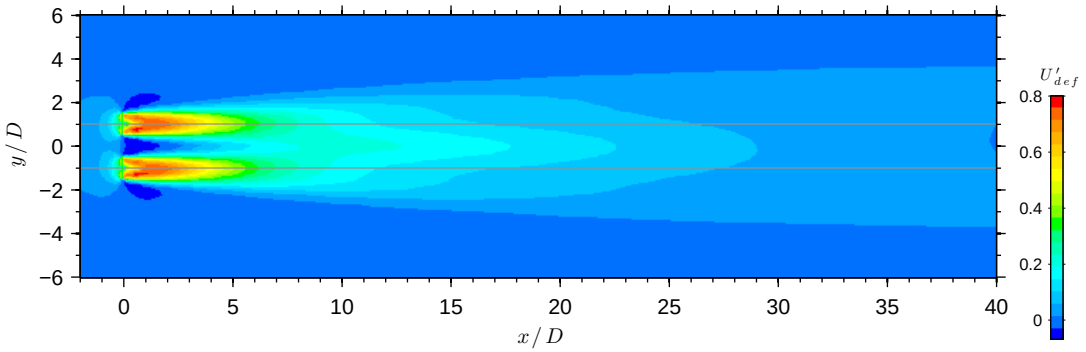

(b) Flat terrain

Figure 5.22. Contours of U'_{def} at hub-height: 2 rotors, $I_{in} = 13\%$.

Fig. 5.22 shows the contours of U'_{def} at hub-height, for both the hill and flat terrain case. Over complex terrain (Fig. 5.21a), the two wakes seem to merge at $x = 20$ D (Fig. 5.22a), where there is a second peak of maximum velocity deficit. Further

downwind, the combined wake seems diverted from the $y = 0$ axis, a behaviour which may also be attributed to the interaction of rotation and complex terrain. At $x = 10$ D a lateral wake expansion is also noticeable. Over flat terrain, the wake merging seems to occur earlier, at approximately $x = 9$ D, although the combined wake is significantly low and it gradually diminishes (Fig. 5.22b), as the far wake asymmetries of the hill case do not appear in this case.

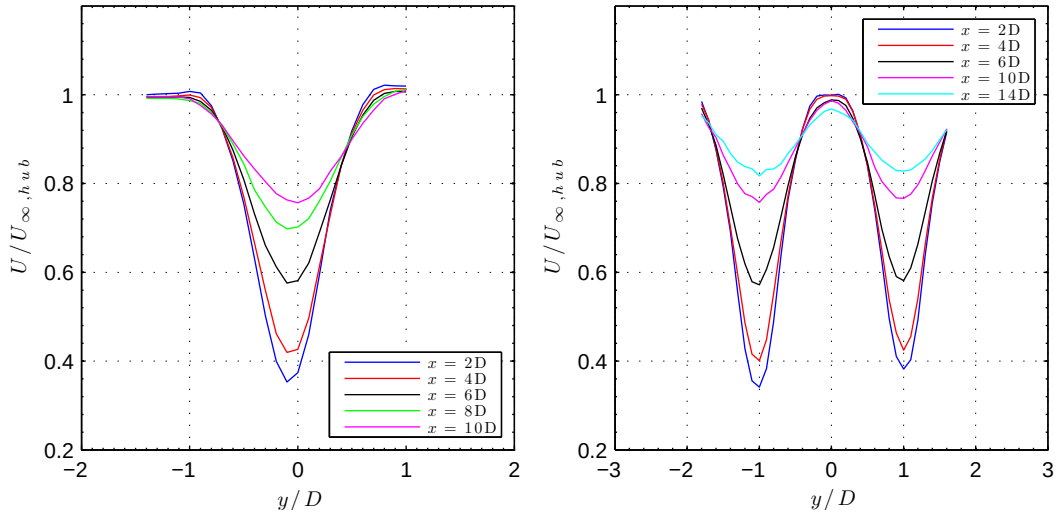

(a) Wind-tunnel measurements [35] ($I_{in} = 0.5\%$)

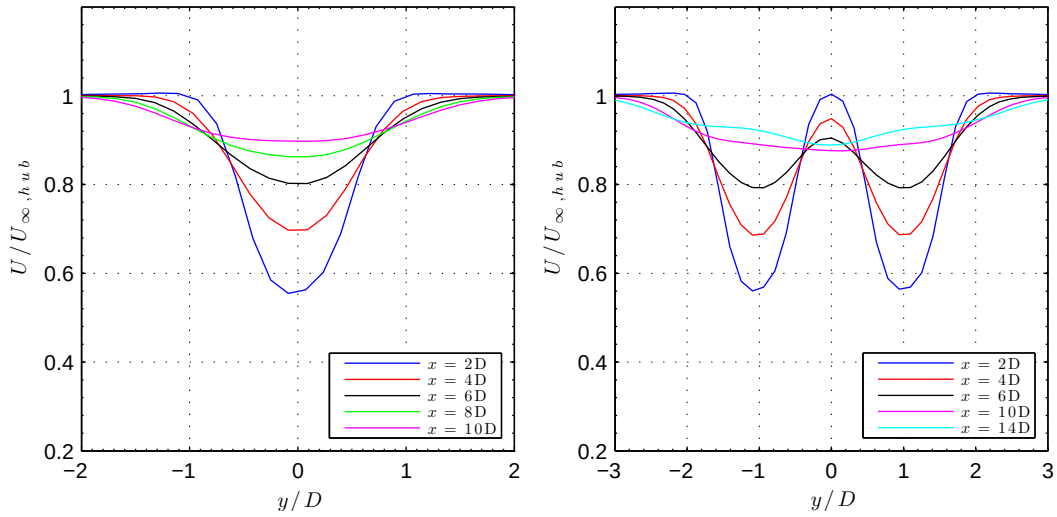

(b) CFD results ($I_{in} = 13\%$)

Figure 5.23. Comparison of single and double wake on flat terrain with measurements [35].

As mentioned in the literature review (Sec. 2.3.3), Alfredsson and Dahlberg [35] performed wind-tunnel measurements of single and double wakes over flat terrain. The double wake measurements involved two upstream rotors placed 2 D apart. The results (Fig. 5.23a) also indicated that the combined wake decays slower than the single wake. Fig. 5.23 shows the comparison with the CFD results (Fig. 5.23b), where wake recovery is faster due to the higher ambient turbulence ($I_{in} = 13\%$). The difference in the speed of wake recovery is more pronounced in the case of higher turbulence.

5.6 Concluding comments

The wake over an ideal hilly terrain was examined using the case of a 5 MW wind turbine operating at the top of a Gaussian hill at different ambient turbulence conditions. The streamwise, lateral and vertical wake developments were examined and compared with the wake of the identical rotor configuration, using the same inlet conditions over flat terrain. The results were in general good agreement with the CFD results of the UpWind project [200], although the different approach in the rotor modelling (VBM, including the rotational effects) as well as the use of a different turbulence model (RSM) were the main reasons for discrepancies.

Faster wake recovery and lower wake deficit were generally found with higher ambient turbulence intensity. A major discrepancy between the two different terrain configurations was that the wake did not dissipate monotonically in the hill case, especially at high ambient turbulence levels; the deficit exhibited a second peak in the far wake. In the high-turbulence case, this peak was higher than the near wake deficit. An increase of ambient turbulence in the hill case enhanced the lateral and vertical wake spread. A decrease of ambient turbulence led to a downshift displacement of the maximum deficit below the turbine axis,

while an increase of turbulence raised the maximum deficit above the turbine axis. The latter effect was more pronounced in the hill case. Another significant observation in the hill case, was a wake 'drift' from the straight streamwise path. Further examination of the wake 'drift' supported the suggestion that it is related to the combination of the rotation and terrain effects. The effect of the wake-added turbulence in the hill case was found to be small in comparison with the flat terrain case.

Finally, the combined wake of two rotors, placed 2 D apart facing the wind direction was examined over the hill and over flat terrain. A slower wake dissipation was found as compared to the single wake case, with the effects more pronounced in the hill case. Similarly to the single wake, the velocity deficit of the hill case appears to have a second peak of velocity deficit and this region was magnified in the combined wake. A wake 'drift' was also noticeable further downwind.

Chapter 6

Modelling of flow over Askervein hill

6.1 Introduction

In this Chapter, the neutral atmospheric flow over a real hill is modelled using CFD and results are validated with full-scale measurements. The examined terrain is the Askervein hill, a case used for the validation of several CFD modelling approaches in the past.

The Askervein Hill project was a well-documented field experimental study of the boundary-layer flow over a low hill performed during September–October 1982 and 1983 under international collaboration [114]. The Askervein Hill (57°11′N, 7°22′W) is a relatively isolated, 116 m high hill (h_{asl} = 126 m), located on the west coast of the island of South Uist, in the Outer Hebrides of Scotland. The Askervein experiments offered an extensive, full-scale dataset for studies of near-neutral atmospheric flow and turbulence over low hills [116]. A summary of some of the main CFD validation efforts using data from the Askervein Project is given in Sec. 2.4.1.

The Askervein hill and surrounding area are shown in Fig. 6.1. Upstream of Askervein hill towards South-West, there is a uniform and flat fetch extending 4 km to the coastline. Fig. 6.1 shows the hilltop (HT) and centre point (CP) of the hill, as well as the location of the Reference Site RS on the flat upwind fetch, about 3 km to the SSW of the hill. The field experiments were performed along lines A, AA (minor axes) and B (major axis) of Fig. 6.1 at a height of 10 m above the hill surface using several measuring devices. At HT and RS in particular, 50 m high towers were used to measure the wind profiles.

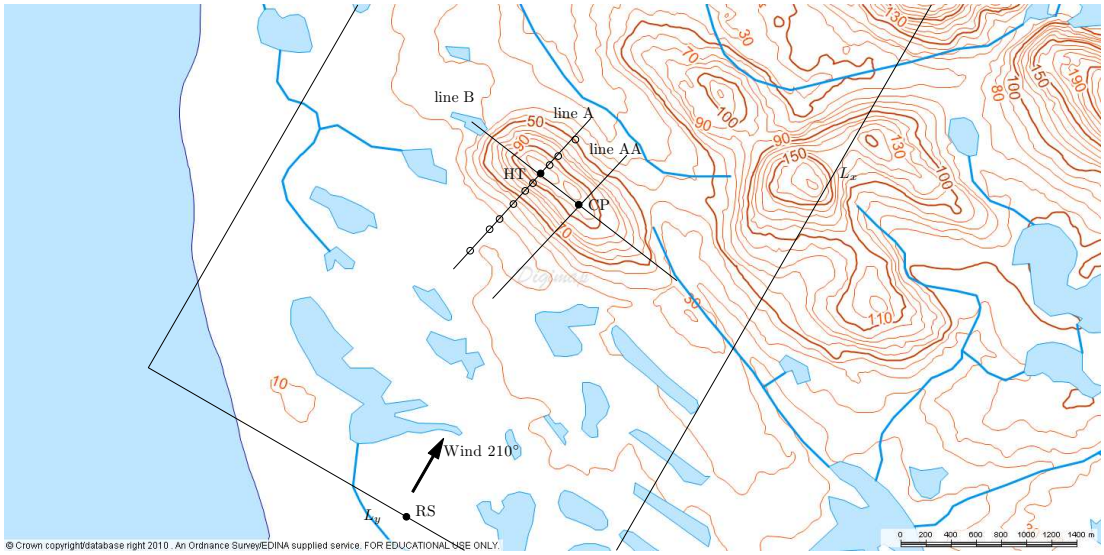

Figure 6.1. Askervein Hill and surrounding area (OS Meridian 2 and Panorama).

The field measurement run No. TU03-B which was performed on October 3rd, 1983 [113] provided the most commonly used dataset and was subsequently selected for the current study. It corresponds to nearly neutral atmospheric wind flow with a direction of 210° (Fig. 6.1), approximately perpendicular to the hill major axis (line B). For the selected wind direction, the hill's characteristic lengths are: $(h, L') \approx$(116 m,215 m) [262], where L' is a characteristic length of the hill defined in Sec. 5.2.1 and h is the hill height. Using Eq. (5.2), the corresponding effective slope is $s \approx 0.27$.

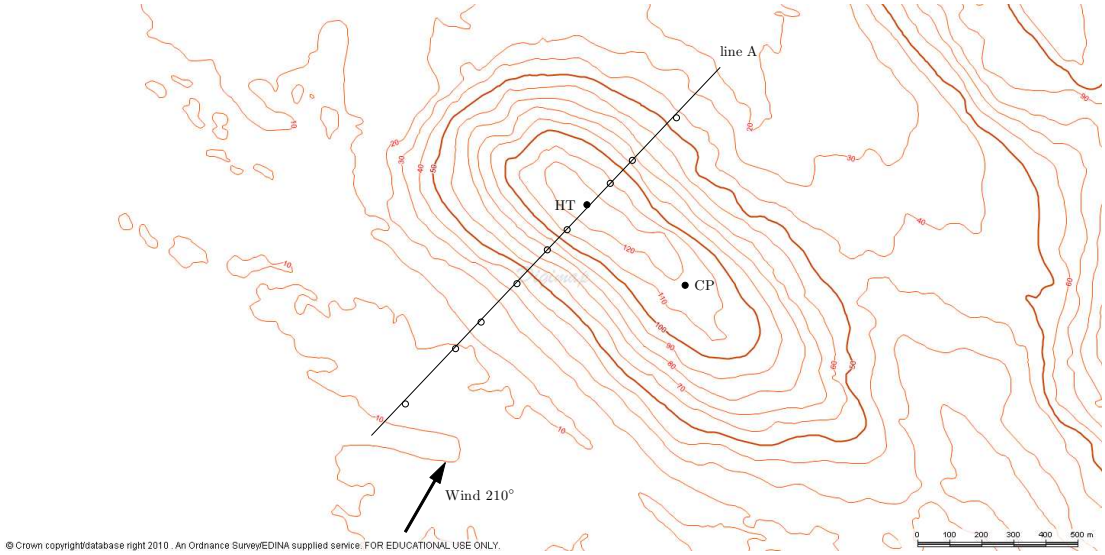

Figure 6.2. The Askervein Hill enlarged (OS Land-Form Profile).

6.2 Measurements

For the selected run TU03-B, the velocity and turbulence σ_u profiles were obtained at RS and HT using cup anemometers at towers 50 m high [113] and are shown in Table 6.1. The velocity profile at RS was used for the estimation of the inlet velocity profile, as described in Sec. 6.3, while the profiles at HT were used for validation of the velocity and turbulence results at the hilltop.

Table 6.1. Averaged data from AES CUP anem. at RS and HT, TU03-B.

Height [m]	Speed(RS) [m/s]	σ_u(RS) [m/s]	Speed(HT) [m/s]	σ_u(HT) [m/s]
3	7.10	1.42	15.71	1.45
5	7.86	1.37	16.38	1.38
8	8.44	1.42	16.30	1.17
15	9.35	1.27	16.63	1.04
24	10.19	1.23	16.15	1.19
34	10.84	1.16	15.77	1.17

(extracted from Table A1.7 of Taylor and Teunissen [113])

The main validation of the results was performed with the measured data from vertical Gill UVW anemometers positioned at $z_{agl} = 10$ m across line A using

information from run TU03-B [113]. The relative measurement locations are shown in the enlarged map of the Askervein, in Fig. 6.2.

Table 6.2. Averaged data from Gill UVW anem. at $z_{agl} = 10$ m, TU03-B.

Dist. from HT [m]	Speed [m/s]	σ_u [m/s]	σ_v [m/s]	σ_w [m/s]	$\overline{u'v'}$ [m^2/s^2]	$\overline{u'w'}$ [m^2/s^2]	$\overline{v'w'}$ [m^2/s^2]
RS	8.6	1.223	0.704	0.413	0.135	−0.247	−0.013
−850	7.8	1.200	0.762	0.463	0.007	−0.239	0.002
−600	7.8	1.379	0.893	0.421	0.154	−0.218	−0.006
−500	6.7	1.350	0.683	0.475	0.099	−0.272	0.015
−350	7.2	1.243	1.038	0.580	0.042	−0.351	−0.033
−200	10.5	1.115	1.126	0.565	0.032	−0.287	−0.004
−100	13.2	1.059	1.232	0.577	0.098	−0.243	−0.049
HT	16.2	1.100	1.034	0.577	0.189	−0.153	0.031
100	12.0	1.758	1.012	0.531	−0.004	−0.241	0.056
200	5.6	2.560	1.502	0.881	−1.431	−0.560	0.206
400	3.0	1.983	1.798	1.192	−0.275	0.694	0.459

(extracted from Table A1.3 of Taylor and Teunissen [113])

An overview of the results along line A is shown in Table 6.2, rows 2–10, while the first column denotes the distance of each measurement location from the hilltop HT. The data from RS are also shown, as the site is chosen to be the reference site for the presentation of the measured results on all the flow locations.

6.3 CFD approach

The CFD approach involved the use of the RANS equations and a Reynolds Stress Model closure along with the pressure-based solver in FLUENT. Pressure-velocity coupling was carried out with the SIMPLEC algorithm and spatial discretisation was Second Order Upwind for Momentum, Turbulent Kinetic Energy, Turbulent Dissipation Rate and Reynolds Stresses while gradients were computed using the Green-Gauss Node-Based method.

The approach for modelling the neutral ABL flow was previously described in

Sec. 3.3 and tested over a flat terrain in Sec. 4.1. Here, particular consideration was taken to create the real complex terrain ground wall surface.

6.3.1 Wall surface creation

An important aspect of the modeling procedure was related to the creation of a wall surface representative of the site elevation and terrain complexities, as explained in Sec. 3.4. Information on ground surface elevation was initially retrieved from the Ordnance Survey Land-Form PROFILE DTM Data file which corresponded to the area. The data file was then converted from the $*$.ntf into an $*$.xyz grid point data file using NTFtoXYZ, a DOS program for converting Ordnance Survey NTF Panorama or Profile Digital Terrain Model (DTM) files to Visual Explorer XYZ format.

The $*$.xyz file consisted of comma-delimited data of (x, y, $z_{a.s.l.}$), where x and y were Ordnance Survey coordinates (first two columns) and $z_{a.s.l.}$ was elevation above sea level (third column) for each of the grid points. The grid points covered an area of 10 km $\times$ 5 km around the site with a 10 m resolution and a total number of $501,501$ grid points. After some modifications, the data file was imported into RHINO, a NURBS-based 3-D modelling software, using the SrfControlPtGrid command to create a surface from the grid points. The created surface was afterwards saved in an $*$.sat ACIS format which is readable in GAMBIT, the preprocessor of FLUENT.

6.3.2 Domain and Meshing

The domain was rotated and the Cartesian x-direction was aligned with the flow direction, as shown in Fig. 6.1, while taking into account the map extension orography. The Cartesian dimensions were (L_x, L_y, L_z) = (8000 m, 4000 m,

2500 m) having positioned the RS location at $x = 0$ and the hilltop location at $y = 2000$ m (Fig. 6.1).

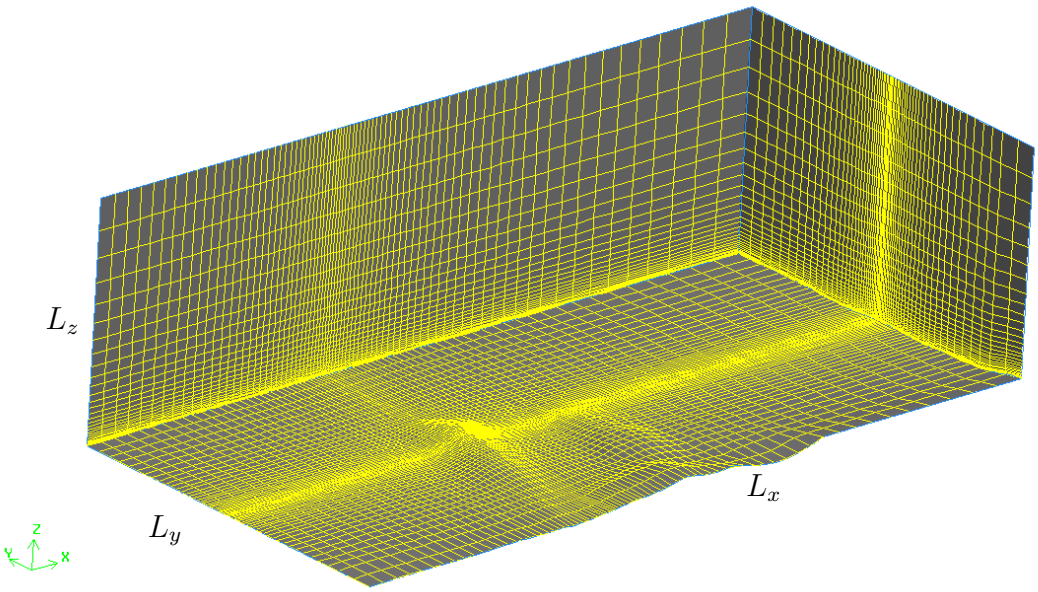

Figure 6.3. The Askervein Hill CFD domain and mesh.

The total number of cells was $N_{tot} = 156,940$, with $(N_x, N_y, N_z) = (76, 59, 35)$ cells at each of the Cartesian directions. The height of the first cell was $z_P = 1$ m, with the mesh density gradually decreasing away from the ground and the hill centreline, as shown in Fig. 6.3.

6.3.3 Boundary Conditions

The Boundary Conditions were chosen according to the procedure described in Sec. 3.5 for a complex terrain.

The inlet plane was chosen to have the same x Cartesian coordinate with the reference site RS (Fig. 6.1) and the inlet flow profiles were chosen taking into account the AES cup anemometer measurements at the 50 m-high tower on RS for the TU03-B run (Table 6.1, taken by Table A1.7 of Taylor and Teunissen [113]).

The inlet velocity profile was chosen to be logarithmic, according to Eq. (3.23) using a roughness length of $z_\circ = 0.03$ m as a single representative value, recommended in the literature [114]. The measured wind speed at RS was fitted with the logarithmic expression of Eq. (3.23) obtaining a friction velocity u_* value of 0.625 m/s. At the top cells, velocity was fixed according to Eq. (3.23) using $z = h_{abl} = 500$ m.

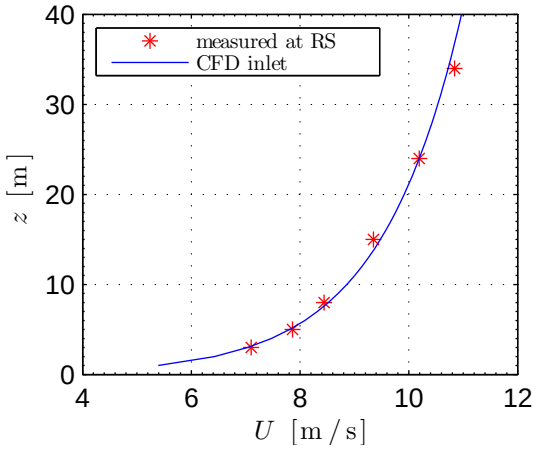

Figure 6.4. Velocity inlet CFD profile and measured at RS.

The normal Reynolds Stresses inlet values ($\overline{u'u'}_{in}$, $\overline{v'v'}_{in}$ and $\overline{w'w'}_{in}$) as well as $\overline{u'v'}_{in}$ and $\overline{v'w'}_{in}$ were chosen according to the values measured at RS (Table 6.2) and the inlet turbulent kinetic energy was derived using Eq. (3.20). The inlet Reynolds shear Stress profile $\overline{u'w'}_{in}$ was taken according to Eq. (3.26). The modifications to the standard wall functions, described in Sec. 3.4.2 were used at the ground wall with $z_\circ = 0.03$ m.

6.4 Results

A precondition for the successful implementation of the wall function modifications of Sec. 3.4.2, is the application of the logarithmic law of the wall, which occurs when $y^* > 11.225$ (Sec.3.4.1). To test if such a condition is maintained,

the y^* values are plotted in Fig. 6.5. The values are very high, confirming that the correct equations were employed for the successful implementation of the modified wall function.

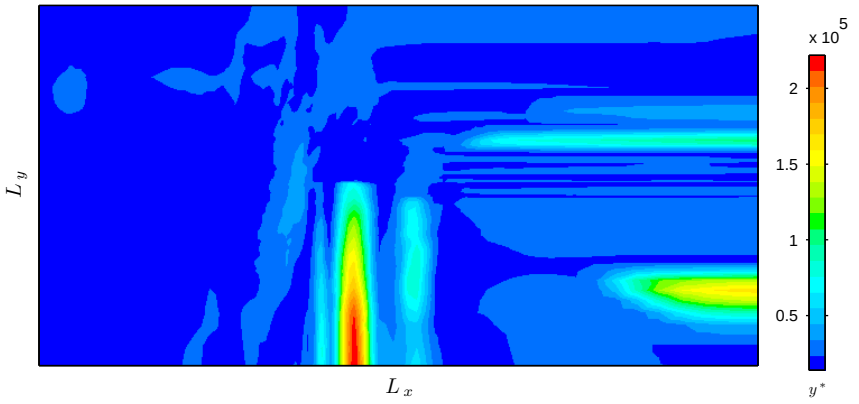

Figure 6.5. Contours of y^* values.

The CFD inlet velocity profile matched to the cup anemometer measurements at RS (Fig. 6.4), was additionally used to obtain the reference velocity at $z_{agl} = 10$ m for the CFD results. It should be noted, that some divergence between the reference velocity values at $z_{RS,agl} = 10$ m between the measurements and the CFD results is to be expected, since Table 6.2 involves measurements from Gill UVW anemometers, whereas the data in Fig. 6.4 were measured with AES cup anemometers. The CFD reference velocity at $z_{RS,agl} = 10$ m was 8.98 m/s, slightly higher than the 8.6 m/s value in Table 6.2.

Velocity was normalised according to Eq. (6.1), where z_{agl} is the local height above ground level. Another commonly used mean of presenting the velocity variation, is the introduction of the non-dimensional velocity increase in Eq. (6.2).

$$u = \frac{U(z_{agl})}{U_{ref}(z_{agl})} \tag{6.1}$$

$$\Delta S = \frac{U(z_{agl}) - U_{ref}(z_{agl})}{U_{ref}(z_{agl})} \tag{6.2}$$

The local turbulent kinetic energy k was also non-dimensionalised in the results with the local wind velocity $U(z_{agl})$, as shown in Eq. (6.3), while the normalised turbulence k increase with reference to the RS k value was also considered, as in Eq. (6.4).

$$k^* = \frac{k(z_{agl})}{U^2(z_{agl})} \tag{6.3}$$

$$\Delta k = \frac{k(z_{agl}) - k_{ref}(z_{agl})}{k_{ref}(z_{agl})} \tag{6.4}$$

The standard deviations of velocity σ_i at each Cartesian direction i were also normalised with the local velocity at each location, providing the turbulence intensity I_i at the specified direction, according to Eq. (6.5).

$$I_i = \frac{\sigma_i(z_{agl})}{U(z_{agl})} \tag{6.5}$$

where $i = u, v$ or w.

6.4.1 Results along line A

The results of the validation with velocity measurements along line A (Table 6.2) are presented in Fig. 6.6. Agreement is good upstream and downstream of HT, but the highest discrepancies are found at HT, where the model predicts a lower maximum velocity increase.

Similar discrepancies at HT have been observed using other CFD models, such as [126, 127, 143, 147]. The difference may be related to the fact that the model assumes a constant, uniform roughness length $z_\circ$, which is an approximation. Zeman and Jensen [105] observed that the area near the hilltop is smoother than the rest of the hill surface and assumed in their calculations that the roughness length decreased over the last 100 m of elevation to the hilltop.

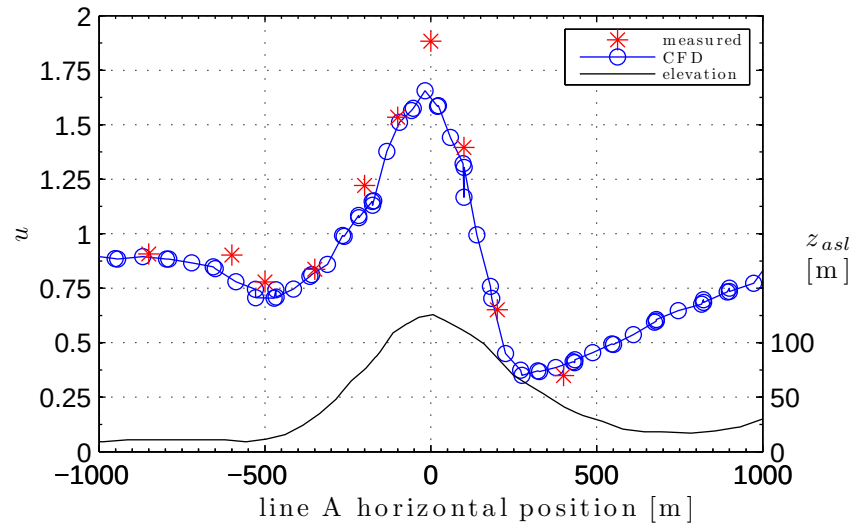

(a) Normalised velocity

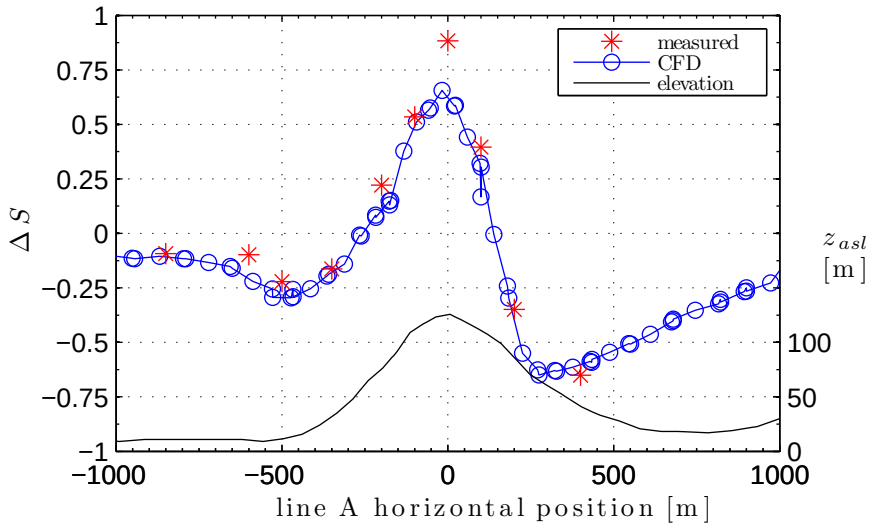

(b) Normalised velocity increase

Figure 6.6. Velocity results comparison.

Results of turbulent kinetic energy k expressed as k^* and Δk are shown in Fig. 6.7a and 6.7b respectively. According to Fig. 6.7a the CFD prediction is very good on all locations, apart from the $x = 400$ m downstream of the hilltop, where predicted k^* is well-below the measured value. According to Fig. 6.7b, CFD overpredicts Δk upstream of the hilltop and it underpredicts the downstream values. The best match is located near the hilltop and 100 m downstream, whereas the largest discrepancy is located 400 m downstream. The results are comparable to other

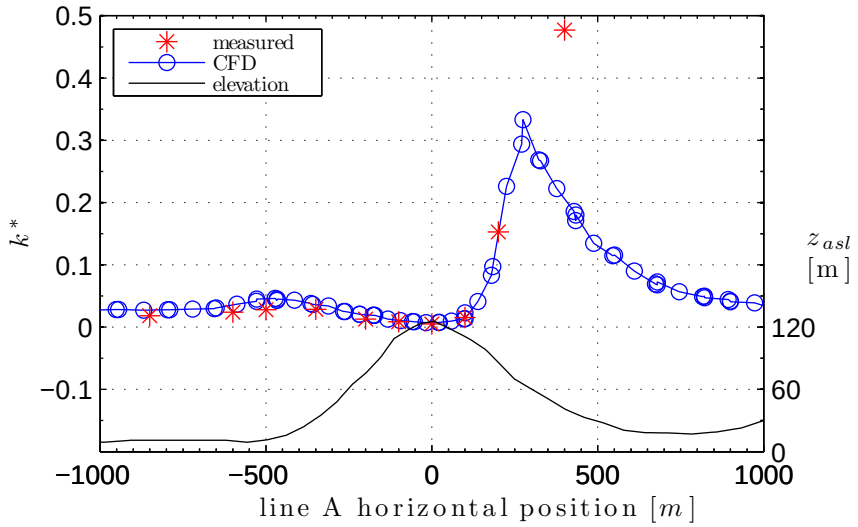

(a) Normalised k

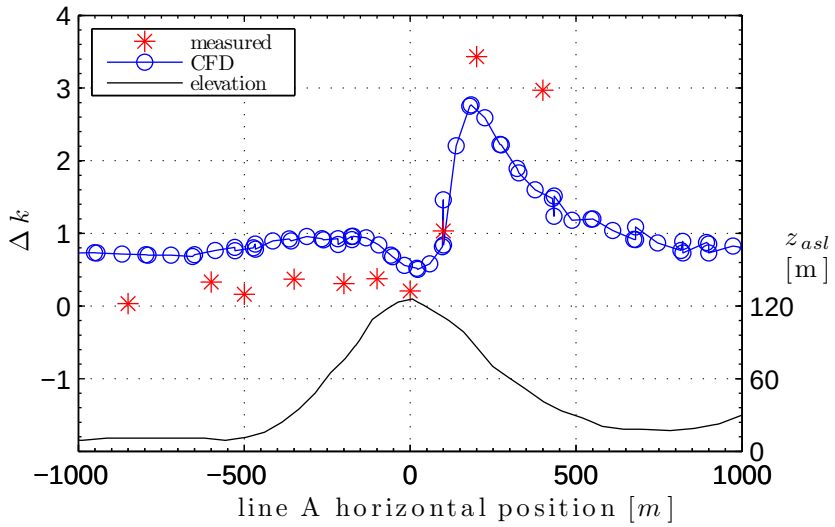

(b) Normalised k increase

Figure 6.7. Turbulence k comparison.

CFD modeling observations, such as [126–128, 139, 142, 145, 147], especially in terms of the underprediction of the turbulent kinetic energy in the lee side of the hill. However, the RSM seems to perform better than the more common two-equation models [145].

The local turbulence intensity calculated in each direction according to Eq. (6.5) is also compared in Fig. 6.8, where σ_u, σ_v and σ_w are the standard deviations

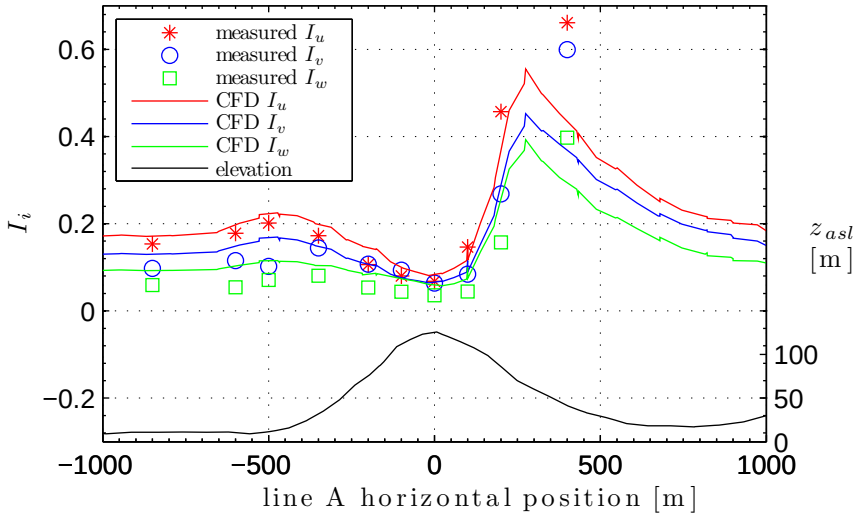

Figure 6.8. Turbulence Intensity comparison.

of velocity at the x, y and z Cartesian direction respectively. According to the Figure, the CFD prediction is good upstream and, especially, near the hilltop. However, at $x = 400$ m downstream, the prediction of turbulence intensity is lower than the measured values, especially towards the x and y directions.

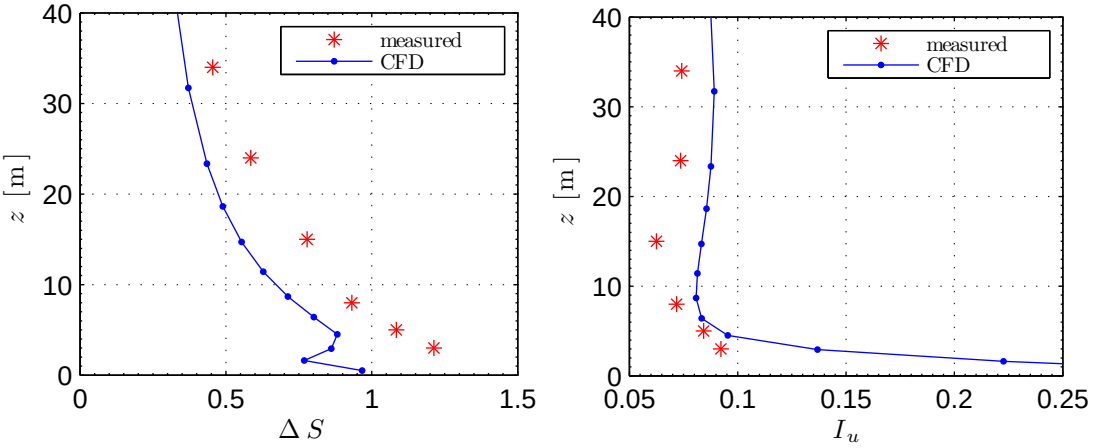

(a) Velocity increase (b) Turbulence Intensity

Figure 6.9. Comparison at hilltop (HT).

6.4.2 Results at hilltop

The hilltop wind profile was also examined in comparison with the measurements from the AES CUP anemometers, shown in Table 6.1. The predicted velocity increase ΔS is significantly lower than the measured values, especially near the ground (Fig. 6.9a). The turbulence intensity results however are satisfactory near the ground and higher than the measurements, suggesting that the real roughness length value near the hilltop is lower than the assumed $z_\circ = 0.03$ m.

Chapter 7

Modelling of flow over forest

7.1 Introduction

This Chapter describes the approach of modelling the flow near forest canopies, which is later applied in Chapter 9 to model the effects of forests on the wind turbine wakes. The details of the canopy model and the various necessary modifications to allow for the use of RSM are initially analysed. The results of the simulation over a simple canopy over flat terrain are then validated with full scale measurements.

7.2 Modified canopy model based on RSM

The applied 3-D canopy model is based on a procedure following Sanz [164] and Lopes da Costa [171]. In the turbulence sources, an isotropic partition of the wake turbulence production term as well as an anisotropic partition of the dissipation term was considered, as suggested by Ayotte et al. [179]. Certain considerations of the Dalpé and Masson approach [170] were also taken into account.

7.2.1 Source terms

Following the approach of Dalpé and Masson [170] in FLUENT, the forest is modelled as a porous medium and a negative source term, $S_{u,i}$, was added into the momentum equations, Eq. (3.5b). In this case, the momentum sink term $S_{u,i}$ expresses the momentum absorbed in the forest in the i direction and it is calculated according to Eq. (7.1):

$$S_{u,i} = -\rho\, C_d\, \alpha\, U\, U_i \tag{7.1}$$

where ρ is the density of air, C_d is the forest drag coefficient, α is the leaf area density, U is the wind velocity magnitude and U_i is the wind velocity at the i direction. The leaf area density is height-dependent and it is defined as the leaf area at a specific level per unit volume of canopy.

Additionally to a momentum sink, the effect of the forest is also modelled in k-ε models by means of k and ε sources, S_k and S_ε, which are added to the k and ε equations respectively. Following Sanz [164], S_k and S_ε are calculated according to Eqs.(7.2) and (7.3) according to the suggestions of Green [162] and Liu et al. [163] respectively. The positive source terms in Eq. (7.2) represent the turbulent wake generation because of the vegetation elements breaking of the mean flow motion, whereas the negative (sink) terms express the wake dissipation due to the short-circuiting of the turbulence cascade [164].

$$S_k = \rho\, C_d\, \alpha(\beta_p\, U^3 - \beta_d\, k\, U) \tag{7.2}$$

$$S_\epsilon = \rho\, C_d\, \alpha\, \frac{\epsilon}{k}\, \left(C_{\epsilon 4}\, \beta_p\, U^3 - C_{\epsilon 5}\, \beta_d\, k\, U\right) \tag{7.3}$$

where β_p, β_d, $C_{\epsilon 4}$, $C_{\epsilon 5}$ are canopy model constants and their calculation is explained by Sanz [164].

In the current work and since the RSM is used, sources of normal Reynolds

Stresses are applied $S_{\overline{u_i' u_i'}}$ instead of S_k, while the ε source S_ε is maintained. Combining Eqs.(3.20) and (7.2), the sum of the normal Reynolds Stress sources can be expressed as:

$$S_{\overline{u'u'}} + S_{\overline{v'v'}} + S_{\overline{w'w'}} = \rho\, C_z \left[2\, \beta_p\, U^3 - \beta_d\, U \left(\overline{u'u'} + \overline{v'v'} + \overline{w'w'}\right)\right] \tag{7.4}$$

According to the approach of Ayotte et al. [179], turbulence within the canopy is close to being isotropic. For that reason, turbulence wake production, which is expressed by the positive term of Eq. (7.4), is partitioned isotropically. However, dissipation, which is expressed by the negative term of Eq. (7.4), acts anisotropically on the normal Reynolds Stresses diminishing the horizontal stress $\overline{u'u'}$ more than the other two ($\overline{v'v'}$ and $\overline{w'w'}$) in order to 'isotropise' turbulence.

According to the above approach a new dissipation coefficient for each of the normal Reynolds stresses ($\beta_{d,u}$, $\beta_{d,v}$, $\beta_{d,w}$) is introduced. Assuming an isotropic partition of the production term and anisotropic partition of the dissipation term [179], each of the source terms is modelled as:

$$S_{\overline{u'u'}} = \rho\, C_z \left[\frac{2}{3}\, \beta_p\, U^3 - \frac{1}{3}\, \beta_{d,u}\, U \, \left(\overline{u'u'} + \overline{v'v'} + \overline{w'w'}\right)\right] \tag{7.5}$$

$$S_{\overline{v'v'}} = \rho\, C_z \left[\frac{2}{3}\, \beta_p\, U^3 - \frac{1}{3}\, \beta_{d,v}\, U \, \left(\overline{u'u'} + \overline{v'v'} + \overline{w'w'}\right)\right] \tag{7.6}$$

$$S_{\overline{w'w'}} = \rho\, C_z \left[\frac{2}{3}\, \beta_p\, U^3 - \frac{1}{3}\, \beta_{d,w}\, U \, \left(\overline{u'u'} + \overline{v'v'} + \overline{w'w'}\right)\right] \tag{7.7}$$

7.2.2 Model constants

The procedure for calculating the canopy model constants is explained in Appendix B and it was based on the work of Sanz [164] and Lopes da Costa [171]. The resulting equations for each of the dissipation constants as a function of the

production coefficient β_p are shown in Eqs.(7.8)–(7.10).

$$\beta_d = \frac{3}{\sigma_k} + \left(\beta_p - \frac{C_2}{2}\right)\left(\frac{2}{\alpha'}\right)^{\frac{2}{3}}\sqrt{C_\mu} \tag{7.8}$$

$$\beta_{d,u} = \frac{3}{\sigma_k} + \left(\beta_p + 1 - \frac{3}{2}C_2\right)\left(\frac{2}{\alpha'}\right)^{\frac{2}{3}}\sqrt{C_\mu} \tag{7.9}$$

$$\beta_{d,v} = \beta_{d,w} = \frac{3}{\sigma_k} + \left(\beta_p - \frac{1}{2}\right)\left(\frac{2}{\alpha'}\right)^{\frac{2}{3}}\sqrt{C_\mu} \tag{7.10}$$

Eqs.(7.8)–(7.10) imply that an assumption of the value of β_p is necessary for the calculation of the dissipation constants. Using the recommendations in the literature [163, 165, 170], β_p was set equal to 1, implying that no mean kinetic energy is lost by viscous drag, which is an approximation of the real flow characteristics [164].

Eq. (7.11) shows the equation for the calculation of the constants $C_{\varepsilon 4}$ and $C_{\varepsilon 5}$ independently of the production and diffusion constants, assuming that they are equal [164].

$$C_{\varepsilon 4}\,(= C_{\varepsilon 5}) = \frac{\frac{6}{\sigma_\varepsilon} - \sqrt{C_\mu}\left(\frac{2}{\alpha'}\right)^{\frac{2}{3}}\frac{C_{\varepsilon 2}-C_{\varepsilon 1}}{2}}{\frac{3}{\sigma_k} - \sqrt{C_\mu}\left(\frac{2}{\alpha'}\right)^{\frac{2}{3}}\frac{C_2}{2}} \tag{7.11}$$

An overview of the calculated values for each of the forest constants is shown in Table 7.1.

Table 7.1. Canopy model constants using RSM

β_d	$\beta_{d,u}$	$\beta_{d,v}$	$\beta_{d,w}$	β_p	$C_{\varepsilon 4}$	$C_{\varepsilon 5}$
5.15	6	4.72	4.72	1	1.07	1.07

The values of Table 7.1 were used along with the other model constants in all the calculations for forest canopies in this thesis.

7.3 Irvine Case Study

7.3.1 Introduction

The proposed method was validated with results presented in a study of a Sitka Spruce (*Picea sitchensis*) forest, performed by Irvine et al. [157]. The measurements were performed across a forest edge at Harwood Forest, Northumberland, England. The examined forest consisted of a uniform plantation of Sitka Spruce, with a mean tree height (h_c) of 7.5 m, while the open ground was almost entirely a rough pasture. Some of the main site characteristics used in the modelling, are summarized in Table 7.2.

Table 7.2. Harwood site characteristics

$z_\circ$ moorland	0.028 m [155]
$z_{\circ f}$ forest	0.563 m
h_c	7.5 m
LAI	2.15

The Leaf Area Index (LAI), first introduced by Watson [263], is a simple measure of the amount of foliage within a canopy. It is defined as the projected one-sided leaf area per unit area of land, or the projected needle area per unit area of land, for coniferous forests [264]. According to the definition, the leaf area index LAI of a canopy of height h_c is related to the leaf area density according to Eq. (7.12):

$$LAI = \int_0^{h_c} \alpha(z)\, dz \tag{7.12}$$

As shown in Table 7.2, the estimated LAI of Harwood Forest was 2.15 [157].

Measurements were performed using four 15 m high, triangular towers. Mast 1 was located in moorland, 6.1 h_c upwind of the forest edge, Mast 2 was positioned at the forest edge, and Mast 3 and 4 were located in the forest, 3.6 h_c and 14.5 h_c downwind of the forest edge respectively.

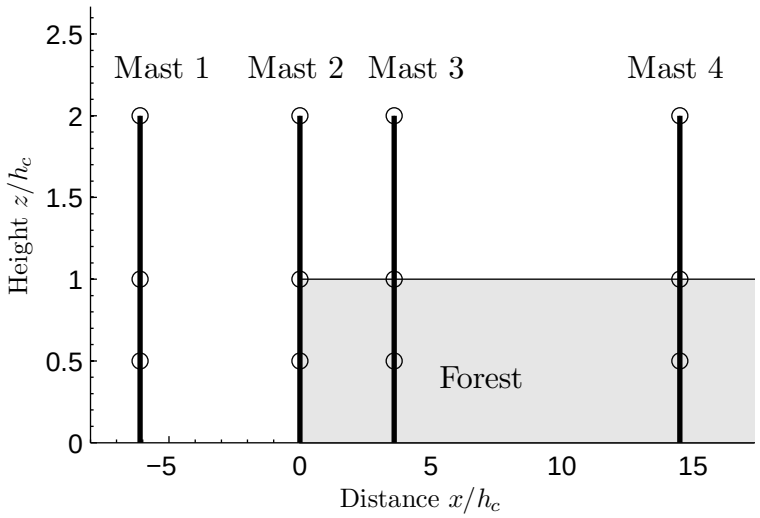

Figure 7.1. Mast and instrument locations relative to the forest edge and height.

Fig. 7.1 shows their locations as well as the locations of the instruments used for the measurements relative to the forest. More details on the instrumentation are included in Irvine et al. [157].

7.3.2 CFD considerations

Domain and Meshing

The domain was created in a 3-D Cartesian Coordinate System with dimensions (L_x, L_y, L_z) = (1000 m, 1400 m, 800 m). The inlet plane was positioned 300 m upwind of the forest edge, while the forest was chosen to have a length of 700 m extending to the outlet and a width of 20 m, since this dimension was not expected to play an important role in the results (Fig. 7.2a).

In a similar procedure to that demonstrated by Dalpé and Masson [170], the computational domain's bottom boundary was lifted to a height equal to the roughness length ($z_\circ$). Downwind of the forest edge, the ground height was equal to $z_{\circ f}$ (Table 7.2). However, only $z_\circ$ was used in the wall function considerations

(following Dalpé and Masson [170]) and not $z_{\circ f}$, as the forest effect was modelled solely through the source terms.

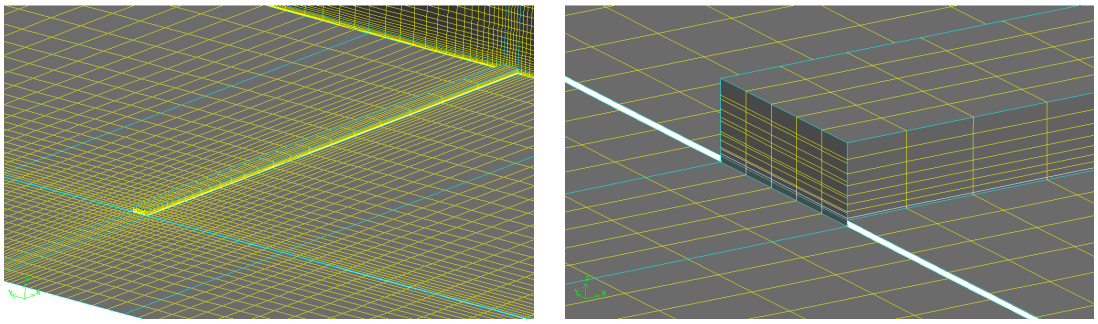

(a) The forest zone in the Domain (b) The forest edge

Figure 7.2. Meshing of the forest zone.

The total number of cells was $N_{tot} = 100,815$, with $(N_x, N_y, N_z) = (41, 65, 36)$ cells and a first cell height of $z_P = 1.2$ m over the ground outside the forest. In the forest zone, z_P was taken as 0.2 m in order to provide more detailed information on the velocity and turbulence profiles inside the canopy. The number of cells inside the forest zone was $(N_x, N_y, N_z) = (25, 5, 8)$ (Fig. 7.2b).

Boundary conditions

Sec. 3.5 explains the procedure for choosing the type of Boundary conditions in FLUENT, carried out throughout this thesis. The scalars of velocity and turbulence at the inlet were chosen according to the Eqs. of Sec. 3.3 for neutral ABL flow. The scalars were also fixed at the top cell zone of the domain, according to Sec. 3.5.

The forest was modeled as a porous medium, applying the sources described in Sec. 7.2.1 with the constants of Table 7.1, which were calculated according to the Eqs. of Sec. 7.2.2.

Drag coefficient

A major challenge was to accurately estimate the forest drag coefficient C_d. Irvine [157] estimated it to have a constant value of $C_d = 0.2$. However, for the case of the spruce canopy, C_d tends to be height dependent, increasing close to the ground [265]. A profile for the drag coefficient, taken from Amiro [265] was also considered (Fig. 7.3). Note that for $z/h < 0.45$, C_d was assumed to be constant, as there was no available information.

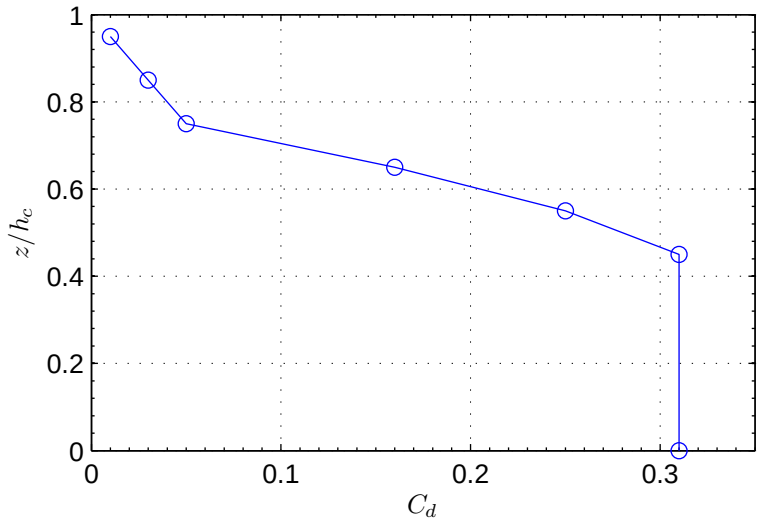

Figure 7.3. Profile of Drag Coefficient [265]

Simulations were run with the C_d profile of Fig. 7.3 as well as using a constant value of $C_d = 0.2$ in order to test whether the predictions are improved.

Leaf area density

The estimation of the leaf area density (LAD) profile $\alpha(z)$ was necessary for applying the canopy source terms, but there was only information about the Leaf Area Index (LAI) of the forest (Table 7.2). In any case, Eq. (7.12) needs to apply. The LAD profile may vary due to various factors (it also has a seasonal variation), thus it is difficult to accurately predict it with only information about the LAI.

Massman [266] has discussed different distributions of LAD, while Teske [264] has used a Weibull distribution, while other authors, such as Bealde et al.[267] and Kerzenmacher and Gardiner [268] have used a Gaussian distribution. In this work, two different LAD profiles were considered, using a Weibull and a Gaussian distribution, while taking into account Eq. (7.12) and they are shown in Fig. 7.4.

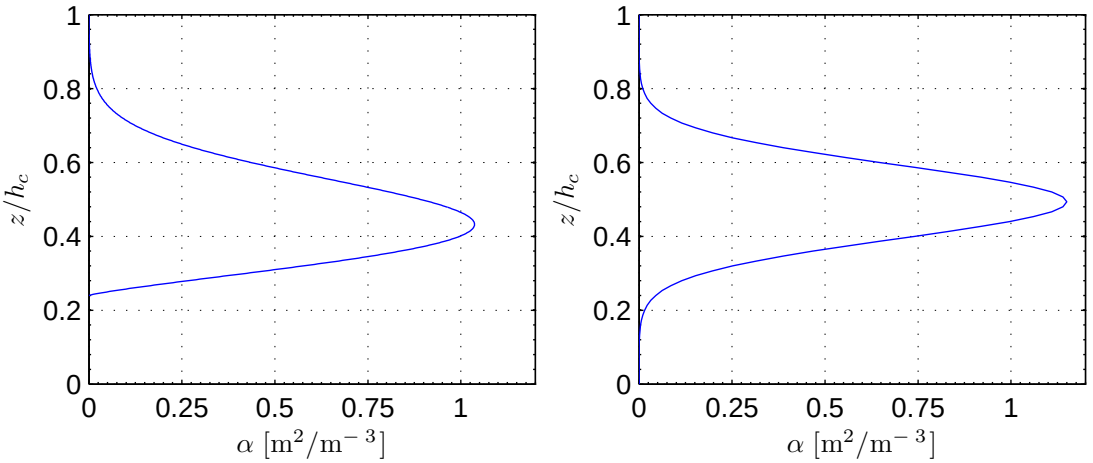

(a) Weibull distribution (b) Gaussian distribution

Figure 7.4. Different configurations of Leaf Area Density profile

The Weibull profile was calculated according to Eq. (7.13), using $sh = 2.2$, $sc = 1.9$ and $z_{min} = 1.8$ m (Fig.7.4a).

$$\alpha(z) = LAI \, \frac{sh}{sc} \left(\frac{z - z_{min}}{sc} \right)^{(sh-1)} \, \mathrm{e}^{-\left(\frac{z-z_{min}}{sc}\right)^{sh}} \tag{7.13}$$

where sh is the shape parameter and sc is the scale parameter of the distribution.

The Gaussian profile was calculated according to Eq. (7.14), using $a_1 = 1.15$ and $b_1 = 3.7$.

$$\alpha(z) = a_1 \, \mathrm{e}^{-\left(\frac{z-b_1}{c_1}\right)^2} \tag{7.14}$$

where a_1 and b_1 are constants and c_1 is calculated from Eq. (7.15).

$$c_1 = \frac{LAI}{a_1 \sqrt{\pi}} \tag{7.15}$$

7.3.3 Results

A comparison between the CFD simulations and the measurements was performed using the different configurations of LAD profile and C_d, described in Sec. 7.3.2. Using Eq. (7.16), the streamwise wind velocity was normalised with the velocity at a height of $z/h_c = 2$ on Mast 1, which was chosen as U_{ref}. The turbulence intensity (I_u) was calculated according to Eq. (5.4).

$$u_x = \frac{U_x}{U_{ref}} \tag{7.16}$$

$$I_u = \frac{\sigma_u}{U_x} \tag{5.4}$$

Fig. 7.5 shows the results using a Gaussian LAD profile and Fig. 7.6 shows the same results using a Weibull LAD profile, using the two different configurations for the drag coefficient.

The velocity predictions are very close to the measured values at Masts 1 and 2, although velocity is slightly underestimated at $z/h_c = 1$. This may be attributed to the fact that the real height of the canopy at the edge, which also affects the results at Mast 1, may be less than the assumed uniform value of $h_c = 7.5$ m. Results downwind of the forest edge are very close to measurements. The speed up at $z/h_c = 2$ of Mast 3 was observed by Irvine et al. [157] and can be attributed to the low pressure region just back the forest edge [269]. The velocity deceleration inside the forest at Masts 3 and 4 was predicted in an acceptable level, although it was slightly underestimated. Finally the velocity deceleration at $z/h_c = 2$ of

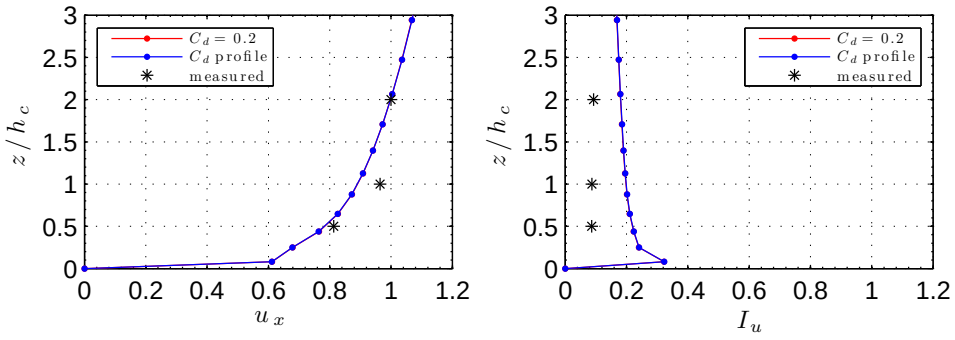

(a) Mast 1: $x/h_c = -6.1$

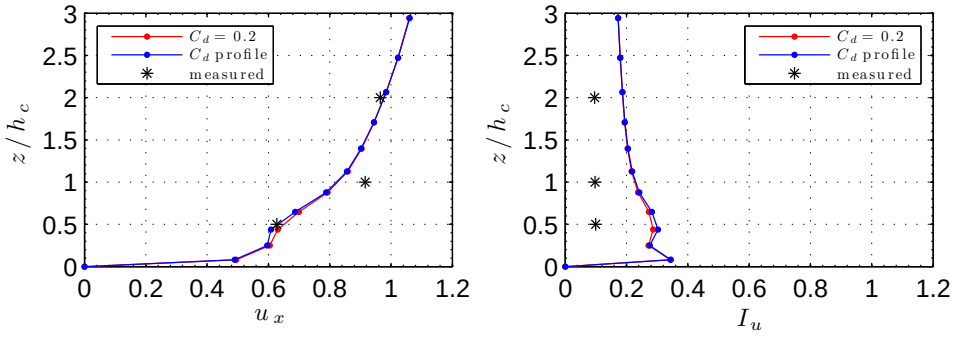

(b) Mast 2: $x/h_c = 0$

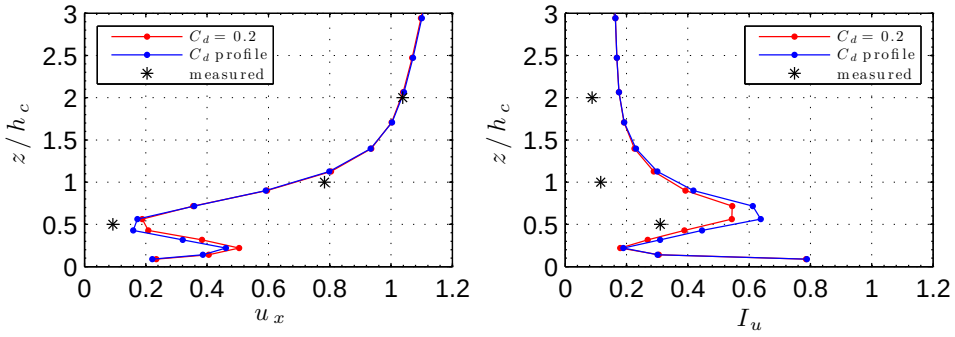

(c) Mast 3: $x/h_c = 3.6$

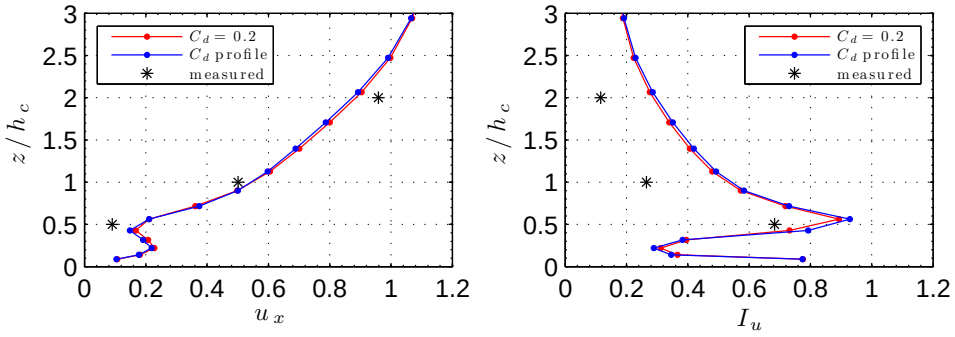

(d) Mast 4: $x/h_c = 14.5$

Figure 7.5. Results using a Gaussian LAD profile.

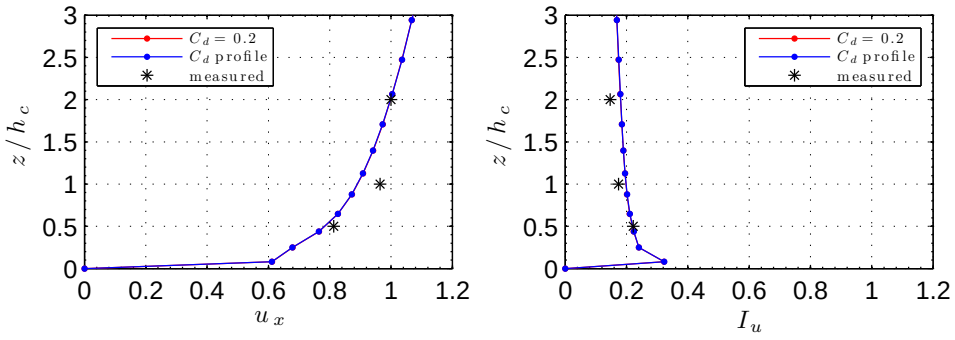

(a) Mast 1: $x/h_c = -6.1$

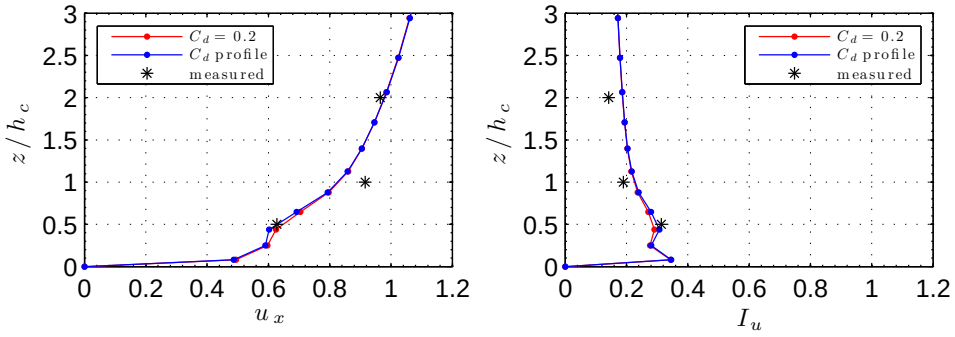

(b) Mast 2: $x/h_c = 0$

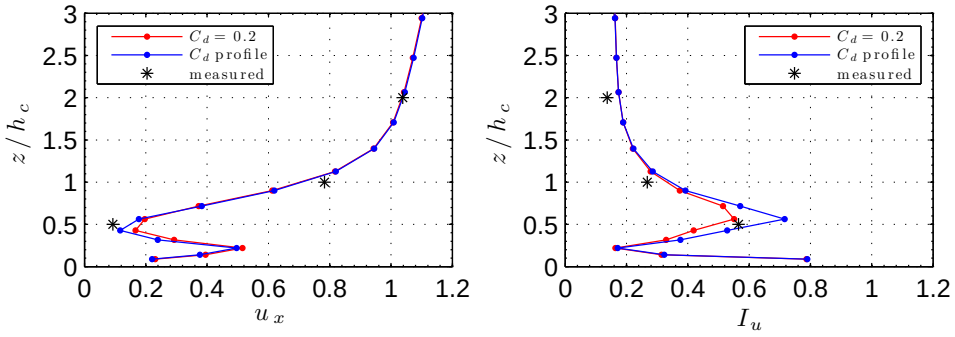

(c) Mast 3: $x/h_c = 3.6$

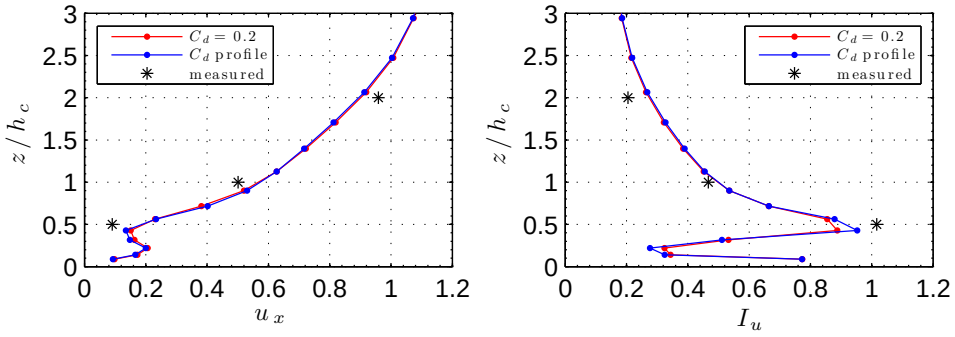

(d) Mast 4: $x/h_c = 14.5$

Figure 7.6. Results using a Weibull LAD profile.

Mast 3 was slightly overpredicted, however as Irvine et al. [157], it was found to be inside the forest internal boundary layer.

The turbulence comparison was also good. The turbulence intensity profile at Mast 1, indicates that the applied wall function, as well as the estimated turbulence values at the inlet, based on a neutral ABL, were able to represent the turbulence profile rather well. The turbulence increase inside, as well as above the forest has been well represented, although at $z/h_c = 0.5$ of Mast 4, it was slightly underestimated, which may be attributed to the overestimation of velocity at the same location.

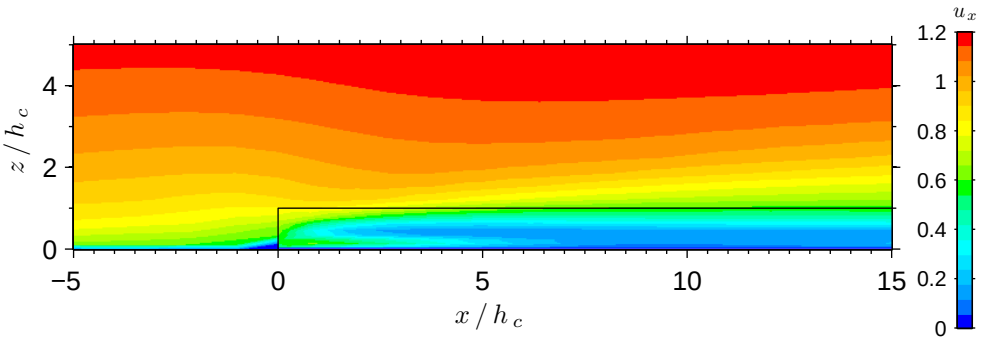

(a) Normalised velocity

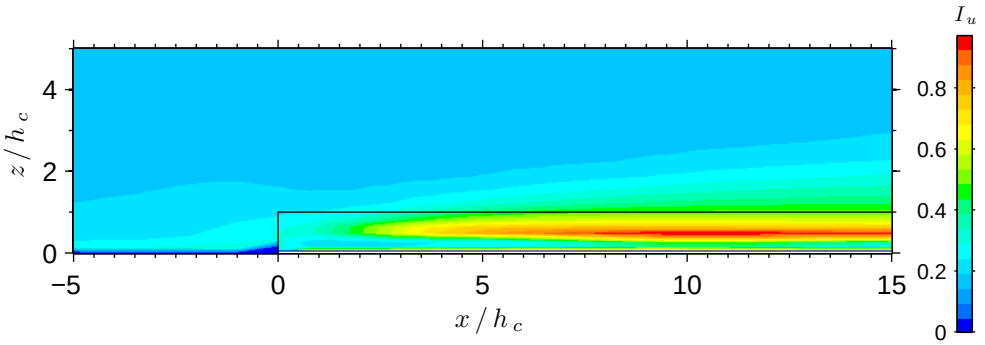

(b) Turbulence intensity

Figure 7.7. Contour results for the case of a Weibull LAD profile and C_d profile.

Considering the two different C_d configurations, a C_d profile provided better predictions inside the forest, however at $z/h_c = 1$ and 2 the differences were negligible. Comparing the effect using different LAD profiles, they seemed to

give very similar results, although a Weibull LAD profile provided slightly closer predictions with the measurements.

Fig. 7.7 shows the contours of normalised streamwise velocity and turbulence intensity for the best matching case of using a Weibull LAD profile and the profile of Fig. 7.3 for C_d. In the figures, the x and z coordinates were normalised with the canopy height. Inside the forest, the loss of momentum and the increase of turbulence intensity are significant. These effects also extend above the forest height further downstream. The flow is also slightly affected upstream of the forest edge.

Chapter 8

Case Study 1: Coastal Complex Terrain Wind Farm

8.1 Introduction

In this Chapter, the previously developed CFD modelling approaches of modelling wind turbine wakes and the flow over complex terrain are validated with wind measurements of a real wind farm, provided by RES (Renewable Energy Systems Ltd. - UK). A comparison is also made with the corresponding results using WAsP (Wind Atlas Analysis and Application Program [270], a commercial software for wind developers based on simple, linear models for wind modelling.

Some additional CFD considerations as well as the WAsP approach are initially described. The procedure in the treatment of the wind farm data is also explained. Finally, the wake of a single machine, as well as the wake interaction of two machines aligned to the flow direction, are examined. The validation was performed using the measured data of a machine operating in the wake of the examined upstream turbines. The purpose was to compare the CFD and WAsP predictions with the measurements.

8.2 The wind farm site

The wind farm is located on a coastal site of moderately complex terrain shown in Fig. 8.1. The maximum elevation is not considered very high, as it reaches 50 m in the site proximity and 140 m at nearby hills. Nevertheless, the complexity of the terrain lies to the fact that it is very near a steep coastline, up to 30 m above sea level and therefore subject to high accelerations. Narrow watercourses leading to the sea also adds to the complexity of the land surface.

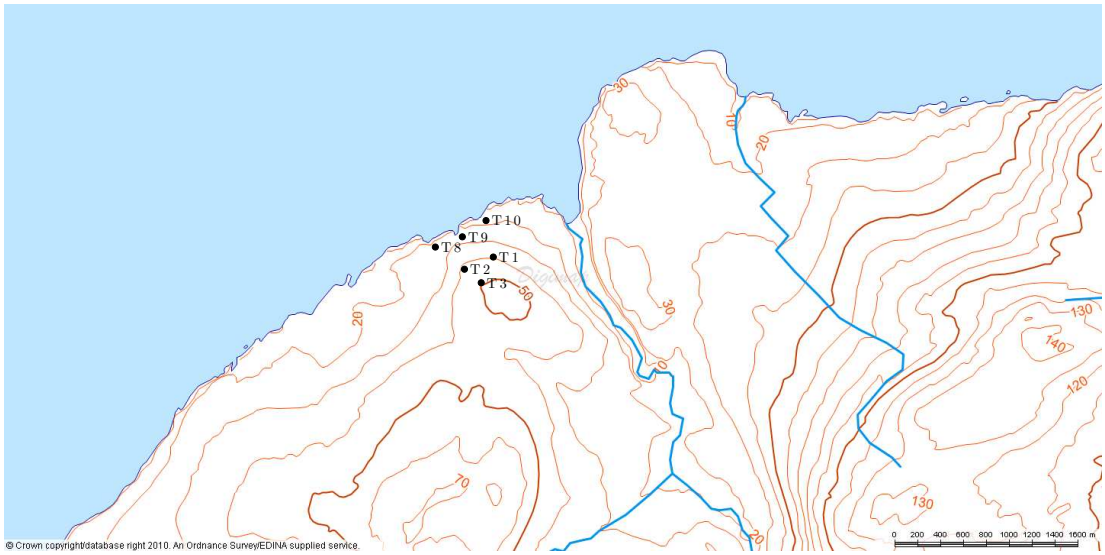

Figure 8.1. The coastal complex terrain wind farm.

The wind farm has a total installed power of 7.2 MW and consists of six wind turbines (T1, T2, T3, T8, T9 and T10) with a hub-height of 47 m, located at the positions shown in Fig. 8.1. At the first stage of the site operation, only T1 and T2 were built, while a Met-Mast (M25) was positioned at the location of T9 in the figure. The wind turbines of the initial arrangement (T1 and T2) are rated 1 MW and have a diameter of 54.2 m, while the other machines (T8, T9 and T10) are of 1.3 MW installed power and 62 m rotor diameter.

8.3 Additional CFD considerations

The rotor wakes and the neutral ABL were modelled according to the methodology described in Chapter 3. As the case involved a real complex terrain surface, some additional considerations related to the surface had to be taken. In particular, a wall CFD surface was created according to information on the site elevation, while an appropriate selection of the surface roughness was made. The procedure for addressing the aforementioned issues is explained in the following paragraphs.

8.3.1 Site surface creation

An important aspect of the modelling procedure was related to the creation of a wall surface representative of the site elevation and terrain complexities, as explained in Sec. 3.4. For that purpose, the following procedure was followed for the creation of the case ground wall.

Information on the site elevation was given in the form of a $*$.xyz grid point data file. The grid points covered an area of 30 km $\times$ 30 km around the site with a 50 m resolution, totalling a number of 361, 201 points. The file consisted of comma-delimited data of (x, y, $z_{a.s.l.}$), where x and y were Ordnance Survey coordinates (first two columns) and $z_{a.s.l.}$ was elevation above sea level (third column) for each of the grid points. After some modifications, the data file was imported into RHINO, a NURBS-based 3-D modelling software, using the SrfControlPtGrid command to create a surface from the grid points. The created surface was afterwards saved in an $*$.sat ACIS format which is readable in GAMBIT, the preprocessor of FLUENT.

8.3.2 Site roughness considerations

As the site consists of a large offshore part near the wind farm, the wall surface was separated in FLUENT into an onshore and an offshore part in order to consider different values of roughness length $z_\circ$ in the wall functions (Sec. 3.4). Different approaches followed into selecting the required values.

Ground roughness

In order to justify the selection of the roughness length for the ground, the site surface was investigated in terms of land use according to the Corine Land Cover 2000 (CLC2000) database available on-line [271]. CLC2000 is an update for the year 2000 of the first CLC database created in the early 1990s as part of the European Commission programme Corine (COoRdinate INformation on the Environment) [272] aimed at providing consistent information on land cover across Europe. Although the dataset does not include roughness length classes, an effort has been made to group and link the CLC land use classes with roughness length classes [273].

According to CLC2000 for the particular site, land use consists predominantly of pastures and natural grassland with some small areas of agricultural land with natural vegetation. Consequently and according to the table created by Silva et al. [273], the selected roughness length was $z_\circ = 0.03$ m.

Sea roughness

Several approaches have been proposed for the choice of the sea roughness length $z_{\circ,sea}$. One of the most notable suggestions is Charnock's relation [274], linking $z_{\circ,sea}$ with the friction velocity u_*, Eq. (8.1).

$$z_{\circ,sea} = a\frac{u_*^2}{g} \tag{8.1}$$

where g is the acceleration due to gravity and a is a constant which is fetch/wind speed-dependent with a typical value of 0.018 in coastal areas [275].

Although the sea roughness length is expected to vary with wind speed, Frank et al. [276] have shown in a modelling study that using a constant roughness of $z_{\circ,sea} = 0.2 \times 10^{-3}$ m instead of other more complex approaches, such as Charnock's [274], provides results with small discrepancies, especially near the coast. For simplicity, as well as the fact that the wind farm is not located offshore, thus some small discrepancies in the sea roughness length are not expected to influence the results, the constant value of $z_{\circ,sea} = 0.2 \times 10^{-3}$ m was also used in the current thesis. Additionally, the later constant value is also the same sea roughness value considered in the WAsP software, thus it provides a common reference for comparison between the models.

8.4 WAsP modeling

Apart from CFD modelling, results from wake modelling using the WAsP model are also considered for comparison. The main function of the program is to estimate wind energy resources and potential wind farm output. It normally uses meteorological data measured at a location and then it generates a local wind climate at which all obstacle, roughness or complex terrain effects are removed. If a wind climate for a wind farm site is required, WAsP reintroduces the local effects [203]. An important advantage of the program is its simplicity and fast calculation, since it incorporates simple linear models. However, it has some limitations, such as in complex terrain cases were flow separation occurs.

8.4.1 WAsP models

WAsP uses simplified models to take into account changes in the power output due to orography or wakes.

WAsP model for orographic effects

Orographic effects over complex terrain are taken into account using the BZ (Bessel Expansion on a Zooming Grid) model [106], a linear model based on Jackson-Hunt theory used extensively for the calculation of the mean flow perturbations in complex terrain. Results are accurate when the surrounding topography is not too steep [277]. The WAsP model has performed well in predicting the flow for the case of Blashaval [107] and Askervein [106], although it failed in the flow speeds close to the ground on the lee side of Askervein where some flow separation occurred.

The main limitations of the WAsP BZ model is that it assumes neutrally-stable conditions and wind flow over low and smooth hills without flow separation [277]. In the case of a steep hill, WAsP over-predicts the flow speed according to several comparisons of observations and predictions described in the literature [277]. According to Bowen and Mortensen [277] prediction errors due to orography are likely to occur for sites with slopes significantly higher than 0.3.

WAsP wake model

The WAsP wake model is based on a simple, mathematical model developed by Jensen [62] to calculate single wakes and further advanced by Katic et al. [61] to be applied to real wind farms. The wake is assumed to have a 'top-hat' profile, with an initial diameter equal to the rotor diameter and a linear lateral and vertical expansion as a function of distance downwind, according to Eq. (8.2).

Inside the wake, velocity is considered constant and the wake centreline is assumed to follow the terrain:

$$D_{wake} = D_{\circ} + 2k'x \tag{8.2}$$

where $D_\circ$ is the rotor (initial wake) diameter, k' is a wake decay constant and x is the downwind horizontal distance.

The effect in downwind rotors is calculated by taking into account the fraction of the wake calculated cross sectional area at the downwind location overlapping the downwind rotor plane $A_{overlap}/A_{downwind\,rotor}$. The velocity deficit U_{def} is calculated according to Eq. (8.3).

$$U_{def} = \left(1 - \sqrt{1 - C_T}\right) \left(\frac{D_\circ}{D_\circ + 2k'x}\right)^2 \frac{A_{overlap}}{A_{downwind\,rotor}} \tag{8.3}$$

The thrust coefficient C_T is related to the initial wind speed deficit and it is calculated from the available $C_T = f(U)$ tables of the specific wind turbine.

The model is simple and does not require high CPU resources. However, the assumption that the wake centreline follows the terrain and expands linearly is oversimplified for some cases, such as over complex terrain.

8.4.2 WAsP procedure

The map file used in WAsP for all examined cases needed to correspond to the specific region. It was created in WAsP MapEditor after importing OS Land-Form PANORAMA data of the site (1:50000 scale) in the form of $*$.ntf files. Two roughness classes were used, with roughness length of 0.03 m over land and 0.2×10^{-3} m over water.

The WAsP wind atlas file is usually created after importing the measured wind data. It corresponds to the local wind climate, fitting a Weibull distribution to the measurements and considering a number of directional sectors. A suitable wind atlas file was needed to match the CFD cases and the measurements. The CFD cases, as well as the measured data were aimed to correspond to a specific wind speed at the upwind rotor (± 0.5 m/s in the data) and direction ($\pm 0.5^\circ$ in the data). However, using fixed wind speed and direction is beyond the designed

operational purpose of WAsP. The wind atlas file (∗.rwc) was therefore modified manually using XML Notepad for each of the examined cases.

For choosing the wind direction, the maximum number of wind directional sectors was used (36), corresponding to a 10° angle for each sector. A sector frequency of 99.3% was created for the directional sector corresponding to the fixed direction of the examined case, while each of the remaining directional sectors were chosen to have a frequency of 0.02%. Therefore, a 'fixed' wind direction was artificially establised.

The second requirement for a fixed wind velocity at a wind turbine site was met by modifying the shape and scale parameters of the Weibull distribution for the directional sector of interest and running trial simulations until the desired wind speed is calculated on the site by WAsP. The parameters of the Weibull distribution were manually chosen, such that the majority of velocity values are concentrated around the desired mean velocity.

8.5 Use of measured data

The available wind data were of two major categories: meteorological data measured at a Met-Mast on the site and wind farm SCADA data measured on each of the machines.

8.5.1 Met-Mast meteorological data

The meteorological data were measured at a Met-Mast, M25, positioned at the location of T9, when only T1 and T2 were built and in operation. The Met-Mast data included wind speed and direction measured with two anemometers (at 35 m and at 50 m a.g.l.) and two wind vanes (at 33 m and at 48 m a.g.l.) providing measurements with reference to the Magnetic North direction. Data

of wind direction from the Met-Mast are generally considered more accurate in comparison to directional measurements and yaw angle information from the wind turbines [278] and were therefore used for the creation of the site wind rose.

The use of the meteorological data involved the creation of a local wind climate based on the measurements at the Met-Mast. As the height of interest was the rotor hub-height of 47 m, the anemometer at 50 m and the wind vane at 48 m were chosen to provide the measurements of wind speed and direction respectively, since their height was closer to the hub-height.

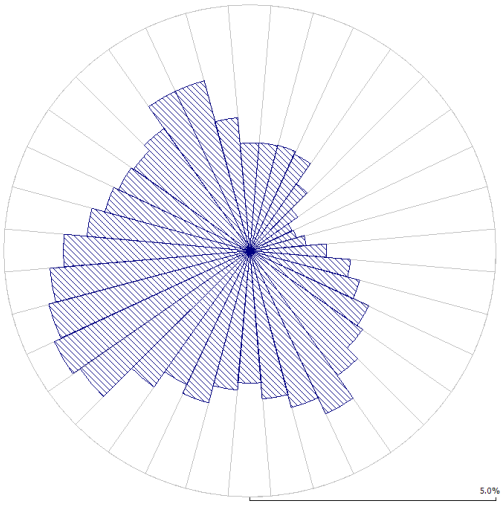

Figure 8.2. WAsP wind rose at $z = 47$ m ($z_\circ = 0.03$ m) calculated from M25 data.

The wind direction measurement of the wind vane was performed with reference to the Magnetic North, thus a modification was needed in order to obtain the direction with respect to True North. The angle between Magnetic North and the True North direction is called magnetic declination and depends on the measurement location and date. The given location coordinates were transformed from Ordnance Survey's National Grid easting and northing into GPS latitude and longitude using an on-line coordinate transformer [279]. The converted coordinates were then used together with information about the date of measurement as input to an on-line magnetic declination calculator [280]. The

resulting magnetic declination was found to be 5° 23′ W changing by 0° 11′ E/year. Thus, 5.383° was added to the measured wind direction in order to correspond to True North reference.

The data were used in the WAsP Climate Analyst software and then exported into WAsP in order to create a local wind climate independent on the location and the resulting wind rose is shown in Fig. 8.2 as a % distribution of the wind direction in 36 sectors of 10° width. It is clear in the figure, that the prevailing wind direction is West to South-West followed by North to North-West and South to South-East.

Table 8.1. WAsP predicted wake losses at each rotor.

Rotor [−]	Machine [−]	Elevation [m] a.s.l.	Hub-height [m] a.g.l.	Wake losses [%]
T1	Bonus 1 MW	38	47	8.10
T2	Bonus 1 MW	40	47	6.77
T3	SWT-1.3-62	48	47	4.80
T8	SWT-1.3-62	22	47	2.53
T9	SWT-1.3-62	19	47	8.22
T10	SWT-1.3-62	13	47	6.91
		Wind Farm		6.09

According to the simulation based on the Met-Mast data, the predicted wake losses for the site are estimated to be 6.09%. The predicted wake losses at each particular rotor are shown in Table 8.1.

8.5.2 Wind farm SCADA data

The wind farm measured data include 10-minute averages of active power, wind speed and yaw angle (both mean and standard deviations) extracted from the SCADA (Supervisory Control And Data Acquisition) database. The SCADA systems ensure that all data are time synchronised [56]. The measurements were performed for a period of approximately four years and three months when T1 and

T2 were operating alone, one and a half years with all six machines in operation and for an additional half year, only data from T3, T8, T9 and T10 were available.

The wind farm data were used for the validation of the wake modelling. The timestamp was used as a key parameter to select the 10-minute average dataset fulfilling some previously specified criteria [53] related to the wind direction and wind speed of interest.

Active Power measurements

The mean active power along with the power curve can be used to calculate the mean 'true wind speed', the wind speed which would have been measured at the hub without the presence of the wind turbine [53]. The true wind speed is obviously slightly different than the data mean wind speed, measured at the nacelle anemometer while the rotor is in operation. However, in order to correctly calculate the true wind speed, the site-specific power curve is needed, as the general power curve of the machine may not be different for the particular site [56, 278].

The mean active power was therefore preferred to the wind speed for wake validation as a method which would avoid such errors. However, in CFD and WAsP the general power curve is used for the power output estimation, therefore an unavoidable error is expected to arise from the fact that the site-specific power curve was not used.

The standard deviation of active power was used for the calculation of turbulence intensity following the approach used by Jørgensen [53] in the analysis of the Middelgrunden Windfarm data. According to this approach, initially proposed by Thomsen and Markkilde-Petersen [281] the wind velocity standard deviation is calculated from Eq. (8.4).

$$\sigma_u = \frac{\sigma_P}{B} \frac{1}{\left(\frac{dP}{dU}\right)_U} \tag{8.4}$$

where σ_u and σ_P are standard deviations of wind speed and power respectively, B is an empirical constant with value specified by Jørgensen between $0.8 - 0.9$ [53].

Wessel [282] has found the constant B to be highly site-dependent. In his work, Wessel successfully applied the Markkilde-Petersen approach for the calculation of the turbulence intensity at the Elisenhof onshore wind farm. He found the approach to be a preferred method for the estimation of turbulence intensity, as the alternative method of using the nacelle anemometer fluctuations provides extra uncertainties, because the flow is disturbed by the nacelle and the rotor.

Yaw Angle measurements

The measured yaw angle at each machine was considered as an indication of the local wind direction at the specific rotor location, assuming that each upwind rotor was yawed perpendicular to the wind, while the yaw errors were not accounted for, as there was no available information. The yaw angles were not measured with reference to True or Magnetic North implying a systematic error in the measurements. In fact, a certain bias in such wind vane measurements at each specific wind turbine in a wind farm has been described as a common feature in the literature [56, 278].

An analysis was needed at each rotor of interest, in order to calibrate the yaw angle according to the maximum wake direction within 1° [56]. Using active power data from a rotor in the machine's proximity and sorting the datasets according to the yaw angle within 1° of the rotor of interest, the yaw angle resulting in the maximum wake was assumed to correspond to the wind direction according to which two rotors are aligned, calculated from the map coordinates. The latter assumption is not always valid in complex terrain since changes in the wind direction, as well as in the wake centreline between the rotors, are not uncommon. However, an effort was made in choosing rotors with small spacing and without significant obstacles to interfere in-between for the yaw angle calibration.

8.5.3 Validation with measurements

Criteria for comparison with CFD and WAsP results

The performed CFD and WAsP modelling efforts involved cases of a specific wind direction and specific 'true' wind speed calculated at the rotor subject to the freestream flow (freestream rotor), not influenced by other wakes. The wake output was calculated in terms of power output at the wake rotor locations, normalised with the power output of the freestream rotor. The measured data filtering was aimed at matching the aforementioned cases.

Initially, data including zero active power or wind speed and 'NaN' observations were excluded, to avoid availability issues. An important filtering criterion was to choose a narrow freestream rotor active power bin to correspond to a 'true' wind speed bin of $U_{hub} \pm 0.5$ m/s, where U_{hub} was the wind speed used in the CFD and WAsP cases. The approach of choosing a narrow wind speed bin is similar to the 'method of bins' [2, 3], using a single specific wind speed bin (± 0.5 m/s). The relevant wind speed margins, $U_{hub} \pm 0.5$ m/s, were converted into active power margins through the use of the machine's power curve.

The yaw angle of the freestream rotor, was considered as the freestream flow direction [56] for each case, having taken into account the calibration considerations described in Sec. 8.5.2. Data were consequently further filtered according to the freestream rotor yaw direction of interest, based on the direction which corresponds to a wake shape power output downwind of the rotor.

The power measurements at the wake rotors were normalised with the freestream rotor power output and averaged within each directional band of 1° width. The averaging was performed using median values as the data were found to be non-parametric (not symmetrically distributed) and to include unusual observations (outliers).

Possible sources of errors

A significant difference between the measurements and the simulations (CFD and WAsP) is the fact the the measurements correspond to different actual wind directions, whereas the simulations were performed for a fixed wind direction and the different directional bins are linked to the lateral (y) distance from the wake centre. In flat terrain, such a difference would not have introduced significant discrepancies. In complex terrain however, different wind directions are linked to different ambient turbulence and flow patterns, especially between flows over sea and land, such as in this case study. The CFD and WAsP simulations only used a fixed wind condition and the aforementioned differences were not taken into account. Additionally, an error is introduced when plotting the lateral wake profile, as the simulation data points were selected at different locations using a fixed hub-height. However, those locations have different elevations above sea-level and the area between the locations and the upwind turbine may correspond to different slopes and obstacles. Furthermore, the power curves used in CFD and WAsP to estimate the power output from the wind speed are not exactly the same as the real power curve for the particular site. For all the above reasons, the simulation results are expected to diverge from the measurements, especially at locations away from the wake centreline.

Another possible source of errors is related to the CFD assumption of neutral ABL, especially for wind directions over sea. As both on- and off-shore conditions were assumed neutral, the change from sea to land was considered solely as a roughness change. In reality, when air flows over a coastal discontinuity, two changes usually occur: a change of roughness (affecting the momentum flux) and changes in the availability of heat and moisture [283]. According to Kaimal and Finnigan [5], these scalars influence the atmospheric stability. The larger thermal capacity of water results in smaller diurnal temperature variations [284] and a delay in the seasonal temperature variations [283] as compared to land.

Additionally, thermally driven effects, such as the sea breeze [285] and low-level jets [286] may occur. For all the above reasons, the assumption of neutral atmospheric conditions for wind directions from the sea may not be always valid.

Furthermore, the CFD simulations did not take into account the effect of wake meandering (Sec. 2.3.2) and predicted the mean velocity deficit for exact wake directions only. However, because of wake meandering the measurements are usually associated with a degree of variability in the wake direction where the turbines are misaligned and the measured wake is partial, instead of a full wake [287]. For this reason, in most cases the CFD wake predictions are expected to overestimate the velocity deficit in comparison with the field measurements.

8.6 Single wake

The first operational phase including only T1 and T2 was considered initially. The two machines are positioned relatively close, with a spacing of approximately 5 D (271.54 m) and 47 m hub-height. The location of T1 was at approximately 38 m a.s.l., whereas T2 was at 41 m a.s.l.. The terrain slope in-between can be considered moderate, however the surrounding coast is steep and highly complex. The aim was to model the single wake of each of the rotors T1 and T2 in the case of one machine operating in the wake of the other. The results were validated with the SCADA power measurements at the machines and also compared the corresponding WAsP results.

8.6.1 The 1 MW wind turbines

Both T1 and T2 machines are of similar type: Bonus 1 MW with a rotor diameter of 54.2 m and 47 m hub-height. Their main characteristics are outlined in Table 8.2 using information taken from Thomsen et al. [288] and the 'Wind Energy Market' website [289], maintained by the German Wind Energy Association.

Table 8.2. Bonus 1 MW characteristics

rated power	1 MW
rotor orientation, configuration	upwind, 3 blades
rotor diameter	54.2 m
hub-height	47 m
cut-in, rated, cut-out wind speed	3 m/s, 15 m/s, 25 m/s
cut-in, rated rotor speed	15 rpm, 22 rpm
power regulation	active stall
blade type	LM 26.1
airfoil type	FFA3-NACA 63200
root, tip chord	2.4 m, 0.7 m (assumed)

The power curve of the Bonus 1 MW machine was found in the WAsP wind turbine database and it is shown in Fig. 8.3a, while Fig. 8.3b shows the derivative of power with respect to the wind speed which was necessary to calculate the turbulence intensity from the measurements according to Eq. (8.4).

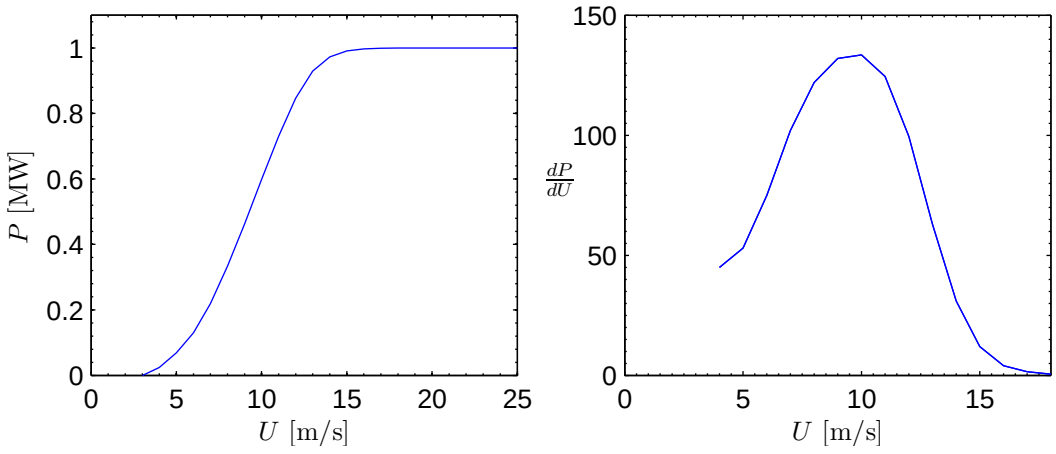

(a) Power curve (b) Power curve derivative

Figure 8.3. Bonus 1 MW power curve graphs.

As mentioned in Sec. 3.1, the VBM requires the use of information of airfoil type, chord and twist spanwise distributions. Due to lack of information on the LM 26.1 blade, the LM 29.2 blade properties were considered [290] in order to obtain some knowledge about the spanwise chord and twist distribution of such blade types. The lift and drag coefficients of a cylinder were considered for the 3 sections close

to the hub, whereas for the rest of the sections three different airfoil types were used.

The airfoil-type spanwise distribution was taken from the data for the LM 19.1 blade [291] modified to match the current case using the NACA 63-206 airfoil information taken from the NACA digitized data [254]. The 2-D lift and drag coefficient tables of FFA-W3-301 and FFA-W3-241 were taken from the work of Fuglsang et al. [292]. All airfoil tables were further expanded using the AirfoilPrep workbook [255] in order to include a $-180°$ to $+180°$ angle of attack range, as required by the VBM. All the relevant data of the considered airfoils are shown in Appendix A.

The blade span was finally split into 16 sections as shown on Table 8.3 and twist and chord data were interpolated for the required spanwise locations.

Table 8.3. Assumed spanwise distribution of the 1 MW blade properties.

Node [−]	Radial location r/R	Twist angle [°]	Chord length [m]	Airfoil type [−]
1	0.00	13.0	2.40	Cylinder-1
2	0.09	13.0	2.40	Cylinder-1
3	0.13	13.0	2.40	Cylinder-2
4	0.21	13.0	2.40	FFA-W3-301
5	0.27	11.0	2.30	FFA-W3-301
6	0.37	8.7	2.10	FFA-W3-301
7	0.44	7.2	2.00	FFA-W3-301
8	0.52	5.6	1.90	FFA-W3-241
9	0.60	4.2	1.70	FFA-W3-241
10	0.69	3.0	1.50	NACA 63-206
11	0.76	1.7	1.20	NACA 63-206
12	0.82	0.8	1.10	NACA 63-206
13	0.87	0.5	0.93	NACA 63-206
14	0.93	0.2	0.85	NACA 63-206
15	0.98	0.1	0.78	NACA 63-206
16	1.00	0.0	0.70	NACA 63-206

In VBM, the rotor speed is also required as input. A linear relationship between the rotor speed Ω and wind speed U was assumed between cut-in and rated conditions, matching cut-in and rated wind speed with the respective cut-in and

rated rotor speed from Table 8.2. For wind speeds above the rated wind speed, the rotor speed was taken as constant and equal to the rated rotor speed (22 rpm).

8.6.2 Wake of T2 (wind at ≈ 247°)

The case of T1 aligned with the wake of T2 was considered initially, which corresponds to a wind direction of 247° with reference to True North. According to WAsP prediction based on the M25 wind data, Sector 26 (250°) has a predicted frequency of 4.3% at T2.

CFD simulation

The CFD domain was created according to the specifications described in Sec. 3.5 taking into account the considerations outlined in Sec. 8.3. The chosen dimensions were: $L_x = 147$ D, $L_y = 88.5$ D and $L_z = 46$ D, where D = 54.2 m is the Bonus 1 MW rotor diameter; the total number of cells was $346,106$. The large rectangle in Fig. 8.4 illustrates the x and y limits of the CFD domain, whereas the smaller rectangle depicts the region chosen to present the contour results at hub-height (Fig. 8.5, left).

The simulation was initially run without the rotor effects to calculate the rotor speed at T2 hub position and examine whether there is any significant deflection in the flow direction at T2 hub, which would result in the rotor disc to yaw. The inlet and top boundary conditions were modified to obtain a horizontal velocity of $U_{T2} \approx 9.5$ m/s at T2 hub position in order to have a common basis for comparison with WAsP and the measurements. According to the results, the velocity was $U_{T2} \approx 9.53$ m/s with no significant deflection in the wind direction. The corresponding rotor speed was found to be $\Omega_{T2} = 18.8$ rpm by interpolation, assuming a linear relationship with the wind speed as explained in Sec. 8.6.1.

Fig. 8.5 shows the contour plots of normalised velocity u without the effects of

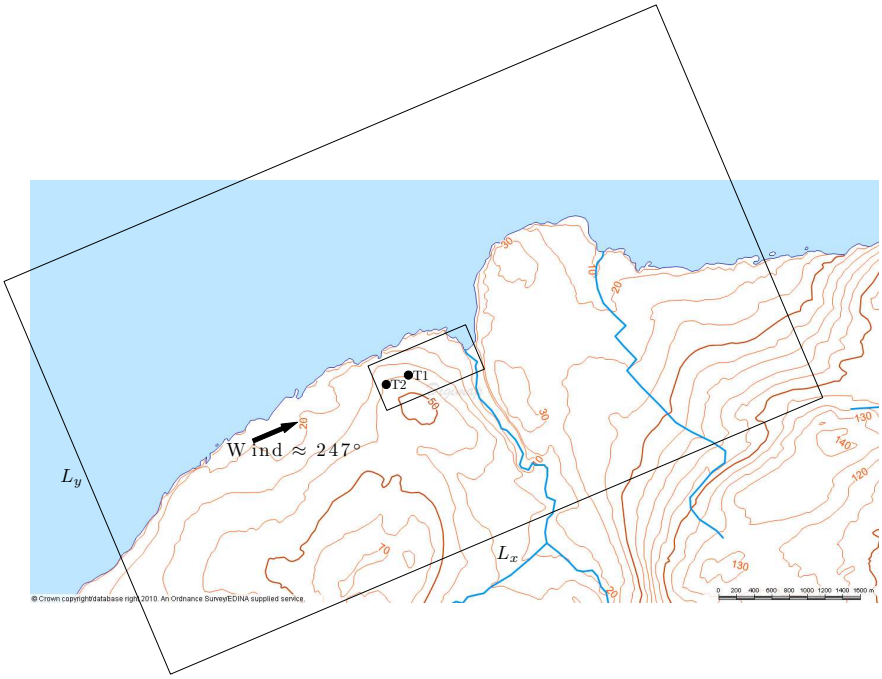

Figure 8.4. T2 wake case and extents of CFD domain and result region.

the rotor T2 (Fig. 8.5a); and u, velocity deficit U_{def}, and turbulence intensity I_u with the rotor effects (Figs. 8.5b, 8.5c and 8.5d respectively). The normalised streamwise velocity u was calculated taking into account possible changes in the wind direction due to the terrain according to Eq. (8.5):

$$u = \frac{U}{U_{top}} \text{ , with } U = \sqrt{U_x^2 + U_y^2} \tag{8.5}$$

where U is the streamwise velocity.

The velocity deficit was calculated using the streamwise velocity of the simulation without the effects of the rotor, according to Eq. (8.6).

$$U_{def} = \frac{U_{(\text{no WT})} - U}{U_{(\text{no WT})}} \tag{8.6}$$

Finally, the turbulence intensity I_u was calculated according to Eq. (8.7).

$$I_u = \frac{\sigma_u}{U_{(\text{no WT})}} \tag{8.7}$$

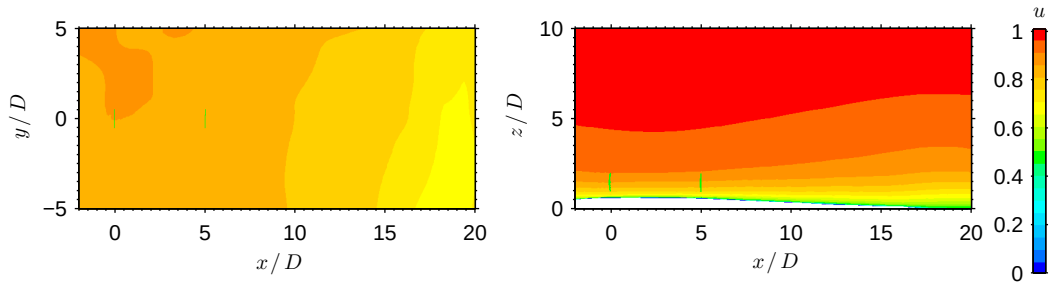

(a) Contours of u, no wake: hub-height (left) and $y = 0$ plane (right)

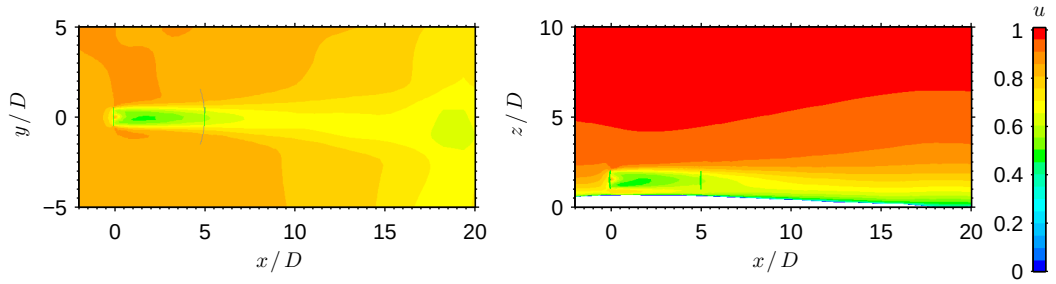

(b) Contours of u, T2 wake: hub-height (left) and $y = 0$ plane (right)

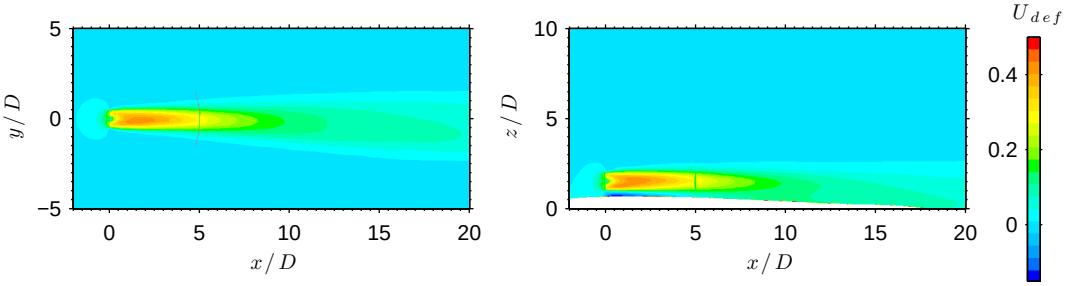

(c) Contours of U_{def}, T2 wake: hub-height (left) and $y = 0$ plane (right)

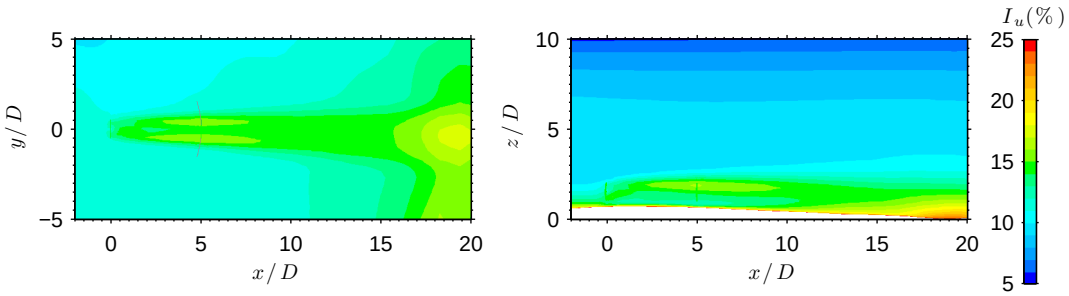

(d) Contours of I_u, T2 wake: hub-height (left) and $y = 0$ plane (right)

Figure 8.5. Contour plots for the case of T2 wake.

Fig. 8.5 (left) shows the results at the hub-height ($z_{a.g.l.}$ = 47 m) at the small rectangular area defined in Fig. 8.4, whereas Fig. 8.5 (right) shows the results at

the $y = 0$ plane, assuming that the origin of the x and y axes coincide with the T2 hub position. Rotors T2 and T1 are also shown in the figures. The arc shown in Figs. 8.5b and 8.5d (left) was created to indicate the region selected for the result comparison and validation in Sec. 8.6.2 using a constant distance of $\approx 5D$ equal to the spacing between T2 and T1.

The results of the simulation without T2, show that the wind speed is decreasing towards T1, as elevation is reduced from the hillside towards the watercourse. Fig. 8.5b shows that the presence of T2 further enhances the velocity decrease (left). A slight asymmetry is found in the near wake ($1-2$ D at Fig. 8.5b and 8.5c, left) which may be responsible for the far wake drift ($15-20$ D). The wake seems to also be asymmetric at the xz plane (Fig. 8.5b and 8.5c, right), which may be attributed to the wind shear due to the surface roughness. According to Fig. 8.5d, turbulence is maximised at $x \approx 18-20$ D downwind (left) which is the location of the watercourse (Fig. 8.4). At T1 ($x = 5$ D), turbulence is higher at approximately 0.5 D on each side of the $y = 0$ axis. In Fig. 8.5d right, turbulence intensity clearly peaks above the turbine axis, at $x \approx 5$ D downwind of T2.

Comparison with WAsP and validation with measurements

The measured data were processed according to the approach described in Secs. 8.5.2 and 8.5.3, using a criterion of $U = \pm 9.5$ m/s of 'true' wind speed at T2. The yaw angle of T2 was corrected according to the maximum wake direction. A discrepancy of 12° was subsequently found between T2 yaw angle and the direction with reference to True North.

Fig. 8.6 shows a scatter plot of the normalised power at T1 as a function of the wind direction 'measured' at T2. The power output in the wake was normalised with the power output of the freestream machine, T2. The data are not normally (symmetrically) distributed for each wind direction and they include

some outliers. For these reasons, the median value was selected for calculating the average P_1/P_2 at each wind direction.

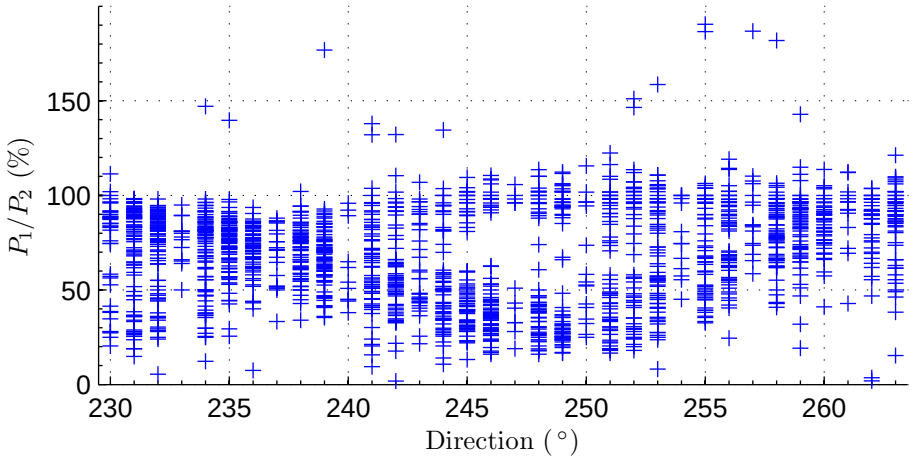

Figure 8.6. Scatter plot of the data - T2 wake.

Fig. 8.7 shows the results of the comparison between the CFD results, WAsP simulation results and measured averages of the normalised power output in the wake of T2 (P_1/P_2). The CFD results of streamwise velocity, U, were converted into power by interpolation, using the power curve in Fig. 8.3a. An arc, using a constant distance from T2 equal to the inter-turbine distance was created in CFD for the comparison with the measurements.

The locations for the WAsP simulations were selected in a similar way, using an arc of a fixed distance and a directional spacing of 2°. One simulation was run for each of the selected wake locations, positioning a Bonus 1 MW rotor at hub-height. WAsP was run according to the procedure described in Sec. 8.4.2 modifying the wind atlas to have a fixed wind direction of 250° and a 'true' wind speed of 9.5 m/s at T2. The power output of the rotor at each of the wake locations was calculated and normalised with the corresponding power output of T2.

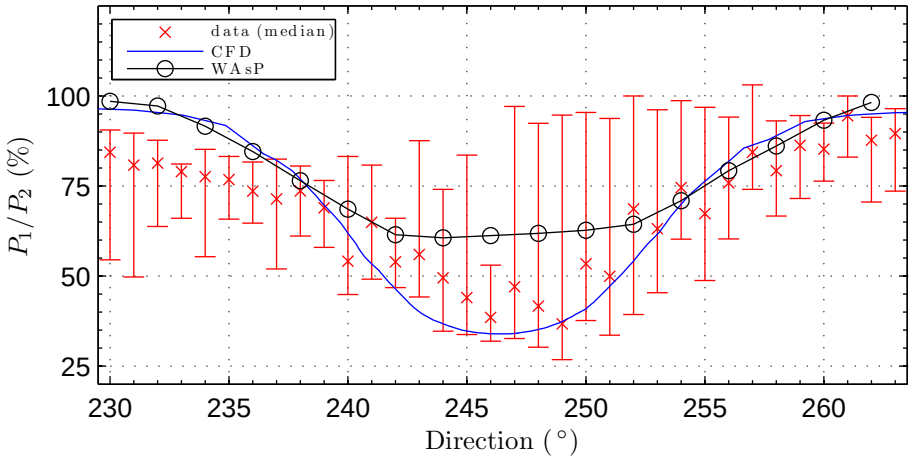

Figure 8.7. Comparison and validation with WAsP and measurements - T2 wake.

As the data were non-parametric (Fig. 8.6) the median values were used for averaging and the interquartile range was used as a measure of the data variability [293]. The error bars indicate the interquartile range: the lower quartile cuts off the lowest 25% of the data (25^{th} percentile) and the upper quartile cuts off the highest 25% of the data (75^{th} percentile). The asymmetric error bars in Fig. 8.7 suggest an increased data dispersion and skewness at some directional bins near the wake centre.

It should be noted that the CFD and WAsP simulations assumed a fixed wind direction ($\approx 247°$) while the measurements were taken for different freestream wind directions, therefore an error is expected in the comparison, especially away from the maximum wake area (see Sec. 8.5.3). For that reason, the validation was particularly focused near the maximum wake direction (247°).

According to Fig. 8.7, the CFD prediction is for a U-shaped wake and a wind direction of $247 \pm 6°$. The predictions are relatively close to the data averages. The WAsP prediction is a 'top-hat' wake shape, as expected (see Sec. 8.4.1). WAsP overestimates the wake power output by approximately 15% in comparison to CFD results near the wake centre. For wind directions of more than 6° away from the wake centre, WAsP and CFD predictions are very close in comparison,

as well as away from the measured averages for wind directions over land ($< 247°$) while being closer for wind directions over sea ($> 250°$).

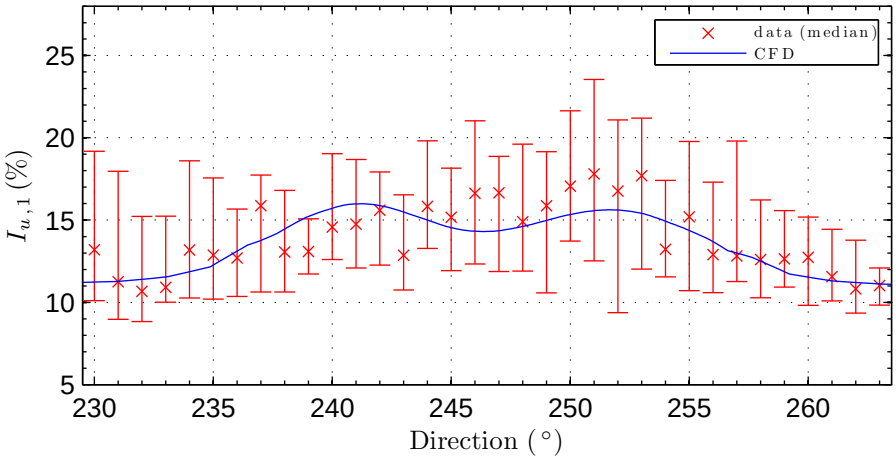

Figure 8.8. Turbulence intensity - T2 wake.

The validation of CFD turbulence intensity results with the values derived from the measured data is shown in Fig. 8.8. The turbulence intensity was calculated in both cases according to Eq. (8.7) and notably the 'measured' values were found using Eq. (8.4) (see Sec. 8.5.2) with $B = 0.9$. The 'real' wind velocity at T1 was derived from the power output by interpolation using the inverse power curve of the machine. In both cases (measured and CFD) the turbulence intensity shape has two peaks, although the 'measured' values predict a higher peak of turbulence intensity and a lateral asymmetry. WAsP does not provide results on turbulence intensity and was thus excluded from the turbulence comparison.

8.6.3 Wake of T1 (wind at 67°)

A similar procedure to the one described in Sec. 8.6.2 was followed for the case of T2 operating in the wake of T1 which corresponds to the opposite wind direction of $\approx 67°$. In this case, the terrain upwind of the rotor T1 can be considered more complex, because the slope is steeper. Based on the meteorological data on M25, WAsP predicts a frequency of 1% on Sector 8 (70°).

CFD simulation

The CFD domain and mesh was the same as in the T2 wake case (Sec. 8.6.2) using the opposite direction as shown in Fig. 8.9. The simulation without rotor effects provided the 'real' wind speed, $U_{T1} \approx 9.57$ m/s, as well as the angle at which the flow is deflected by approximately 0.928° towards the North, at T1 hub position. The deflection occurs due to the presence of a hill to the South-east of T1, as shown in Fig. 8.9.

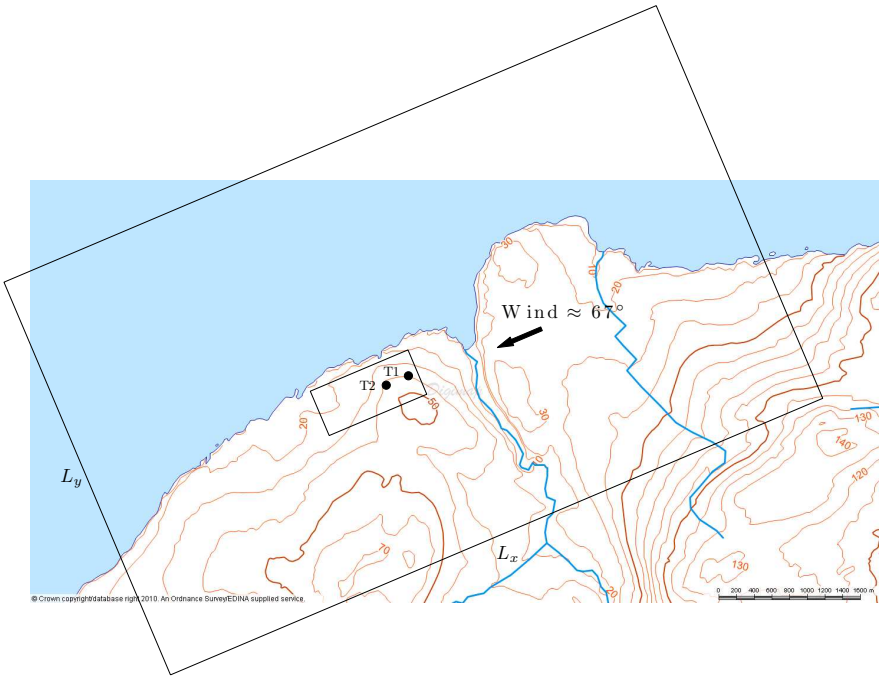

Figure 8.9. T1 wake case and extents of CFD domain and result region.

The 'real' wind speed U_{T1} was used to obtain the rotational speed of the rotor, $\Omega_{T1} = 18.83$ rpm, through interpolation (see Sec. 8.6.1), to be used as input in the VBM. The deflection angle was used to apply a yaw angle of the same magnitude at the disc T1 towards the South assuming that the rotor is facing the wind perpendicularly. This approach is similar to the approach followed by Prospathopoulos et al. [204]. The change of the yaw angle was also incorporated in VBM by changing the 'bank angle' ψ in the model [18], thus $\psi_{T1} = 0.98°$.

Fig. 8.10 shows the contour plots of u for the case without the effect of the rotor, and u, U_{def} and I_u for the case of T1 wake. The figures on the left refer to the region defined by the small rectangle in Fig. 8.9 at hub-height (with a positive y-direction oriented towards the South-East). Results on the right refer to the $y = 0$ plane defined by the T1 and T2 hub y-position. The variables u, U_{def} and I_u were calculated according to Eqs. (8.5), (8.6) and (8.7) respectively.

The contours of u without the rotor T1 effects (Fig. 8.10a) show an increase of velocity from T1 to T2 as elevation is also increased. Downwind of T2, ground elevation is decreasing leading to a reduction in velocity which is more pronounced to the South (positive y), where the change in elevation is more significant.

Figs. 8.10b and 8.10c show the contours of u and U_{def} respectively with the rotor T1 in operation. The maximum wake deficit seems to occur at $x = 1 - 2$ D downwind of T1. Results on the $y = 0$ plane show that the wake is approximately symmetrical and the wake centre remains at hub-height. According to Fig. 8.10d (left), turbulence intensity is maximized at $x = 0.5 - 1$ D in the wake centre and at the region of approximately $y = \pm 0.5$ D away from the turbine axis, at $x = 2.5 - 4.5$ D. A second increase occurs at $x = 15 - 20$ D downwind, which can be linked to the velocity reduction of that region. Fig. 8.10d (right) indicates that the maximum turbulence intensity is located above hub-height, in agreement with several experimental observations.

Comparison with WAsP and validation with measurements

The measured data were filtered in a similar procedure to the previous case (Sec. 8.6.2), using a criterion of $U_{T1} = 9.5 \pm 0.5$ m/s and averaging at T1 yaw directional bins of 1°. A discrepancy of 6° was found between T1 yaw angle and the wind direction with reference to True North, using the criterion that the maximum wake deficit at T2 occurs when T1 and T2 are aligned to the

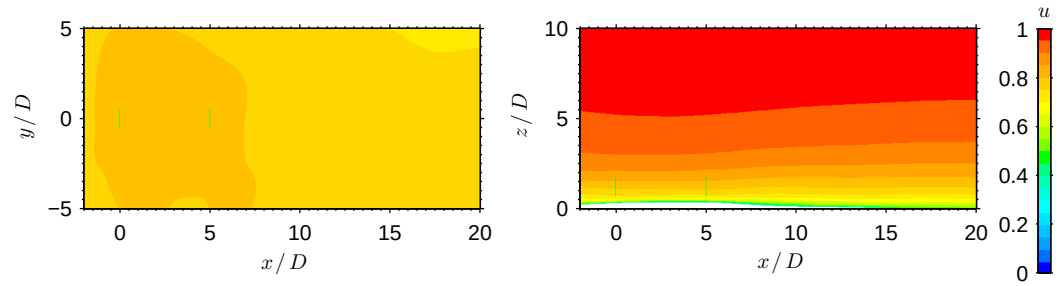

(a) Contours of u, no wake: hub-height (left) and $y = 0$ plane (right)

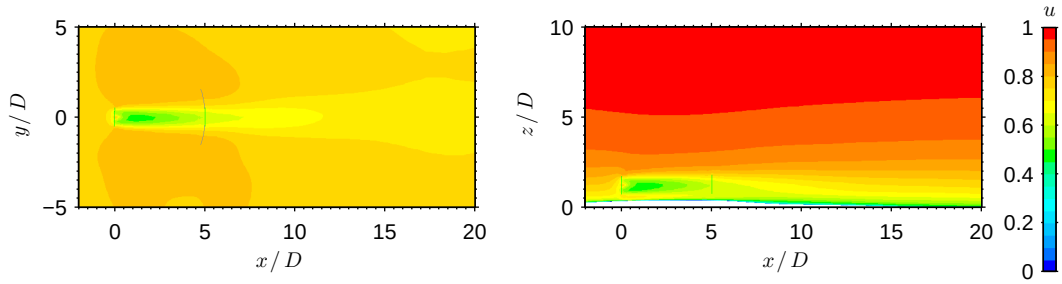

(b) Contours of u, T1 wake: hub-height (left) and $y = 0$ plane (right)

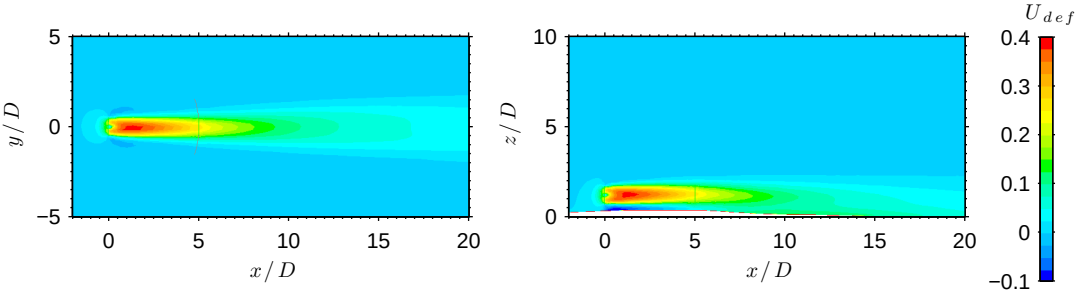

(c) Contours of U_{def}, T1 wake: hub-height (left) and $y = 0$ plane (right)

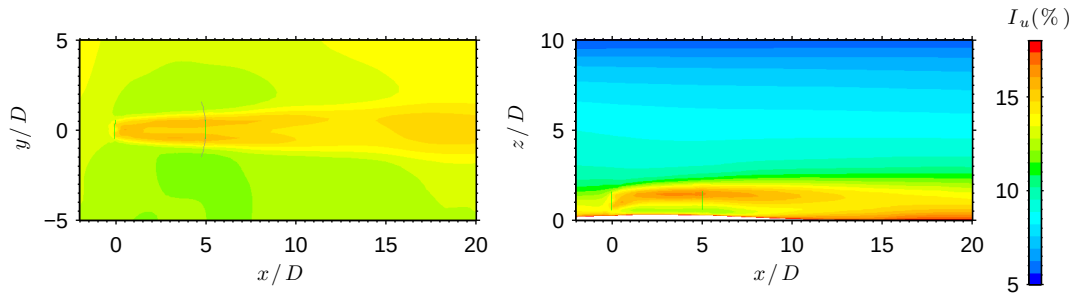

(d) Contours of I_u, T1 wake: hub-height (left) and $y = 0$ plane (right)

Figure 8.10. Contour plots for the case of T1 wake

wind direction. Fig. 8.11 shows a scatter plot of the data, which seem to be non-parametric (not symmetrically distributed).

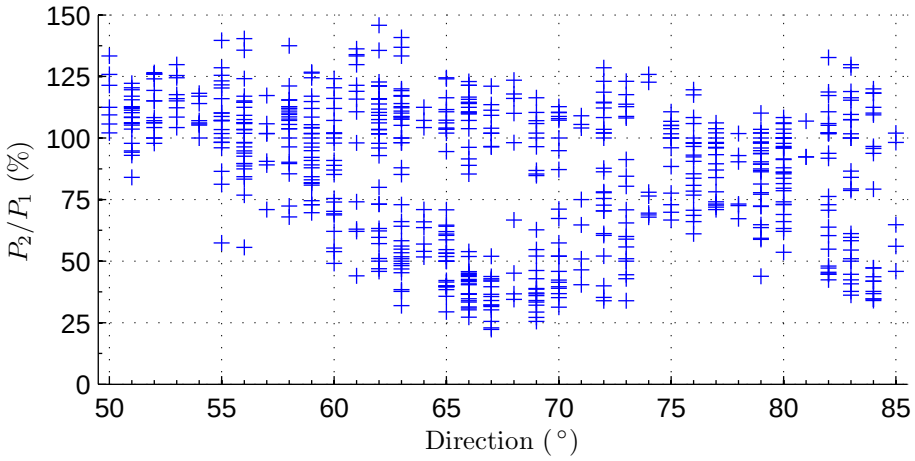

Figure 8.11. Scatter plot of the data - T1 wake.

Results and comparison of the data (median values and interquartile range) and WAsP and CFD simulations in terms of normalised power output (P_2/P_1) is shown in Fig. 8.12. A comparison between WAsP and CFD results, shows that WAsP is predicting a wider, 'top-hat' wake shape which 'flattens' at the region $\pm 5°$ around the centre, whereas CFD predicts a U-shaped wake with a higher deficit near the centre. CFD power estimation near the wake centre is approximately 20% less than the WAsP prediction.

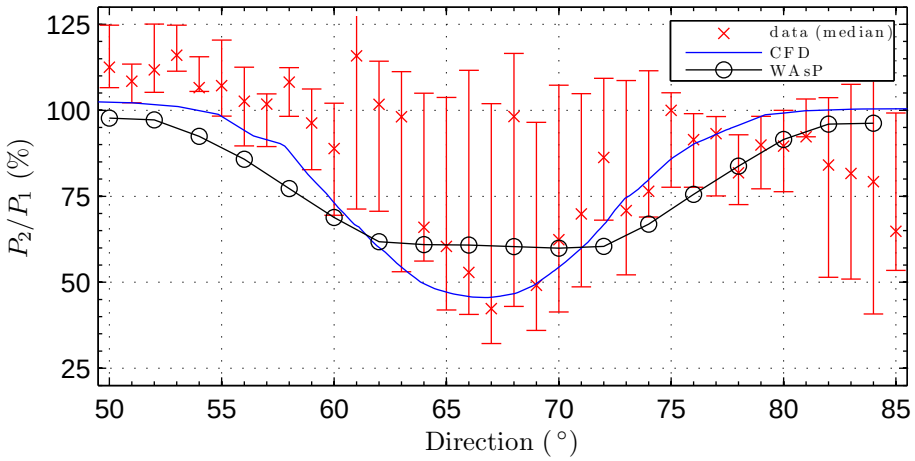

Figure 8.12. Comparison and validation with WAsP and measurements - T1 wake.

The 'measured' data seem to be highly skewed near the wake centre, while the

averages seem to have a second drop for South-Eastern wind directions $> 80°$, which can be attributed to the terrain complexity, such as a hill presence which could have changed the power output ratio between T1 and T2 rotors. WAsP and CFD cannot account for the latter effects, since they only consider a single wind direction. The CFD prediction seems to match better with the median values as compared to the WAsP results. The CFD wake shape and width are also better predicted.

In comparison with the previously examined wake of T2, it can be concluded that the wake over a downwards slope (T2 wake in Fig. 8.7) is wider and more pronounced than the wake over an upwards slope (T1 wake, Fig. 8.12). This was found in both the measured averages and the CFD predictions, whereas WAsP predicted a similar wake in both cases.

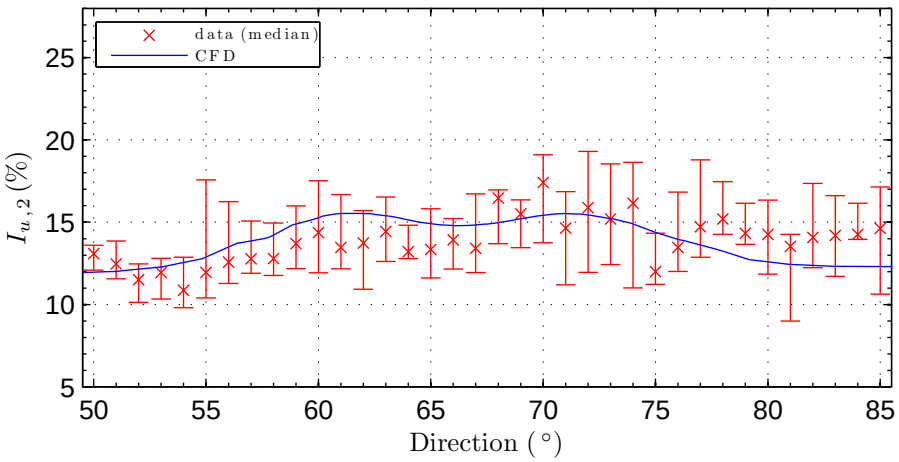

Figure 8.13. Turbulence intensity - T1 wake.

Fig. 8.13 shows a comparison of the turbulence intensity between the CFD predictions and averaged (median) values based on the measurements (see Sec. 8.5.2). The discrepancies are relatively low (maximum of 2.5%) and the double peak of turbulence intensity is found in both the 'measured' averages and the CFD predictions. However, CFD fails to predict the clearly asymmetrical behaviour and errors increase for wind directions $> 80°$.

8.7 Double wake interaction

The second operational phase of the wind farm included the deployment of four additional machines, T3, T8, T9 and T10, positioned as shown in Fig. 8.1. The current section was aimed at studying the combined wake of two rotors aligned to the flow direction and validate CFD and WAsP results with measurements at a third rotor also aligned to the same flow direction.

8.7.1 The 1.3 MW wind turbines

The rotors of the second phase were slightly larger than T1 and T2, with 1.3 MW rated power, 62 m rotor diameter and 47 m hub-height. Their characteristics are outlined in Table 8.4 using information taken from on-line wind turbine databases [294, 295] as well as from manufacturer's technical specifications [296].

Table 8.4. Bonus/Siemens 1.3 MW characteristics

rated power	1.3 MW
rotor orientation, configuration	upwind, 3 blades
rotor diameter	62 m
hub-height	47 m
cut-in, rated, cut-out wind speed	3 m/s , 14 m/s , 25 m/s
cut-in, rated rotor speed	13 rpm , 19 rpm
power regulation	active stall
blade type	LM 29.0
airfoil type	FFA-W3, NACA 63.6xx
rotor tilt	5°
rotor cone	1°
root, tip chord	2.4 m , 0.8 m

The power curve of the 1.3 MW machine is shown in Fig. 8.14a, taken from the WAsP wind turbine database. Fig. 8.14b also shows the derivative of power with respect to the wind speed which was used to derive the turbulence intensity from the measured data according to Eq. (8.4).

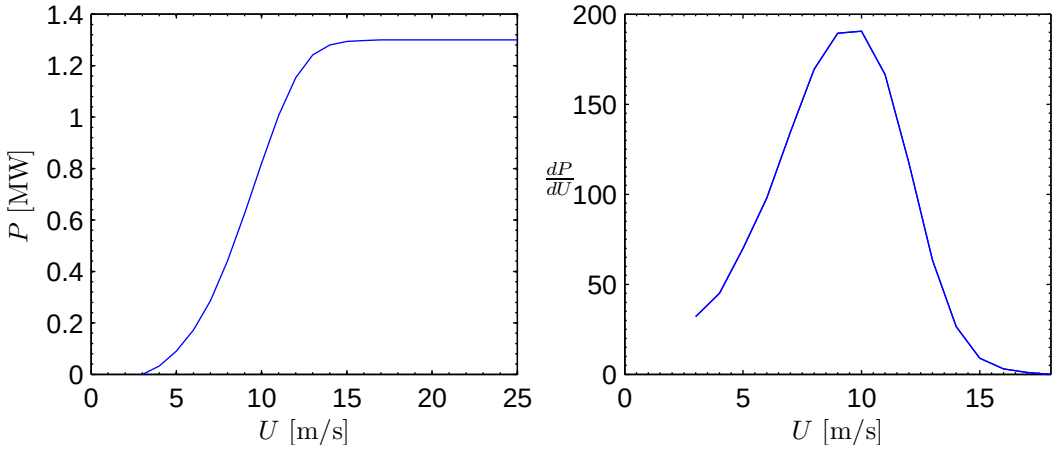

(a) Power curve (b) Power curve derivative

Figure 8.14. Bonus/Siemens 1.3 MW power curve graphs.

Table 8.5. Assumed spanwise distribution of the 1.3 MW blade properties

Node [–]	Radial location r/R	Twist angle [°]	Chord length [m]	Airfoil type [–]
1	0.00	13.0	2.40	Cylinder-1
2	0.09	13.0	2.40	Cylinder-1
3	0.13	13.0	2.40	Cylinder-2
4	0.21	13.0	2.40	FFA-W3-301
5	0.27	11.0	2.30	FFA-W3-301
6	0.37	8.7	2.10	FFA-W3-301
7	0.44	7.2	2.00	FFA-W3-301
8	0.52	5.6	1.90	FFA-W3-241
9	0.60	4.2	1.70	FFA-W3-241
10	0.69	3.0	1.50	NACA 63_3-618
11	0.76	1.7	1.20	NACA 63_3-618
12	0.82	0.8	1.10	NACA 63_3-618
13	0.87	0.5	0.93	NACA 63_3-618
14	0.93	0.2	0.85	NACA 63_3-618
15	0.98	0.1	0.78	NACA 63_3-618
16	1.00	0.0	0.70	NACA 63_3-618

The assumed distribution of the 1.3 MW rotor blade properties is shown in Table 8.5. The spanwise chord and twist distributions were chosen to be the same as in the case of the 1 MW rotor (Table 8.3). However, NACA 63_3-618 airfoil was considered in nodes 10–16 to take into account the characteristics in Table 8.4. The NACA 63_3-618 airfoil information was taken from the NACA

digitized data [254], further expanded to a $-180°$ to $+180°$ angle of attack range using the AirfoilPrep workbook [255].

Similarly to the 1 MW rotor, the rotational speed was calculated assuming a linear relationship with the 'real' wind speed U in the region between cut-in and rated (matching cut-in and rated conditions from Table 8.4), whereas above rated, the rotor speed was taken equal to the constant rated speed (19 rpm).

8.7.2 Wake of T8 and T9 (wind at ≈ 242.4°)

The combined wake of T8 and T9 was initially examined. The case was chosen assuming that T8 and T10 are aligned to the flow, corresponding to a direction of approximately 242.4°. The rotors T8, T9 and T10 are positioned along a descending slope in a close proximity to the steep coast (Fig. 8.1), at a height of 22 m, 19 m and 13 m a.s.l. respectively. They have an inter-spacing of approximately 4 D, where D = 62 m is the diameter of the 1.3 MW rotor. Based on the meteorological data on M25, WAsP predicts a frequency of 4.2% at T8, Sector 25 (240°).

CFD simulation

The CFD domain was enlarged in order to make sure that the outlet boundary does not affect the wake flow. The domain Cartesian dimensions were chosen as $L_x \approx 274$ D , $L_y \approx 64.5$ D and $L_z \approx 40.5$ D. An indication of the domain dimension in the xy plane is shown in the large rectangle of Fig. 8.15. The terrain characteristics not shown were included to extent of the domain.

The simulation was initially run without the rotor effects in order to obtain a desirable 'real' wind speed at T8, $U_{T8} = 9.5$ m/s and estimate the rotational speed of T2 as well as potential change in the wind direction which would require yawing the rotor. Afterwards, the simulation with T8 in operation was run and

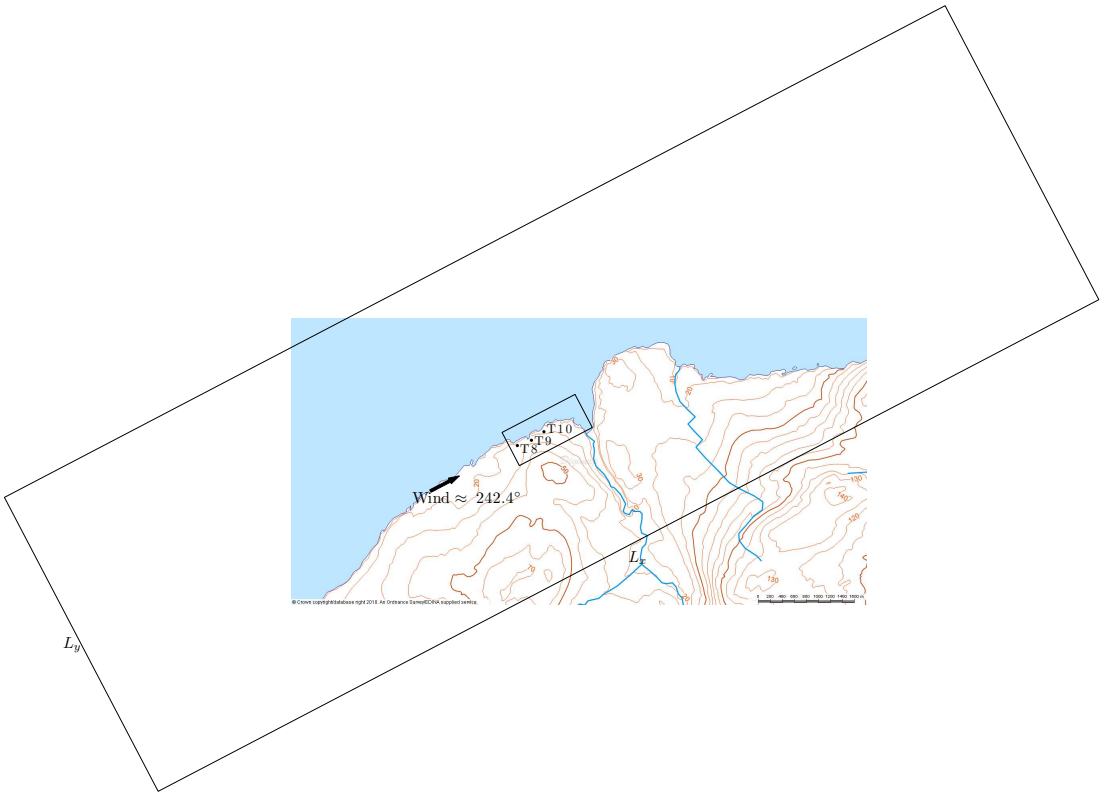

Figure 8.15. CFD selected surfaces (wind at ≈ 242.4°).

velocity and wind direction at T9 rotor were derived, before running the final simulation with both T8 and T9. A yaw of 1.2° to the North was found at T8, thus $\psi_{T1} = 1.2°$.

Fig. 8.16 shows contour results of the undisturbed flow and the combined wake in the region indicated in the small rectangle of Fig. 8.15. As shown in the hub-height figures on the left, the three rotors are not exactly aligned, as T9 is approximately 7° South with respect to the considered wind direction. The complex coastal terrain is responsible for some local fluctuations of the velocity (Fig. 8.16a, left). As T8 and T9 rotors interact, the velocity deficit and turbulence intensity are increased. The velocity deficit seems not to extend vertically, and especially downwind of the second rotor, it seems to decrease in height (Fig. 8.16c, right).

Fig. 8.16d (right) shows once again, that the maximum turbulence intensity is

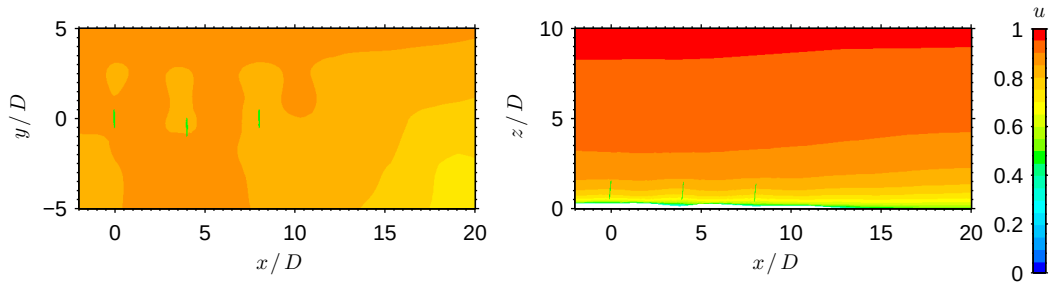

(a) Contours of u, no wake: hub-height (left) and $y = 0$ plane (right)

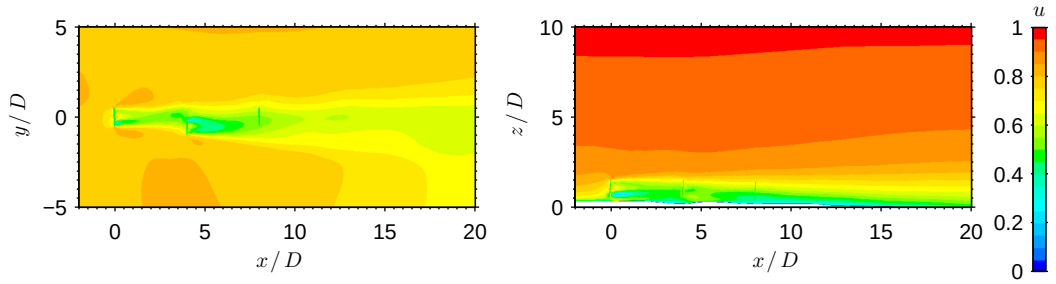

(b) Contours of u, T8 and T9 wake hub-height (left) and $y = 0$ plane (right)

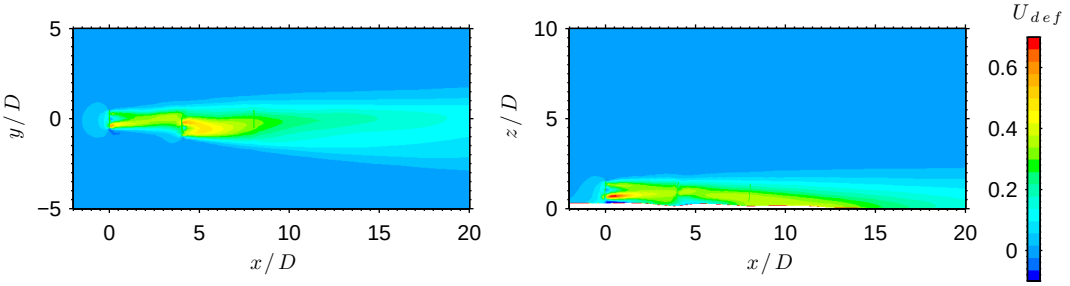

(c) Contours of U_{def}, T8 and T9 wake: hub-height (left) and $y = 0$ plane (right)

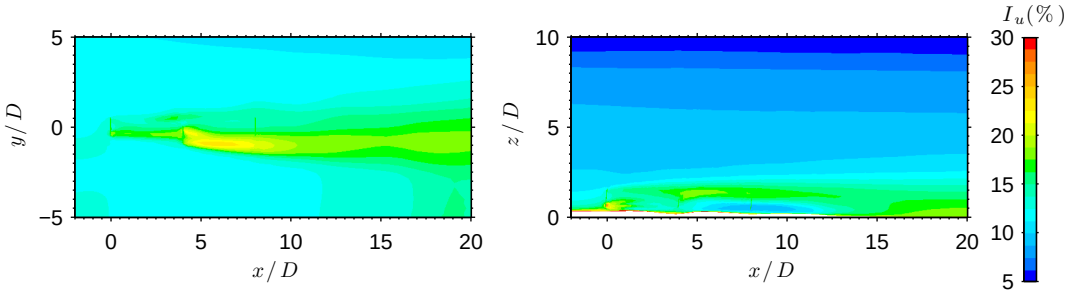

(d) Contours of I_u, T8 and T9 wake: hub-height (left) and $y = 0$ plane (right)

Figure 8.16. Contour plots for the case of T8 and T9 wake

above the turbine axis. A noticeable effect is a significant increase of turbulence intensity downwind of the second rotor, but away from the double wake centre

(Fig. 8.16d, left). This can be attributed to the fact that the wind shear, which is responsible for the production of wake turbulence, is higher on the side between the undisturbed flow and the wake. On the other side, the flow is decelerated due to the wake of the first rotor, thus the wind shear is not so significant. The increase of turbulence intensity on one side of the double wake, may also be responsible for the faster wake dissipation on this side, as shown in Fig. 8.16c (left).

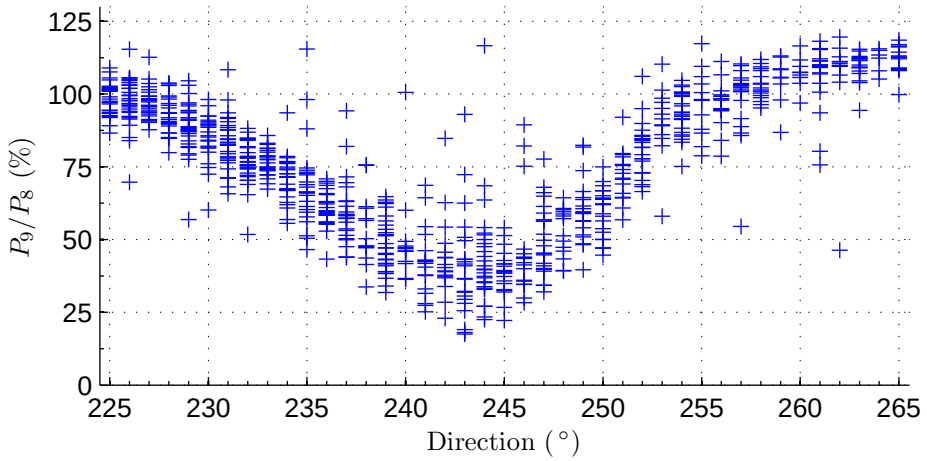

(a) Single wake at T9

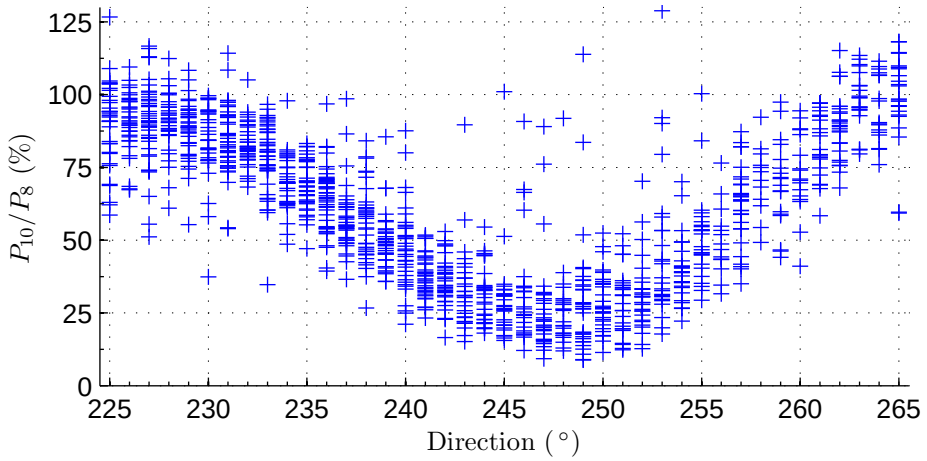

(b) Double wake at T10

Figure 8.17. Scatter plots of the data - T8 and T9 wake.

Comparison with WAsP and validation with measurements

In a similar procedure to the one followed in the previous cases, the CFD results were compared with the corresponding WAsP predictions, as well as the measured data averages, using a criterion of $U_{T8} = 9.5$ m/s for WAsP and $U_{T8} = 9.5 \pm 0.5$ m/s for the data.

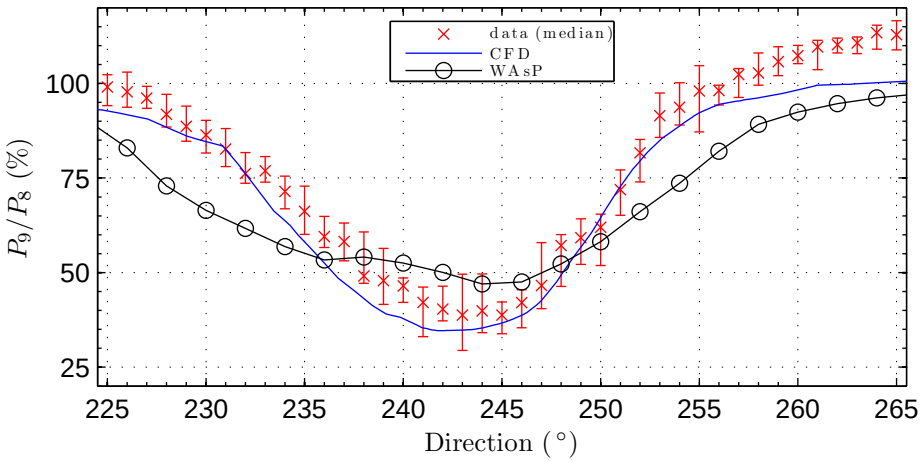

(a) Single wake at T9

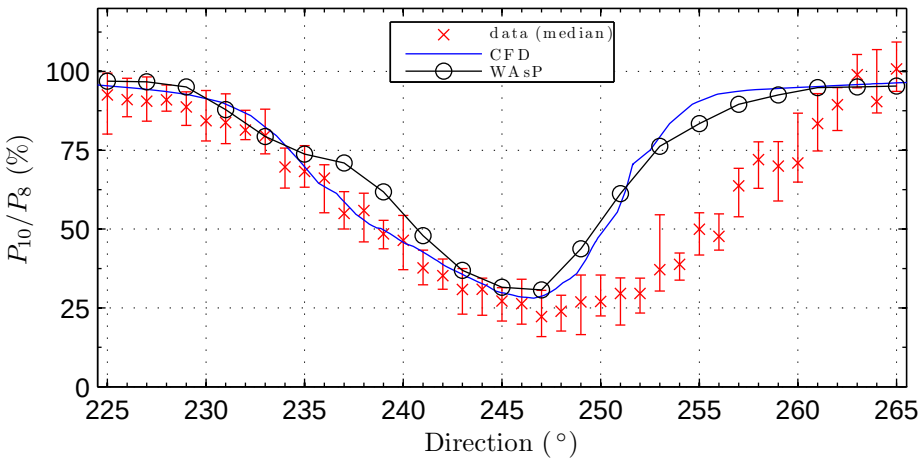

(b) Double wake at T10

Figure 8.18. Comparison with WAsP and measurements - T8 and T9 wake.

Scatter plots of the measured data are shown in Fig. 8.17. Fig. 8.17a represents the single wake of T8 'measured' at T9 and Fig. 8.17b shows the combined wake of T8 and T9 'measured' at T10. In spite of the existence of outliers in the

data, they seem more concentrated as compared to the previous cases (Secs. 8.6.2 and 8.6.3).

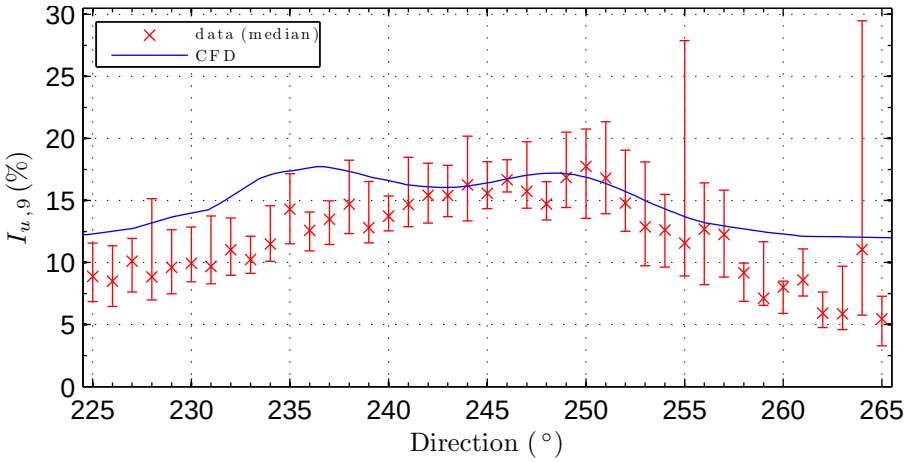

(a) Turbulence intensity of single wake at T9

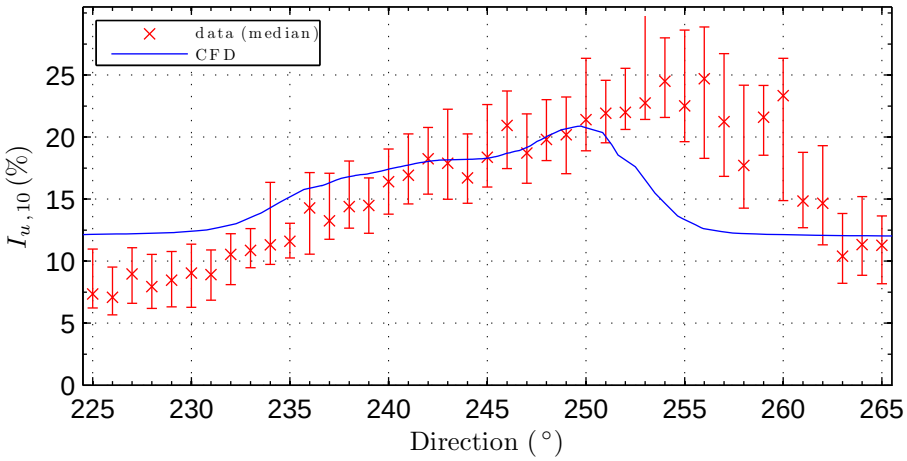

(b) Turbulence intensity of double wake at T10

Figure 8.19. Turbulence intensity - T8 and T9 wake.

The comparison between the 'measured' data and the CFD and WAsP predictions are shown in Fig. 8.18: the single wake of T8 in Fig. 8.18a, and the double wake of T8 and T9 in Fig. 8.18b. The median value and interquartile range are used in the measured data analysis. The validation of the single wake results show a very good match with CFD, whereas WAsP underpredicts the wake deficit near the centre and overpredicts the wake width. The asymmetry of wake output at T10 (Fig. 8.18b) may be partly due to the fact that the three rotors are not aligned,

but it can also be attributed to a faster wake dissipation on one side. Again, CFD results are closer to the measurements than the WAsP results, although the latter are significantly improved in the double wake maximum deficit predictions.

Similarly to the previous cases, the turbulence intensity CFD results are compared with the estimations from the measurements according to the procedure of Sec. 8.5.2. The single wake CFD results (Fig. 8.19a) do not seem to capture a measured local asymmetry, although they are close to the averages near the wake centre. The double wake turbulence intensity however (Fig. 8.19b), is confirmed by the measurements to have an asymmetric shape, due to the higher turbulence production on one side, as explained previously.

8.7.3 Wake of T3 and T2 (wind at ≈ 127.9°)

The combined wake of T3 and T2 was also examined. The rotors T3, T2 and T8 are aligned to a direction of approximately 127.9° as can be seen in Fig. 8.20. They are positioned at the lee side of a relatively smooth hill with elevation descending downwind: T3 is located at approximately 48 m, T2 at 40 m and T8 at 22 m a.s.l.. T3 and T2 are closely spaced at a distance of approximately 3 D (D = 62 m), while T2 and T8 have a spacing of nearly 5.13 D. Rotors T3 and T8 are of the 1.3 MW type with D = 62 m, whereas rotor T2 is rated 1 MW with D = 54.2. Based on the meteorological data on M25, WAsP predicts a frequency of 2.7% at T3, Sector 14 (130°).

CFD simulation

The CFD Cartesian dimensions were $L_x \approx 274$ D, $L_y \approx 64.5$ D and $L_z \approx 40.3$ D, where D= 62 m and the extends on the xy plane are shown in Fig. 8.20.

Since the predicted mean wind speed was low at T3 for the given wind direction, a 'real' wind speed of $U_{T3} = 8.5$ m/s was pursued at the T3 rotor hub position,

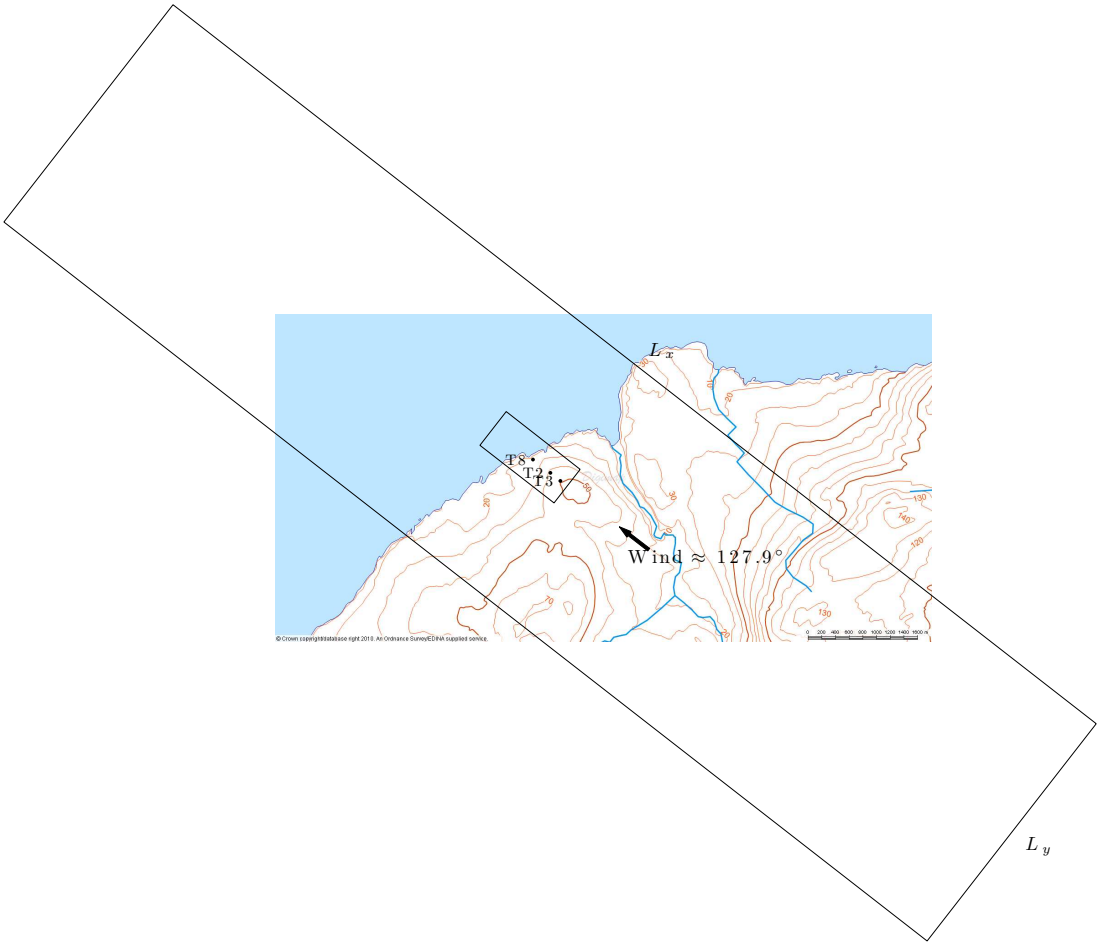

Figure 8.20. CFD selected surfaces (wind at ≈ 127.9°).

from the simulation without the rotor effect. In a similar manner to the previous case (Sec. 8.7.2), the simulation was initially run without the rotors, afterwards with the effect of T3 and finally with the additional effect of T2. Before the 'entry' of each rotor in the simulation, the streamwise wind speed U and the potential deflection angle were calculated at the rotor hub, in order to obtain the rotational speed as well as a potential yaw angle. A yaw angle of 0.92° to the South was found at T2, thus $\psi_{T2} = 1.2°$ in this case.

The contour results of the CFD simulations are shown in Fig. 8.21. The undisturbed flow simulation shows a reduction of wind speed with elevation from the hill towards the steep coast. The close spacing of T3 and T2 creates a

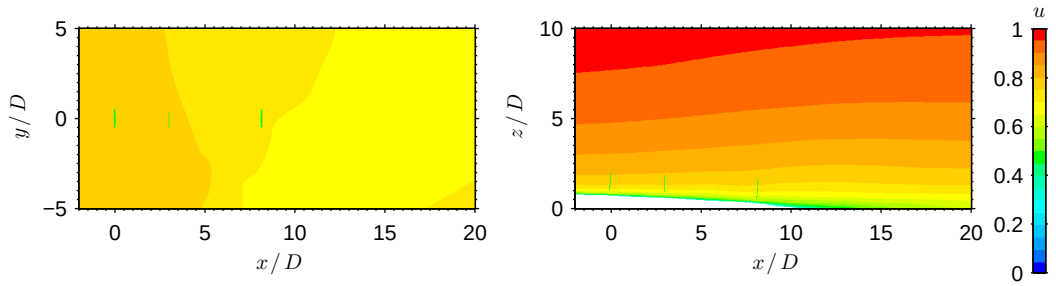

(a) Contours of u, no wake: hub-height (left) and $y = 0$ plane (right)

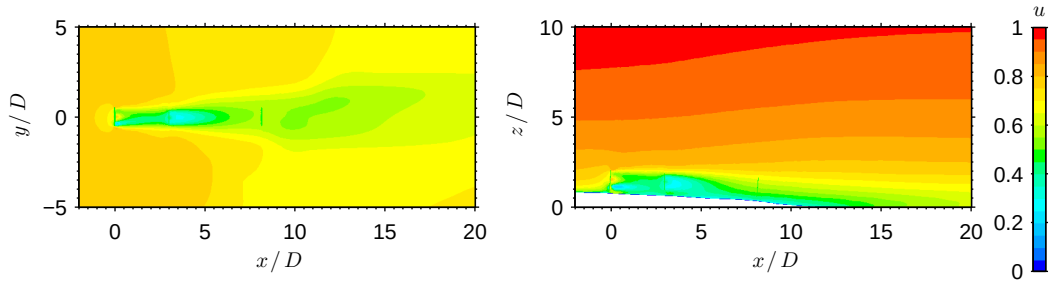

(b) Contours of u, T3 and T2 wake hub-height (left) and $y = 0$ plane (right)

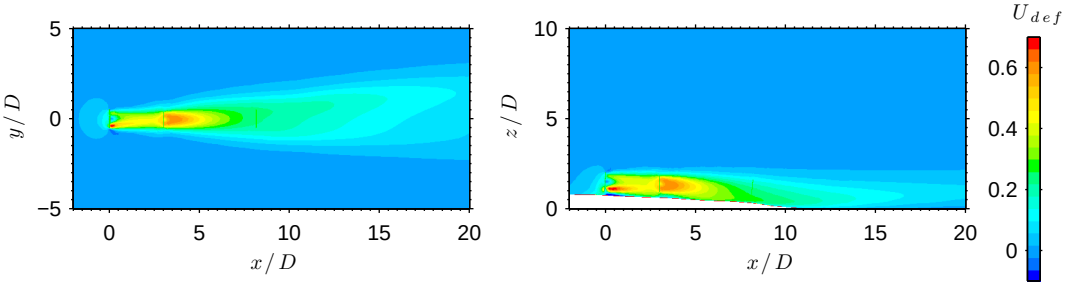

(c) Contours of U_{def}, T3 and T2 wake: hub-height (left) and $y = 0$ plane (right)

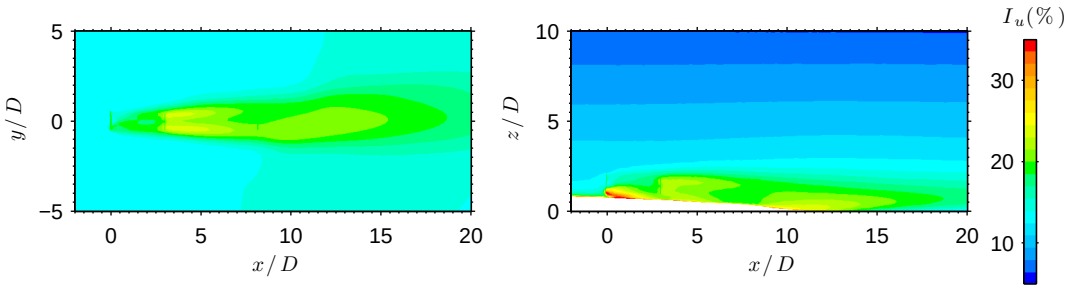

(d) Contours of I_u, T3 and T2 wake: hub-height (left) and $y = 0$ plane (right)

Figure 8.21. Contour plots for the case of T3 and T2 wake

significant deficit in the near wake of T2, with a slight asymmetrical shape at the far wake (Fig. 8.21c, left).

There is also a considerable increase of wake deficit and turbulence intensity in the single wake of T3. The shapes of U_{def} and I_u of T3 wake are asymmetrical in both the lateral and the vertical directions, with the effects being more pronounced near the ground.

The deficit of the double wake seems to follow the hill geometry (Fig. 8.21c, right) with the maximum deficit located below the turbine axis in the far wake. Turbulence intensity is also significantly increased near T2 (Fig. 8.21d, left) and it is maximised at the wake shear layer, up to 2.5 D downwind of T2, and $y = \pm 0.5$ D and $z = \pm 0.5$ D on each side of the turbine axis. At the $y = 0$ plane (Fig. 8.21d, right), turbulence intensity is shown to further increase near the ground, at approximately $x = 10$ D, due to the the terrain slope.

Comparison with WAsP and validation with measurements

The scatter plots of the measured power output at T2 and T8, normalised with the power output at T3, are shown in Fig. 8.22. The data seem non-parametric, especially the values measured at T2 (Fig. 8.22a).

A comparison between CFD and WAsP results with the corresponding data averages is shown in Fig. 8.23. According to Fig. 8.23a, both CFD and WAsP provide a good prediction of the maximum single wake deficit; however, the WAsP 'top-hat' wake shape is wider than the CFD predictions and the measured averages (median values). Results of the double wake (Fig. 8.23b) are also satisfactory, especially the WAsP predictions, suggesting that the model performs well in moderate slopes and when the rotors are aligned.

Fig. 8.24 shows the turbulence intensity comparison between CFD results and 'measured' averages, following Thomsen and Markkilde-Petersen approach [281]. The single wake comparison (Fig. 8.24a) is not considered satisfactory, since CFD predicts a symmetrical, inverse-W shape of turbulence intensity, instead of capturing the asymmetrical peak near the wake centre. The estimated error is

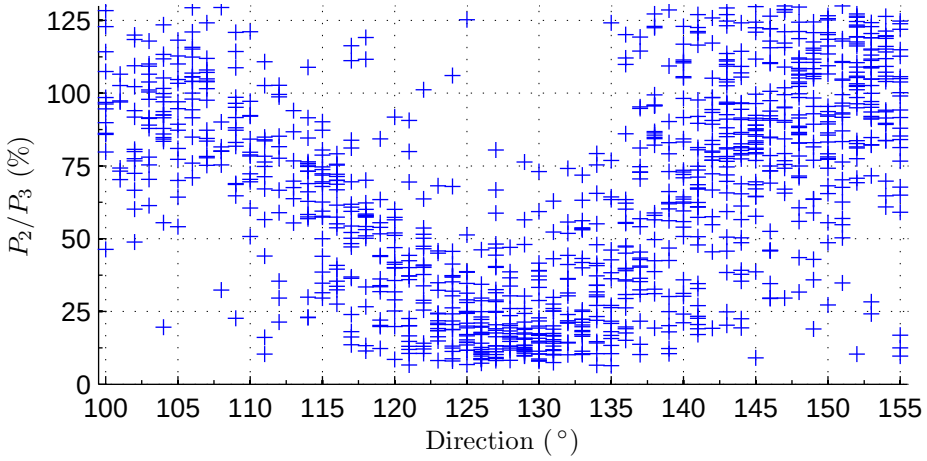

(a) Single wake at T2

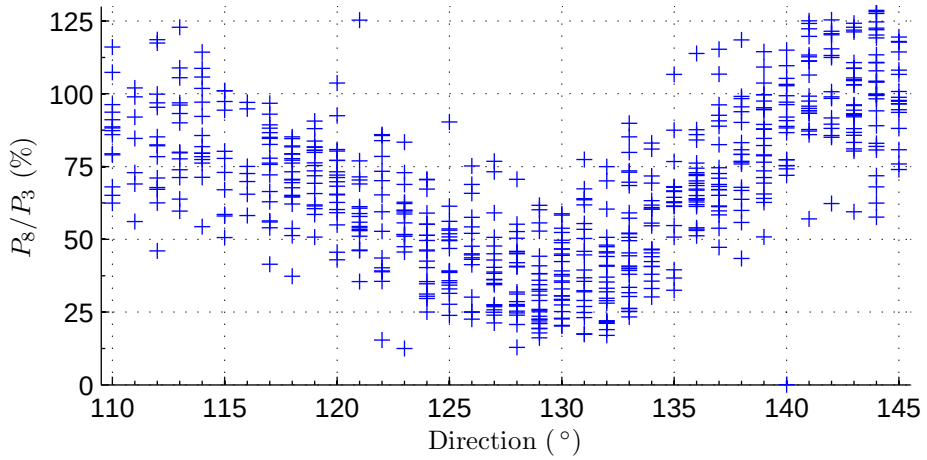

(b) Double wake at T8

Figure 8.22. Scatter plots of the data - T3 and T2 wake.

approximately $5-7\%$ near the wake centre, while away from the centre the error dicreases significantly. The reasons for this discrepancy are not clear, since the rest of the 'measured' average turbulence intensity profiles suggest an inverse-W asymmetrical shape. It is suggested that the peak is related to some factors not taken into account upwind of the rotor or possible faults in the measurements.

The double wake results (Fig.8.24b) are more satisfactory near the wake centre with a maximum error of approximately 2%. The inverse-W shape is correctly predicted, although the 'measured' asymmetry is inverted.

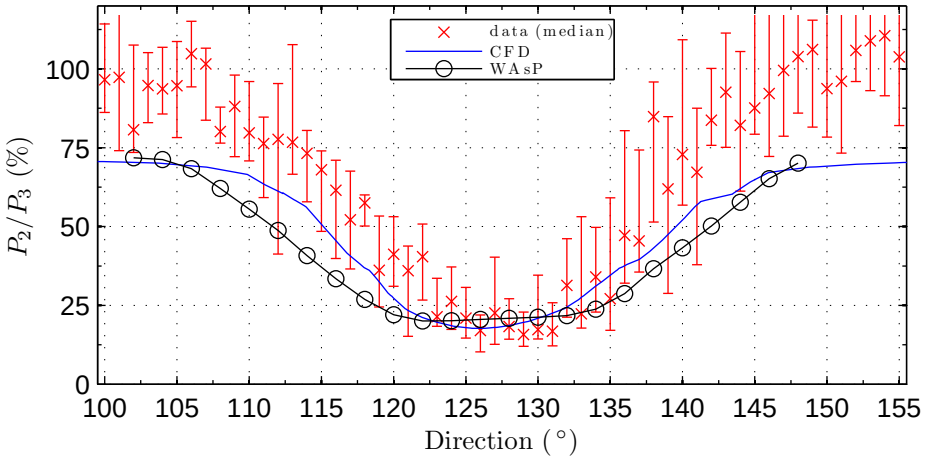

(a) Single wake at T2

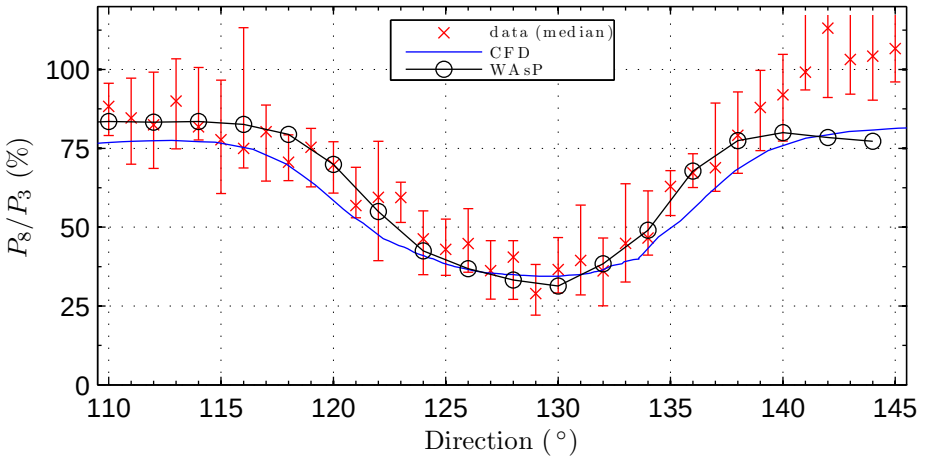

(b) Double wake at T8

Figure 8.23. Comparison with WAsP and measurements - T3 and T2 wake.

8.8 Concluding remarks

Several wake configurations were modelled with CFD and validated against measurements over a small, coastal, complex terrain wind farm. The cases included single and double wakes of wind turbines aligned to the flow direction. Apart from CFD, WAsP simulations were also performed.

According to the CFD simulations, maximum wake turbulence intensity of single wakes was found above the turbine axis, as observed is several other studies including the wind shear (Chapter 2). Two lateral peaks of turbulence intensity

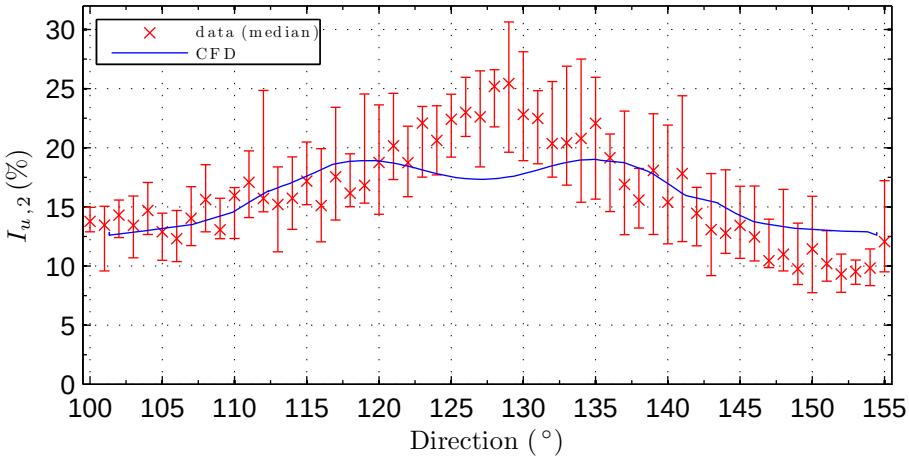

(a) Turbulence intensity of single wake at T2

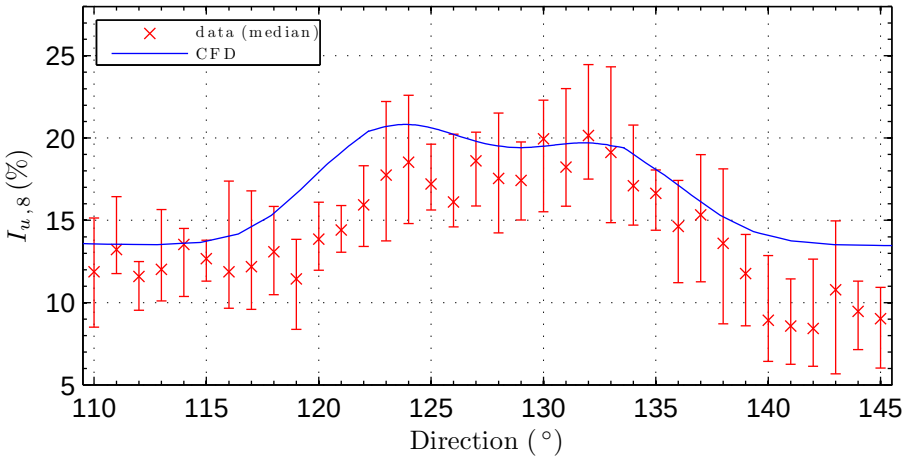

(b) Turbulence intensity of double wake at T8

Figure 8.24. Turbulence intensity - T3 and T2 wake.

were observed in agreement with the measurements. The wake over a downwards slope was found to dissipate more slowly, as compared to the wake over an upwards slope, in agreement with the observations by Taylor and Smith [181] and Smith [182].

The power deficit of a third rotor operating in the double wake, was found to be comparable to (and in some cases lower than) the power deficit of the single wake at the second rotor. A significant observation was that when the two rotors were not exactly aligned, the high wind shear on one lateral side, resulted in significant

turbulence increase and faster dissipation of the double wake on that side, further downstream.

WAsP predictions were in general close to the CFD results and the measurements. However, the 'top-hat' profile applied by WAsP to a single wake, often resulted in predictions with wider wake profiles and lower power deficits in comparison to the measurements and the CFD results. The double wake WAsP predictions were better than the single wake predictions, both in terms of wake shape and maximum wake deficit.

Chapter 9

Case Study 2: Complex terrain wind farm near forests

9.1 Introduction

In this Chapter, the influence of forest canopies on wind turbine wakes and wind farm power output is investigated. Previously established approaches of modelling real complex terrain wind farms (Chapter 8) and forest canopies (Chapter 7) were applied to the case of a relatively highly complex terrain wind farm. The results were validated with SCADA measurements, which were provided by RES.

The issue of the effects of forest canopies on the operation of wind farms was previously addressed in the Workshop on the Influence of Trees on Wind Farm Energy Yields [297], organised by the BWEA (British Wind Energy Association). Highlighted problems were the reduction of wind speed, the increase of turbulence intensity and the increase of wind shear. Ignoring the effect of forests may be the reason for an overestimation of the power output in a resource assessment. The increase of turbulence and wind shear affects the turbine loading and power performance. High wind shear also creates problems related to the correct

estimation of the power curves, since it undermines the assumption that the hub-height wind speed is representative of the average wind speed across the rotor disc [298]. There are also added uncertainties to the aforementioned effects, due to the tree growth.

Nielsen and Stiesdal [298] proposed the application of a 'rule of thumb' when siting wind turbines near forest canopies. The approach provides an estimation of the maximum tree height $h_{c,max}$ according to which the wind shear does not exceed the value of 0.2. The three-stage, distance-dependent, linear relationship, relates $h_{c,max}$ with the turbine hub height h_{hub}, diameter D, and distance between the forest edge and the machine $x_{c.edge}$, and it is shown in Eq. (9.1).

$$h_{c,max} = \begin{cases} h_{hub} - 0.67\text{D} & \text{if } x_{c.edge} \leq 5\text{D} \\ h_{hub} - 0.67\text{D} + 0.17\text{D}\left(\frac{x_{c.edge}}{5\text{D}} - 1\right) & \text{if } 5\text{D} \leq x_{c.edge} \leq 10\text{D} \\ \text{no restrictions} & \text{if } x_{c.edge} > 10\text{D} \end{cases} \quad (9.1)$$

Reutter et al. [299] tested the 'rule of thumb' using WAsP in the case of a real forested complex terrain and found it to have a good practicability.

9.2 The wind farm site

The modelled wind farm was sited over a hill with maximum height of approximately 340 m a.s.l., surrounded by various forest canopies. According to the online Corine Land Cover 2000 (CLC2000) database for surface land use [271], the area consists predominantly of pastures, moors and heathland. Using the roughness classification proposed by Silva et al. [273], the ground roughness length was assumed to be 0.03 m.

The various forest canopies included mainly shelter belts, with some additional large forests and new planted trees (3 years old) in the East (Fig. 9.1). The tree

type was predominantly Sitka Spruce; the average height was estimated to be 16 m at the shelter belts, and 18 m at the large forests; the new planted trees were reported 3 years before the data collection to be only 1–2 m tall. As shown in Fig. 9.1, one of the shelter belts was located very close to the rotors T15 and T21, as well as T20 and T22, and was therefore removed as it was expected to affect the performance of the surrounding machines.

The wind farm had an installed power of 28.6 MW and it consisted of a total number of 22 wind turbines, positioned as shown in Fig. 9.1. The spacing was varied with a minimum of 4 D, where D = 62 m is the rotor diameter.

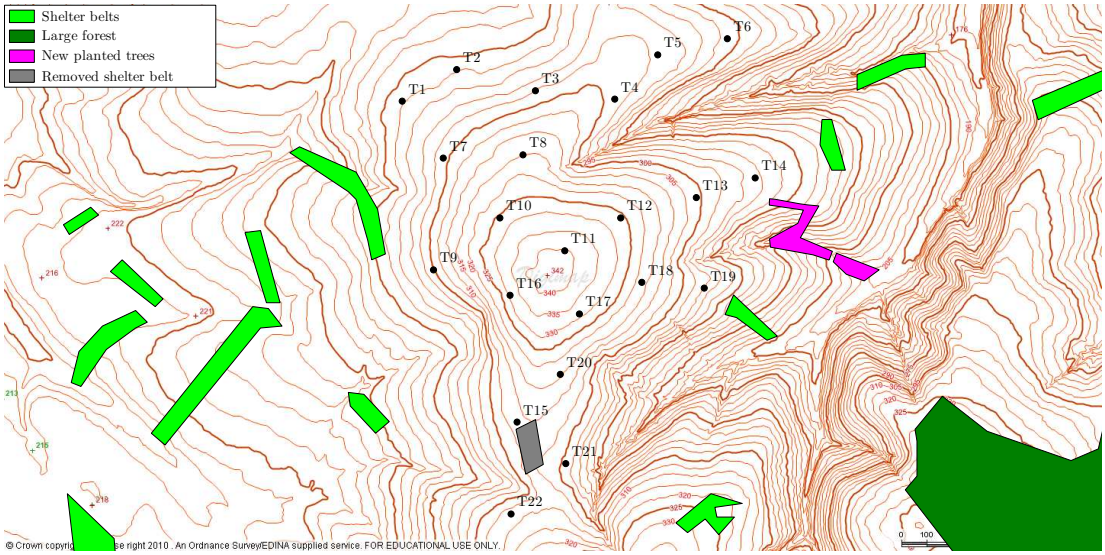

Figure 9.1. The complex terrain wind farm and surrounding forest canopies.

The wind turbines were of similar type to the machines used in the wind farm of Chapter 8: 1.3 MW installed power, a rotor diameter of 62 m and a hub-height of 47 m. Further information can be found in Sec. 8.7.1, while an outline of their main characteristics is shown in Table 8.4.

Additional information was provided for the mean pitch angle of T15 as a function of power output (Fig. 9.2). The data were used for the estimation of the blade pitch angle of all the machines, by interpolation, after estimating the power output. This was calculated using the power curve (Fig. 8.14) and the 'true'

wind speed at the hub (see Sec. 8.5.2). The blade pitch angle in Fig. 9.2) does not exceed the 1°, therefore the wake results are not expected to be very sensitive to changes in the pitch angle.

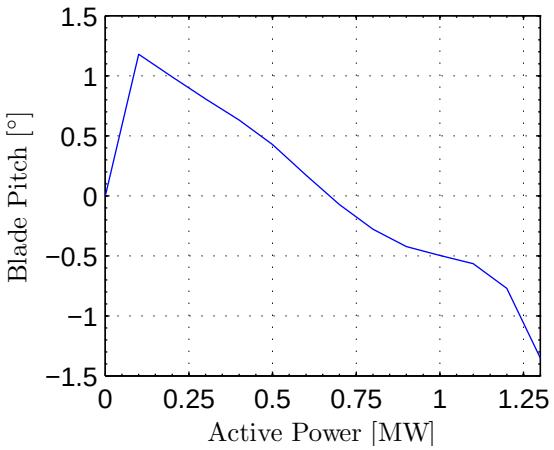

Figure 9.2. Mean blade pitch angle as a function of active power at T15

9.3 Met-Mast data

Wind data were collected before the installation of the wind farm using several Met-Masts at various locations, as shown in Fig. 9.3. The data contained information on wind speed (m/s) measured at anemometers, located at 40 m and 50 m a.g.l. and wind direction with reference to magnetic North, measured by a wind vane at 48.5 m a.g.l..

In a similar approach as in Sec.8.5.1, a wind rose was created for the site, using WAsP and the measurements at M49, since it provided data for a longer period of time. Data from the anemometer at $z_{agl} = 50$ m and the wind vane at $z_{agl} = 48.5$ m were considered as a measurement of wind speed and direction respectively. The wind direction measurements were corrected from a Magnetic North reference to a True North reference, using the procedure of Sec. 8.5.1. The

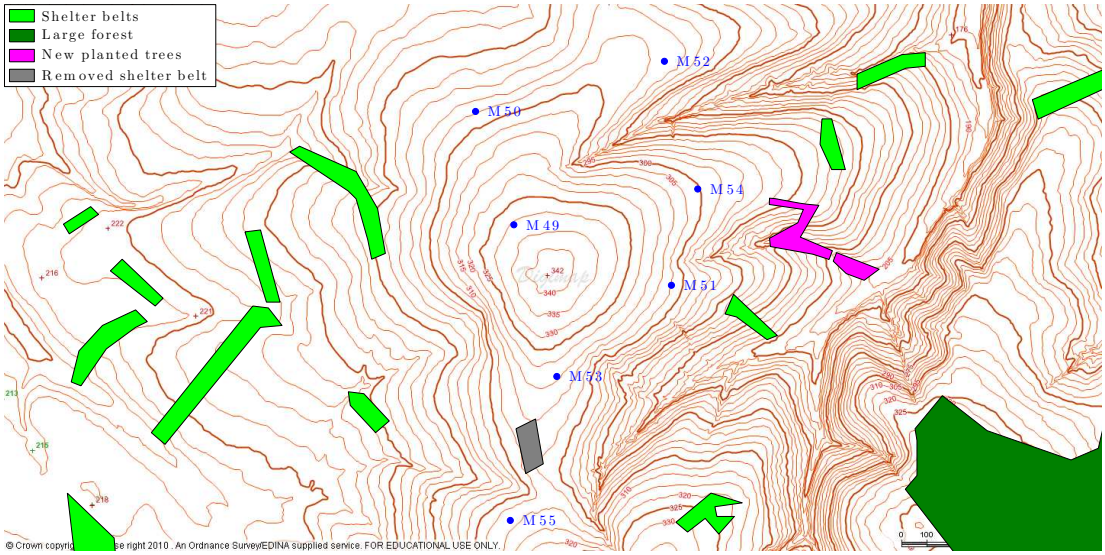

Figure 9.3. Locations of Met-Masts.

magnetic declination for the specific location and measurement date was found to be 4.25°W [280] and was added to the measured wind direction.

In WAsP Climate Analyst, a 'local wind climate' was created and then imported in WAsP along with the digitized map of the site. A regional wind climate was calculated based on the local wind climate [270] and a wind rose was produced, shown in Fig. 9.4. The wind rose shows the % distribution of the wind direction in 36 directional sectors of 10° width. The prevailing wind direction is found to be South West (220°). Based on the created regional Wind Climate, WAsP estimated the total wake losses for the whole wind farm to be approximately 10.11%.

9.4 CFD modeling

9.4.1 General approach

The CFD modelling approach presented in the previous Chapters was also followed in this Chapter. The ground surface was created based on a ∗.xyz grid

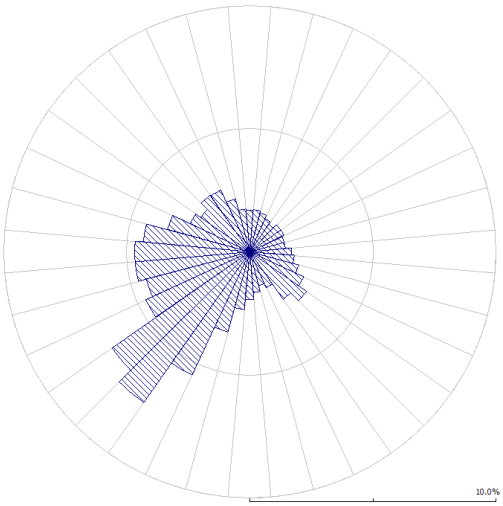

Figure 9.4. WAsP wind rose at $z = 47$ m based on M49 data.

point data file covering an area of 20 km $\times$ 20 km, centred at M49, and a 50 m resolution, totalling a number of 160,801 points. The procedure is described in Sec. 8.3.1.

All cases were initially run without the rotor effects. The streamwise velocity and the deflection angle from the assumed wind direction at the upwind rotor hub location were subsequently obtained and were assumed to correspond to the rotor 'true wind speed' and yaw angle respectively. The 'true wind speed' was used to calculate the rotor rotational speed and blade pitch angle through interpolation. After the calculation of the rotor yaw angle, the domain was re-meshed and the actuator disc was rotated towards the flow direction. The same procedure was followed for all the downwind machines, adding them by the order the appear at the examined wind direction.

9.4.2 Additional mesh considerations

Since the case involved a combination of rotors and forest canopies of varied and complex shape (Fig. 9.1), the mesh was mixed and not only uniform away from the rotors, as it was in Chapter 8.

The domain was split into several volumes in order to simplify the meshing procedure. The volumes which did not include forest or rotor zones were uniformly meshed with hexahedral cuboid or parallelepiped elements using the Hex Map scheme [237]. The volumes including forests or rotors, were meshed with a mix of hexahedral and wedge elements, using the Cooper mesh scheme [237]: The mesh node patterns were swept through the volume using the ground wall face mesh as a 'source'. The ground wall face was meshed using a size function, with the perimeters of the forests and the rotor 'boxes' (see Chapter 4) as sources. Fig. 9.5 shows an example of the meshing approach.

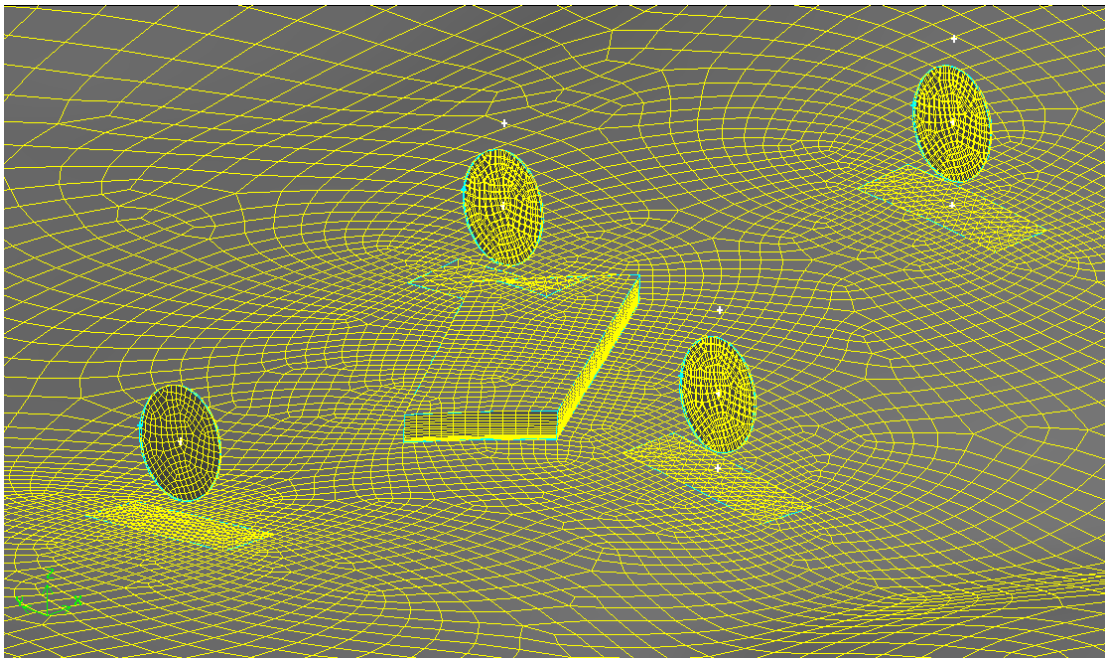

Figure 9.5. Example of meshing of the ground wall face, rotors T22, T21, T15 and T20 and forest F15 (wind at $\approx 199.4°$).

Outside the forest zones, the height of the first cell was 1.2 m. Inside the forest zones, the first cell height was 0.4 m and 13 vertical intervals were used.

9.4.3 Forest model

Modelling of the forest canopies was performed according to the approach in Chapter 7. Certain parameters related to the forest were needed to be estimated, since there was no information for the specific forest. The drag coefficient C_d was considered to have a profile as a function of the normalised height according to Fig. 7.3. The assumed leaf area density profile was based on the estimation of the leaf area index (LAI).

Several values of LAI have been used in the literature for Sitka Spruce forests. Amiro [300] estimated it to be 10 for a 10 m high spruce canopy, Gardiner [156] used a value of 10.2 for a 15 m tree height, while Kerzenmacher and Gardiner [268] considered LAI to be 10.9 in their simulations. Here, a value of 10.2 was considered, since the tree height in the case of Gardiner [156] is very close to the height of the examined forest. However, an unknown level of uncertainty in the calculations may be related to the approximation of the LAI.

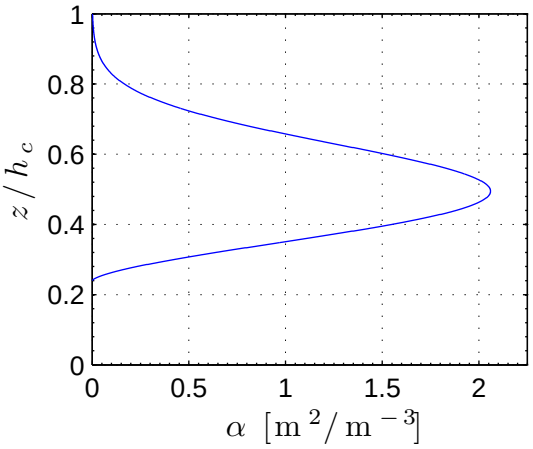

Figure 9.6. LAD profile using a Weibull distribution

The leaf area density profile was created using a Weibull distribution, in a similar way as in Sec. 7.3.2 using $sh = 2.5$, $sc = 5$ and $z_{min} = 3.84$ m in Eq. (7.13). The resulting profile is shown in Fig. 9.6.

9.5 Single wake at T21 (wind at ≈ 310.4°)

9.5.1 Case description

The shelter belt F15 in Fig. 9.22 was removed before the operation of the wind farm, due to expected negative effects in the wind farm performance. It was decided to examine the effects, by running simulations and examining the wake of rotor T15 at T21, both with and without the presence of shelter belt F15.

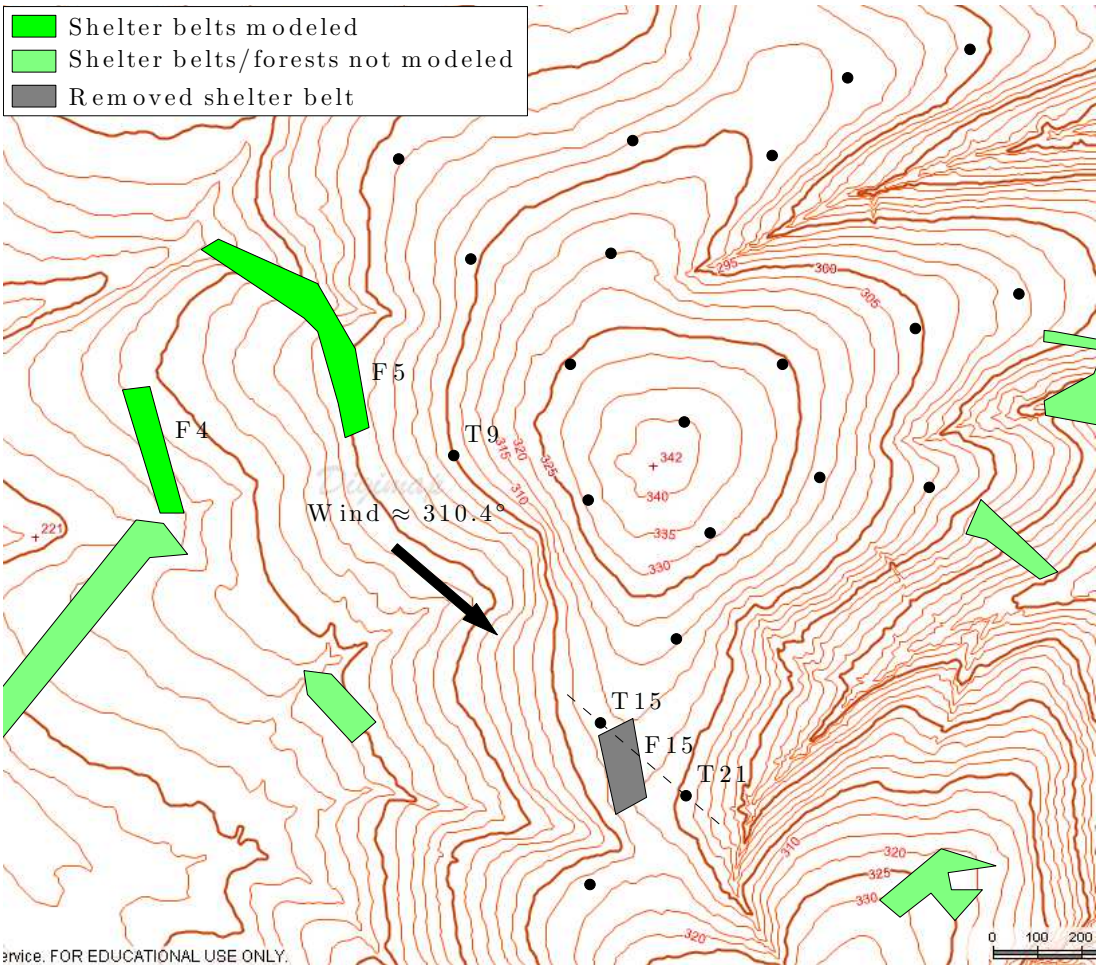

Figure 9.7. Case of ≈ 310.4° map.

The direction of ≈ 310.4° was chosen to approximate the case of T15 and T21 being aligned to the flow, while a large part of the forest belt would have been located in-between (Fig. 9.22). The spacing of the two rotors was relatively

low (4.2 D) and they were operating at different elevations, with T15 positioned higher, at 307 m a.s.l., while T21 was at 295 m a.s.l.; for all the aforementioned reasons, wake effects were expected to be significant.

F15 was chosen to have a mean height of 16 m and was located according to the initial planning (Fig. 9.7). The forest edges would have been very close to T15 (approximately 0.4D), as well as T21 (approximately 1.4D). Applying the rule of thumb of Eq. (9.1), the maximum canopy height is found to be 5.67 m.

Two additional forest belts (F4 and F5), located approximately 13.5 D from T15, as well as rotor T9, were included in the simulations (Fig. 9.7), as it was decided that they might affect the flow upwind of T15, either in terms of added turbulence or of wind speed and direction. The Cartesian dimensions of the CFD domain were $L_x \approx 193.5$ D, $L_y \approx 80.6$ D and $L_z \approx 41.9$ D. Applying the meshing approach explained in Sec. 9.4.2, the total number of cells was $370,044$.

9.5.2 Results and validation

The CFD results were validated with the measurements at T21, filtered according to previously established approaches in Chapter 8. In order to have a common basis for the comparison, the measured data were filtered using a 'true' wind speed bin of 9 ± 0.5 m/s at T15. A scatter plot of the power output at T21 normalised with the power output at T15 is shown in Fig. 9.8.

The comparison between CFD simulations with and without F15 effects was performed by adding or removing the source terms from the F15 fluid zone and running the simulations, without changing the mesh, except if there was a need to redefine the yaw angle of the rotor T15 (see Sec. 9.4.1). Based on the simulations without T15 in operation, the 'true' wind speed and rotor yaw angle were derived and, subsequently, the rotational speed, pitch angle and yaw angle of T15 were calculated.

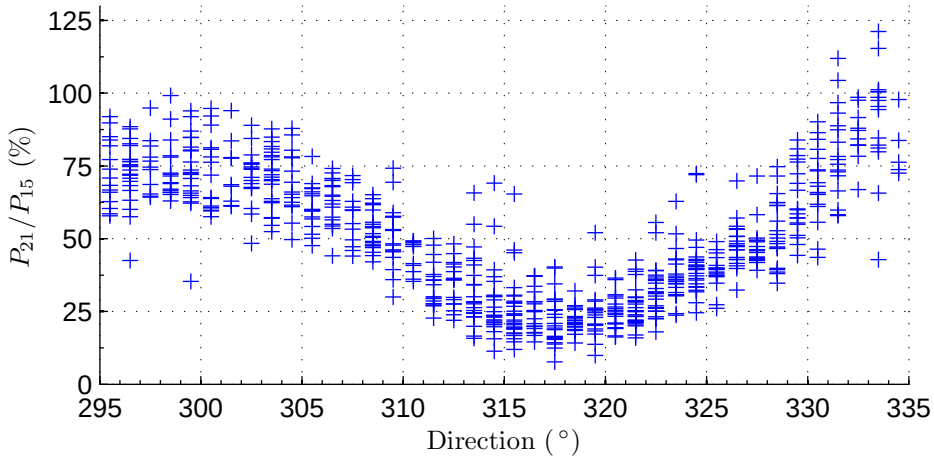

Figure 9.8. Scatter plot of the data at T21.

Table 9.1 shows the calculated T15 properties. It can be seen that the 'true' wind speed is reduced at T15 with the presence of the forest, even though it is located upwind of F15. The yaw angle is also altered by approximately 0.7°. In both cases, the wind direction is different from the assumed direction of 310.4°, which must be attributed to the complexity of the terrain near the rotor.

Table 9.1. Calculated rotor properties at T15.

Rotor [–]	'True' wind speed [m/s]	Yaw angle [°]	Pitch angle [°]	Rot. speed [rpm]
T15 (with F15)	9.00	-6.2	0.112	16.27
T15 (no F15)	9.30	-5.5	−0.031	16.43

In Fig. 9.9, power at T21 was normalised with the power at T15 without the effect of F15. The simulation results without the effect of F15 are very close to the measurements, as expected. The simulations with the inclusion of the forest belt show a reduction in normalised power output by up to 15%.

Fig. 9.10 shows the results of turbulence intensity. The large discrepancies away from the wake centreline may be related to the fact that the CFD results correspond to locations of different height a.s.l. at the lee side of the hill, where turbulence intensity is expected to be higher than the values at the fixed location

of T21, which correspond to the measured data. The increase of turbulence intensity due to the forest belt was found to be significant, approximating a 5% maximum.

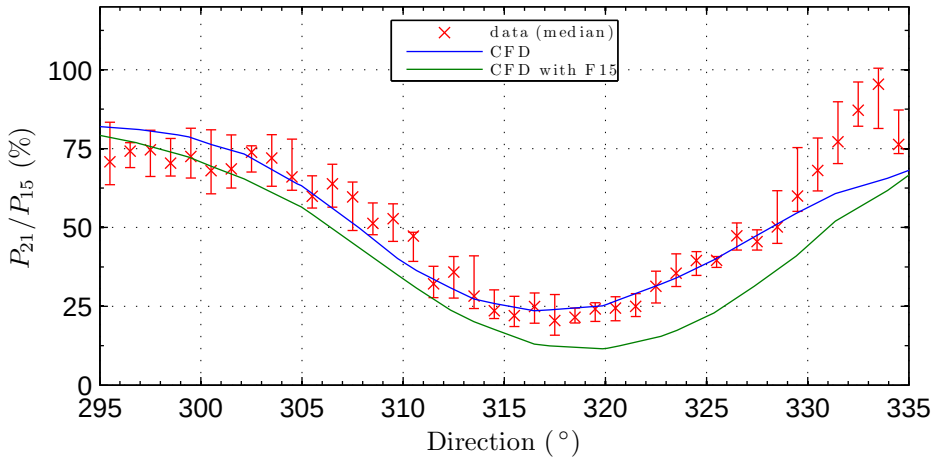

Figure 9.9. Normalised power at T21.

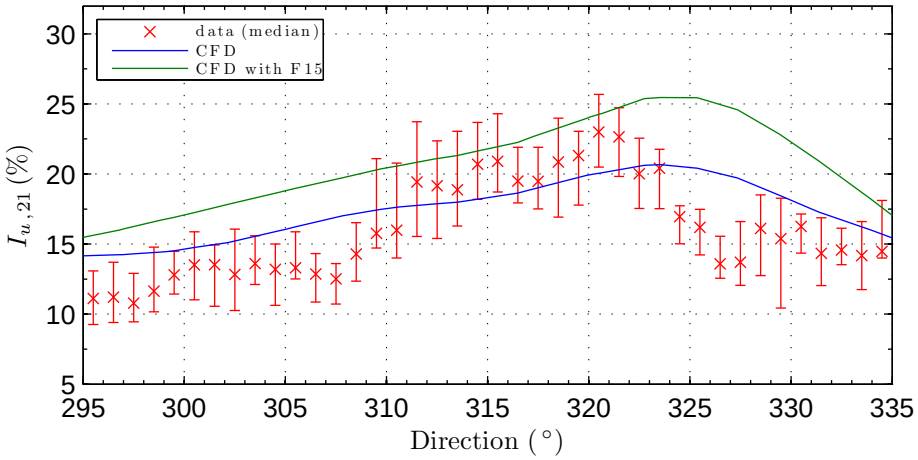

Figure 9.10. Turbulence intensity at T21.

The vertical profiles of streamwise velocity and turbulence intensity of T15 wake at T21 were also examined in Fig. 9.11: with and without the forest belt effects. The undisturbed profiles without wake or forest effects are also shown as a reference. In Fig. 9.11a, streamwise velocity was normalised with the velocity at the top. F15 is found to increase the wind shear of the wake at T21 significantly, while almost exclusively at the region below the hub height, changing the wake U-shape

into a more logarithmic shape. At the lowest rotor height, velocity with the effect of the forest belt is less than half of the wake velocity without F15. The effect in the turbulence intensity vertical profile is also very significant (Fig. 9.11b). It extents from the ground up to the rotor axis, but the most considerable increase is at the lowest rotor height, where it is found to rise by more than 40%.

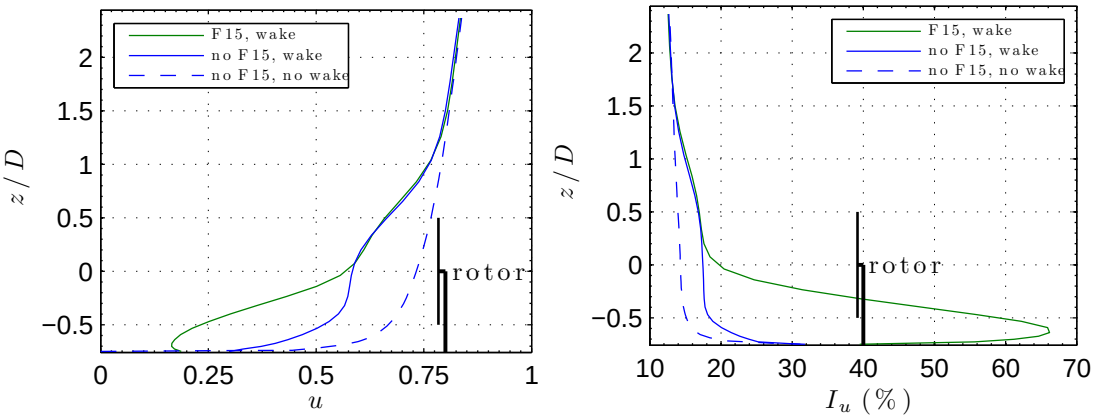

(a) Wind shear (b) Vertical turbulence intensity

Figure 9.11. Effect of F15 on vertical profiles at T21 (T15 wake).

9.5.3 Contour plots

Fig. 9.12 shows contour plots of the results at the xy plane with (left) and without (right) the forest belt F15.

The x axis is aligned with rotors T15 and T21. The meshes of the T15 disc, the forest belt F15 and the arc selected, for the results in Figs. 9.9 and 9.10 are also visible in the contour plots.

Fig. 9.12a shows the normalised streamwise velocity u without the wake effects of T15. The contribution of the forest in the momentum deficit is clearly visible, as it interacts with the wind speed deceleration due to the decrease in elevation.

Fig. 9.12b shows the streamwise velocity contours with the rotor in operation. It can be seen that the rotor yaw is considerable, compared to the assumed wind

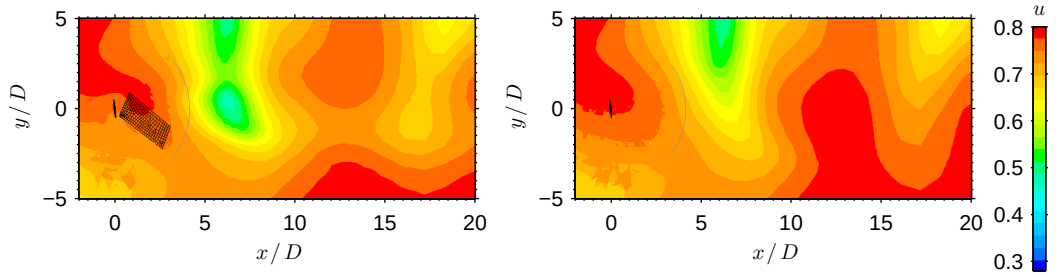

(a) Contours of u, no WT: with (left) and without F15 (right)

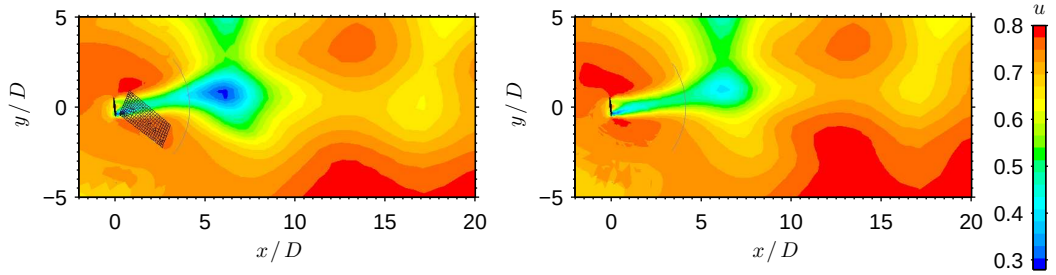

(b) Contours of u, T15 wake: with (left) and without F15 (right)

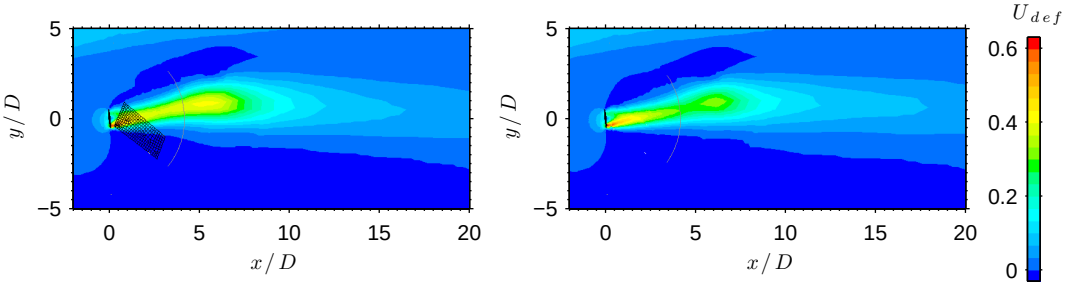

(c) Contours of U_{def}, T15 wake: with (left) and without F15 (right)

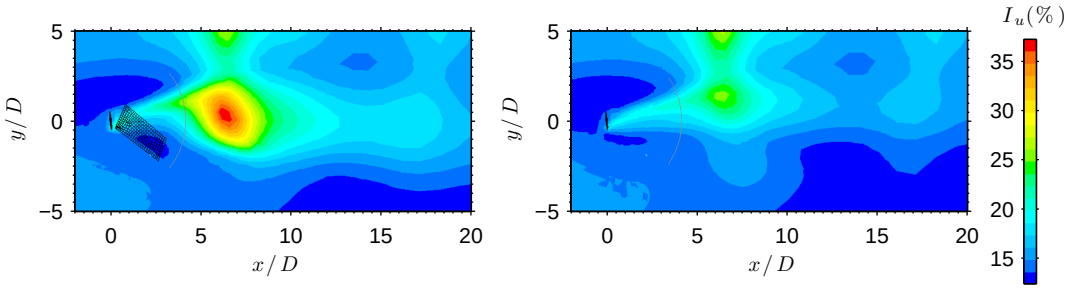

(d) Contours of I_u, T15 wake: with (left) and without F15 (right)

Figure 9.12. Contour plots at the xy plane for the case of T15 wake

direction of $310,4°$, which implies that T21 (also located at $y = 0$) was not inside the wake centre. The effect of the forest widens the wake region and maximizes the velocity deficit, U_{def}, at $x \approx 6$ D downwind (Fig. 9.12c).

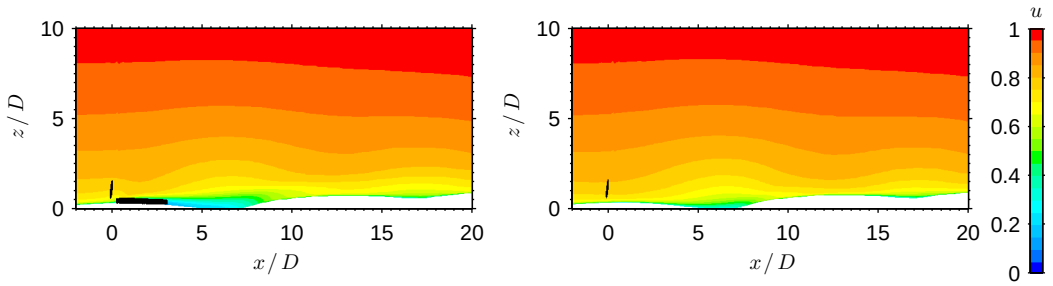

(a) Contours of u, no WT: with (left) and without F15 (right)

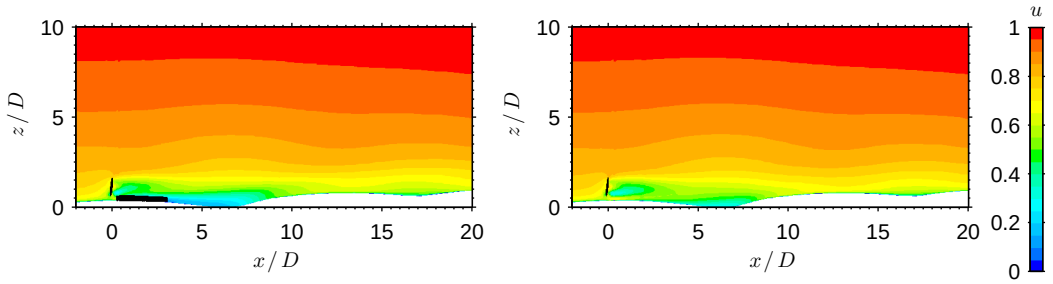

(b) Contours of u, T15 wake: with (left) and without F15 (right)

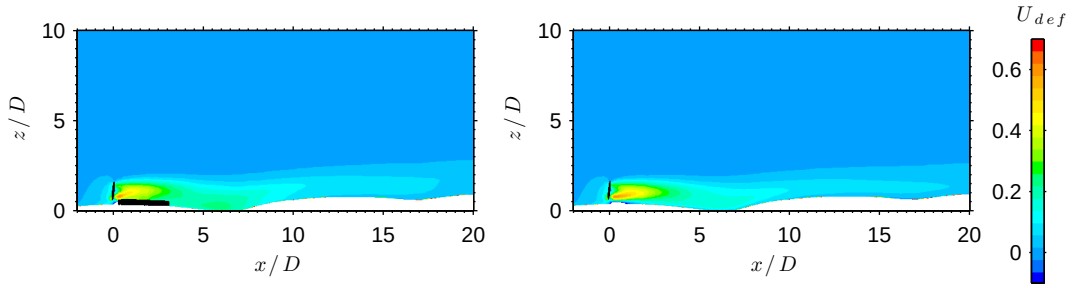

(c) Contours of U_{def}, T15 wake: with (left) and without F15 (right)

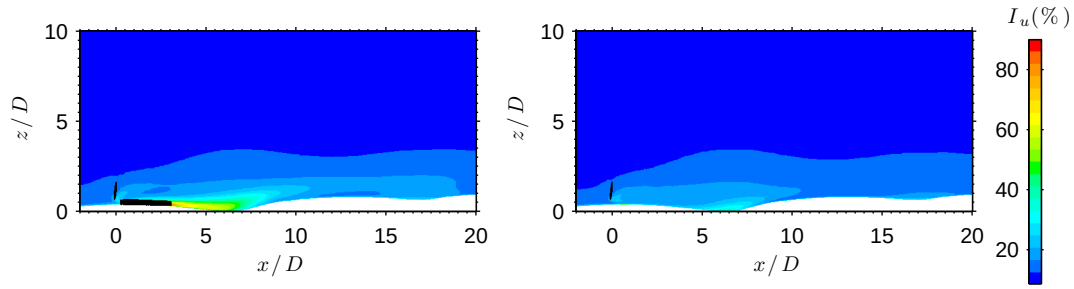

(d) Contours of I_u, T15 wake: with (left) and without F15 (right)

Figure 9.13. Contour plots at the xz plane for the case of T15 wake

According to Fig. 9.12d, there is a significant increase of turbulence intensity I_u due to the forest (left) at $x \approx 6$ D downwind, which is added to the turbulence generated by the wake as well as the hill slope.

Contour plots at the xz axis are shown in Fig. 9.13. In the figures on the left, the region of the forest zone is also shown. In Fig. 9.13a, where no wake was considered, it is clear that the forest decelerates the flow significantly downwind.

The flow deceleration is then intensified when it interacts with the rotor wake (Fig. 9.13b, left). The canopy presence seems to lift the wake centre (maximum deficit) upwards, above the turbine axis (Fig. 9.13c, left). A region of high velocity deficit is also created in the wake of the forest, at a low height.

According to Fig. 9.13d (left), turbulence intensity is also increased significantly in the wake of the forest and the region of high turbulence extents 3 D downwind the canopy edge. The forest wake turbulence intensity seems to move upwards further downstream of the forest. Maximum turbulence in the case without F15 (Fig. 9.13d right) is located further downwind at $x = 5 - 7$ D, created by the hill slope.

9.6 Wake at T20 and T17 (wind at ≈ 199.4°)

9.6.1 Case description

The effect of the forest belt F15 was also examined in the direction of ≈ 199.4°, where T22 is aligned with T20 (Fig. 9.14). The nearest edge of F15 is approximately 3.7 D near T20, well within the limit of the first condition in Nielsen and Stiesdal [298] rule of thumb (9.1).

In order to examine the combined wake at T20 and T17, rotors T22, T21, T15 and T20 were modelled. Information on the spacing between the rotors of interest, as well as the elevation a.s.l. of their locations is shown in Table 9.2. It can be seen that T20 and T17 are positioned towards the upward slope of the hill.

The forest belts F11 and F12 (Fig. 9.14), located approximately 14.8 D upstream of T22, were also included in the simulations in order to include possible

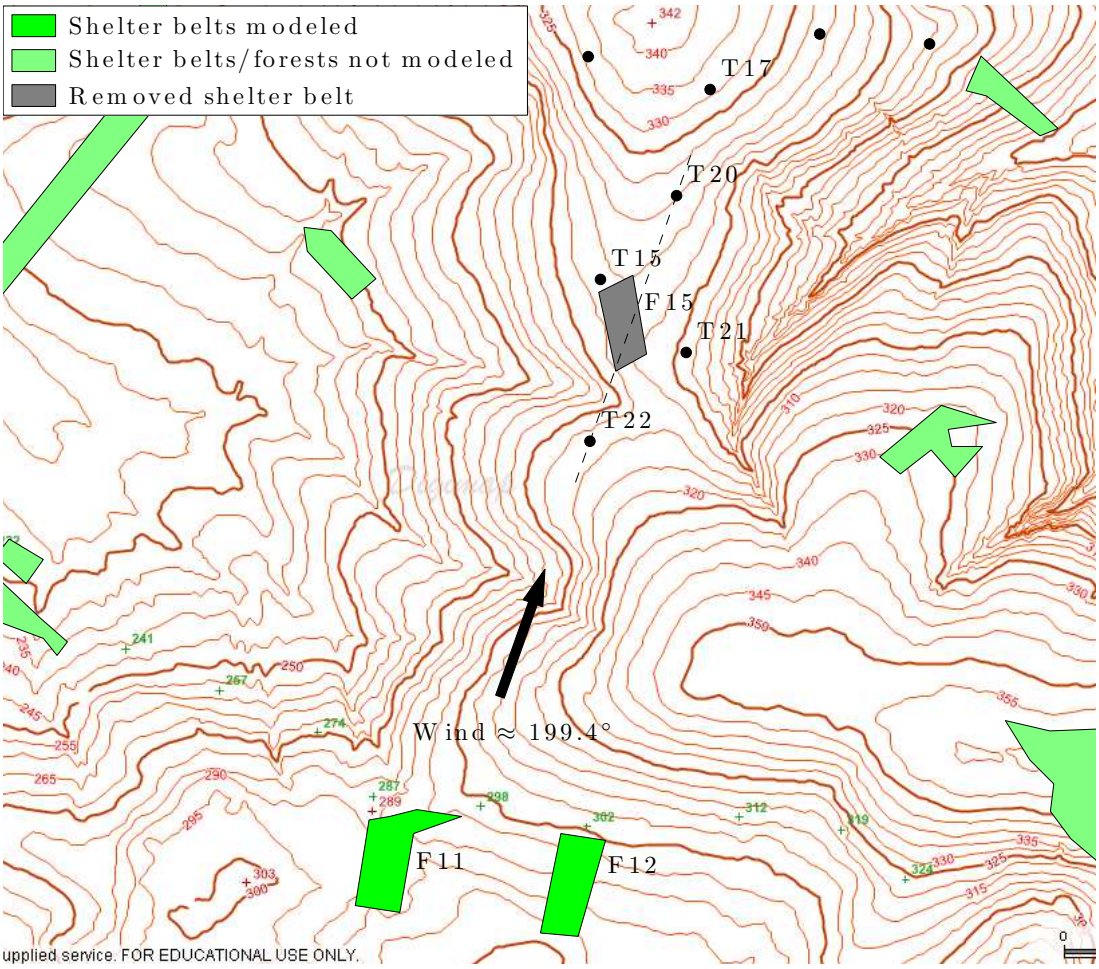

Figure 9.14. Case of ≈ 199.4° map.

Table 9.2. Rotor spacing and elevation (direction of ≈ 199.4°).

Rotor [–]	Distance from T22 [×D]	Elevation [m a.s.l.]	Hub height [m a.g.l.]
T22	–	306	47
T21	4.8	295	47
T15	6.0	307	47
T20	9.6	313	47
T17	13.7	329	47

discrepancies to the flow. The CFD domain, Cartesian dimensions were chosen as $L_x \approx 143$ D, $L_y \approx 65.2$ D and $L_z \approx 41.9$ D and the total number of cells was 492, 389.

9.6.2 Results and validation

The comparisons between the measurements and the CFD simulations were performed at T20 and T17. The measured data were filtered using a 'true' wind speed bin of 8.5 ± 0.5 m/s at T22. The scatter plots of the power output at T20 and T17 normalised with the power output at T22 are shown in Fig. 9.15. The data seem highly non-parametric, especially at T17.

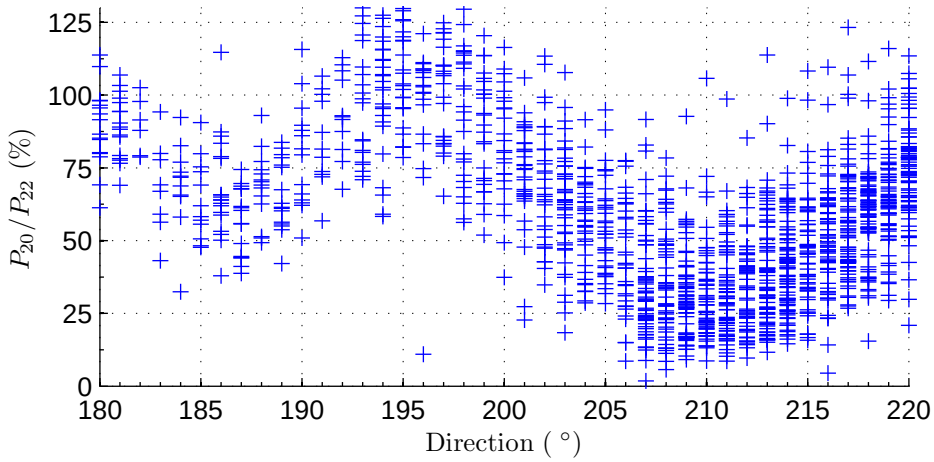

(a) Normalised power at T20

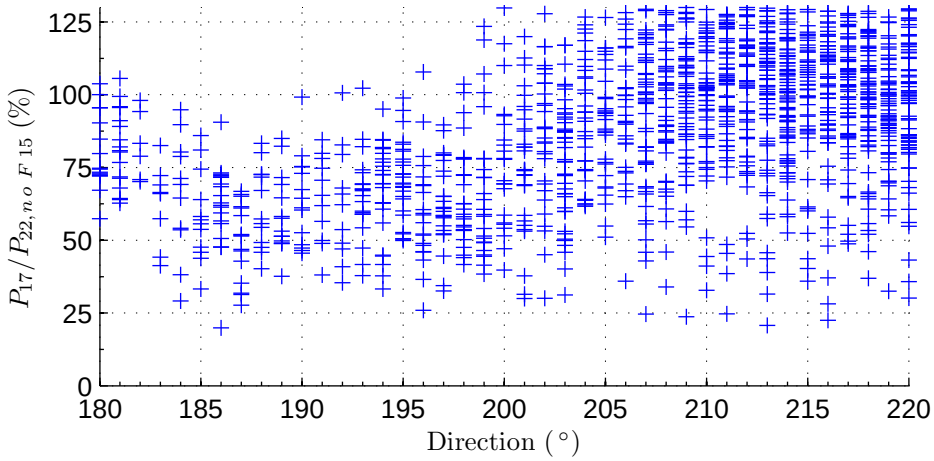

(b) Normalised power at T17

Figure 9.15. Scatter plot of the data at T20 and T17.

As in the previous case, the simulations were run both with and without F15, adding each time the rotor first to the flow. Table 9.3 shows the 'true' wind

speed and yaw and pitch angles, calculated for each of the modelled rotors. As expected, F15 marginally reduces the 'true' wind speed at T22 and affects the wind direction, more significantly at T21, T15 and T20. However, the simulation with F15 shows an increased 'true' wind speed at T21 and T15, which are located on each side facing the flow. This effect, also observed by Irvine et al. [157], Li et al. [269] and Dalpé and Masson [170] has been attributed to the creation of a low-pressure region, just behind the forest edge, extending well above it [170].

Table 9.3. Calculated rotor properties at T22, T21, T15, T20.

Rotor [−]	'True' wind speed [m/s]	Yaw angle [°]	Pitch angle [°]	Rot. speed [rpm]
T22 (F15)	8.65	5.0	0.272	16.08
T22 (no F15)	8.69	4.9	0.246	16.11
T21 (F15)	8.53	8.2	0.329	16.02
T21 (no F15)	8.47	7.9	0.356	15.98
T15 (F15)	8.77	5.5	0.217	16.15
T15 (no F15)	8.69	5.8	0.255	16.10
T20 (F15)	7.74	6.4	0.628	15.59
T20 (no F15)	8.02	6.1	0.539	15.74

Fig. 9.16 presents the validation of the CFD predictions with the data median values, in terms of normalised power output at T20 and T17. The power at T22 without the effect of F15 was taken as a reference for the normalisation.

Fig. 9.16a shows the result with only T22, T21 and T15 in operation. Results without F15 compare relatively well with the measurements near the CFD wind direction (199.4°). However, this is not the case for the entire range of the wind directions, where discrepancies reach more than 25% in some directional bins. F15 seems to increase the power deficit by a maximum of 10% in a directional range of 20°.

The discrepancies between the CFD results and measured median values, may be attributed to the complexity of the case, since the modelled rotors are not aligned to the flow and a change in the wind direction would result in a different wake

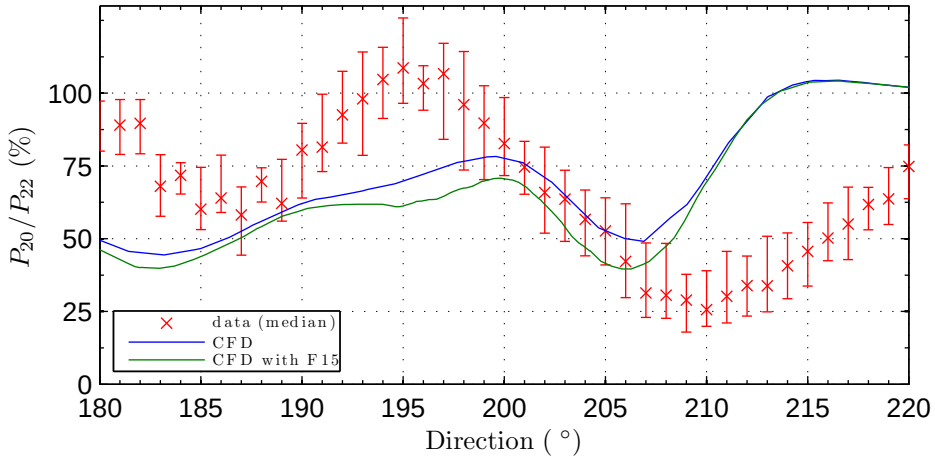

(a) Normalised power at T20

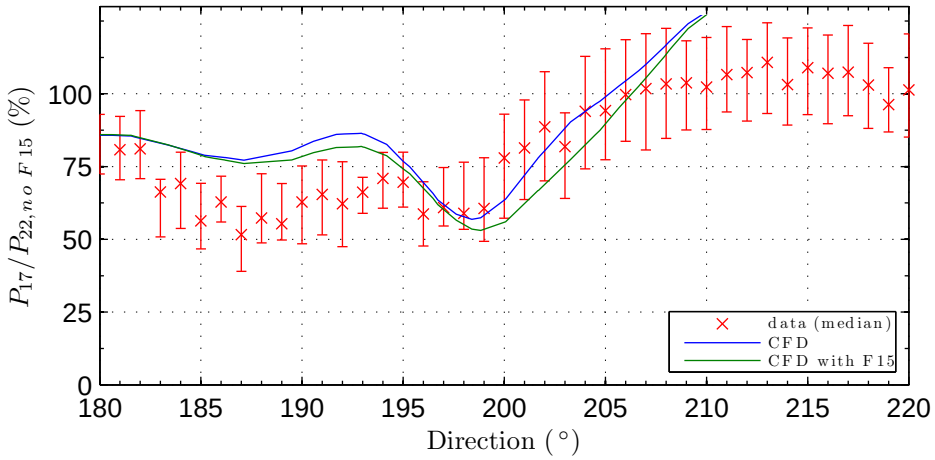

(b) Normalised power at T17

Figure 9.16. Normalised power at T20 and T17.

profile. T22 is also yawed in the CFD case (Table 9.3), as the CFD wind direction at T22 was changed from the initial value of 199.4.

In Fig. 9.16b, four rotors were in operation (T22, T21, T15 and T20). The effect of the forest in the flow remains at a maximum of 10%, although in a smaller directional range. The results compare relatively well with the measurements in the direction of ≈ 204.4°, but similar to Fig. 9.16a, the discrepancies increase significantly, away from the CFD wind direction.

The turbulence intensity profiles are shown in Fig. 9.17. Fig. 9.17a shows the turbulence at T20, with T22, T21 and T15 in operation. Results of the simulations

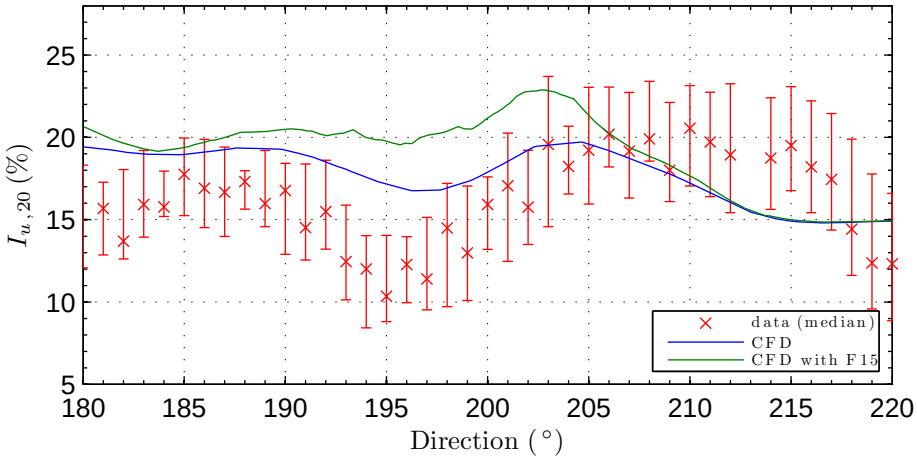

(a) Turbulence intensity at T20

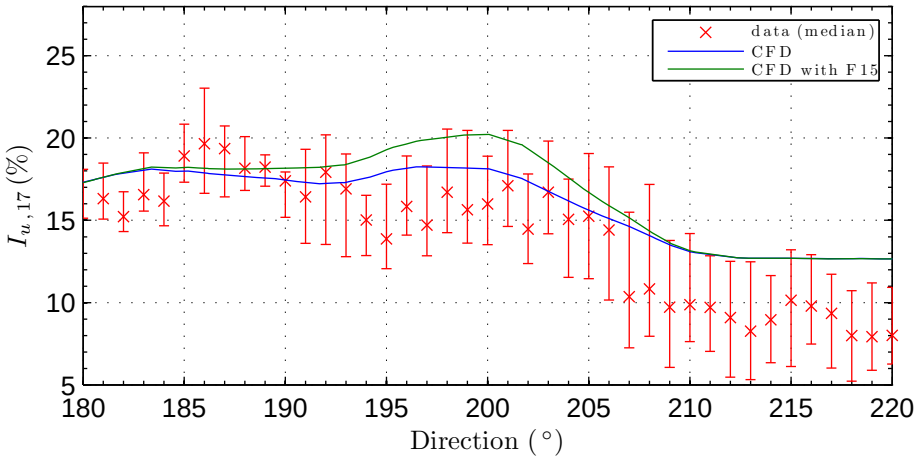

(b) Turbulence intensity at T17

Figure 9.17. Turbulence intensity at T20 and T17.

without F15 compare relatively well, within $1-3\%$, with the averaged results based on the measurements. The forest simulations predict a maximum increase of I_u by approximately 4%, which is the case for a direction of 204.4°. In Fig. 9.17b, the increase in turbulence intensity due to F15 is reduced having a maximum of 2.5% in 200°. Once more, results show small dicrepancies in 204°, but this is not the case for the entire directional range.

The vertical profiles of u and I_u at T20 and T17 were additionally compared in Fig. 9.18. The profiles of the simulation without the effects of F15 or any of the rotors were also included as a reference. In Fig. 9.18a (left), F15 is shown

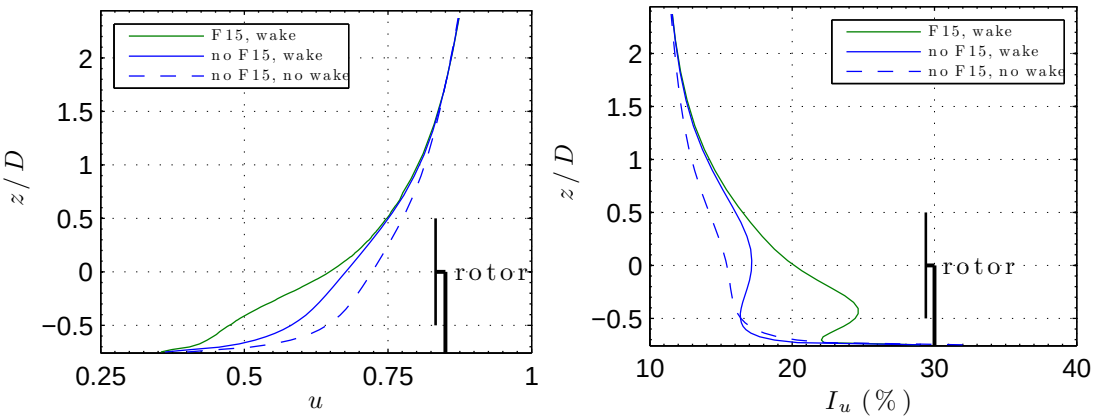

(a) profiles at T20 (T22, T21, T15 wake)

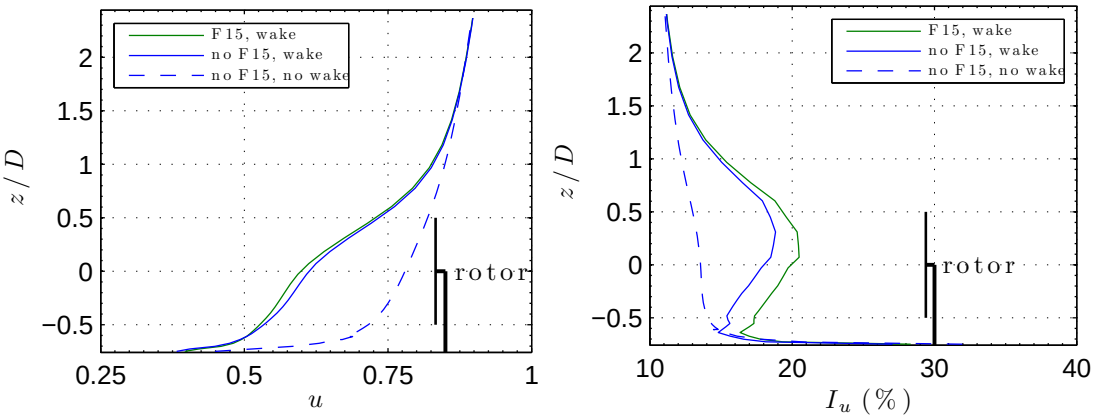

(b) profiles at T17 (T22, T21, T15, T20 wake)

Figure 9.18. Effect of F15 on vertical profiles at T20 and T17.

to increase the wind shear considerably. Turbulence intensity is also increased with F15 and it is almost doubled at the lower region of the rotor. The peak of turbulence intensity is moved downwards, below the turbine axis, instead of above it, which is the case in the simulation without F15. However, the F15 effects are milder in comparison to the results in the previous case (Fig. 9.11), even though the increase of turbulence intensity extents further upwards, even above the turbine axis.

At T17, the effect of F15 in the wind shear is almost negligible (Fig. 9.18b, left). However, turbulence intensity is increased by approximately 2% almost uniformly, up to 1 D above the turbine axis. The presence of the forest seems to assist in the downwards displacement of the turbulence intensity maximum.

9.6.3 Contour plots

The contour plots of the CFD simulation results in the xy plane with and without F15 are shown in Fig. 9.19.

The direction of the x axis was chosen to coincide with inlet wind flow direction (199.4°) and the origins of x and y axis where chosen at the T22 hub location. In Fig. 9.19a (left), it shown that F15 adds to the momentum deficit in the simulation without the rotor effects downwind as well as upwind the canopy. However, it contributes to a slight increase of velocity at the rotors placed alongside, facing the wind. At the location of T22, velocity is reduced due to the descending slope of the terrain, but velocity is increasing downwind of T20, towards the hilltop.

Figs. 9.19b and 9.19c show the wake velocity interactions in the xy plane. F15 seems to enforce the wake mixing of T15 and T20. The turbulence intensity increase in the effect of F15 is visible in Fig. 9.19d, especially in the wake of T20.

Contour plots are also shown in the xz plane ($y = 0$) in Fig. 9.20. Fig. 9.21 shows a more detailed view of the effect of the forest F15. T22, T20 and F15 are visible in the figures, whereas T21 and T15 were not shown, since they are not coplanar with the $y = 0$ plane. The upwards slope of the hill is also visible downwind of T20. The momentum deficit of F15 in Fig. 9.21a is added to the wake deficit in Fig. 9.21b clearly increasing the wind shear at T20.

A comparison of the velocity deficit in Fig. 9.20c indicates that the wake profile of T20 is altered by the presence of F15: maximum wake deficit is located above the rotor axis at $x = 1 - 5$ D downwind of T20, whereas in the case without the forest effects, the maximum deficit remains below the hub height.

In Fig. 9.20d (left) and Fig. 9.21d, turbulence intensity is significantly increased in the wake of the forest F15. The presence of the forest also creates a second peak at the lowest region of rotor T20. However, in both cases (with and without F15),

turbulence is reduced downwind of T20, due to the upward hill slope (Fig. 9.20d).

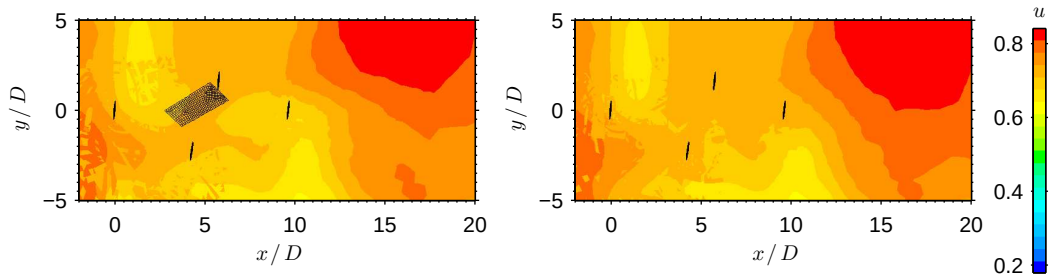

(a) Contours of u, no WT: with (left) and without F15 (right)

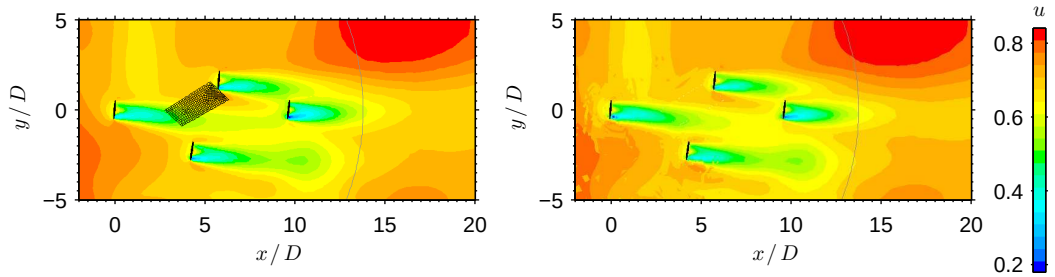

(b) Contours of u, T22, T21, T15 wake: with (left) and without F15 (right)

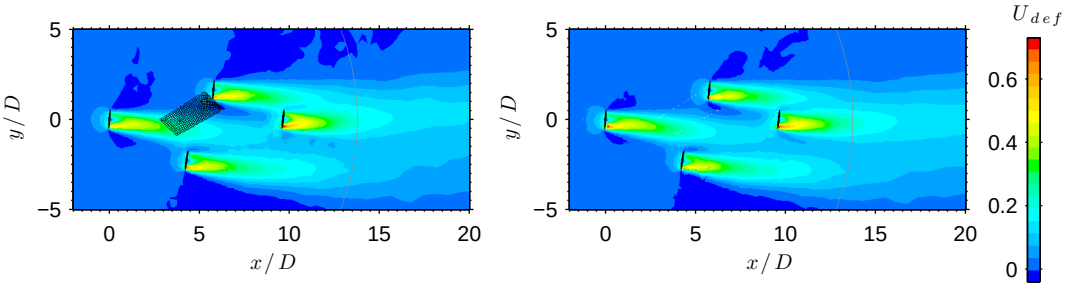

(c) Contours of U_{def}, T22, T21, T15 wake: with (left) and without F15 (right)

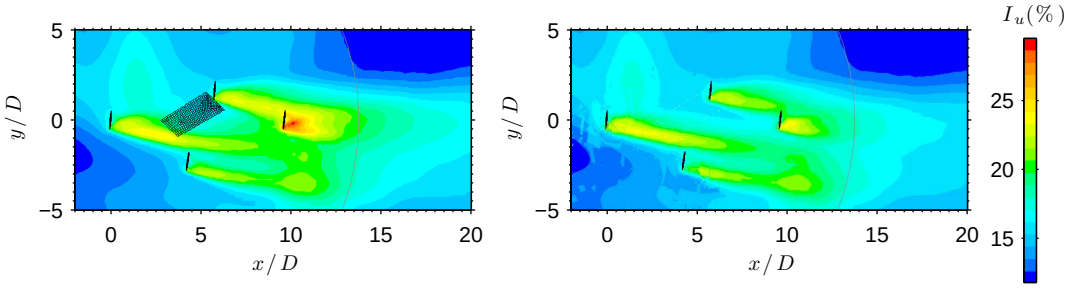

(d) Contours of I_u, T22, T21, T15 wake: with (left) and without F15 (right)

Figure 9.19. Contour plots at the xy plane for the case of T22, T21, T15 wake

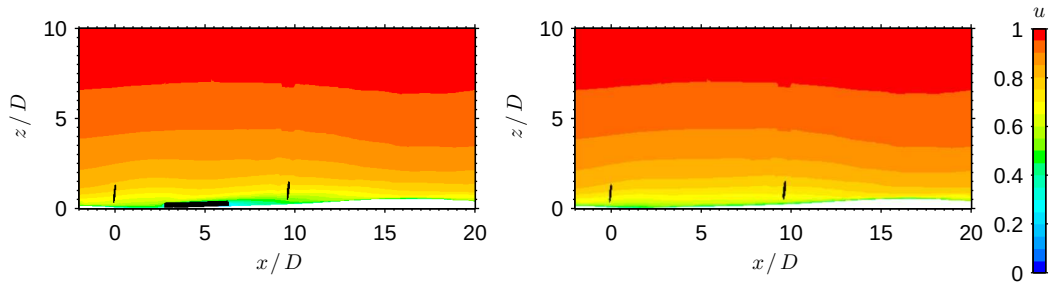

(a) Contours of u, no WT: with (left) and without F15 (right)

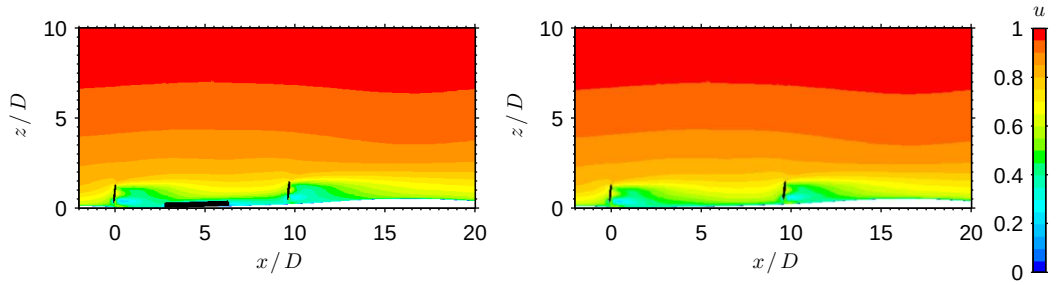

(b) Contours of u, T22, T21, T15 wake: with (left) and without F15 (right)

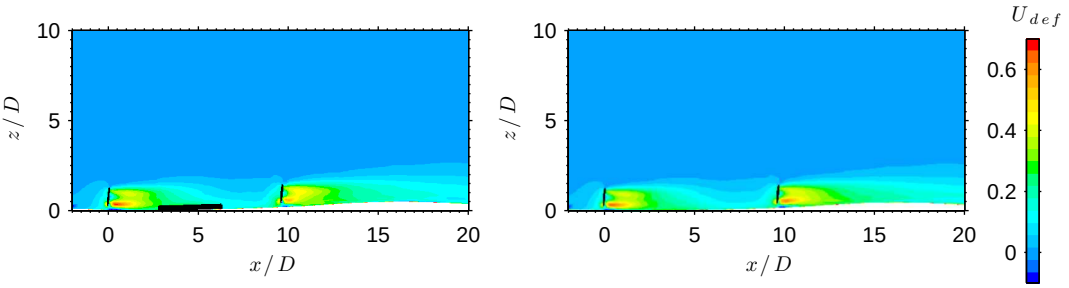

(c) Contours of U_{def}, T22, T21, T15 wake:with (left) and without F15 (right)

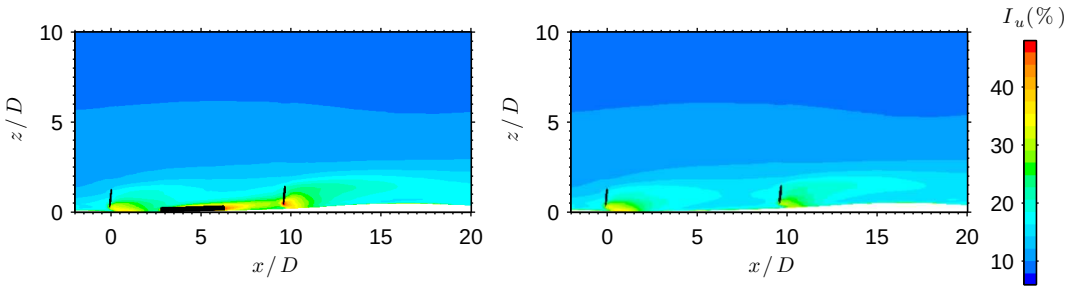

(d) Contours of I_u, T22, T21, T15 wake: with (left) and without F15 (right)

Figure 9.20. Contour plots at the xz plane for the case of T22, T21, T15 wake

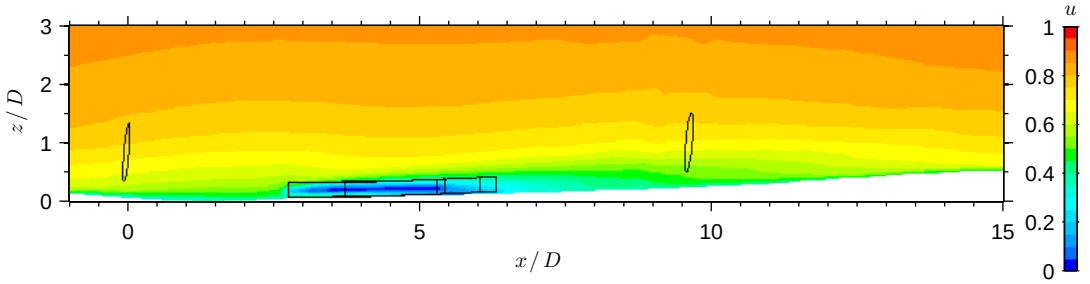

(a) Contours of u with F15: no WT

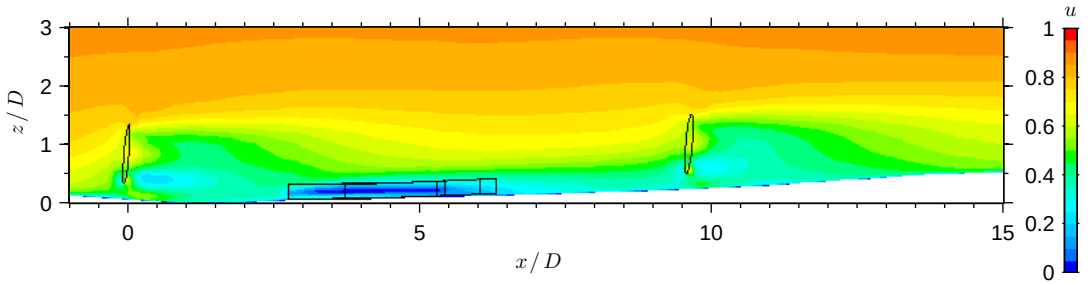

(b) Contours of u with F15: T22, T21, T15 wake

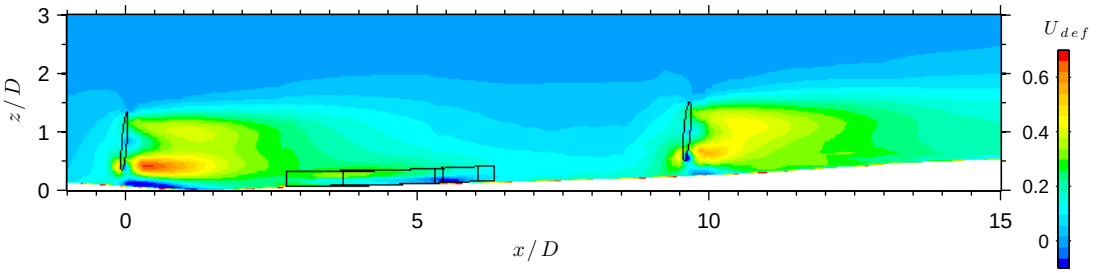

(c) Contours of U_{def} with F15: T22, T21, T15 wake

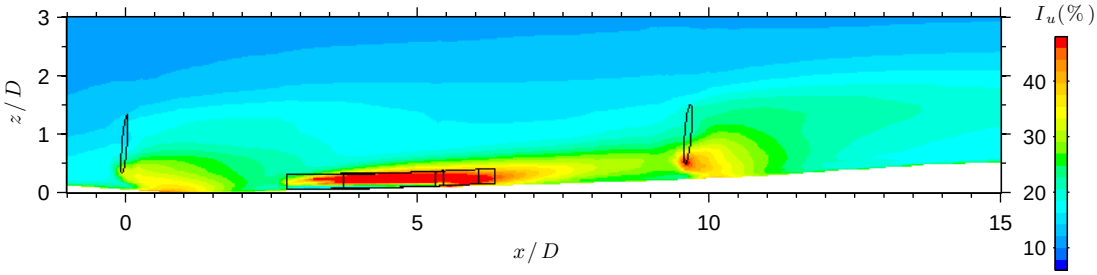

(d) Contours of I_u with F15: T22, T21, T15 wake

Figure 9.21. Detailed contour plots at the xz plane: T22, T21, T15 wake with F15

9.7 Wake at T13 and T12 (wind at ≈ 71.6°)

9.7.1 Case description

A case when the forest canopy is positioned upwind of all the rotors was examined last. For this purpose, a wind direction of ≈ 71.6° aligned with rotors T14 and T13 (Fig. 9.22) was selected in order to investigate the effect of the existing shelter belt F25 in the wake. These effects were expected to be shown in the measurements, because F25 was not removed, as in the previous cases. The wakes were investigated at T13 and T12, which are positioned ascending towards the hilltop. Spacing between T14 and T13 is relatively small, approximately 4 D, whereas T13 and T12 are positioned 5.1 D apart.

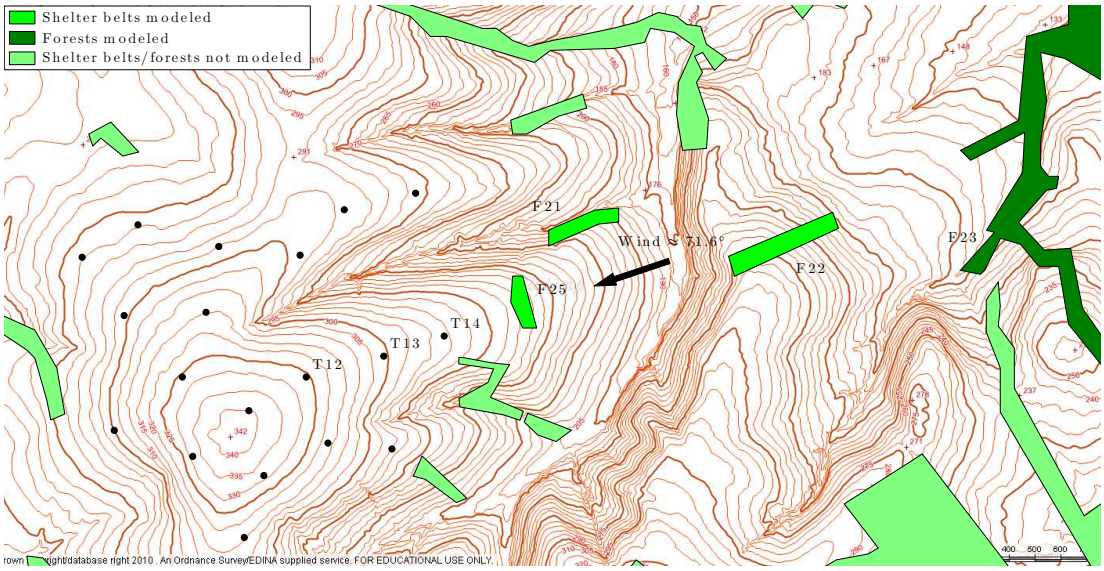

Figure 9.22. Case of ≈ 71.6° map.

The edge of F25 is located 4.6 D upwind of T14, which is within the first stage of the empirical relationship [298] for estimating $h_{c,max}$. Using Eq. (9.1) for this case, the maximum canopy height was found to be $h_{c,max} = 5.47$ m, while the real canopy height was estimated to be 16 m. In addition to F25, two other forest belts were also included in the simulations, as well as the large forest F23, using a height of 18 m.

The CFD domain was chosen to have a positive x-direction at $\approx 71.6°$ and the chosen Cartesian dimensions were $L_x \approx 193.5$ D, $L_y \approx 80.6$ D and $L_z \approx 41.9$ D . The total number of cells used was $585,493$.

9.7.2 Results and validation

The wakes were examined at T13 and T12. The data were filtered using a 'true' wind speed bin of 9 ± 0.5 m/s at T14. The scatter plots of the normalised data are shown in Fig. 9.23. The data seem non-parametric, especially at T12. Additionally, the data number is very low.

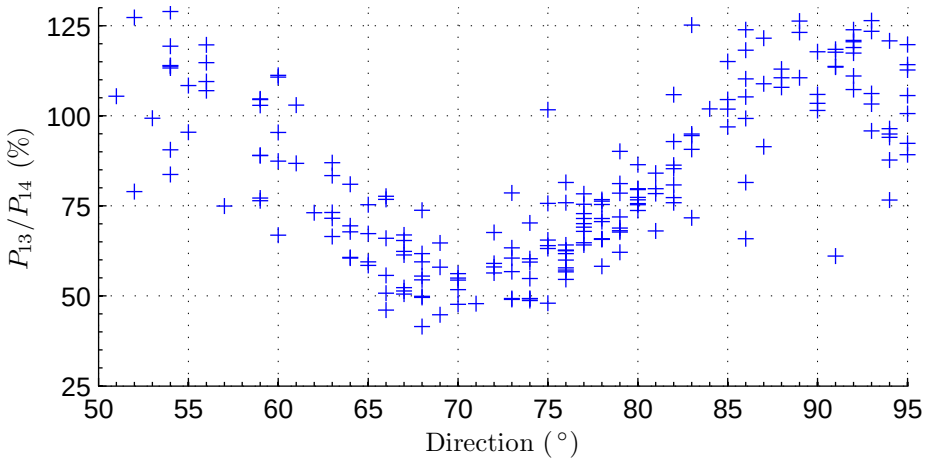

(a) Normalised power at T13

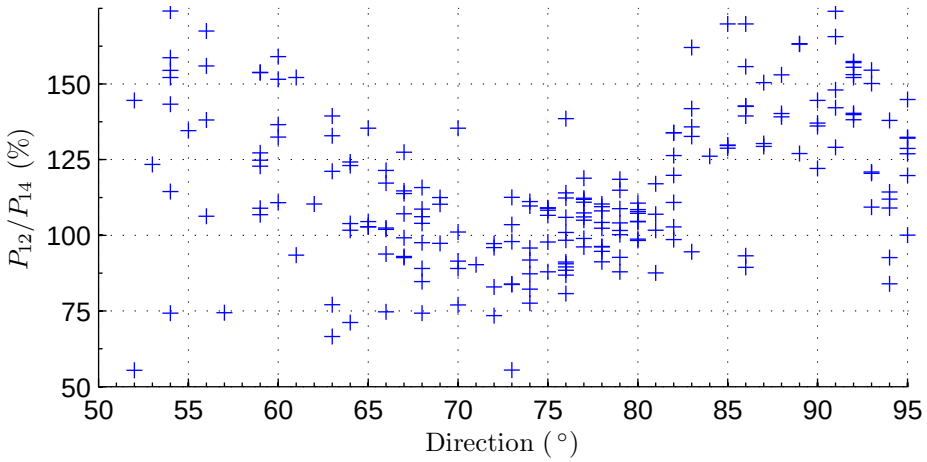

(b) Normalised power at T12

Figure 9.23. Scatter plots of the data at T13 and T12.

In a similar approach as in the previous cases, the CFD simulations were run with and without the effects of the forest belt of interest, which is F25 in this case. Table 9.4 shows the calculated properties for each simulated rotor. As expected, F25 reduces the 'true' wind speed at the rotor hubs, while it also slightly affects the direction of the streamwise velocity, altering the yaw angle of the rotors by 0.1°.

Fig. 9.24 shows comparison of the CFD results with the measurements in terms of normalised power output at T13 in the wake of T14 (Fig. 9.24a) and also at T12, downwind both T14 and T13 (Fig. 9.24b). As the 'true' wind speeds at T14 (Table 9.4) are different for each of the CFD cases (with and without F25) the power output of T14 at the case with F25 is considered as a common reference in the normalisation.

Table 9.4. Calculated rotor properties at T14, T13.

Rotor [−]	'True' wind speed [m/s]	Yaw angle [°]	Pitch angle [°]	Rot. speed [rpm]
T14 (F25)	8.79	−1.2	0.240	16.12
T14 (no F25)	9.14	−1.3	0.043	16.35
T13 (F25)	7.01	1.7	0.831	15.18
T13 (no F25)	7.17	1.6	0.786	15.27

The lateral CFD profiles at T13 seem to have a similar shape, although the wake of the forest simulation is slightly wider and the predicted power output lower, as expected. The largest discrepancies between the two simulations are found away from the wake centre. This may be attributed to the forest geometry and position relative to the wind direction and the machines. The CFD results with F25 compare well with the measured data, although the maximum wake power deficit is slightly overestimated by approximately 5%.

The double wake at T12 (Fig. 9.24b) shows fewer discrepancies between the two CFD simulations (with and without F25), indicating that the effect of the forest has been reduced. However, the CFD results with the F25 effects show that

a higher wake deficit and a wider lateral profile are maintained. The largest discrepancies between the two simulations are again found away from the wake centre. A good match with the measurements is only found near the wake centre, while away from the chosen wind direction, other factors influence the measurements. For instance, the asymmetry and the slight increase of wake deficit towards the positive direction in Fig. 9.24b, may be attributed to the fact that T14, T13 and T12 are not exactly aligned.

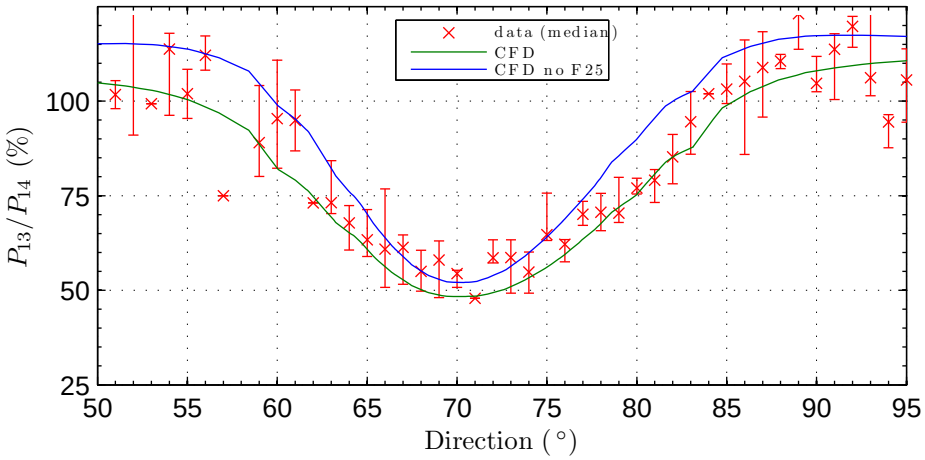

(a) Normalised power at T13

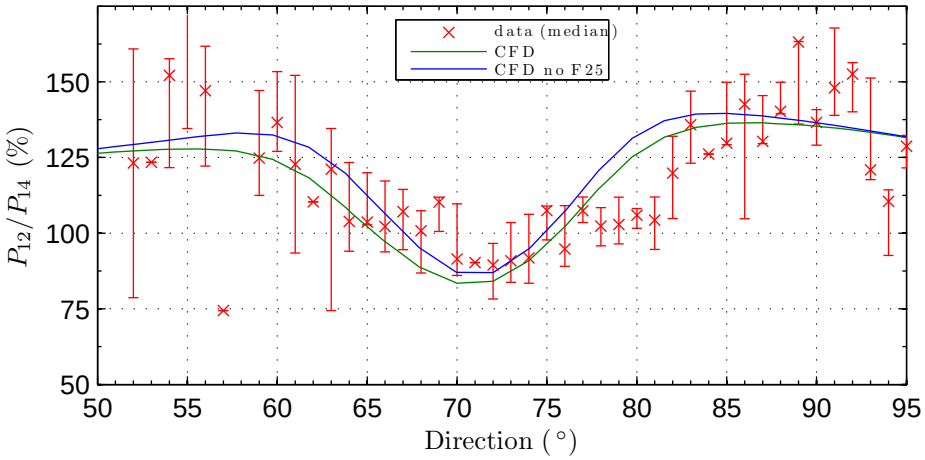

(b) Normalised power at T12

Figure 9.24. Normalised power at T13 and T12.

Fig. 9.25 shows the turbulence intensity lateral profiles. The inverse W-shape of the measurements seems to be well represented in the CFD results at T13

(Fig. 9.25a), with the forest simulation producing higher turbulence, as expected. The highest increase (approximately 2%) is located at one side of the wake. CFD results in Fig. 9.25b did not produce a satisfactory match with the 'measured' profiles: the prediction was for a peak in turbulence intensity near the wake centre, whereas the measurements indicate that the inverse W-shape is preserved. The discrepancies near the wake centre are approximately 5% and the reason for such a divergence is not clear. It may be attributed to a lack of a sufficient number of data near the wake centre (Fig. 9.23).

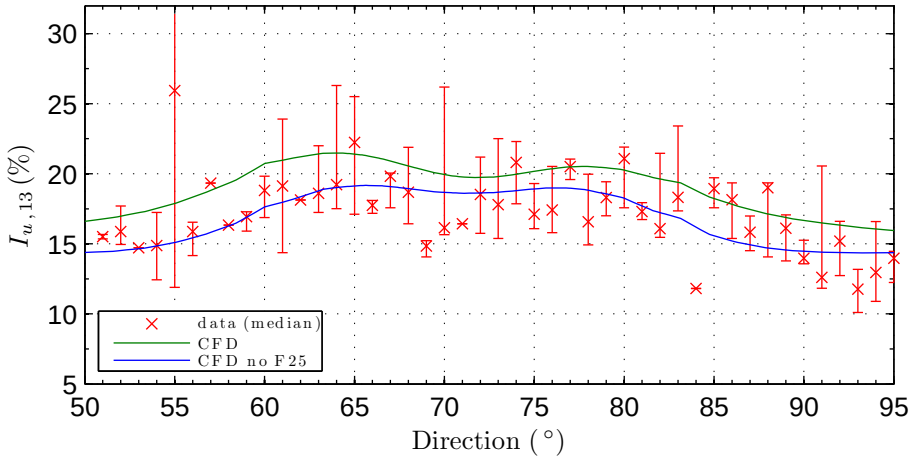

(a) Turbulence intensity at T13

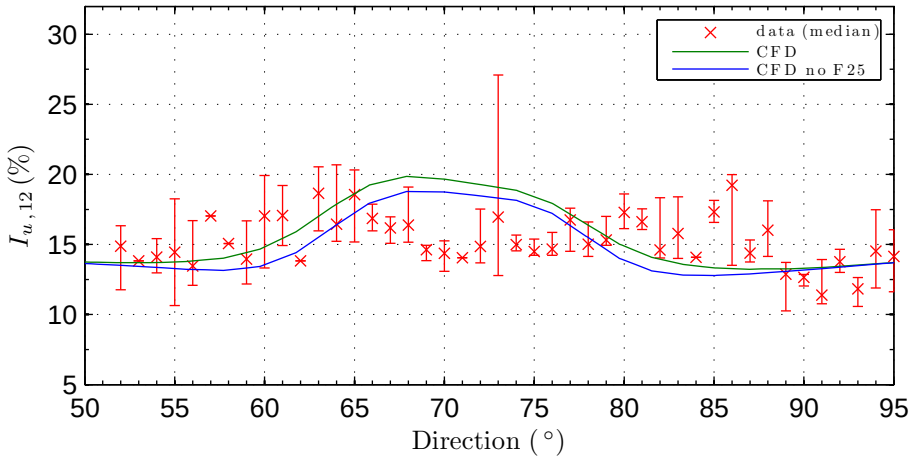

(b) Turbulence intensity at T12

Figure 9.25. Turbulence intensity at T13 and T12.

The vertical profiles of normalised streamwise velocity and turbulence intensity

of the CFD simulations are shown Fig. 9.26. The simulations with and without F25 are compared and the forest simulation without wakes is also shown as a reference. In both cases, the forest seems to add to the wind shear of the wake, although not significantly. The momentum deficit seems to be maintained at T12. The increase of turbulence intensity is slightly more significant until 1 D above the turbine axis with a maximum of approximately 2% at T13, while in T12 the effect is less pronounced.

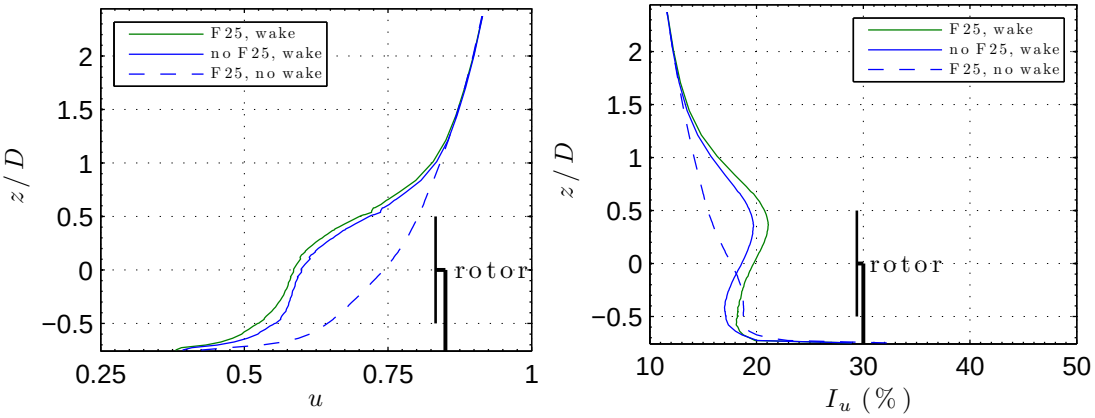

(a) profiles at T13 (T14 wake)

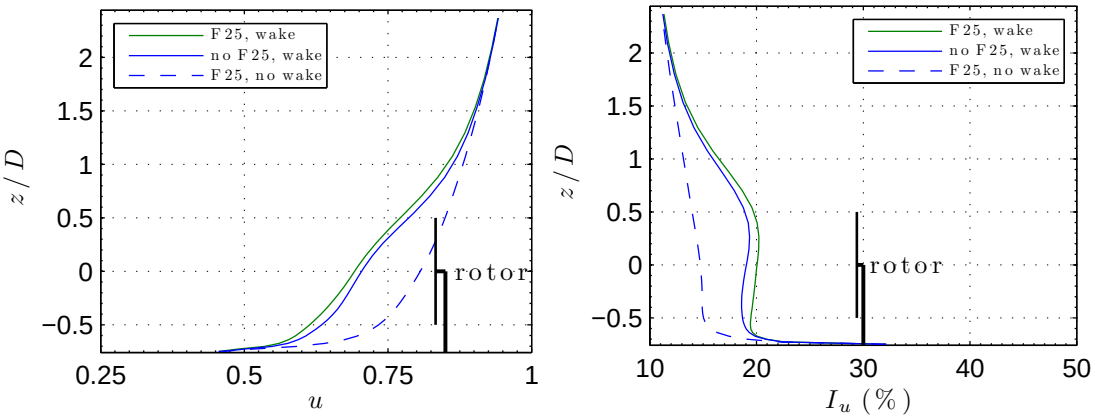

(b) profiles at T12 (T14, T13 wake)

Figure 9.26. Effect of F25 on vertical profiles at T13 and T12.

9.7.3 Contour plots

Similarly to the previous cases, the contour plots of the simulations with and without the forest canopy are shown in Figs. 9.27 (xy plane) and 9.28 (xz plane).

According to Fig. 9.27a, the presence of F25 upwind T14 has a significant effect in the streamwise velocity, as it creates a clearly visible wake. The effect is more pronounced towards the negative y direction (North, North-West), where the presence of the forest is more significant and it diminishes further downstream, as velocity is increase due to the rise of elevation.

Figs. 9.27b and 9.27c show the streamwise velocity u and velocity deficit U_{def} respectively. The wakes of each of the two simulations seem comparable in their size and shape. Turbulence intensity however (Fig. 9.27d) is significantly higher, especially downwind of T14 which is closer to F25. Further downstream the wake turbulence seems to dissipate in a similar manner.

The contour plots of Fig. 9.28 show the results at the xz plane. In Fig. 9.28a, it is clear that the forest wake upwind of T14 creates an increased wind shear, as velocity is reduced especially below the turbine axis.

The effects of F25 in the wake can be observed more clearly in Figs. 9.28c and 9.28d, where the wake velocity deficit and turbulence intensity are presented. According to Fig. 9.28c, the maximum wake deficit of rotor T14 at the presence of F25 is moved upwards. This also affects the wake of T13 to some degree, however in this case the maximum deficit is moved downwards, as it is affected by the hill slope.

Turbulence intensity is significantly increased in the wake of the forest (Fig. 9.28d) also maximising the turbulence intensity of the near wake of T14, below the machine axis. Further downwind and also in the wake of T13, the peak of turbulence intensity is moved upwards, as expected, however this is less pronounced in the forest simulation.

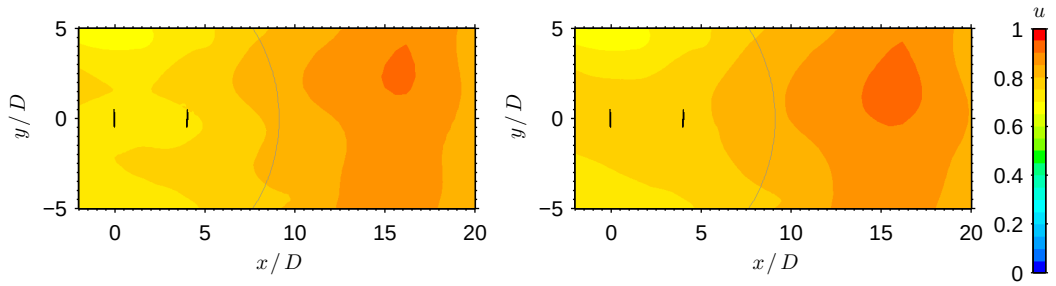

(a) Contours of u, no WT: with (left) and without F25 (right)

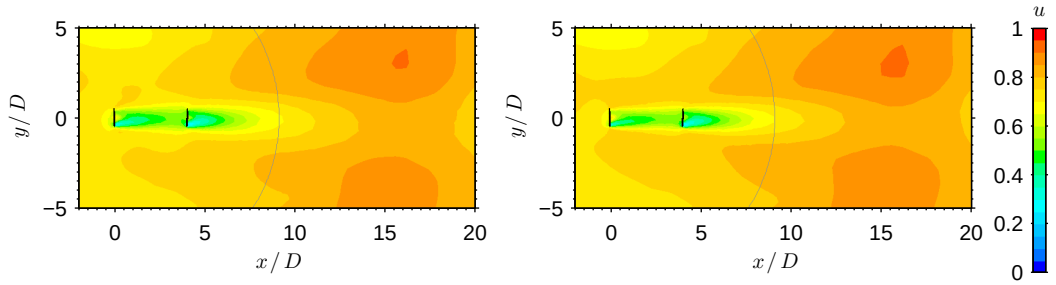

(b) Contours of u, T14 and T13 wake: with (left) and without F25 (right)

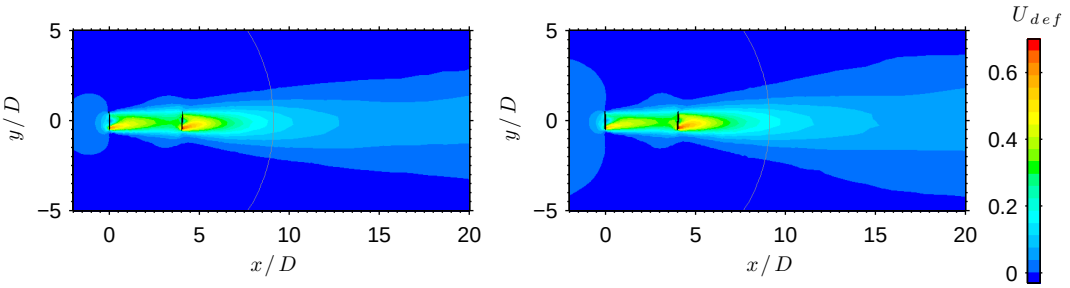

(c) Contours of U_{def}, T14 and T13 wake: with (left) and without F25 (right)

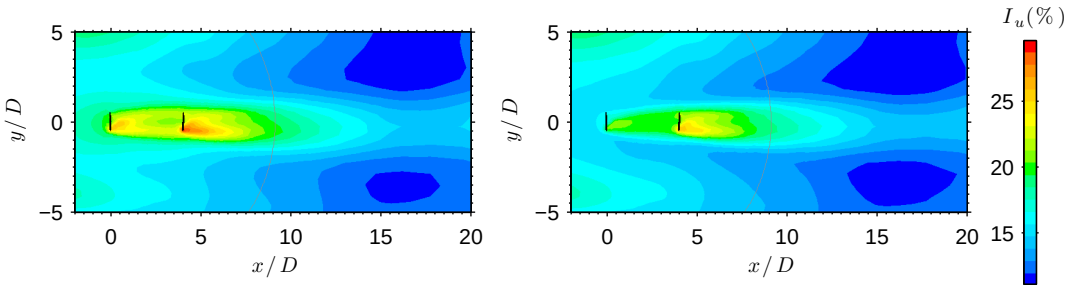

(d) Contours of I_u, T14 and T13 wake: with (left) and without F25 (right)

Figure 9.27. Contour plots at the xy plane for the case of T8 and T9 wake

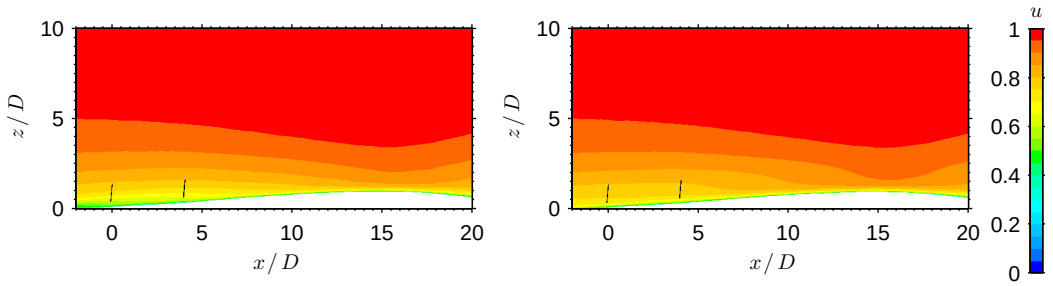

(a) Contours of u, no WT: with (left) and without F25 (right)

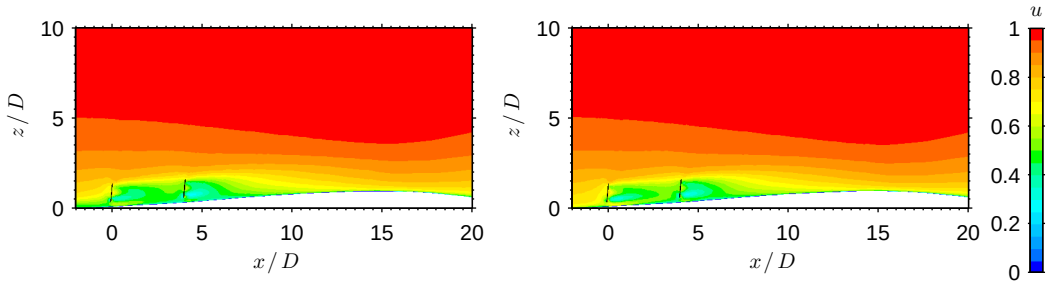

(b) Contours of u, T14 and T13 wake: with (left) and without F25 (right)

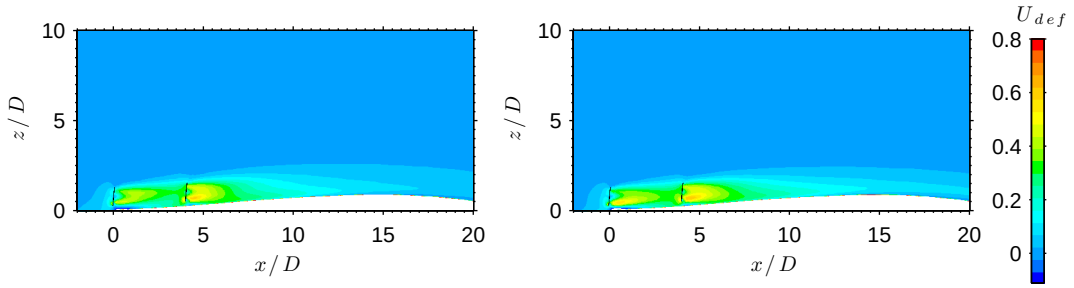

(c) Contours of U_{def}, T14 and T13 wake: with (left) and without F25 (right)

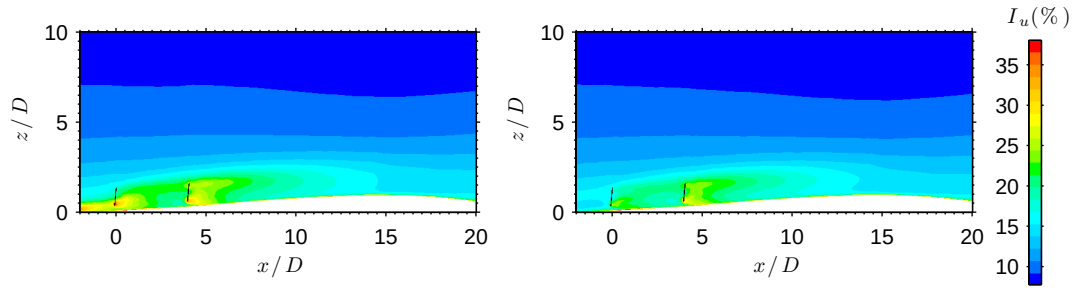

(d) Contours of I_u, T14 and T13 wake: with (left) and without F25 (right)

Figure 9.28. Contour plots at the xz plane for the case of T8 and T9 wake

9.8 Concluding remarks

The interactions between the wakes of forest canopies with the wakes of wind turbines were examined over complex terrain and the results were validated with measurements. In two cases, the forest canopy was situated in the wake of a machine, whereas in the third case, the forest was located upwind of the wake generating machine. In most cases, CFD results compared well with the measured averages.

The presence of a forest canopy close to and within a wind turbine wake, was found to considerably increase the wake deficit and turbulence intensity, especially near the ground. Wind shear is also significantly intensified and wake width is increased.

When turbines were located next to the forest edge and facing the flow, then the forest caused a slight increase of wind speed, which is related to a low-pressure region created just behind the edge [170]. A similar increase of wind speed above the forest and near the forest edge was also observed in Chapter 7.

The presence of the forest also resulted in an upwards shift of the maximum wake deficit, above the turbine axis and a downwards shift of maximum turbulence intensity below the turbine axis, due to the wake of the forest.

When the canopy was located 4.6 D upwind of the wake generating rotor over an ascending slope, the effects on the lateral profiles of wake velocity and turbulence intensity were not as significant. The effect on the wake wind shear was almost negligible, even at 4 D downwind of T14. Lateral wake turbulence intensity and velocity were only slightly affected, mainly in the single wake.

The lateral range of the aforementioned canopy effects were found to vary considerably with respect to the canopy geometry and the wind direction; they may be maximum away from the wind turbine wake centre.

Chapter 10

Conclusions and further work

The interactions of wind turbine wakes with the neutral atmospheric wind flow over complex terrain were investigated using the commercial CFD software FLUENT. The Virtual Blade Model (VBM) was implemented for the simulation of the rotor effects, based on the Blade Element Theory. Assuming a 3-D, steady-state flow, the RANS equations were solved, along with the Reynolds Stress Model (RSM) to account for the anisotropy of atmospheric turbulence. The following paragraphs present the main conclusions derived from each of the Chapters which contained simulation results.

10.1 Main conclusions

The single wake over flat terrain was initially simulated and the results were validated against full-scale measurements (Chapter 4). The velocity and turbulence intensity results were examined at four downwind locations at the vertical and lateral directions. The predicted wake deficit was in good agreement with the measurements. Some discrepancies were found in the vertical velocity deficit profile, as the CFD model overestimated the wake deficit above the turbine axis

and underestimated it near the ground. As a result, the downshift of the maximum wake deficit below the turbine axis was not predicted. The wake turbulence profile shapes were in good match with the measurements, although the model consistently overpredicted the turbulence intensity. The CFD results also showed an expected vertical asymmetry of the turbulence profile, caused by the increased shear in the wake shear layer above the turbine axis.

The wake of a wind turbine positioned on top of a Gaussian hill was also examined for different ambient turbulence conditions (Chapter 5). The comprehensive study included the streamwise, lateral and vertical variations of velocity deficit and turbulence intensity and a comparison with a single wake case over flat terrain with the same inlet conditions. An increase of ambient turbulence resulted in faster wake recoveries, as expected. However, the wake did not dissipate monotonically over the hill, as it did over flat terrain; a second region of maximum wake deficit was found away from the near wake and attached to the ground with the effect being more pronounced at increased ambient turbulence. In the high-turbulence case, the second peak of velocity deficit was higher than the near wake deficit. An increase of ambient turbulence intensity also enhanced the lateral and vertical wake expansion and raised the maximum deficit location above the turbine axis. A lateral wake 'drift' from the expected straight streamwise path was also observed in the hill case, especially at high ambient turbulence levels. It was argued that this effect was caused by the combination of the rotor rotation and the terrain, as low velocity air moves from near the ground towards one side of the wake and high velocity air from a higher level moves downwards on the other side. The simulation of two rotors positioned next to each other, at the top of the hill and facing the flow, showed that the combined wake dissipation is slower, as compared to a single wake. The region of maximum velocity deficit in the far wake was also expanded.

The case of undisturbed, neutral atmospheric wind flow over a smooth real hill was also simulated and the results were validated with full-scale measurements

(Chapter 6). The comparison of streamwise variations of velocity and turbulence showed a fair agreement both upstream and downstream of the hilltop; the only discrepancies were an underestimation of the velocity increase at the hilltop and of the turbulence intensity at the lee side of the hill. The same discrepancies have also been reported by other several other authors. The vertical profiles of velocity and turbulence at the hilltop were also compared with the measurements. Turbulence predictions were a better match near the ground whereas velocity predictions compared better away from the ground.

A new approach of modelling the flow over a forest using RSM closure was also developed (Chapter 7), based on previous modelling techniques. The canopy model was validated against measurements of the wind flow over a Sitka Spruce forest. The results were also compared using different configurations of leaf area density (LAD) and drag coefficient profiles. The vertical profiles of velocity and turbulence intensity were examined at different locations both inside and outside the forest. Results were satisfactory, although some minor discrepancies were found: velocity deficit was slightly underpredicted inside and overpredicted outside the forest, while turbulence intensity was slightly underpredicted inside and overpredicted outside the forest. The choice of using a drag coefficient profile and a Weibull LAD profile provided the best results as compared to the choice of using a constant drag coefficient and a Gaussian LAD profile.

The previously established CFD techniques where used for modelling a real complex terrain wind farm, located at a coastal site (Chapter 8). Several single and double wake cases of machines aligned to the flow were simulated and validated with SCADA, 10 min. measured averages. The same cases were also modelled with WAsP and a comparison was made with the CFD predictions. The vertical profiles of turbulence intensity showed that the peak is located above the turbine axis, in agreement with other observations. The lateral profiles showed two peaks of turbulence intensity on each side of the turbine axis. The wake over an upwards slope was found to dissipate faster than the wake over a downwards

slope. In a double wake case when the rotors were not exactly aligned to the flow, it was found that turbulence increased significantly only at the side not affected by the upstream wake, as on the other side the turbulence-producing shear is not significant. As a result, the double wake dissipation is also faster on this side. The CFD predictions were in the most cases very close to the measured averages. WAsP results were not as satisfactory: the 'top-hat' single wake profile resulted in wider wake profiles and an underestimation of the wake deficit near the wake centre. The double wake predictions of WAsP were better, both in terms of wake shape and maximum wake deficit.

A second case study was finally examined, involving a wind farm situated on a relatively complex hilly terrain with several forest canopies (Chapter 9). The results investigated the effects of forest canopies to the wake deficit, wind shear and turbulence intensity. The examined forests were located in close proximity to the machines: either downwind or upwind of the wake generating rotors. The forest canopy within a wind turbine wake was found to considerably increase the wake deficit and the turbulence intensity, especially near the ground. Wind shear and wake width were also increased. However, it was found that the machines located next to the canopy, near the forest edge and facing the flow, experienced a slight increase of wind speed. This effect was argued to be related to a low-pressure region created just behind the forest edge and extending well above it. Moreover, the forest caused the maximum wake deficit to move upwards, above the turbine axis and the maximum turbulence intensity to move below the turbine axis, due to the forest generated turbulence. In the case of the forest being located upwind of the rotor over an ascending slope, the canopy was found to have a minimal impact in the wake velocity, wind shear and turbulence. Only turbulence intensity was found to be moderately affected in the single wake. The canopy geometry and layout with respect to the wind direction and rotor location were found to play a very significant role in the lateral distribution of the canopy effects.

The main conclusions presented in the paragraphs above, are believed to be of

some contribution towards the understanding of the wake behaviour over complex terrain.

10.2 Further work

The wake 'drift' found in Chapter 5 may further be investigated. The simulation of cases with increased hill slopes and different roughness configurations may provide a better understanding of the effect. Moreover, the wind turbine may be positioned on different locations over the hill, in order to examine the differences in the wake behaviour.

This work can further be extended to include the effects of various thermal stratifications. Alinot and Masson [76, 77, 229] have used FLUENT for the simulation of wind turbines operating in the ABL under various thermal stratifications. The inclusion of thermal effects will require, among other considerations, the use of the energy equation, the addition of buoyancy terms and the calibration of the model constants. The application of a different inlet wind profile will also be necessary.

The developed CFD approach can also be used for the investigation of wakes in offshore wind farms. This appears to be a relatively straight-forward option, as the flat sea surface is much easier to mesh in comparison to a complex terrain. The results may be validated using the data from the Middelgrunden [53], Nysted [56] or Horns Rev [54, 55] wind farms, taking into account that VBM may be used for the simulation of up to 10 wind turbines. A comparison with the UpWind project results [28, 201–203, 278, 301, 302] may also be useful in order to test the performance of the VBM approach in comparison with other CFD approaches. The modelling of the offshore cases may also require to take into account different atmospheric stability types [278].

An extension to an unsteady analysis is an attractive option, as it may include

the examination of effects such as wake meandering and rotor-tower interaction. However, it would require a different rotor modelling approach, or a further development of the existing VBM, since the latter is designed only for steady-state Navier-Stokes simulations. Another possible next step, is to consider a wind farm with a large number of machines in operation. However, that would require considerable CPU resources and an extension of the VBM capabilities to include more than 10 machines, which is the current maximum.

References

[1] A. Bechmann, *Large-Eddy Simulation of Atmospheric Flow over Complex Terrain*. PhD thesis, Technical University of Denmark, Roskilde, Denmark, 2006.

[2] J. F. Manwell, J. G. McGowan, and A. L. Rogers, *Wind Energy Explained. Theory, Design and Application.* John Wiley & Sons Ltd., 2002.

[3] T. Burton, D. Sharpe, N. Jenkins, and E. Bossanyi, *Wind Energy Handbook*. John Wiley & Sons Ltd., 2001.

[4] H. A. Panofsky and J. A. Dutton, *Atmospheric turbulence*. John Wiley & Sons Ltd., 1984.

[5] J. C. Kaimal and J. J. Finnigan, *Atmospheric Boundary Layer Flows: Their Structure and Measurement*. Oxford University Press, Inc., 1994.

[6] M. Magnusson and A.-S. Smedman, "A Practical Method to Estimate Wind Turbine Wake Characteristics from Turbine Data and Routine Wind Measurements," *Wind Engineering*, vol. 20, no. 2, pp. 73–92, 1996.

[7] D. L. Elliott, "Status of wake and array loss research," in *Wind Power 1991 Conference*, (Palm Springs, California), PNL-SA-19978, Pacific Northwest Lab., Richland, WA (United States), 1991.

[8] G. Smith, W. Schlez, A. Liddell, A. Neubert, and A. Peña, "Advanced wake model for very closely spaced turbines," in *EWEC 2006*, (Athens, Greece), pp. 1–10, 2006.

[9] B. Sanderse, "Aerodynamics of wind turbine wakes," Literature review ECN-E–09-016, ECN, 2009.

[10] H. Snel, "Review of the Present Status of Rotor Aerodynamics," *Wind Energy*, vol. 1, no. S1, pp. 46–69, 1998.

[11] H. Snel, "Review of Aerodynamics for Wind Turbines," *Wind Energy*, vol. 6, no. 3, pp. 203–211, 2003.

[12] A. Crespo, J. Hernández, and S. Frandsen, "Survey of Modelling Methods for Wind Turbine Wakes and Wind Farms," *Wind energy*, vol. 2, no. 1, pp. 1–24, 1999.

[13] L. J. Vermeer, J. N. Sørensen, and A. Crespo, "Wind turbine wake aerodynamics," *Progress in Aerospace Sciences*, vol. 39, no. 6-7, pp. 467–510, 2003.

[14] J. Sumner, C. S. Watters, and C. Masson, "CFD in Wind Energy: The Virtual, Multiscale Wind Tunnel," *Energies*, vol. 3, no. 5, pp. 989–1013, 2010.

[15] B. Sanderse, van der Pijl, and B. S. P., Koren, "Review of computational fluid dynamics for wind turbine wake aerodynamics," *Wind Energy*, vol. 14, no. n/a, pp. 1–28, 2011. doi: 10.1002/we.458.

[16] M. O. L. Hansen, *Aerodynamics of Wind Turbines*. Earthscan/James & James, second ed., 2008.

[17] S. T. Frandsen, "Turbulence and turbulence-generated structural loading in wind turbine clusters," Tech. Rep. Risø-R-1188(EN), Risø National Laboratory, Roskilde, Denmark, 2007.

[18] M. R. Ruith, "Unstructured, Multiplex Rotor Source Model with Thrust and Moment Trimming - Fluent's VBM Model," Technical Notes TN293, Fluent Inc., 2005.

[19] J. F. Ainslie, "Calculating the flowfield in the wake of wind turbines," *Journal of Wind Engineering and Industrial Aerodynamics*, vol. 27, no. 1-3, pp. 213–224, 1988.

[20] D. C. Quarton and J. F. Ainslie, "Turbulence in Wind Turbine Wakes," *Wind Engineering*, vol. 14, no. 1, pp. 15–23, 1990.

[21] J. G. Schepers, "ENDOW: Validation and improvement of ECN's wake model," Tech. Rep. ECN-C-03-034, ECN, 2003.

[22] A. Crespo, J. Hernández, E. Fraga, and C. Andreu, "Experimental validation of the UPM computer code to calculate wind turbine wakes and comparison with other models," *Journal of Wind Engineering and Industrial Aerodynamics*, vol. 27, no. 1, pp. 77–88, 1988.

[23] D. Smith and G. J. Taylor, "Further analysis of turbine wake development and interaction data," in *Proceedings of the 13th BWEA Wind Energy Conference*, (Swansea, UK), pp. 325–331, 1991.

[24] N. Troldborg, *Actuator Line Modeling of Wind Turbine Wakes*. PhD thesis, Department of Mechanical Engineering, Technical University of Denmark, 2008.

[25] R. Gómez-Elvira, A. Crespo, E. Migoya, and F. Manuel, "An explicit algebraic turbulent model to reproduce the anisotropy of the momentum turbulent flows in a wind turbine wake.," in *EWEC 2003*, 2003.

[26] R. Gómez-Elvira, A. Crespo, E. Migoya, and F. Manuel, "Anisotropy of turbulence in wind turbine wakes," *Journal of Wind Engineering and Industrial Aerodynamics*, vol. 93, no. 10, pp. 797–814, 2005.

[27] P. B. S. Lissaman, A. Zaday, and G. W. Gyatt, "Critical issues in the design and assessment of wind turbine arrays," in *Proceedings of the 4th International Symposium on Wind Energy Systems*, vol. 2, (Stockholm, Sweden), pp. 411–423, 1982.

[28] R. J. Barthelmie, S. T. Frandsen, K. Hansen, J. G. Schepers, K. Rados, W. Schlez, A. Neubert, L. E. Jensen, and S. Neckelmann, "Modelling the impact of wakes on power output at Nysted and Horns Rev," in *European Wind Energy Conference*, (Marseille, France), 2009.

[29] P. J. H. Builtjes and P. E. J. Vermeulen, "Turbulence in wind turbine clusters," in *4th International Symposium on Wind Energy Systems*, vol. 2, (Stockholm, Sweden), pp. 449–464, 1982.

[30] D. J. Milborrow, "Wind tunnel measurements on wind turbine clusters," in *1st BWEA Wind Energy Workshop*, vol. 1, (Cranfield, UK), pp. 190–198, 1979.

[31] P.-H. Alfredsson and J.-Å. Dahlberg, "A preliminary wind tunnel study of windmill wake dispersion in various flow conditions," Technical Note AU-1499, FFA: The Aeronautical Research Institute of Sweden, Stockholm, Sweden, 1979.

[32] P. B. S. Lissaman, "Energy Effectiveness of Arbitrary Arrays of Wind Turbines," *AIAA paper*, vol. 79-0114, pp. 1–7, 1979.

[33] J. Counihan, "An improved method of simulating an atmospheric boundary layer in a wind tunnel," *Atmospheric Environment*, vol. 3, no. 2, pp. 197–214, 1969.

[34] P. H. Alfredsson, J. A. Dahlberg, and F. H. Bark, "Some properties of the wake behind horizontal axis wind turbines," in *3rd International Symposium on Wind Energy Systems*, vol. 1, (Lyngby, Denmark), pp. 469–484, 1980.

[35] P.-H. Alfredsson and J.-Å. Dahlberg, "Measurements of Wake Interaction Effects on the power output from small wind turbine models," Technical Note HU-2189, FFA: The Aeronautical Research Institute of Sweden, Stockholm, Sweden, 1981.

[36] P. J. H. Builtjes and D. J. Milborrow, "Modelling of wind turbine arrays," in *3rd International Symposium on Wind Energy Systems*, vol. 1, (Lyngby, Denmark), pp. 417–430, 1980.

[37] D. Smith, "Multiple wake measurements and analysis," in *Proceedings of the 12th BWEA Wind Energy Conference*, pp. 53–58, 1990.

[38] T. Maeda, T. Yokota, Y. Shimizu, and K. Adachi, "Wind Tunnel Study of the Interaction between Two Horizontal Axis Wind Turbines," *Wind Engineering*, vol. 28, no. 2, pp. 197–212, 2004.

[39] D. Medici, "Wind Turbine Wakes - Control and Vortex Shedding," licentiate thesis, KTH, Mechanics, Royal Institute of Technology, 2004.

[40] D. Medici, "Experimental Studies of Wind Turbine Wakes - Power Optimisation and Meandering," tech. rep., KTH, Mechanics, Royal Institute of Technology, 2005.

[41] D. Medici and P. H. Alfredsson, "Measurements on a Wind Turbine Wake: 3D Effects and Bluff Body Vortex Shedding," *Wind Energy*, vol. 9, no. 3, pp. 219–236, 2006.

[42] D. Medici and P. H. Alfredsson, "Measurements behind model wind turbines: further evidence of wake meandering," *Wind Energy*, vol. 11, no. 2, pp. 211–217, 2008.

[43] G. España, S. Aubrun, P. Devinant, L. Laporte, and E. Dupont, "Properties of the far wake of a wind turbine in an atmospheric boundary layer," in *International Workshop on Physical Modelling of Flow and Dispersion Phenomena (PHYSMOD 2007)*, 2007.

[44] L. P. Chamorro and F. Porté-Agel, "A Wind-Tunnel Investigation of Wind-Turbine Wakes: Boundary-Layer Turbulence Effects," *Boundary-Layer Meteorology*, vol. 132, no. 1, pp. 129–149, 2009.

[45] L. P. Chamorro and F. Porté-Agel, "Effects of Thermal Stability and Incoming Boundary-Layer Flow Characteristics on Wind-Turbine Wakes: A Wind-Tunnel Study," *Boundary-Layer Meteorology*, vol. 136, no. 3, pp. 515–533, 2010.

[46] F. Porté-Agel, H. Lu, and Y.-T. Wu, "A large-eddy simulation framework for wind energy applications," in *Fifth International Symposium on Computational Wind Engineering (CWE2010)*, 2010.

[47] Y.-T. Wu and F. Porté-Agel, "Large-Eddy Simulation of Wind-Turbine Wakes: Evaluation of Turbine Parametrisations," *Boundary-Layer Meteorology*, vol. 138, no. 3, pp. 345–366, 2011.

[48] U. Högström, D. N. Asimakopoulos, H. Kambezidis, C. G. Helmis, and A. Smedman, "A field study of the wake behind a 2 MW wind turbine," *Atmospheric environment*, vol. 22, no. 4, pp. 803–820, 1988.

[49] G. J. Taylor, "Wake measurements on the Nibe wind turbines in Denmark," Technical Report ETSU WN 5020, National Power - Technology and Environment Centre, 1990.

[50] M. Magnusson, K. G. Rados, and S. G. Voutsinas, "A Study of the Flow Downstream of a Wind Turbine Using Measurements and Simulations," *Wind Engineering*, vol. 20, no. 6, pp. 389–403, 1996.

[51] P. J. Eecen, S. A. M. Barhorst, H. Braam, A. P. W. M. Curvers, H. Korterink, L. A. H. Machielse, R. J. Nijdam, L. W. M. M. Rademakers, J. P. Verhoef, P. A. van Der Werff, A. J. Werkhoven, and D. H. van Dok, "Measurements at the ECN Wind Turbine Test Location Wieringermeer," in *EWEC 2006*, (Athens, Greece), 2006.

[52] L. A. H. Machielse, P. J. Eecen, H. Korterink, S. P. van der Pijl, and J. G. Schepers, "ECN test farm measurements for validation of wake models," in *European Wind Energy Conference*, (Milan, Italy), ECN, IOP Publishing, 2007.

[53] H. E. Jørgensen, S. Frandsen, and P. Vølund, "Wake effects on Middelgrund Windfarm," Tech. Rep. Risø-R-1415(EN), Risø National Laboratory, Roskilde, Denmark, 2003.

[54] L. E. Jensen, C. Mørch, P. B. Sørensen, and K. H. Svendsen, "Wake measurements from the Horns Rev wind farm," in *EWEC 2004*, 2004.

[55] C. B. Hasager, A. Peña, T. Mikkelsen, M. Courtney, I. Antoniou, S.-E. Gryning, P. Hansen, and P. B. Sørensen, "12MW Horns Rev experiment," Tech. Rep. Risø-R-1506(EN), Risø National Laboratory, Roskilde, Denmark, 2007.

[56] S. Frandsen, R. Barthelmie, O. Rathmann, H. E. Jørgensen, J. Badger, K. Hansen, S. Ott, P.-E. Rethore, S. E. Larsen, and L. E. Jensen, "Summary report: The shadow effect of large wind farms: measurements, data analysis and modelling," Tech. Rep. Risø-R-1615(EN), Risø National Laboratory, Roskilde, Denmark, 2007.

[57] S. Frandsen, L. Chacn, A. Crespo, P. Enevoldsen, R. Gmez-Elvira, J. Herndez, J. Hjstrup, F. Manuel, K. Thomsen, and P. Srensen, "Measurements

on and Modelling of Offshore Wind Farms," Tech. Rep. Risø-R-903(EN), Risø National Laboratory, Roskilde, Denmark, 1996.

[58] S. G. Voutsinas, K. G. Rados, and A. Zervos, "On the Analysis of Wake Effects in wind parks," *Journal of Wind Engineering and Industrial Aerodynamics*, vol. 14, no. 4, pp. 204–19, 1990.

[59] P. E. J. Vermeulen, "An experimental analysis of wind turbine wakes," in *3rd International Symposium on Wind Energy Systems*, vol. 1, (Lyngby, Denmark), pp. 431–450, 1980.

[60] A. Crespo, F. Manuel, D. Moreno, E. Fraga, and J. Hernández, "Numerical Analysis of Wind Turbine Wakes," in *Proceedings of the Delphi Workshop on "Wind Energy-Applications"*, (Delphi, Greece), pp. 15–25, 1985.

[61] I. Katic, J. Højstrup, and N. O. Jensen, "A simple model for cluster efficiency," in *European Wind Energy Association Conference and Exhibition*, (Rome, Italy), pp. 407–410, 1986.

[62] N. O. Jensen, "A note on Wind Generator Interaction," Tech. Rep. Risø-M-2411, Risø National Laboratory, Roskilde, Denmark, 1984.

[63] G. C. Larsen, J. Højstrup, and H. A. Madsen, "Wind fields in wakes," in *Proceedings of the 1996 European Union Wind Energy Conference*, (G"øteborg, Sweden), pp. 764–768, 1996.

[64] H. Schlichting, *Boundary-layer Theory*. New York: McGraw-Hill, seventh ed., 1978.

[65] J. Blazek, *Computational Fluid dynamics: principles and applications*. Elsevier Science Ltd., first ed., 2001.

[66] J. F. Ainslie, "Development of an eddy viscosity model for wind turbine wakes," in *Proceedings of the 7th BWEA Wind Energy Conference*, (Oxford, U.K.), pp. 61–66, 1985.

[67] B. Lange, H.-P. Waldl, R. J. Barthelmie, A. G. Guerrero, and D. Heinemann, "Modelling of offshore wind turbine wakes with the wind farm program FLaP," *Wind Energy*, vol. 6, no. 1, pp. 87–104, 2003.

[68] G. C. Larsen, H. A. Madsen, T. J. Larsen, and N. Troldborg, "Wake modeling and simulation," Tech. Rep. Risø-R-1653(EN), Risø National Laboratory, Roskilde, Denmark, 2008.

[69] J. Hernández and A. Crespo, "Wind turbine wakes in the atmospheric surface layer," *Phoenics Journal of Computational Fluid Dynamics and its Applications*, vol. 3, pp. 330–361, 1990.

[70] J. G. Schepers and S. P. van Der Pijl, "Improved modelling of wake aerodynamics and assessment of new farm control strategies," in *The Science of Making Torque from Wind*, vol. 75, Journal of Physics: Conference Series, IOP Publishing, 2007.

[71] N. N. Sørensen and J. Johansen, "UPWIND , Aerodynamics and aeroelasticity Rotor aerodynamics in atmospheric shear flow," in *European Wind Energy Conference*, (Milan, Italy), 2007.

[72] F. Zahle, N. N. Sørensen, and J. Johansen, "Rotor Aerodynamics in Atmospheric Shear Flow," in *European Wind Energy Conference*, (Brussels, Belgium), 2008.

[73] P.-E. Réthoré, *Wind Turbine Wake in Atmospheric Turbulence*. PhD thesis, Aalborg University - Department of Civil Engineering, 2009.

[74] I. Ammara, C. Leclerc, and C. Masson, "A Viscous Three-Dimensional Differential/Actuator-Disk Method for the Aerodynamic Analysis of Wind Farms," *Journal of Solar Energy Engineering*, vol. 124, pp. 345–356, 2002.

[75] C. Masson, A. Smaïli, and C. Leclerc, "Aerodynamic Analysis of HAWTs Operating in Unsteady Conditions," *Wind Energy*, vol. 4, no. 1, pp. 1–22, 2001.

[76] C. Alinot and C. Masson, "Aerodynamics of wind turbines in thermally stratified turbulent atmospheric boundary layer," in *Proceedings of the 10^{th} Annual Conference of the CFDSC*, pp. 553–559, 2002.

[77] C. Alinot and C. Masson, "Aerodynamic simulations of wind turbines operating in atmospheric boundary layer with various thermal stratifications," in *A Collection of the 2002 ASME Wind Energy Symposium Technical Papers*, pp. 206–215, 2002.

[78] A. El Kasmi and C. Masson, "An extended k-ε model for turbulent flow through horizontal-axis wind turbines," *Journal of Wind Engineering and Industrial Aerodynamics*, vol. 96, no. 1, pp. 103–122, 2008.

[79] J. Sørensen and C. Kock, "A model for unsteady rotor aerodynamics," *Journal of wind engineering and industrial aerodynamics*, vol. 58, no. 3, pp. 259–275, 1995.

[80] J. N. Sørensen, W. Z. Shen, and X. Munduate, "Analysis of wake states by a full-field actuator disc model," *Wind Energy*, vol. 1, no. 2, pp. 73–88, 1998.

[81] D. Cabezón, J. Sanz, I. Marti, and A. Crespo, "CFD modelling of the interaction between the Surface Boundary Layer and rotor wake," in *EWEC 2009*, (Marseille, France), pp. 1–7, 2009.

[82] J. M. Prospathopoulos, E. S. Politis, P. K. Chaviaropoulos, and K. G. Rados, "Enhanced CFD Modelling of Wind Turbine Wakes," in *Euromech Colloquium 508 on Wind Turbine Wakes*, (Madrid, Spain), 2009.

[83] J. M. Prospathopoulos, E. S. Politis, K. G. Rados, and P. K. Chaviaropoulos, "Evaluation of the effects of turbulence model enhancements on wind turbine wake predictions," *Wind Energy*, vol. 14, no. 2, pp. 285–300, 2011.

[84] A. Jimenez, A. Crespo, E. Migoya, J. Garcia, and F. Manuel, "Large eddy simulation of a wind turbine wake," in *EWEC 2006*, vol. 3, 2006.

[85] A. Jimenez, A. Crespo, E. Migoya, and J. Garcia, "Advances in large-eddy simulation of a wind turbine wake," in *The Science of Making Torque from Wind*, vol. 75, Journal of Physics: Conference Series, IOP Publishing, 2007.

[86] A. Jimenez, A. Crespo, E. Migoya, and J. Garcia, "Large-eddy simulation of spectral coherence in a wind turbine wake," *Environmental Research Letters*, vol. 3, p. 015004, 2008.

[87] J. N. Sørensen and W. Z. Shen, "Numerical modeling of wind turbine wakes," *Journal of fluids engineering*, vol. 124, no. 2, pp. 393–399, 2002.

[88] R. Mikkelsen, *Actuator disc methods applied to wind turbines*. PhD thesis, Technical University of Denmark, 2003.

[89] S. S. A. Ivanell, "Numerical Computations of Wind Turbine Wakes," licentiate thesis, Royal Institute of Technology, Stockholm, Sweden, 2005.

[90] S. Ivanell, R. Mikkelsen, J. Srensen, and D. Henningson, "Three dimensional actuator disc modelling of wind farm wake interaction," in *EWEC 2008*, (Brussels, Belgium), 2008.

[91] S. Ivanell, J. N. Sørensen, R. Mikkelsen, and D. Henningson, "Analysis of Numerically Generated Wake Structures," *Wind Energy*, vol. 12, pp. 63–80, 2009.

[92] R. Mikkelsen, J. N. Sørensen, S. Øye, and N. Troldborg, "Analysis of power enhancement for a row of wind turbines using the actuator line technique," in *The Science of Making Torque from Wind*, vol. 75, Journal of Physics: Conference Series, IOP Publishing, 2007.

[93] N. Troldborg, J. N. Sørensen, and R. Mikkelsen, "Actuator line simulation of wake of wind turbine operating in turbulent inflow," in *The Science of Making Torque from Wind*, vol. 75, Journal of Physics: Conference Series, IOP Publishing, 2007.

[94] N. Troldborg, J. N. Sørensen, and R. Mikkelsen, "Numerical Simulations of Wakes of Wind Turbines Operating in Sheared and Turbulent Inflow," in *European Wind Energy Conference*, (Marseille, France), 2009.

[95] N. Troldborg, J. N. Sørensen, and R. Mikkelsen, "Numerical simulations of wake characteristics of a wind turbine in uniform inflow," *Wind energy*, vol. 13, pp. 86–99, 2010.

[96] W. Z. Shen, J. N. Sørensen, and J. H. Zhang, "Actuator Surface Model for Wind Turbine Flow Computations," in *European Wind Energy Conference and Exhibition*, (Milan, Italy), 2007.

[97] I. Dobrev, F. Massouh, and M. Rapin, "Actuator surface hybrid model," in *The Science of Making Torque from Wind*, vol. 75, Journal of Physics: Conference Series, IOP Publishing, 2007.

[98] P.-E. Réthoré and N. N. Sørensen, "Validation of an Actuator Disc Model," in *EWEC 2010*, (Warsaw, Poland), 2010.

[99] N. Wood, "Wind flow over complex terrain: a historical perspective and the prospect for large-eddy modelling," *Boundary-Layer Meteorology*, vol. 96, no. 1, pp. 11–32, 2000.

[100] P. Jackson and J. C. R. Hunt, "Turbulent wind flow over a low hill," *Quarterly Journal of the Royal Meteorological Society*, vol. 101, no. 430, pp. 929–955, 1975.

[101] P. J. Mason and R. I. Sykes, "Flow over an isolated hill of moderate slope," *Quarterly Journal of the Royal Meteorological Society*, vol. 105, no. 444, pp. 383–395, 1979.

[102] P. J. Mason and J. C. King, "Measurements and predictions of flow and turbulence over an isolated hill of moderate slope," *Quarterly Journal of the Royal Meteorological Society*, vol. 111, no. 468, pp. 617–640, 1985.

[103] J. L. Walmsley, P. A. Taylor, and T. Keith, "A simple model of neutrally stratified boundary-layer flow over complex terrain with surface roughness modulations (MS3DJH/3R)," *Boundary-Layer Meteorology*, vol. 36, no. 1, pp. 157–186, 1986.

[104] P. A. Taylor, J. L. Walmsley, and J. R. Salmon, "A simple model of neutrally stratified boundary-layer flow over real terrain incorporating wavenumber-dependent scaling," *Boundary-Layer Meteorology*, vol. 26, no. 2, pp. 169–189, 1983.

[105] O. Zeman and N. O. Jensen, "Modification of turbulence characteristics in flow over hills," *Quarterly Journal of the Royal Meteorological Society*, vol. 113, no. 475, pp. 55–80, 1987.

[106] I. Troen, "A high resolution spectral model for flow in complex terrain," in *Ninth Symposium on Turbulence and Diffusion*, (Roskilde, Denmark), pp. 417–420, 1990.

[107] J. L. Walmsley, I. Troen, D. P. Lalas, and P. J. Mason, "Surface-layer flow in complex terrain: comparison of models and full-scale observations," *Boundary-Layer Meteorology*, vol. 52, no. 3, pp. 259–281, 1990.

[108] K. W. Ayotte, "Computational modelling for wind energy assessment," *Journal of Wind Engineering and Industrial Aerodynamics*, vol. 96, no. 10-11, pp. 1571–1590, 2008.

[109] E. F. Bradley, "An experimental study of the profiles of wind speed, shearing stress and turbulence at the crest of a large hill," *Quarterly Journal of the Royal Meteorological Society*, vol. 106, no. 447, pp. 101–123, 1980.

[110] P. J. Mason, "Flow over the summit of an isolated hill," *Boundary-Layer Meteorology*, vol. 37, no. 4, pp. 385–405, 1986.

[111] J. R. Salmon, H. W. Teunissen, R. E. Mickle, and P. A. Taylor, "The Kettles Hill Project: Field observations, wind-tunnel simulations and numerical model predictions for flow over a low hill," *Boundary-Layer Meteorology*, vol. 43, no. 4, pp. 309–343, 1988.

[112] P. A. Taylor and H. W. Teunissen, "ASKERVEIN 82: Report on the September/October 1982 Experiment to Study Boundary-Layer Flow over Askervein, South Uist," Tech. Rep. MSRB-83-8, Atmospheric Environment Service, Downsview, Ontario, Canada, 1983.

[113] P. A. Taylor and H. W. Teunissen, "The Askervein Hill Project: Report on the Sep./Oct. 1983, Main Field Experiment," Tech. Rep. MSRB-84-6, Atmospheric Environment Service, Downsview, Ontario, Canada, 1985.

[114] P. A. Taylor and H. W. Teunissen, "The Askervein Hill project: overview and background data," *Boundary-Layer Meteorology*, vol. 39, no. 1, pp. 15–39, 1987.

[115] R. E. Mickle, N. J. Cook, A. M. Hoff, N. O. Jensen, J. R. Salmon, P. A. Taylor, G. Tetzlaff, and H. W. Teunissen, "The Askervein Hill Project: Vertical profiles of wind and turbulence," *Boundary-Layer Meteorology*, vol. 43, no. 1, pp. 143–169, 1988.

[116] J. L. Walmsley and P. A. Taylor, "Boundary-layer flow over topography: impacts of the Askervein study," *Boundary-Layer Meteorology*, vol. 78, no. 3, pp. 291–320, 1996.

[117] S. Finardi, G. Brusasca, M. G. Morselli, F. Trombetti, and F. Tampieri, "Boundary-layer flow over analytical two-dimensional hills: A systematic comparison of different models with wind tunnel data," *Boundary-Layer Meteorology*, vol. 63, no. 3, pp. 259–291, 1993.

[118] C. E. Skupniewicz, R. F. Kamada, and G. E. Schacher, "Turbulence measurements over complex terrain," *Boundary-Layer Meteorology*, vol. 48, no. 1, pp. 109–128, 1989.

[119] H. A. Panofsky, D. Larko, R. Lipschutz, G. Stone, E. F. Bradley, A. J. Bowen, and J. Højstrup, "Spectra of velocity components over complex terrain," *Quarterly Journal of the Royal Meteorological Society*, vol. 108, no. 455, pp. 215–230, 1982.

[120] D. Founda, M. Tombrou, D. P. Lalas, and D. N. Asimakopoulos, "Some measurements of turbulence characteristics over complex terrain," *Boundary-Layer Meteorology*, vol. 83, no. 2, pp. 221–245, 1997.

[121] S. B. Vosper, S. D. Mobbs, and B. A. Gardiner, "Measurements of the near-surface flow over a hill," *Quarterly Journal of the Royal Meteorological Society*, vol. 128, no. 585, pp. 2257–2280, 2002.

[122] "The Bolund Experiment." `http://www.risoe.dtu.dk/research/sustainable_energy/wind_energy/projects/vea_bolund.aspx/`. Last accessed 21-March-2011.

[123] A. Bechmann, J. Berg, M. Courtney, H. Ejsing Jørgensen, J. Mann, and N. N. Sørensen, "The Bolund Experiment: Overview and Background," Tech. Rep. Risø-R-1658(EN), Risø DTU, Roskilde, Denmark, 2009.

[124] L. Landberg, L. Myllerup, O. Rathmann, E. L. Petersen, B. H. Jorgensen, J. Badger, and N. G. Mortensen, "Wind Resource Estimation—An Overview," *Wind Energy*, vol. 6, no. 3, pp. 261–271, 2003.

[125] J. M. L. M. Palma, F. A. Castro, L. F. Ribeiro, A. H. Rodrigues, and A. P. Pinto, "Linear and nonlinear models in wind resource assessment and wind turbine micro-siting in complex terrain," *Journal of Wind Engineering and Industrial Aerodynamics*, vol. 96, no. 12, pp. 2308–2326, 2008.

[126] H. G. Kim and V. C. Patel, "Test of turbulence models for wind flow over terrain with separation and recirculation," *Boundary-Layer Meteorology*, vol. 94, no. 1, pp. 5–21, 2000.

[127] H. G. Kim, V. C. Patel, and C. M. Lee, "Numerical simulation of wind flow over hilly terrain," *Journal of Wind Engineering and Industrial Aerodynamics*, vol. 87, no. 1, pp. 45–60, 2000.

[128] O. Undheim, H. I. Andersson, and E. Berge, "Non-linear, microscale modelling of the flow over Askervein Hill," *Boundary-Layer Meteorology*, vol. 120, no. 3, pp. 477–495, 2006.

[129] A. El Kasmi and C. Masson, "Turbulence modeling of atmospheric boundary layer flow over complex terrain: a comparison of models at wind tunnel and full scale," *Wind Energy*, vol. 13, pp. 689–704, 2010.

[130] D. Cabezón, J. Sanz, and J. van Beeck, "Sensitivity analysis on turbulence models for the ABL in complex terrain," in *European Wind Energy Conference*, (Milan, Italy), 2007.

[131] D. Cabezón, A. Iniesta, E. Ferrer, and I. Martí, "Comparing linear and non linear wind flow models," in *EWEC 2006*, (Athens, Greece), 2006.

[132] D. Cabezón, A. Iniesta, and Martí, "Comparing WAsP and Fluent for Highly Complex Terrain Wind Prediction," in *Wind Energy. Proceedings of the Euromech Colloquium*, pp. 275–279, Springer, 2006.

[133] A. C. M. Beljaars, J. L. Walmsley, and P. A. Taylor, "A mixed spectral finite-difference model for neutrally stratified boundary-layer flow over roughness changes and topography," *Boundary-Layer Meteorology*, vol. 38, no. 3, pp. 273–303, 1987.

[134] A. C. M. Beljaars, J. L. Walmsley, and P. A. Taylor, "Modelling of turbulence over low hills and varying surface roughness," *Boundary-Layer Meteorology*, vol. 41, no. 1, pp. 203–215, 1987.

[135] G. Bergeles, I. Glekas, I. Prospathopoulos, and S. Voutsinas, "Statistical and physical modelling of wind resources in complex terrain: Assessment of the applicability of a 3D Navier Stokes Code," in *Proceedings of the 1996 European Wind Energy Conference*, (Göteborg, Sweden), pp. 560–563, 1996.

[136] P. K. Chaviaropoulos and D. I. Douvikas, "Mean-flow-field simulations over complex terrain using a 3-D Reynolds Averaged Navier-Stokes solver," in *Computational Fluid Dynamics '98, Proceedings of the Fourth ECCOMAS Conference*, (Athens, Greece), pp. 842–848, John Wiley & Sons Ltd., 1998.

[137] A. Theodorakakos and G. C. Bergeles, "A Telescopic Local Grid Refinement Technique for Wind Flow Simulation over Complex Terrain," *Wind Energy*, vol. 4, no. 2, pp. 77–98, 2001.

[138] N. N. Sørensen, "General Purpose Flow Solver Applied to Flow over Hills," Tech. Rep. Risø-R-827(EN), Risø National Laboratory, 2003.

[139] F. A. Castro, J. M. L. M. Palma, and A. Silva Lopes, "Simulation of the Askervein Flow. Part 1: Reynolds Averaged Navier-Stokes Equations (k-ε

turbulence model)," *Boundary-Layer Meteorology*, vol. 107, no. 3, pp. 501–530, 2003.

[140] N. Mandas, F. Cambuli, G. Crasto, and G. Cau, "Numerical simulation of the Atmospheric Boundary Layer (ABL) over complex terrains," in *EWEC 2004*, (London, UK), 2004.

[141] P. Stangroom, *CFD Modelling of Wind Flow Over Terrain*. PhD thesis, The University of Nottingham, 2004.

[142] K. J. Eidsvik, "A system for wind power estimation in mountainous terrain. Prediction of Askervein hill data," *Wind Energy*, vol. 8, no. 2, pp. 237–249, 2005.

[143] J. Prospathopoulos and S. G. Voutsinas, "Implementation Issues in 3D Wind Flow Predictions Over Complex Terrain," *Journal of Solar Energy Engineering*, vol. 128, no. 4, pp. 539–553, 2006.

[144] A. Bechmann, N. N. Sørensen, and J. Johansen, "Atmospheric Flow over Terrain using Hybrid RANS/LES," in *European Wind Energy Conference*, (Milan, Italy), pp. 1–7, 2007.

[145] G. Crasto, *Numerical Simulations of the Atmospheric Boundary Layer*. PhD thesis, University of Cagliari, 2007.

[146] M. Q. Andersen and J. Laursen, "Comparison on different CFD models for modelling the wind conditions on wind turbine sites," in *European Wind Energy Conference*, (Brussels, Belgium), 2008.

[147] X. Zhang, "CFD simulation of neutral ABL flows," Tech. Rep. Risø-R-1688(EN), Risø National Laboratory, Roskilde, Denmark, 2009.

[148] T. B. Gatski and C. G. Speziale, "On explicit algebraic stress models for complex turbulent flows," *Journal of Fluid Mechanics*, vol. 254, pp. 59–78, 1993.

[149] A. Bechmann, "Presentations from "The Bolund Experiment: Workshop" $3 - -4^{\text{th}}$ December 2009," Tech. Rep. Risø-R-1745(EN), Risø DTU, Roskilde, Denmark, 2010.

[150] J. J. Finnigan, "Turbulence in plant canopies," *Annual Review of Fluid Mechanics*, pp. 519–571, 2000.

[151] M. R. Raupach and A. S. Thom, "Turbulence in and above plant canopies," *Annual Review of Fluid Mechanics*, vol. 13, no. 1, pp. 97–129, 1981.

[152] P. A. Durbin and B. A. Pettersson Reif, *Statistical Theory and Modeling for Turbulent Flows*. John Wiley & Sons, Ltd., 2001.

[153] X. Lee, "Air motion within and above forest vegetation in non-ideal conditions," *Forest Ecology and management*, vol. 135, no. 1-3, pp. 3–18, 2000.

[154] G. S. Raynor, "Wind and Temperature Structure in a Coniferous Forest and a Contiguous Field," *Forest Science*, vol. 17, no. 3, pp. 351–363, 1971.

[155] J. H. C. Gash, "Observations of turbulence downwind of a forest-heath interface," *Boundary-Layer Meteorology*, vol. 36, pp. 227–237, 1986.

[156] B. A. Gardiner, "Wind and wind forces in a plantation spruce forest," *Boundary-Layer Meteorology*, vol. 67, pp. 161–186, 1994.

[157] M. R. Irvine, B. A. Gardiner, and M. K. Hill, "The evolution of turbulence across a forest edge," *Boundary-Layer Meteorology*, vol. 84, no. 3, pp. 467–496, 1997.

[158] A. P. Morse, B. A. Gardiner, and B. J. Marshall, "Mechanisms controlling turbulence development across a forest edge," *Boundary-Layer Meteorology*, vol. 103, no. 2, pp. 227–251, 2002.

[159] S. Dupont, J. M. Bonnefond, M. R. Irvine, E. Lamaud, and Y. Brunet, "Long-distance edge effects in a pine forest with a deep and sparse trunk space: In situ and numerical experiments," *Agricultural and Forest Meteorology*, 2010.

[160] S. Dupont and Y. Brunet, "Influence of foliar density profile on canopy flow: a large-eddy simulation study," *Agricultural and Forest Meteorology*, vol. 148, no. 6-7, pp. 976–990, 2008.

[161] U. Svensson and K. Häggkvist, "A two-equation turbulence model for canopy flows," *Journal of Wind Engineering and Industrial Aerodynamics*, vol. 35, pp. 201–211, 1990.

[162] S. R. Green, "Modelling turbulent air flow in a stand of widely-spaced trees," *Phoenics Journal of Computational Fluid Dynamics and its Applications*, vol. 5, pp. 294–312, 1992.

[163] J. Liu, J. M. Chen, T. A. Black, and M. D. Novak, "E-ε modelling of turbulent air flow downwind of a model forest edge," *Boundary-Layer Meteorology*, vol. 77, pp. 21–44, 1996.

[164] C. Sanz, "A note on k-ε modelling of vegetation canopy air-flows," *Boundary-Layer Meteorology*, vol. 108, no. 1, pp. 191–197, 2003.

[165] G. G. Katul, L. Mahrt, D. Poggi, and C. Sanz, "One- and Two- Equation Models for Canopy Turbulence," *Boundary-Layer Meteorology*, vol. 113, pp. 81–109, 2004.

[166] L. Liang, L. Xiaofeng, L. Borong, and Z. Yingxin, "Improved k-ε two-equation turbulence model for canopy flow," *Atmospheric Environment*, vol. 40, no. 4, pp. 762–770, 2006.

[167] A. Sogachev and O. Panferov, "Modification of two-equation models to account for plant drag," *Boundary-Layer Meteorology*, vol. 121, no. 2, pp. 229–266, 2006.

[168] Lopes Da Costa, Jose Carlos and Castro, F. A. and Palma, J. M. L. M. and Stuart, Peter, "Computer simulation of atmospheric flows over real forests for wind energy resource evaluation," *Journal of Wind Engineering and Industrial Aerodynamics*, vol. 94, no. 8, pp. 603–620, 2006.

[169] A. Sogachev, "A note on two-equation closure modelling of canopy flow," *Boundary-Layer Meteorology*, vol. 130, no. 1, pp. 423–435, 2009.

[170] B. Dalpé and C. Masson, "Numerical simulation of wind flow near a forest edge," *Journal of Wind Engineering and Industrial Aerodynamics*, vol. 97, no. 5-6, pp. 228–241, 2009.

[171] J. C. P. Lopes Da Costa, *Atmospheric Flow over Forested and Non-Forested Complex Terrain*. PhD thesis, Universidade do Porto, 2007.

[172] J. D. J.-P. Pinard and J. D. Wilson, "First-and second-order closure models for wind in a plant canopy," *Journal of Applied Meteorology*, 2001.

[173] N. R. Wilson and R. H. Shaw, "A Higher Order Closure Model for Canopy Flow," *Journal of Applied Meteorology*, vol. 16, pp. 1197–1205, 1977.

[174] J. D. Wilson, "A second-order closure model for flow through vegetation," *Boundary-Layer Meteorology*, vol. 42, 1988.

[175] G. G. Katul and J. D. Albertson, "An investigation of higher-order closure models for a forested canopy," *Boundary-Layer Meteorology*, vol. 89, pp. 47–74, 1998.

[176] G. G. Katul and W.-H. Chang, "Principal Length Scales in Second-Order Closure Models for Canopy Turbulence," *Journal of Applied Meteorology*, vol. 38, pp. 1631–1643, 1999.

[177] G. G. Katul and J. D. Albertson, "Modeling CO_2 sources, sinks, and fluxes within a forest canopy," *Journal of Geophysical Research*, vol. 104, no. D6, pp. 6081–6091, 1999.

[178] W. J. Massman and J. C. Weil, "An analytical one-dimensional second-order closure model of turbulence statistics and the Lagrangian time scale within and above plant canopies of arbitrary structure," *Boundary-Layer Meteorology*, vol. 91, no. 1, pp. 81–107, 1999.

[179] K. W. Ayotte, J. J. Finnigan, and M. R. Raupach, "A second-order closure for neutrally stratified vegetative canopy flows," *Boundary-Layer Meteorology*, pp. 189–216, 1999.

[180] D. Poggi, G. G. Katul, and J. D. Albertson, "Momentum transfer and turbulent kinetic energy budgets within a dense model canopy," *Boundary-Layer Meteorology*, vol. 111, pp. 589–614, 2004.

[181] G. J. Taylor and D. Smith, "Wake measurements over complex terrain," in *Proceedings of the 13th BWEA Wind Energy Conference*, (Swansea, UK), pp. 335–342, 1991.

[182] D. Smith, *An experimental and theoretical investigation of wind turbine wakes in arrays and complex terrain.* PhD thesis, Council for National Academic Awards, 1991.

[183] R. W. Baker and S. N. Walker, "Wake measurements behind a large horizontal axis wind turbine generator," *Solar Energy*, vol. 33, no. 1, pp. 5–12, 1984.

[184] D. L. Elliott and J. C. Barnard, "Observations of Wind Turbine Wakes and Surface Roughness Effects on Wind Flow Variability," *Solar Energy*, vol. 45, no. 5, pp. 265–283, 1990.

[185] A. M. Scott, "Wake Interaction Studies on the HWP-300/22 and WEG MS-1 Wind Turbine Generators on Burgar Hill, Orkney," Report on UK Department of Energy Contract E/5A/CON/5039/1277, James Howden & Co. Ltd., 1987.

[186] C. G. Helmis, K. H. Papadopoulos, D. N. Asimakopoulos, P. G. Papageorgas, and A. T. Soilemes, "An experimental study of the near-wake structure of a wind turbine operating over complex terrain," *Solar energy*, vol. 54, no. 6, pp. 413–428, 1995.

[187] K. H. Papadopoulos, C. G. Helmis, A. T. Soilemes, P. G. Papageorgas, and D. N. Asimakopoulos, "Study of the turbulent characteristics of the near-wake field of a medium-sized wind turbine operating in high wind conditions," *Solar energy*, vol. 55, no. 1, pp. 61–72, 1995.

[188] N. C. Stefanatos, E. E. Morfiadakis, and G. L. Glinou, "Wake measurements in complex terrain," in *Proceedings of the 1996 European Union Wind Energy Conference*, (Göteborg, Sweden), pp. 773–777, 1996.

[189] S. G. Voutsinas, K. G. Rados, and A. Zervos, "The effect of the non-uniformity of the wind velocity field in the optimal design of wind parks," in *Proceedings of the 1990 European Community Wind Energy Conference*, (Madrid, Spain), pp. 181–185, 1990.

[190] A. Hemon, S. Huberson, and A. Zervos, "Numerical study of wind turbine operation in complex terrain," in *Proceedings of the 13th BWEA Wind Energy Conference*, (Swansea, UK), pp. 343–50, 1991.

[191] E. Migoya, A. Crespo, J. Garcia, F. Moreno, F. Manuel, A. Jiménez, and A. Costa, "Comparative study of the behavior of wind-turbines in a wind farm," *Energy*, vol. 32, no. 10, pp. 1871–1885, 2007.

[192] P. Günther, M. Fallen, and T. Wolfanger, "Numerical wake simulation of a HAWT considering topography and using a mesoscale turbulence model," in *1993 European Community Wind Energy Conference*, (Travemünde, Germany), pp. 448–450, 1993.

[193] A. Crespo, F. Manuel, J. C. Grau, and J. Hernández, "Modelization of wind farms in complex terrain. Application to the Monteahumada wind farm," in *Proceedings of the 1993 European Community Wind Energy Conference*, (Travemünde, Germany), pp. 440–443, 1993.

[194] P. K. Chaviaropoulos and D. Douvikas, "Mean Wind Field Prediction over Complex Terrain in the Presence of Wind Turbines," in *EWEC 1999*, (Nice, France), pp. 1208–1211, 1999.

[195] M. Lee, S. H. Lee, N. Hur, and C.-k. Choi, "A numerical simulation of flow field in a wind farm on complex terrain," in *The Seventh Asia-Pacific Conference on Wind Engineering*, (Taipei, Taiwan), 2009.

[196] C. Montavon, I. Jones, C. Staples, C. Strachan, and I. Gutierrez, "Practical issues in the use of CFD for modelling wind farms," in *European Wind Energy Conference*, 2009.

[197] K. Rados, G. C. Larsen, R. Barthelmie, W. Schlez, U. Hassan, B. Lange, I. Waldl, and M. Magnusson, "A comparison of wake model performances in an offshore environment," in *EWEC 2001*, 2001.

[198] F. Menter, "Two-equation eddy-viscosity turbulence models for engineering applications," *AIAA journal*, vol. 32, no. 8, pp. 1598–1605, 1994.

[199] J. M. Prospathopoulos, E. S. Politis, and P. K. Chaviaropoulos, "Modelling wind turbine wakes in complex terrain," in *European Wind Energy Conference*, (Brussels, Belgium), 2008.

[200] J. M. Prospathopoulos, E. S. Politis, R. J. Barthelmie, and D. Cabezón, "Evaluating Wake Models for Use in Complex Terrain," Deliverable 8.3, Centre for Renewable Energy Sources, Pikermi, Greece, 2008.

[201] R. J. Barthelmie, J. G. Schepers, S. P. van Der Pijl, O. Rathmann, S. T. Frandsen, D. Cabezón, E. Politis, J. Prospathopoulos, K. Rados, K. Hansen,

W. Schlez, J. Phillips, and A. Neubert, "Flow and wakes in complex terrain and offshore: Model development and verification in UpWind," in *European Wind Energy Conference*, (Milan, Italy), 2007.

[202] R. J. Barthelmie, O. Rathmann, S. T. Frandsen, K. S. Hansen, E. S. Politis, J. M. Prospathopoulos, K. G. Rados, D. Cabezón, W. Schlez, J. Phillips, A. Neubert, J. G. Schepers, and S. P. van Der Pijl, "Modelling and measurements of wakes in large wind farms," in *The Science of Making Torque from Wind*, vol. 75, Journal of Physics: Conference Series, IOP Publishing, 2007.

[203] R. J. Barthelmie, S. T. Frandsen, O. Rathmann, K. Hansen, E. S. Politis, J. M. Prospathopoulos, D. Cabezón, K. G. Rados, S. P. van Der Pijl, J. G. Schepers, W. Schlez, J. Phillips, and A. Neubert, "Flow and wakes in large wind farms in complex terrain and offshore," in *European Wind Energy Conference*, (Brussels, Belgium), 2008.

[204] J. M. Prospathopoulos, E. S. Politis, P. K. Chaviaropoulos, K. G. Rados, J. G. Schepers, D. Cabezón, K. Hansen, and R. J. Barthelmie, "CFD Modelling of Wind Farms in Complex Terrain," in *EWEC 2010*, (Warsaw, Poland), 2010.

[205] D. Cabezón, K. Hansen, and R. J. Barthelmie, "Analysis and validation of CFD wind farm models in complex terrain . Effects induced by topography and wind turbines," in *EWEC 2010*, (Warsaw, Poland), pp. 1–4, 2010.

[206] L. A. J. Zori and R. G. Rajagopalan, "Navier–Stokes Calculations of Rotor–Airframe Interaction in Forward Flight," *Journal of the American Helicopter Society*, vol. 40, no. 2, pp. 57–67, 1995.

[207] Z. Yang, L. N. Sankar, M. J. Smith, and O. Bauchau, "Recent Improvements to a Hybrid Method for Rotors in Forward Flight," in *38th AIAA Aerospace Sciences Meeting*, (Reno, NV), pp. 1–12, 2000.

[208] M. R. Ruith, "The Osprey Takes Off with Virtual Blade Modeling," *Fluent News Summer 2005*, pp. 20–22, 2005.

[209] Wirogo, Sutikno and Ruith, Michael, "Virtual Blade Model – UGM 2004," in *2004 CFD Summit*, 2004.

[210] M. R. Ruith, S. Shashidhar, T. Vishak, and R. Kumar, "A Powerful Wind of Change," *Fluent News fall 2004*, pp. S4–S5, 2004.

[211] B. Simpson, "Virtual Blade Model," in *UGM 2005*, 2005.

[212] A. N. Modha, T. A. Blaylock, and W. Y. F. Chan, "Brown-out – Flow Visualisation using FLUENT® VBM," in *International Aerospace CFD Conference*, (Paris), pp. 1–10, 2007.

[213] Fluent Inc., Lebanon, NH, *FLUENT 6.3 User's Guide*, 2006.

[214] O. Reynolds, "On the Dynamical Theory of Incompressible Viscous Fluids and the Determination of the Criterion," in *Philosophical Transactions of the Royal Society of London. A*, vol. 186, pp. 123–164, The Royal Society, 1895.

[215] D. C. Wilcox, *Turbulence modeling for CFD*. La Canada, CA: DCW Industries, Inc., third ed., 2006.

[216] H. K. Versteeg and W. Malalasekera, *An Introduction to Computational Fluid Dynamics: The Finite Volume Method*. Pearson Education Limited, second ed., 2007.

[217] "Introduction to CFD Analysis." Introductory FLUENT Notes, 2001. Fluent User Services Center, Fluent Inc.

[218] B. E. Launder and D. B. Spalding, "The numerical computation of turbulent flows," *Computer methods in applied mechanics and engineering*, vol. 3, no. 2, pp. 269–289, 1974.

[219] F. Inc., "Modeling Turbulent Flows." Fluent Software Training TRN-99-003, 2001.

[220] D. C. Wilcox, *Turbulence modeling for CFD*. La Canada, CA: DCW Industries, Inc., second ed., 1998.

[221] F. Menter, M. Kuntz, and R. Langtry, "Ten Years of Industrial Experience with the SST Turbulence model, Turbulence," *Heat and Mass Transfer*, vol. 4, pp. 625–632, 2003.

[222] ANSYS Canada Ltd., *CFX-5 Solver Modelling*, 2004.

[223] B. Bell, "Turbulent Flow Case Studies." Fluent Software Training UGM 2003, 2003.

[224] P. R. Spalart, W. H. Jou, M. Strelets, and S. R. Allmaras, "Comments on the feasibility of LES for wings, and on a hybrid RANS/LES approach," in *Advances in DNS/LES: proceedings of the 1st AFOSR International Conference on DNS/LES*, (Louisiana Tech University, Ruston, Louisiana), 1997.

[225] F. S. Lien and M. A. Leschziner, "Assessment of Turbulent Transport Models Including Non-Linear RNG Eddy-Viscosity Formulation and Second-Moment Closure for flow over a backward-facing step," *Computers and Fluids*, vol. 23, no. 8, pp. 983–1004, 1994.

[226] P. J. Richards and R. P. Hoxey, "Appropriate boundary conditions for computational wind engineering models using the k-ε turbulence model," *Journal of wind engineering and Industrial aerodynamics*, vol. 46–47, pp. 145–153, 1993.

[227] B. Blocken, T. Stathopoulos, and J. Carmeliet, "CFD simulation of the atmospheric boundary layer: wall function problems," *Atmospheric environment*, vol. 41, no. 2, pp. 238–252, 2007.

[228] ESDU, "Characteristics of atmospheric turbulence near the ground. Part II: single point data for strong winds (neutral atmosphere)," Data Item 85020, Engineering Sciences Data Unit, 1985.

[229] C. Alinot and C. Masson, "k-ε Model for the Atmospheric Boundary Layer Under Various Thermal Stratifications," *Journal of Solar Energy Engineering*, vol. 127, no. 4, pp. 438–443, 2005.

[230] J. Franke, C. Hirsch, A. G. Jensen, H. W. Krüs, S. Miles, M. Schatzmann, P. Westbury, J. A. Wisse, and N. G. Wright, "Recommendations on the Use of CFD in Wind Engineering," in *Proceedings of the International Conference on Urban Wind Engineering and Building Aerodynamics. COST Action C*, pp. 1–11, 2004.

[231] J. Franke, A. Hellsten, H. Schlünzen, and B. Carissimo, eds., *Best Practice Guideline for the CFD Simulation of flows in the Urban Environment.* COST Office, 2007. COST Action 732: Quality Assurance and Improvement of Microscale Meteorological Models.

[232] B. Blocken, J. Carmeliet, and T. Stathopoulos, "CFD evaluation of wind speed conditions in passages between parallel buildings—effect of wall-function roughness modifications for the atmospheric boundary layer flow," *Journal of Wind Engineering and Industrial Aerodynamics*, vol. 95, no. 9–11, pp. 941–962, 2007.

[233] B. Blocken, G. Dezsö, J. van Beeck, and J. Carmeliet, "Comparison of calculation models for wind-driven rain deposition on building facades," *Atmospheric Environment*, vol. 44, no. 14, pp. 1714–1725, 2010.

[234] D. M. Hargreaves and N. G. Wright, "On the use of the k-ε model in commercial CFD software to model the neutral atmospheric boundary layer," *Journal of Wind Engineering and Industrial Aerodynamics*, vol. 95, no. 5, pp. 355–369, 2007.

[235] P. J. Richards, A. D. Quinn, and S. Parker, "A 6 m cube in an atmospheric boundary layer flow Part 2. Computational solutions," *Wind and Structures*, vol. 5, no. 2–4, pp. 177–192, 2002.

[236] B. Blocken, T. Stathopoulos, P. Saathoff, and X. Wang, "Numerical evaluation of pollutant dispersion in the built environment: Comparisons between models and experiments," *Journal of Wind Engineering and Industrial Aerodynamics*, vol. 96, no. 10–11, pp. 1817–1831, 2008.

[237] Fluent Inc., Lebanon, NH, *GAMBIT 2.3 Documentation*, 2006.

[238] J. D. Anderson, Jr., *Computational Fluid Dynamics: The Basics with Applications*. McGraw-Hill, Inc, 1995.

[239] H. K. Versteeg and W. Malalasekera, *An Introduction to Computational Fluid Dynamics: The Finite Volume Method*. Prentice Hall, first ed., 1995.

[240] O. C. Zienkiewicz, R. L. Taylor, and P. Nithiarasu, *The Finite Element Method for Fluid Dynamics*. Elsevier Butterworth-Heinemann, sixth ed., 2005.

[241] S. V. Patankar, *Numerical Heat Transfer and Fluid Flow*. Hemisphere Publishing, 1980.

[242] P. Nielsen, "The wind power program of the ministry of energy and the electric utilities in Denmark," in *4th International Symposium on Wind Energy Systems* (H. S. Stephens and D. H. Goodes, eds.), (Stockholm, Sweden), pp. 35–46, BHRA Fluid Engineering, 1982.

[243] E. Hau, *Wind Turbines: Fundamentals, Technologies, Application, Economics*. Springer, second ed., 2006.

[244] B. M. Pedersen and P. Nielsen, "Description of the two Danish 630 KW Wind Turbines, NIBE-A and NIBE-B, and some preliminary test results," in *3rd International Symposium on Wind Energy Systems*, (Lyngby, Denmark), pp. 223–238, BHRA Fluid Engineering, 1980.

[245] U. Hassan, G. J. Taylor, and A. D. Garrad, "The dynamic response of wind turbines operating in a wake flow," *Journal of Wind Engineering and Industrial Aerodynamics*, vol. 27, no. 1-3, pp. 113–126, 1988.

[246] A. Crespo and J. Hernández, "Turbulence characteristics in wind-turbine wakes," *Journal of Wind Engineering and Industrial Aerodynamics*, vol. 61, no. 1, pp. 71–85, 1996.

[247] A. Wessel and B. Lange, "A new approach to calculate the turbulence intensity inside a wind farm," in *EWEC 2004*, pp. 1–6, 2004.

[248] G. N. Abramovich, *The Theory of Turbulent Jets*. Cambridge, Massachusetts: MIT Press, 1963.

[249] S. G. Voutsinas, J. P. Glekas, and A. Zervos, "Investigation of the effect of the initial velocity profile on the wake development of a wind turbine," *Journal of Wind Engineering and Industrial Aerodynamics*, vol. 39, no. 1-3, pp. 293–301, 1992.

[250] S. G. Voutsinas, K. G. Rados, and A. Zervos, "On the effect of the rotor geometry on the formation and the development of its wake," *Journal of Wind Engineering and Industrial Aerodynamics*, vol. 39, no. 1-3, pp. 283–291, 1992.

[251] P.-E. Réthoré and N. N. Sørensen, "Turbulence Closure Strategies for Modelling Wind Turbines Wake in Atmopsheric Turbulence," in *Euromech Colloquium 508 on Wind Turbine Wakes*, (Madrid, Spain), 2009.

[252] P.-E. Réthoré, N. N. Sørensen, A. Bechmann, and F. Zhale, "Study of the atmospheric wake turbulence of a CFD actuator disc model," *European Wind Energy Conference*, 2009.

[253] P.-E. Réthoré, N. N. Sørensen, and A. Bechmann, "CFD Model of wind turbine wake in atmospheric turbulence using body forces," in *IEA Offshore Wake Workshop*, 2009.

[254] I. H. Abbott, A. E. Von Doenhoff, and L. S. Stivers, Jr., "Summary of airfoil data," Tech. Rep. 824, National Advisory Committee for Aerodynamics, Langley Memorial Aeronautical Laboratory, Langley Field, Va., 1945.

[255] "NWTC Design Codes (AirfoilPrep by Dr. Craig Hansen)." `http://wind.nrel.gov/designcodes/preprocessors/airfoilprep/`. Last modified 09-March-2010; accessed 09-March-2010.

[256] "NPARC Alliance CFD Verification and Validation Web Site: Examining Spatial (Grid) Convergence." `http://http://www.grc.nasa.gov/WWW/wind/valid/tutorial/spatconv.html`. Last accessed 06-December-2011.

[257] P. J. Roache, "Quantification of Uncertainty in Computational Fluid Dynamics," *Annual Review of Fluid Mechanics*, vol. 29, no. 1, pp. 123–160, 1997.

[258] P. J. Roache, "Perspective: A Method for Uniform Reporting of Grid Refinement Studies," *Journal of Fluids Engineering*, vol. 116, pp. 405–413, 1994.

[259] H. G. Kim, C. M. Lee, H. C. Lim, and N. H. Kyong, "An experimental and numerical study on the flow over two-dimensional hills," *Journal of Wind Engineering and Industrial Aerodynamics*, vol. 66, no. 1, pp. 17–33, 1997.

[260] J. M. Jonkman, "Dynamics Modeling and Loads Analysis of an Offshore Floating Wind Turbine," Technical Report NREL/TP-500-41958, National Renewable Energy Laboratory, Golden, Colorado, November 2007.

[261] J. Jonkman, S. Butterfield, W. Musial, and G. Scott, "Definition of a 5-MW Reference Wind Turbine for Offshore System Development," Technical Report NREL/TP-500-38060, National Renewable Energy Laboratory, Golden, Colorado, 2009.

[262] P. A. Taylor, P. J. Mason, and E. F. Bradley, "Boundary-layer flow over Low Hills," *Boundary-Layer Meteorology*, vol. 39, no. 1, pp. 107–132, 1987.

[263] D. J. Watson, "Comparative physiological studies on the growth of field crops: I. variation in net assimilation rate and leaf area between species and varieties, and within and between years," *Annals of Botany*, vol. 11, no. 1, pp. 41–76, 1947.

[264] M. E. Teske and H. W. Thistle, "A library of forest canopy structure for use in interception modeling," *Forest Ecology and Management*, vol. 198, no. 1-3, pp. 341–350, 2004.

[265] B. D. Amiro, "Drag coefficients and Turbulence Spectra within three Boreal Forest Canopies," *Boundary-Layer Meteorology*, vol. 52, pp. 227–246, 1990.

[266] W. J. Massman, "Foliage distribution in old-growth coniferous tree canopies," *Canadian Journal of Forest Research*, vol. 12, no. 1, pp. 10–17, 1982.

[267] C. L. Bealde, H. Talbot, and P. G. Jarvis, "Canopy Structure and Leaf Area Index in a Mature Scots Pine Forest," *Forestry*, vol. 55, no. 2, pp. 105–123, 1982.

[268] T. Kerzenmacher and B. Gardiner, "A mathematical model to describe the dynamic response of a spruce tree to the wind," *Trees-Structure and Function*, vol. 12, no. 6, pp. 385–394, 1998.

[269] Z. Li, J. D. Lin, and D. R. Miller, "Air flow over and through a forest edge: a steady-state numerical simulation," *Boundary-Layer Meteorology*, vol. 51, no. 1, pp. 179–197, 1990.

[270] N. G. Mortensen, D. N. Heathfield, L. Myllerup, L. Landberg, and O. Rathmann, "Getting Started With WAsP 9," Tech. Rep. Risø-I-2571(EN), Risø National Laboratory, Roskilde, Denmark, 2007.

[271] "Corine Land Cover interactive map viewer, CORINE 2000." `http://www.eea.europa.eu/themes/landuse/interactive/clc-viewer`. Last accessed 09-February-2011.

[272] European Environment Agency, "Corine land cover 2000: mapping a decade of change." OPOCE (Office for Official Publications of the European Communities), 2004.

[273] J. Silva, C. Ribeiro, and R. Guedes, "Roughness length classification of Corine Land Cover classes," in *European Wind Energy Conference*, pp. 1–10, 2007.

[274] H. Charnock, "Wind stress on a water surface," *Quarterly Journal of the Royal Meteorological Society*, vol. 81, no. 350, pp. 639–640, 1955.

[275] R. J. Barthelmie, "Evaluating the impact of wind induced roughness change and tidal range on extrapolation of offshore vertical wind speed profiles," *Wind Energy*, vol. 4, no. 3, pp. 99–105, 2001.

[276] H. Frank, S. Larsen, and J. Højstrup, "Simulated Wind Power Off-shore Using Different Parametrizations for the Sea Surface Roughness," *Wind Energy*, vol. 3, no. 2, pp. 67–79, 2000.

[277] A. J. Bowen and N. G. Mortensen, "WAsP prediction errors due to site orography," Tech. Rep. Risø-R-995(EN), Risø National Laboratory, Roskilde, Denmark, 2004.

[278] K. S. Hansen, R. Barthelmie, D. Cabezon, and E. Politis, "Wake measurements used in the model evaluation," Deliverable D8.1, Project UpWind, 2008.

[279] "National GPS Network - Coordinate transformer - Great Britain." `http://gps.ordnancesurvey.co.uk/etrs89geo_natgrid.asp`. Ordnance Survey website. Last accessed 15-February-2011.

[280] "NOAA's Geophysical Data Center - Geomagnetic Data." `http://www.ngdc.noaa.gov/geomagmodels/struts/calcDeclination`. National Geophysical Data Center (NGDC) website. Last accessed 15-February-2011.

[281] K. Thomsen and S. Markkilde Petersen, "Experimental investigation of gear box duration loadings on stall and pitch controlled wind turbines," Tech. Rep. Risø-R-653(EN), Risø National Laboratory, Roskilde, Denmark, 1992.

[282] A. Wessel, *Development of a physical model for calculation of the turbulence inside wind farms*. PhD thesis, University of Oldenburg, 2008.

[283] R. J. Barthelmie, "The effects of atmospheric stability on coastal wind climates," *Meteorological Applications*, vol. 6, no. 1, pp. 39–47, 1999.

[284] R. J. Barthelmie, B. Grisogono, and S. C. Pryor, "Observations and simulations of diurnal cycles of near-surface wind speeds over land and sea," *Journal of Geophysical Research*, vol. 101, no. D16, pp. 21,327–21,337, 1996.

[285] J. P. Coelingh, A. van Wijk, and A. A. M. Holtslag, "Analysis of wind speed observations on the North Sea coast," *Journal of Wind Engineering and Industrial Aerodynamics*, vol. 73, no. 2, pp. 125–144, 1998.

[286] M. Z. Jacobson, *Fundamentals of Atmospheric Modeling*. Cambridge University Press, second ed., 2005.

[287] R. J. Barthelmie, L. Folkerts, G. C. Larsen, K. Rados, S. C. Pryor, F. S. T., B. Lange, and G. Schepers, "Comparison of Wake Model Simulations with Offshore Wind Turbine Wake Profiles Measured by Sodar," *Journal of Atmospheric and Oceanic Technology*, vol. 23, no. 7, pp. 888–901, 2006.

[288] K. Thomsen, P. Fuglsang, and G. Schepers, "Potentials for Site-Specific Design of MW Sized Wind Turbines," *Journal of Solar Energy Engineering*, vol. 123, pp. 304–309, 2001.

[289] "Details: AN Bonus 1 MW/54." `http://www.wind-energy-market.com/en/wind-turbines/big-plants/details/bp/an-bonus-1-mw54/`. Website maintained by the German Wind Energy Association (BWE). Last accessed 15-February-2011.

[290] P. Fuglsang and H. A. Madsen, "Optimization method for wind turbine rotors," *Journal of Wind Engineering and Industrial Aerodynamics*, vol. 80, no. 1-2, pp. 191–206, 1999.

[291] C. Bak, P. Fuglsang, N. N. Sørensen, H. A. Madsen, W. Z. Shen, and J. N. Sørensen, "Airfoil Characteristics for Wind Turbines," Tech. Rep. Risø-R-1065(EN), Risø National Laboratory, Roskilde, Denmark, 1999.

[292] P. Fuglsang, I. Antoniou, K. S. Dahl, and H. A. Madsen, "Wind Tunnel Tests of the FFA-W3-241, FFA-W3-301 and NACA 63-430 Airfoils," Tech. Rep. Risø-R-1041(EN), Risø National Laboratory, Roskilde, Denmark, 1998.

[293] A. McCluskey and A. G. Lalkhen, "Statistics II: Central tendency and spread of data," *Continuing Education in Anaesthesia, Critical Care & Pain*, vol. 7, no. 4, 2007.

[294] "Technical data about Siemens SWT-1.3-62 wind turbine." `http://www.thewindpower.net/wind-turbine-datasheet-24-siemens-swt-1.3-62.php`. The Wind Power: Wind turbines and windfarms database. Last accessed 10-March-2011.

[295] "Details: AN Bonus/Siemens 1.3 MW/62." `http://www.wind-energy-market.com/en/wind-turbines/big-plants/details/bp/an-bonussiemens-13-mw62/`. Website maintained by the German Wind Energy Association (BWE). Last accessed 10-March-2011.

[296] BONUS Energy A/S, *BONUS 1.3 MW B30 Technical Specificiations*, 2002.

[297] BWEA, "Workshop on the influence of trees on wind farm energy yields." `http://www.bwea.com/planning/trees.html`, 2004. Last accessed 10-April-2011.

[298] B. S. Nielsen and H. Stiesdal, "Trees , Forests and Wind Turbines - A Manufacturer s View," in *Workshop on the influence of trees on wind farm energy yields*, (Glasgow, UK), 2004.

[299] K. Reutter, R. G. J. Flay, and E. M. McIntosh, "An Application of the WAsP Program in Complex, Forested Terrain as Part of a Wind Farm Feasibility Study," *Wind Engineering*, vol. 29, no. 6, pp. 491–502, 2005.

[300] B. D. Amiro, "Comparison of Turbulence Statistics within three Boreal Forest Canopies," *Boundary-Layer Meteorology*, vol. 51, pp. 99–121, 1990.

[301] R. J. Barthelmie, E. S. Politis, J. M. Prospathopoulos, K. Hansen, K. G. Rados, S. T. Frandsen, O. Rathmann, W. Schlez, J. Phillips, G. Schepers, S. P. van Der Pijl, and D. Cabezón, "Wakes in large offshore wind farms; model evaluation in upwind," in *EOW 2007*, (Berlin, Germany), 2007.

[302] R. J. Barthelmie, S. Pryor, S. T. Frandsen, K. Hansen, J. G. Schepers, K. Rados, W. Schlez, A. Neubert, L. E. Jensen, and S. Neckelmann, "Improved modelling of power output in large offshore wind farms based on data from Nysted and Horns Rev," in *Euromech Colloquium 508 on Wind Turbine Wakes*, (Madrid, Spain), 2009.

[303] I. H. Abbott and A. E. Von Doenhoff, *Theory of wing sections*. Dover Publications, 1959.

Appendix A

Airfoil lift and drag coefficients

This Appendix includes the graphs generated by the tables of lift and drag coefficient vs. angle of attack, which were used in the VBM. For the procedure of generating the airfoil aerodynamic tables, see Sec. 4.5. In most cases, the data were taken from the NACA Report TR-824 [254]. The same data were also included in the book "Theory of Wing Sections" by Abott and Von Doenhoff [303]. Using the AirfoilPrep workbook [255], the data were further expanded to include a $-180°$ to $+180°$ angle of attack range, as required by the VBM.

Fig. A.1 shows a plot of the airfoil aerodynamic data used in the Nibe rotor of Chapter 4. The data were taken from the NACA Report TR-824 [254].

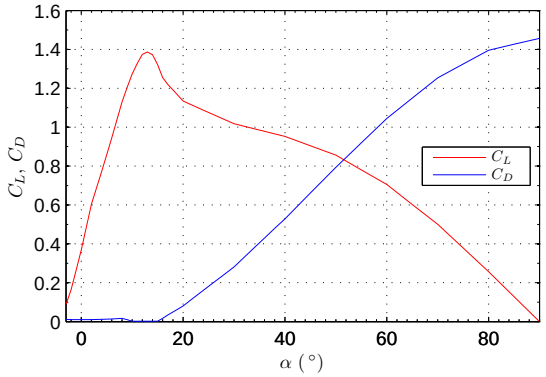

Figure A.1. Lift and drag coefficients of the NACA-4412 airfoil, based on [254].

Fig. A.2 presents the data of the NREL 5 MW rotor airfoils, used in Chapter 5. The data were taken from a NREL technical report prepared by Jonkman [260].

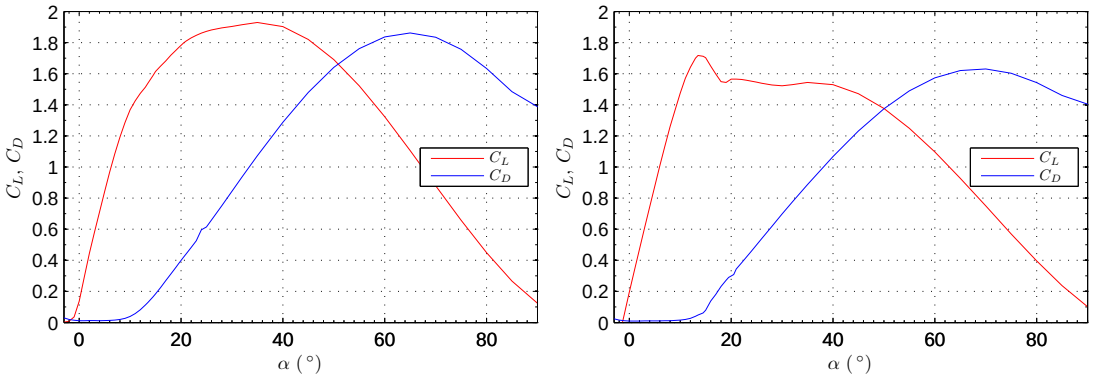

(a) DU 40 (b) DU 35

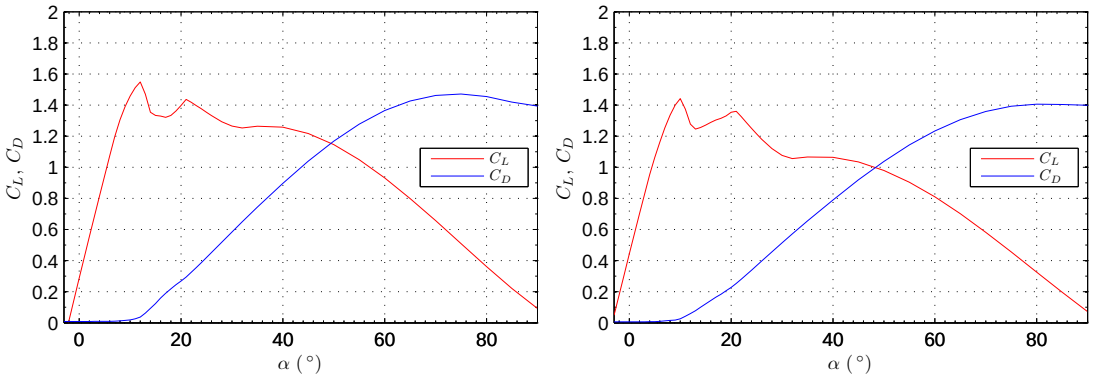

(c) DU 30 (d) DU 25

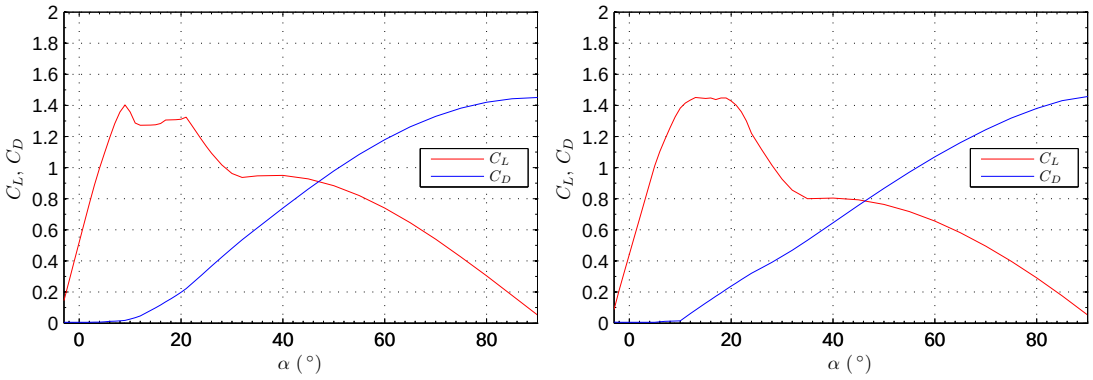

(e) DU 21 (f) NACA 64618

Figure A.2. Lift and drag coefficients of the NREL 5 MW rotor airfoils, based on [260].

Finally, Fig. A.3 displays the graphs of the lift and drag coefficient data, which

correspond to the airfoils of the 1 MW and 1.3 MW rotors used in Chapters 8 and 9. The data of the FFA-W3-301 and FFA-W3-241 airfoils were taken from Fuglsang et al. [292], whereas the data from the NACA 63-206 and NACA 63_3-618 airfoils were based on the the NACA Report TR-824 [254].

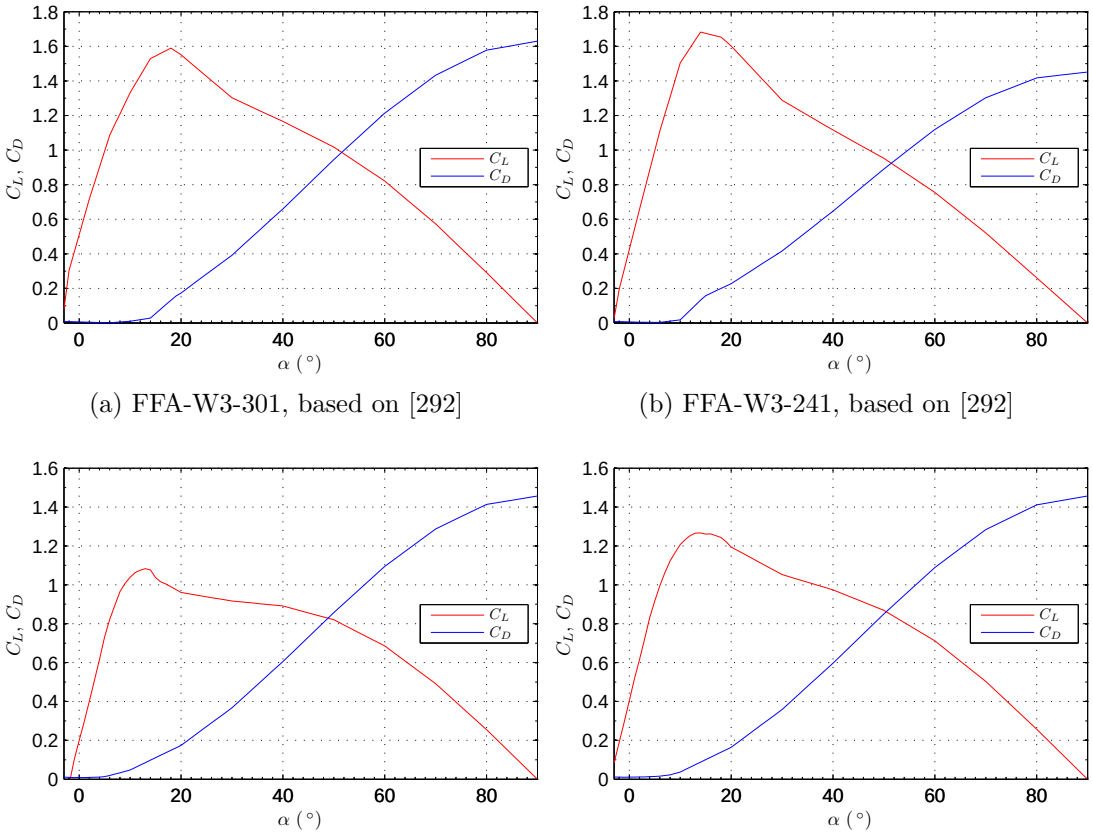

(a) FFA-W3-301, based on [292]

(b) FFA-W3-241, based on [292]

(c) NACA 63-206, based on [254]

(d) NACA 63_3-618, based on [254]

Figure A.3. Lift and drag coefficients of the 1 MW and 1.3 MW rotor airfoils.

Appendix B

Calculation of the canopy model constants

B.1 Simplified RSM equations

The calculation of the constants of the canopy model was performed according to the procedure by Sanz [164], also followed recently by Lopes da Costa [171].

The calculations are based on the assumption of one-dimensional, neutrally stratified, fully developed flow. Another important assumption is that turbulence inside the forest is nearly isotropic, which is also noted by Ayotte et al. [179]. Such an assumption was also necessary, since the k-ε canopy models on which the current approach is based, also assume isotropic turbulence.

Within the canopy, the momentum equation, Eq. (3.5b), becomes:

$$0 = \frac{d}{dz}\left(\mu_t \frac{dU}{dz}\right) - \rho\, C_z\, U^2 \tag{B.1}$$

where $C_z = C_d\, \alpha$.

Using a Cartesian coordinate system in Eqs.(3.13), the normal Reynolds stress

equations in the canopy, become as follows:

$$0 = \frac{d}{dz}\left(\frac{\mu_t}{\sigma_k}\,\frac{d(\overline{u_i' u_i'})}{dz}\right) + P_{ii} + \phi_{ii} - \varepsilon_{ii} + S_{\overline{u_i' u_i'}} \tag{B.2}$$

where $i = x, y, z$.

Finally the ε equation (3.19) becomes:

$$0 = \frac{d}{dz}\left(\frac{\mu_t}{\sigma_\varepsilon}\,\frac{d\varepsilon}{dz}\right) + C_{\varepsilon 1}\,\frac{1}{2}\,P_{xx}\,\frac{\varepsilon}{k} - C_{\varepsilon 2}\,\rho\,\frac{\varepsilon^2}{k} + S_\varepsilon \tag{B.3}$$

In Eq. (B.2), P_{ii} is the normal Stress Production term calculated from Eq. (3.14) on each Cartesian coordinate as:

$$P_{xx} = -2\,\rho\,\overline{u'w'}\,\frac{dU}{dz} \tag{B.4}$$

$$P_{yy} = P_{zz} = 0 \tag{B.5}$$

Assuming that the Boussinesq approximation applies inside the forest, as in the k-ε model, and using Eq. (3.7) with Eq. (B.4), the normal Stress Production at the x-direction becomes:

$$P_{xx} = 2\,\mu_t\left(\frac{dU}{dz}\right)^2 \tag{B.6}$$

The normal Pressure Strain term ϕ_{ii} is modeled according to Eq. (3.15), which becomes:

$$\phi_{ii} = -C_1\,\rho\,\frac{\varepsilon}{k}\left(\overline{u_i' u_i'} - \frac{2}{3}\,k\right) - C_2\,P_{ii} \tag{B.7}$$

Using Eq. (3.17), the Dissipation term becomes:

$$\varepsilon_{ii} = \frac{2}{3}\,\rho\,\varepsilon \tag{B.8}$$

B.2 Source terms

The normal Reynolds stress source terms $S_{\overline{u_i' u_i'}}$ in Eq. B.2 were derived from the k source equation S_k proposed by Sanz [164]:

$$S_k = \rho\, C_z \left(\beta_p\, U^3 - \beta_d\, U\, k\right) \tag{B.9}$$

Using Eq. (3.20) and eqAp:Sk1, the sum of the normal Reynolds Stress sources can be expressed as:

$$S_{\overline{u'u'}} + S_{\overline{v'v'}} + S_{\overline{w'w'}} = \rho\, C_z \left(2\, \beta_p\, U^3 - 2\, \beta_d\, Uk\right) \tag{B.10}$$

According to the approach of Ayotte et al. [179], turbulence within the canopy is close to being isotropic and for that reason, the turbulence wake production, which is expressed by the positive term of Eq. (B.10), is partitioned isotropically. However, dissipation, which is expressed by the negative term of Eq. (B.10), acts anisotropically on the normal Reynolds Stresses diminishing the horizontal stress $\overline{u'u'}$ more than the other two ($\overline{v'v'}$ and $\overline{w'w'}$) in order to "isotropise" turbulence.

According to the above approach a new dissipation coefficient for each of the normal Reynolds stresses ($\beta_{d,u}$, $\beta_{d,v}$, $\beta_{d,w}$) is introduced. Assuming an isotropic partition of the production term and anisotropic partition of the dissipation term [179], each of the source terms is modelled as:

$$S_{\overline{u'u'}} = \rho\, C_z \left(\frac{2}{3}\, \beta_p\, U^3 - \frac{2}{3}\, \beta_{d,u}\, U\, k\right) \tag{B.11}$$

$$S_{\overline{v'v'}} = \rho\, C_z \left(\frac{2}{3}\, \beta_p\, U^3 - \frac{2}{3}\, \beta_{d,v}\, U\, k\right) \tag{B.12}$$

$$S_{\overline{w'w'}} = \rho\, C_z \left(\frac{2}{3}\, \beta_p\, U^3 - \frac{2}{3}\, \beta_{d,w}\, U\, k\right) \tag{B.13}$$

Using Eqs.(B.11)–(B.13) in (B.10), it follows that:

$$\beta_d = \frac{\beta_{d,u} + \beta_{d,v} + \beta_{d,w}}{3} \tag{B.14}$$

Finally, the ε source S_ε was modelled according to Liu et al. [163] and Sanz [164], as following:

$$S_\varepsilon = \rho\, C_z \left(C_{\varepsilon 4}\, \beta_p\, \frac{\varepsilon}{k}\, U^3 - C_{\varepsilon 5}\, \beta_d\, U\, \varepsilon \right) \tag{B.15}$$

B.3 Canopy flow variables

Away from any boundaries and within a dense and homogeneous canopy the mixing length l_m can be assumed to be constant. According to the procedure followed by Sanz [164] the turbulence viscosity μ_t can be linked to the mixing length l_m according to Eq. (B.16).

$$\mu_t = \rho\, l_m^2\, \frac{dU}{dz} \tag{B.16}$$

Following a model by Wilson and Shaw [173], the mixing length is defined as:

$$l_m = \frac{\alpha'}{C_z} \tag{B.17}$$

where α' is a dimensionless coefficient, estimated by Massman and Weil [178] to have a value of 0.05.

According to Sanz [164], the exponentially decaying velocity profile which satisfies Eq. (B.1), using Eqs.(B.16) and (B.17) is the following:

$$\frac{dU}{dz} = \frac{C_z}{(2\alpha'^2)^{1/3}}\, U \tag{B.18}$$

The turbulent viscosity can also be expressed as:

$$\mu_t = \rho \, C_\mu^{\frac{1}{4}} \, l_m \, k^{\frac{1}{2}} \tag{B.19}$$

Using (B.16) with (B.18) and equalling with (B.19), an expression for k is derived:

$$k = \frac{\left(\frac{\alpha'}{2}\right)^{\frac{2}{3}}}{C_\mu^{\frac{1}{2}}} \, U^2 \tag{B.20}$$

The turbulence dissipation rate ε can be calculated using Kolmogorov's relation for high Reynolds number flows:

$$\varepsilon = C_\mu^{\frac{3}{4}} \, \frac{k^{\frac{3}{2}}}{l_m} \tag{B.21}$$

Combining Eqs.(B.21), (B.20) and (B.17):

$$\varepsilon = \frac{C_z}{2} \, U^3 \tag{B.22}$$

The vertical derivatives of k and ε are also useful in the following calculations, thus their expressions were simplified into:

$$\frac{dk}{dz} = \frac{C_z}{\sqrt{C_\mu}} \, U^2 \tag{B.23}$$

$$\frac{d\varepsilon}{dz} = 3 \, \frac{C_z^2}{(4\alpha')^{\frac{2}{3}}} \, U^3 \tag{B.24}$$

B.4 Canopy model coefficients

B.4.1 Calculation of β_p and β_d

Considering the sum of only the normal stress equations of Eq. (B.2) ($i = x, y$ and z) and using the equations of Sec. B.3, the terms of Eq. (B.2) can be transformed into simpler expressions.

Taking into account Eq. (3.20), the sum of the Diffusion term becomes:

$$\sum_{i=x,y,z} \frac{d}{dz}\left(\frac{\mu_t}{\sigma_k}\frac{d(\overline{u_i' u_i'})}{dz}\right) = \frac{6}{\sigma_k}\left(\frac{\alpha'}{2}\right)^{\frac{2}{3}} \frac{1}{\sqrt{C_\mu}}\,\rho\, C_z\, U^3 \tag{B.25}$$

The Stress Production term of Eq. (B.6) can be written as:

$$\sum_{i=x,y,z} P_{ii} = P_{xx} = \rho\, C_z\, U^3 \tag{B.26}$$

The Pressure Strain term of Eq. (B.7), is calculated as:

$$\sum_{i=x,y,z} \phi_{ii} = -C_2\, P_{xx} = -C_2\, \rho\, C_z\, U^3 \tag{B.27}$$

and the Dissipation term:

$$\sum_{i=x,y,z} \varepsilon_{ii} = 2\,\rho\,\varepsilon = \rho\, C_z\, U^3 \tag{B.28}$$

Finally the sum of the source terms is:

$$\sum_{i=x,y,z} S_{\overline{u_i' u_i'}} = 2\, S_k = 2\,\rho C_z\, U^3 \left[\beta_p - \beta_d \left(\frac{\alpha'}{2}\right)^{\frac{2}{3}} \frac{1}{\sqrt{C_\mu}}\right] \tag{B.29}$$

Taking the sum of the normal Reynolds stress equations of Eq. (B.2) and using Eqs.B.25, (B.26), (B.27), (B.28), (B.11) in combination with the Eqs. of Sec. B.3,

a new relation between β_d and β_p is derived:

$$\beta_d = \frac{3}{\sigma_k} + \left(\beta_p - \frac{C_2}{2}\right)\left(\frac{2}{\alpha'}\right)^{\frac{2}{3}}\sqrt{C_\mu} \tag{B.30}$$

Using $\beta_p = 1$, $\beta_d \approx 5.15$.

B.4.2 Calculation of $\beta_{d,u}$, $\beta_{d,v}$ and $\beta_{d,w}$

Each of the normal Reynolds Stress equations (B.2) is considered separately as in Sec. B.4.1, for the calculation of the dissipation coefficients $\beta_{d,u}$, $\beta_{d,v}$ and $\beta_{d,w}$, assuming isotropic turbulence inside the forest ($\overline{u'u'} = \overline{v'v'} = \overline{w'w'} = 2k/3$).

For the horizontal normal stress $\overline{u'u'}$ equation each terms are calculated as following:

$$\frac{d}{dz}\left(\frac{\mu_t}{\sigma_k}\frac{d(\overline{u'u'})}{dz}\right) = \frac{2}{\sigma_k}\left(\frac{\alpha'}{2}\right)^{\frac{2}{3}}\frac{1}{\sqrt{C_\mu}}\,\rho\,C_z\,U^3 \tag{B.31}$$

$$P_{xx} = \rho\,C_z\,U^3 \tag{B.32}$$

$$\phi_{xx} = -C_2\,P_{xx} = -C_2\,\rho\,C_z\,U^3 \tag{B.33}$$

$$\varepsilon_{xx} = \frac{1}{3}\rho\,C_z\,U^3 \tag{B.34}$$

$$S_{\overline{u'u'}} = \frac{2}{3}\,\rho C_z\,U^3\left[\beta_p - \beta_{d,u}\left(\frac{\alpha'}{2}\right)^{\frac{2}{3}}\frac{1}{\sqrt{C_\mu}}\right] \tag{B.35}$$

The relation between $\beta_{d,u}$ as a function of β_p is found to be:

$$\beta_{d,u} = \frac{3}{\sigma_k} + \left(\beta_p + 1 - \frac{3}{2}\,C_2\right)\left(\frac{2}{\alpha'}\right)^{\frac{2}{3}}\sqrt{C_\mu} \tag{B.36}$$

Using $\beta_p = 1$ the dissipation coefficient is found to be $\beta_{d,u} \approx 6$.

A similar procedure is followed using the Reynolds Stress equations in the y and z direction. The terms are found to be the same and they are summarized as

follows:

$$\frac{d}{dz}\left(\frac{\mu_t}{\sigma_k}\frac{d(\overline{v'v'})}{dz}\right) = \frac{d}{dz}\left(\frac{\mu_t}{\sigma_k}\frac{d(\overline{w'w'})}{dz}\right) = \frac{2}{\sigma_k}\left(\frac{\alpha'}{2}\right)^{\frac{2}{3}}\frac{1}{\sqrt{C_\mu}}\,\rho\,C_z\,U^3 \tag{B.37}$$

$$P_{yy} = P_{zz} = 0 \tag{B.38}$$

$$\phi_{yy} = \phi_{zz} = 0 \tag{B.39}$$

$$\varepsilon_{yy} = \varepsilon_{zz} = \frac{1}{3}\rho\,C_z\,U^3 \tag{B.40}$$

$$S_{\overline{v'v'}} = \frac{2}{3}\,\rho C_z\,U^3\left[\beta_p - \beta_{d,v}\left(\frac{\alpha'}{2}\right)^{\frac{2}{3}}\frac{1}{\sqrt{C_\mu}}\right] \tag{B.41}$$

$$S_{\overline{w'w'}} = \frac{2}{3}\,\rho C_z\,U^3\left[\beta_p - \beta_{d,w}\left(\frac{\alpha'}{2}\right)^{\frac{2}{3}}\frac{1}{\sqrt{C_\mu}}\right] \tag{B.42}$$

The resulting dissipation coefficients $\beta_{d,v}$ and $\beta_{d,w}$ and found to be:

$$\beta_{d,v} = \beta_{d,w} = \frac{3}{\sigma_k} + \left(\beta_p - \frac{1}{2}\right)\left(\frac{2}{\alpha'}\right)^{\frac{2}{3}}\sqrt{C_\mu} \tag{B.43}$$

The resulting values were $\beta_{d,v} = \beta_{d,w} = 4.72$.

The values of β_d, $\beta_{d,u}$, $\beta_{d,v}$ and $\beta_{d,w}$ verify Eq. (B.30).

B.4.3 Calculation of $C_{\varepsilon 4}$ and $C_{\varepsilon 5}$

A similar procedure is followed for the calculation of $C_{\varepsilon 4}$ and $C_{\varepsilon 5}$ using Eq. (B.3). The terms of the ε equation can be transformed in the following expressions:

$$\frac{d}{dz}\left(\frac{\mu_t}{\sigma_\varepsilon}\frac{d\varepsilon}{dz}\right) = \frac{3}{\sigma_\varepsilon}\rho C_z^2 U^4 \tag{B.44}$$

$$C_{\varepsilon 1}\,\frac{1}{2}\,P_{xx}\,\frac{\varepsilon}{k} = \frac{1}{4}\,C_{\varepsilon 1}\,\rho\,C_z^2\,U^4\,\sqrt{C_\mu}\left(\frac{2}{\alpha'}\right)^{\frac{2}{3}} \tag{B.45}$$

$$-C_{\varepsilon 2}\,\rho\,\frac{\varepsilon^2}{k} = -\frac{1}{4}\,C_{\varepsilon 2}\,\rho\,C_z^2\,U^4\,\sqrt{C_\mu}\left(\frac{2}{\alpha'}\right)^{\frac{2}{3}} \tag{B.46}$$

$$S_\varepsilon = \frac{1}{2}\,\rho\,C_z^2\,U^4\left[C_{\varepsilon 4}\beta_p\,\sqrt{C_\mu}\left(\frac{2}{\alpha'}\right)^{\frac{2}{3}} - C_{\varepsilon 5}\beta_d\right] \tag{B.47}$$

The calculations lead to the expression:

$$C_{\varepsilon 5}\beta_d = \sqrt{C_\mu}\left(\frac{2}{\alpha'}\right)^{\frac{2}{3}}\left(C_{\varepsilon 4}\beta_p - \frac{C_{\varepsilon 2}-C_{\varepsilon 1}}{2}\right) + \frac{6}{\sigma_\varepsilon} \tag{B.48}$$

which was also derived by Sanz [164], as the ε equation in the RSM is essentially the same as in the k-ε model [213].

However, using Eq. (B.48) with (B.30), the final expression for $C_{\varepsilon 4}$ and $C_{\varepsilon 5}$ is different:

$$C_{\varepsilon 4}\,(=C_{\varepsilon 5}) = \frac{\frac{6}{\sigma_\varepsilon} - \sqrt{C_\mu}\left(\frac{2}{\alpha'}\right)^{\frac{2}{3}}\frac{C_{\varepsilon 2}-C_{\varepsilon 1}}{2}}{\frac{3}{\sigma_k} - \sqrt{C_\mu}\left(\frac{2}{\alpha'}\right)^{\frac{2}{3}}\frac{C_2}{2}} \tag{B.49}$$

Taking into account the constants of the RSM, and the previously calculated β_p and β_d, the value of the constants $C_{\varepsilon 4}$ and $C_{\varepsilon 5}$ is found to be 1.07.

Appendix C

Example of a User-Defined Function

The following UDF was used for the simulations of the case of Sec. 9.6. A similar approach was used in all the other cases.

```
/*********************************************************

   Calculations - Wind Farm near forests:  Case T22-T21-T15

/*********************************************************/

#include "udf.h"        /* necessary for UDF */
#define pi 4.*atan(1.)  /* define pi */

real h=16.;         /* Height of the forest */
real h_ABL=1000.;   /* Height of ABL*/
real z_top=2550.;     /* Height of the top cell centroids */
real u_top=11.95;     /* Velocity at the top zone */
real z_o=0.028;     /* Roughness length of the ground*/
real z_of=0.563;    /* Roughness length of the forest*/

/* forest constants */
```

```
real Cmu=0.033;
real Ce1=1.44;
real Ce2=1.92;
real sigmak=0.82;
real sigmae=1.0;
real Ce4=1.07;
real Ce5=1.07;
real betap=1.0;
real betad=5.15;
real betadu=6;
real betadv=4.72;
real betadw=4.72;

/*forest constants*/
real LAI=10.0;
real sh=2.2;  /*for the Weibull distr */
real sc=2.2;
real hmin=3.84; /*hmin =  0.24*16 = 3.84*/



DEFINE_ON_DEMAND(on_demand_wall)    /*wall distance*/
{
Domain *d;
d = Get_Domain(1);
real xc[ND_ND];
Thread *ct;
cell_t c;

/*calculate the wall distance, store it as UDMI 0*/
thread_loop_c(ct,d)
  {
  begin_c_loop(c,ct)
    {
    C_CENTROID(xc,c,ct);
```

```
    C_UDMI(c,ct,0)=C_WALL_DIST(c,ct);
    }
  end_c_loop(c,ct)
  }
/*end of define_on_demand function*/
}

DEFINE_ON_DEMAND(on_demand_vel)    /*velocity*/
{
Domain *d;
d = Get_Domain(1);
real xc[ND_ND];
Thread *ct;
cell_t c;

/*calculate the hor.vel., store it as UDMI 1*/
thread_loop_c(ct,d)
  {
  begin_c_loop(c,ct)
    {
    C_CENTROID(xc,c,ct);
    C_UDMI(c,ct,1)=sqrt(C_U(c,ct)*C_U(c,ct)+C_V(c,ct)*C_V(c,ct));
    }
  end_c_loop(c,ct)
  }
/*end of define_on_demand function*/
}



/**********************************************
    UDF for the profile at the top zone
 **********************************************/


DEFINE_PROFILE(x_vel_top,thread,index)
```

```
{
  cell_t c;
  begin_c_loop(c,thread)
  {
  real x[ND_ND];
  C_CENTROID(x,c,thread);
  F_PROFILE(c,thread,index) = u_top;
  }
  end_c_loop(c,thread)
}

DEFINE_PROFILE(e_top,thread,index)
{
  cell_t c;
  begin_c_loop(c,thread)
  {
  real z, u_star;
  z = C_UDMI(c,thread,0);
  u_star=KAPPA*u_top/log((h_ABL+z_o)/z_o);

  F_PROFILE(c,thread,index) = u_star*u_star*u_star/(KAPPA*(z+z_o));
  }
  end_c_loop(c,thread)
}



/*********************************************************/
/*     UDF for specifying the forest    source terms      */
/*********************************************************/


DEFINE_SOURCE(k_source,c,t,dS,eqn)      /* k-source term */
{
  real x[ND_ND],z;
  real source, alpha, CD;
```

```
  real u=(C_U(c,t));
  real v=(C_V(c,t));
  real w=(C_W(c,t));
  real rho=C_R(c,t);
  real k=C_K(c,t);

  C_CENTROID(x,c,t);

z=C_UDMI(c,t,0)+z_of;

/*CD profile*/
real znorm = z/h;
if (znorm>0. && znorm<=0.45)
{CD=0.31;}
if (znorm>0.45 && znorm<=0.55)
{CD=-0.6*znorm+0.58;}
if (znorm>0.55 && znorm<=0.65)
{CD=-0.9*znorm+0.745;}
if (znorm>0.65 && znorm<=0.75)
{CD=-1.1*znorm+0.875;}
if (znorm>0.75 && znorm<=1.0)
{CD=-0.2*znorm+0.2;}

/*LAD profile */
if (z>hmin)
{alpha = LAI * (sh/sc) *pow((z-hmin)/sc,(sh-1)) * exp(-pow((z-hmin)/
    sc,sh));}
if (z<hmin)
{alpha =0;}

source = rho*CD*alpha*( betap*pow(u*u+v*v+w*w,3/2) - betad*k*sqrt(u*
    u+v*v+w*w) );
dS[eqn] = -1*rho*CD*alpha*betad*sqrt(u*u+v*v+w*w);

  return source;
```

```
}


DEFINE_SOURCE(e_source,c,t,dS,eqn)      /* epsilon-source term */
{
  real x[ND_ND],z,c1;
  real source, alpha, CD;
  real u=(C_U(c,t));
  real v=(C_V(c,t));
  real w=(C_W(c,t));
  real rho=C_R(c,t);
  real k=C_K(c,t);
  real e=C_D(c,t);

  C_CENTROID(x,c,t);

z=C_UDMI(c,t,0)+z_of;

/*CD profile*/
real znorm = z/h;
if (znorm>0. && znorm<=0.45)
{CD=0.31;}
if (znorm>0.45 && znorm<=0.55)
{CD=-0.6*znorm+0.58;}
if (znorm>0.55 && znorm<=0.65)
{CD=-0.9*znorm+0.745;}
if (znorm>0.65 && znorm<=0.75)
{CD=-1.1*znorm+0.875;}
if (znorm>0.75 && znorm<=1.0)
{CD=-0.2*znorm+0.2;}

/*LAD profile */
if (z>hmin)
{alpha = LAI * (sh/sc) *pow((z-hmin)/sc,(sh-1)) * exp(-pow((z-hmin)/
    sc,sh));}
```

```
if (z<hmin)
{alpha =0;}

source = rho*CD*alpha*(e/k)*( Ce4*betap*pow(u*u+v*v+w*w,3/2) - Ce5*
    betad*k*sqrt(u*u+v*v+w*w) );
dS[eqn] = (rho*CD*alpha/k)*( Ce4*betap*pow(u*u+v*v+w*w,3/2) - Ce5*
    betad*k*sqrt(u*u+v*v+w*w) );

  return source;
}


DEFINE_SOURCE(uu_source,c,t,dS,eqn)    /* uu-source term */
{
  real x[ND_ND],z;
  real source, alpha, CD;
  real u=(C_U(c,t));
  real v=(C_V(c,t));
  real w=(C_W(c,t));
  real rho=C_R(c,t);
  real uu=C_RUU(c,t);
  real vv=C_RVV(c,t);
  real ww=C_RWW(c,t);
  real k=C_K(c,t);
  real e=C_D(c,t);

  C_CENTROID(x,c,t);

z=C_UDMI(c,t,0)+z_of;

/*CD profile*/
real znorm = z/h;
if (znorm>0. && znorm<=0.45)
{CD=0.31;}
if (znorm>0.45 && znorm<=0.55)
```

```
{CD=-0.6*znorm+0.58;}
if (znorm>0.55 && znorm<=0.65)
{CD=-0.9*znorm+0.745;}
if (znorm>0.65 && znorm<=0.75)
{CD=-1.1*znorm+0.875;}
if (znorm>0.75 && znorm<=1.0)
{CD=-0.2*znorm+0.2;}

/*LAD profile */
if (z>hmin)
{alpha = LAI * (sh/sc) *pow((z-hmin)/sc,(sh-1)) * exp(-pow((z-hmin)/
    sc,sh));}
if (z<hmin)
{alpha =0;}

source = rho*CD*alpha*( betap*pow(u*u+v*v+w*w,3/2)*2/3 - betadu*(
    uu+vv+ww)*sqrt(u*u+v*v+w*w)/3 );
dS[eqn] = - betadu* rho*CD*alpha*sqrt(u*u+v*v+w*w)/3;

  return source;
}


DEFINE_SOURCE(vv_source,c,t,dS,eqn)    /* vv-source term */
{
  real x[ND_ND],z;
  real source, alpha, CD;
  real u=(C_U(c,t));
  real v=(C_V(c,t));
  real w=(C_W(c,t));
  real rho=C_R(c,t);
  real uu=C_RUU(c,t);
  real vv=C_RVV(c,t);
  real ww=C_RWW(c,t);
  real e=C_D(c,t);
```

```
  real k=C_K(c,t);

  C_CENTROID(x,c,t);

z=C_UDMI(c,t,0)+z_of;

/*CD profile*/
real znorm = z/h;
if (znorm>0. && znorm<=0.45)
{CD=0.31;}
if (znorm>0.45 && znorm<=0.55)
{CD=-0.6*znorm+0.58;}
if (znorm>0.55 && znorm<=0.65)
{CD=-0.9*znorm+0.745;}
if (znorm>0.65 && znorm<=0.75)
{CD=-1.1*znorm+0.875;}
if (znorm>0.75 && znorm<=1.0)
{CD=-0.2*znorm+0.2;}

/*LAD profile */
if (z>hmin)
{alpha = LAI * (sh/sc) *pow((z-hmin)/sc,(sh-1)) * exp(-pow((z-hmin)/
    sc,sh));}
if (z<hmin)
{alpha =0;}

source = rho*CD*alpha*( betap*pow(u*u+v*v+w*w,3/2)*2/3 - betadv*(
    uu+vv+ww)*sqrt(u*u+v*v+w*w)/3 );
dS[eqn] = - betadv* rho*CD*alpha*sqrt(u*u+v*v+w*w)/3;

  return source;
}


DEFINE_SOURCE(ww_source,c,t,dS,eqn)    /*ww-source term */
```

```
{
  real x[ND_ND],z;
  real source, alpha, CD;
  real u=(C_U(c,t));
  real v=(C_V(c,t));
  real w=(C_W(c,t));
  real rho=C_R(c,t);
  real uu=C_RUU(c,t);
  real vv=C_RVV(c,t);
  real ww=C_RWW(c,t);
  real e=C_D(c,t);
  real k=C_K(c,t);

  C_CENTROID(x,c,t);

z=C_UDMI(c,t,0)+z_of;

/*CD profile*/
real znorm = z/h;
if (znorm>0. && znorm<=0.45)
{CD=0.31;}
if (znorm>0.45 && znorm<=0.55)
{CD=-0.6*znorm+0.58;}
if (znorm>0.55 && znorm<=0.65)
{CD=-0.9*znorm+0.745;}
if (znorm>0.65 && znorm<=0.75)
{CD=-1.1*znorm+0.875;}
if (znorm>0.75 && znorm<=1.0)
{CD=-0.2*znorm+0.2;}

/*LAD profile */
if (z>hmin)
{alpha = LAI * (sh/sc) *pow((z-hmin)/sc,(sh-1)) * exp(-pow((z-hmin)/
    sc,sh));}
if (z<hmin)
```

```
{alpha =0;}

source = rho*CD*alpha*( betap*pow(u*u+v*v+w*w,3/2)*2/3 - betadw*(
    uu+vv+ww)*sqrt(u*u+v*v+w*w)/3 );
dS[eqn] = - betadw* rho*CD*alpha*sqrt(u*u+v*v+w*w)/3;

  return source;
}


DEFINE_SOURCE(xmom_source,c,t,dS,eqn)    /* xmom-source term */
{
  real x[ND_ND],z;
  real source, alpha, CD;
  real u=(C_U(c,t));
  real v=(C_V(c,t));
  real w=(C_W(c,t));
  real rho=C_R(c,t);
  C_CENTROID(x,c,t);

z=C_UDMI(c,t,0)+z_of;

/*CD profile*/
real znorm = z/h;
if (znorm>0. && znorm<=0.45)
{CD=0.31;}
if (znorm>0.45 && znorm<=0.55)
{CD=-0.6*znorm+0.58;}
if (znorm>0.55 && znorm<=0.65)
{CD=-0.9*znorm+0.745;}
if (znorm>0.65 && znorm<=0.75)
{CD=-1.1*znorm+0.875;}
if (znorm>0.75 && znorm<=1.0)
{CD=-0.2*znorm+0.2;}
```

```
/*LAD profile */
if (z>hmin)
{alpha = LAI * (sh/sc) *pow((z-hmin)/sc,(sh-1)) * exp(-pow((z-hmin)/
    sc,sh));}
if (z<hmin)
{alpha =0;}

source = -rho*CD*alpha*sqrt(u*u+v*v+w*w)*u;
dS[eqn] = -rho*CD*alpha*(2*u*u+v*v+w*w)/sqrt(u*u+v*v+w*w);

  return source;
}


DEFINE_SOURCE(ymom_source,c,t,dS,eqn)    /* ymom-source term */
{
  real x[ND_ND],z, c1;
  real source, alpha, CD;
  real u=(C_U(c,t));
  real v=(C_V(c,t));
  real w=(C_W(c,t));
  real rho=C_R(c,t);
  C_CENTROID(x,c,t);

z=C_UDMI(c,t,0)+z_of;

/*CD profile*/
real znorm = z/h;
if (znorm>0. && znorm<=0.45)
{CD=0.31;}
if (znorm>0.45 && znorm<=0.55)
{CD=-0.6*znorm+0.58;}
if (znorm>0.55 && znorm<=0.65)
{CD=-0.9*znorm+0.745;}
if (znorm>0.65 && znorm<=0.75)
```

```
{CD=-1.1*znorm+0.875;}
if (znorm>0.75 && znorm<=1.0)
{CD=-0.2*znorm+0.2;}

/*LAD profile */
if (z>hmin)
{alpha = LAI * (sh/sc) *pow((z-hmin)/sc,(sh-1)) * exp(-pow((z-hmin)/
    sc,sh));}
if (z<hmin)
{alpha =0;}

source = -rho*CD*alpha*sqrt(u*u+v*v+w*w)*v;
dS[eqn] = -rho*CD*alpha*(u*u+2*v*v+w*w)/sqrt(u*u+v*v+w*w);

  return source;
}


DEFINE_SOURCE(zmom_source,c,t,dS,eqn)    /* ymom-source term */
{
  real x[ND_ND],z, c1;
  real source, alpha, CD;
  real u=C_U(c,t);
  real v=C_V(c,t);
  real w=C_W(c,t);
  real rho=C_R(c,t);
  C_CENTROID(x,c,t);

z=C_UDMI(c,t,0)+z_of;

/*CD profile*/
real znorm = z/h;
if (znorm>0. && znorm<=0.45)
{CD=0.31;}
if (znorm>0.45 && znorm<=0.55)
```

```
{CD=-0.6*znorm+0.58;}
if (znorm>0.55 && znorm<=0.65)
{CD=-0.9*znorm+0.745;}
if (znorm>0.65 && znorm<=0.75)
{CD=-1.1*znorm+0.875;}
if (znorm>0.75 && znorm<=1.0)
{CD=-0.2*znorm+0.2;}

/*LAD profile */
if (z>hmin)
{alpha = LAI * (sh/sc) *pow((z-hmin)/sc,(sh-1)) * exp(-pow((z-hmin)/
    sc,sh));}
if (z<hmin)
{alpha =0;}

source = -rho*CD*alpha*sqrt(u*u+v*v+w*w)*w;

dS[eqn] = -rho*CD*alpha*(u*u+v*v+2*w*w)/sqrt(u*u+v*v+w*w);

  return source;
}



/************************************************
        Inlet profiles
 ************************************************/


DEFINE_PROFILE(in_Ux, thread, index)     /* velocity in x-direction
    */
{
real position[ND_ND], z, u_star;
face_t f;
Thread *tc0;
cell_t c0;
```

```
u_star=KAPPA*u_top/log((h_ABL+z_o)/z_o);

begin_f_loop(f,thread)
{
  F_CENTROID(position, f, thread);
  c0 = F_C0(f,thread);
  tc0 = THREAD_T0(thread);
  z = C_UDMI(c0,tc0,0);
  if(z<=h_ABL)
    {F_PROFILE(f, thread, index)= u_star*log((z+z_o)/z_o)/KAPPA;}
  else
    {F_PROFILE(f, thread, index)= u_top;}
  }
end_f_loop(f,thread)
}


DEFINE_PROFILE(in_k_RSM, thread, index)      /* k profile for RSM */
{
real position[ND_ND], z, u_star;
face_t f;
Thread *tc0;
cell_t c0;

u_star=KAPPA*u_top/log((h_ABL+z_o)/z_o);

begin_f_loop(f,thread)
  {
  F_CENTROID(position, f, thread);
  c0 = F_C0(f,thread);
  tc0 = THREAD_T0(thread);
  z = C_UDMI(c0,tc0,0);

  if(z<=h_ABL)
```

```
    {F_PROFILE(f,thread,index) = 0.5*((u_star*u_star*2.4*2.4)+(
        u_star*u_star*1.9*1.9)+(u_star*u_star*1.25*1.25));}
  else
    {F_PROFILE(f, thread, index)= 0.0;}
  }
end_f_loop(f,thread)
}


DEFINE_PROFILE(in_e, thread, index)      /* turbulence epsilon */
{
real position[ND_ND], z, u_star;
face_t f;
Thread *tc0;
cell_t c0;

u_star=KAPPA*u_top/log((h_ABL+z_o)/z_o);

begin_f_loop(f,thread)
  {
  F_CENTROID(position, f, thread);
  c0 = F_C0(f,thread);
  tc0 = THREAD_T0(thread);
  z = C_UDMI(c0,tc0,0);
  F_PROFILE(f, thread, index)= u_star*u_star*u_star/(KAPPA*(z+z_o));
  }
end_f_loop(f,thread)
}


DEFINE_PROFILE(uu_stress, thread, index)  /* uu Reynolds stress */
{
real position[ND_ND], z, y, u_star;
face_t f;
Thread *tc0;
```

```
cell_t c0;

u_star=KAPPA*u_top/log((h_ABL+z_o)/z_o);

begin_f_loop(f,thread)
  {
  F_CENTROID(position, f, thread);
  c0 = F_C0(f,thread);
  tc0 = THREAD_T0(thread);
  z = C_UDMI(c0,tc0,0);

  if(z<=h_ABL)
    {F_PROFILE(f,thread,index) = u_star*u_star*2.4*2.4;}
  else if(z>h_ABL)
  {F_PROFILE(f, thread, index)= 0.0;}
  }
end_f_loop(f,thread)
}


DEFINE_PROFILE(vv_stress, thread, index)  /* vv Reynolds stress */
{
real position[ND_ND], z, u_star;
face_t f;
Thread *tc0;
cell_t c0;

u_star=KAPPA*u_top/log((h_ABL+z_o)/z_o);

begin_f_loop(f,thread)
  {
  F_CENTROID(position, f, thread);
  c0 = F_C0(f,thread);
  tc0 = THREAD_T0(thread);
  z = C_UDMI(c0,tc0,0);
```

```
  if(z<=h_ABL)
    {F_PROFILE(f,thread,index) = u_star*u_star*1.9*1.9;}
  else
    {F_PROFILE(f, thread, index)= 0.0;}
  }
end_f_loop(f,thread)
}


DEFINE_PROFILE(ww_stress, thread, index)  /* ww Reynolds stress */
{
real position[ND_ND], z, u_star;
face_t f;
Thread *tc0;
cell_t c0;

u_star=KAPPA*u_top/log((h_ABL+z_o)/z_o);

begin_f_loop(f,thread)
  {
  F_CENTROID(position, f, thread);
  c0 = F_C0(f,thread);
  tc0 = THREAD_T0(thread);
  z = C_UDMI(c0,tc0,0);

  if(z<=h_ABL)
    {F_PROFILE(f,thread,index) = u_star*u_star*1.25*1.25;}
  else
    {F_PROFILE(f, thread, index)= 0.0;}
  }
end_f_loop(f,thread)
}
```

```
DEFINE_PROFILE(uw_stress, thread, index)  /* uw Reynolds shear
    stress */
{
real position[ND_ND], z, u_star;
face_t f;
Thread *tc0;
cell_t c0;

u_star=KAPPA*u_top/log((h_ABL+z_o)/z_o);

begin_f_loop(f,thread)
  {
  F_CENTROID(position, f, thread);
  c0 = F_C0(f,thread);
  tc0 = THREAD_T0(thread);
  z = C_UDMI(c0,tc0,0);

  if(z<=h_ABL)
    {F_PROFILE(f,thread,index) = u_star*u_star*(1-(z/h_ABL))*(1-(z/
        h_ABL));}
  else
    {F_PROFILE(f, thread, index)= 0.0;}
  }
end_f_loop(f,thread)
}



/*****************************************************
      Wall function
 *****************************************************/

DEFINE_PROFILE(Cs, thread, index)        /*Cs profile */
{
face_t f;
Thread *tc0;
```

```
cell_t c0;
real zp;

begin_f_loop(f,thread)
  {
  c0 = F_C0(f,thread);
  tc0 = THREAD_T0(thread);
  zp=C_UDMI(c0,tc0,0);
  F_PROFILE(f, thread, index)= 9.793*z_o/zp;
  }
end_f_loop(f,thread)
}

DEFINE_PROFILE(ks_prof, thread, index)     /*ks profile */
{
face_t f;
Thread *tc0;
cell_t c0;
real zp;

begin_f_loop(f,thread)
  {
  c0 = F_C0(f,thread);
  tc0 = THREAD_T0(thread);
  zp=C_UDMI(c0,tc0,0);
  F_PROFILE(f, thread, index)= zp;
  }
end_f_loop(f,thread)
}


/* summary of UDM values: --2--
0:wall distance
1:horizontal velocity
*/
```